UNIVERSITAT DE BARCELONA

Dark Matter and Massive Neutrinos: Cosmological Probes of Physics Beyond the Standard Model

Kathleen Short

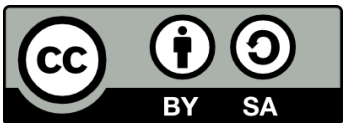

Doctoral Thesis

Dark Matter and Massive Neutrinos: Cosmological Probes of Physics Beyond the Standard Model

Kathleen Short

Universitat de Barcelona

TESI DOCTORAL

Dark Matter and Massive Neutrinos: Cosmological Probes of Physics Beyond the Standard Model

Memoria presentada para optar al grado de doctor
por la
Universitat de Barcelona
Programa de doctorado en Física

Autora:	*Tutor:*	*Directora:*
Kathleen SHORT	Dr. Alberto MANRIQUE	Prof. Licia VERDE

UNIVERSITAT DE BARCELONA

Publications

This thesis is based on the following publications:

[1] K. Short, J. L. Bernal, A. Raccanelli, L. Verde, and J. Chluba, *Enlightening the dark ages with dark matter*, J. Cosmology Astropart. Phys. **2020**, 020, 020 (2020), arXiv:1912.07409 [astro-ph.CO]

Presented in Chapter 2.

[2] K. Short, J. L. Bernal, K. K. Boddy, V. Gluscevic, and L. Verde, *Dark matter-baryon scattering effects on temperature perturbations and implications for cosmic dawn*, submitted to: J. Cosmology Astropart. Phys. (2022), arXiv:2203.16524 [astro-ph.CO]

Presented in Chapter 3.

[3] R. Jimenez, C. Pena-Garay, K. Short, F. Simpson, and L. Verde, *Neutrino masses and mass hierarchy: evidence for the normal hierarchy*, J. Cosmology Astropart. Phys. **2022**, 006 (2022), arXiv:2203.14247 [hep-ph]

Presented in Chapter 4.

Abstract

The overwhelming evidence for the existence of dark matter (DM) in the Universe, and the discovery of the neutrino masses, are striking indicators of the need for new physics beyond the ΛCDM and Standard Model paradigms. DM constitutes $\sim 85\%$ of the matter in the Universe, but its fundamental nature remains a mystery. Moreover, the physical mechanism responsible for the neutrino masses is unknown. A complete theoretical framework – consistent with all observations – that incorporates a microscopic description of DM into the standard models of cosmology and particle physics, as well as an understanding of the origin and scale of the neutrino masses, is a key common goal.

Cosmological observables are promising in this regard and can provide unique insights into the nature of these elusive particles. In this thesis, I focus on the synergy between cosmology and particle physics in answering these fundamental questions. To this end, I present examples of how upcoming measurements probing the high-redshift Universe can unveil new insights into the nature of DM and the complementarity between cosmological observations and terrestrial experiments in determining the neutrino mass hierarchy.

The first part of this thesis studies the electromagnetic signatures of non-gravitational DM interactions on cosmological observables. I compute the effects of DM decay and annihilation on the thermal and ionization history of the Universe, and the imprint on the cosmological 21 cm signal from the dark ages. I examine the potential to detect such a signature with forthcoming 21 cm line-intensity mapping measurements, presenting forecasted constraints for both upcoming and next-generation experiments.

Next, the effects of DM-baryon scattering on the post-recombination Universe are explored. In this work, I consider for the first time the direct contribution of such interactions on the baryon and DM temperature perturbations and the resulting evolution of cosmological density perturbations. In particular, I show that these contributions lead to a large enhancement of the baryon temperature power spectrum and a further suppression of matter clustering at small scales, which can alter both the amplitude and time evolution of the 21 cm signal from cosmic dawn and reionization.

Finally, I look at the question of neutrino masses and the mass hierarchy from the lens of cosmology. Cosmological surveys provide the tightest constraints on the absolute mass scale of neutrinos, and are closing in on the minimum mass bound allowed under the inverted hierarchy. Using the latest results from global fits to neutrino oscillations experiments combined with cosmological constraints on the sum of the masses, I perform a Bayesian analysis to constrain the individual neutrino masses and evaluate the Bayesian evidence for each of the neutrino mass orderings. The results show that current data provide a strong Bayesian preference for the normal mass hierarchy, even under widely different prior assumptions, which has important implications for particle physics.

Resumen

Las pruebas irrefutables de la existencia de la materia oscura (DM) en el Universo, y el descubrimiento de las masas de neutrinos, son llamativos indicadores de la necesidad de una nueva física más allá de los paradigmas ΛCDM y del Modelo Estándar. DM constituye el $\sim 85\%$ de la materia del Universo, pero su naturaleza fundamental sigue siendo un misterio. Además, se desconoce el mecanismo físico responsable de las masas de los neutrinos. Un marco teórico completo – coherente con todas las observaciones – que incorpore una descripción microscópica de la materia oscura a los modelos estándar de cosmología y física de partículas, así como una comprensión del origen y la escala de las masas de neutrinos, es un objetivo común clave.

Los observables cosmológicos son prometedores en este sentido y pueden proporcionar una visión única de la naturaleza de estas elusivas partículas. Esta tesis se centra en la sinergia entre la cosmología y la física de partículas para responder a estas cuestiones fundamentales. Para ello, presento ejemplos de cómo las próximas sondas cosmológicas pueden desvelar nuevos conocimientos sobre la naturaleza de la DM y la complementariedad entre las observaciones cosmológicas y los experimentos terrestres para determinar la jerarquía de masas de los neutrinos.

La primera parte de la investigación presentada en esta tesis estudia las firmas de las interacciones no gravitacionales de la DM en los observables cosmológicos. Calculo los efectos de la desintegración y la aniquilación de DM en la historia térmica y de ionización del Universo, y la huella en la señal cosmológica de 21 cm de las Dark Ages. Examino el potencial para detectar dicha señal con las futuras observaciones de 21 cm y presento las limitaciones previstas para los experimentos próximos y de próxima generación. A continuación, se exploran los efectos cosmológicos de la dispersión elástica entre el DM y los bariones. En este trabajo, considero por primera vez la contribución directa de estas interacciones en las perturbaciones de temperatura de los bariones y de la DM y la evolución resultante de las perturbaciones de densidad cosmológicas. En particular, muestro que estas contribuciones conducen a un gran aumento del espectro de potencia de la temperatura de los bariones y a una mayor supresión de las fluctuaciones de la materia a escalas pequeñas, lo que puede alterar tanto la amplitud como la evolución temporal de la señal de 21 cm de las épocas del Cosmic Dawn y la Reionización.

En la segunda parte de esta tesis, examino la cuestión de las masas de los neutrinos y la jerarquía de masas desde el punto de vista de la cosmología. Los estudios cosmológicos proporcionan las restricciones más estrictas sobre la escala de masa absoluta de los neutrinos, y se están acercando al límite mínimo de masa permitido bajo la jerarquía invertida. Utilizando los últimos resultados de los ajustes globales de los experimentos de oscilaciones de neutrinos, combinados con las restricciones cosmológicas sobre la suma de las masas, realizo un análisis Bayesiano para inferir las masas individuales de los neutrinos y evaluar la evidencia Bayesiana para cada uno de los ordenamientos de masas de neutrinos. Los resultados muestran que los datos actuales proporcionan una fuerte

preferencia Bayesiana por la jerarquía de masas normal, incluso bajo probabilidades a priori muy diferentes, lo que tiene importantes implicaciones para la física de partículas.

Finalmente, concluyo la tesis con un resumen de los resultados clave y examino su relevancia dentro del contexto más amplio del campo. Además, discuto las perspectivas futuras y las posibles vías de seguimiento de este trabajo.

Contents

Chapter 1

Introduction

Cosmology is the science of understanding the origin, evolution and composition of the Universe as a whole. Having its roots in ancient philosophy, in the last few decades, the field of cosmology has transformed into an observational, data-driven science. We are now in the era of so-called "precision cosmology" thanks to advances in technology providing us with a wealth of cosmological observations, enabling the study of the Universe from its infancy – moments after the Big Bang – via the Cosmic Microwave Background (CMB) to the present day distribution of matter and galaxies from measurements of the Large-Scale Structure (LSS) of the Universe. These measurements, in combination with other observations on galactic scales, have confirmed that the Universe is filled with an invisible *dark matter* component. Moreover, measurements of the recessional velocities of Type Ia supernovae (SNeIa) have led to the discovery of the late-time accelerated expansion of the Universe, driven by *dark energy*. These observations in tandem with major theoretical developments have led to the establishment of the prevailing paradigm of cosmology today: the Λ-Cold Dark Matter (ΛCDM) model, describing a Universe dominated by a cosmological constant Λ (dark energy) and cold dark matter (CDM).

ΛCDM is a concordance model. It is the simplest and most explanatory model that can reproduce exceptionally well a whole host of independent cosmological observations, spanning vastly different physical scales and times in cosmic history. It expands upon the original hot Big Bang model to include the theory of inflation, dark matter and dark energy. However, despite its enormous success, it remains a mostly phenomenological model; the dark components of the Universe contribute $\sim$95% of the cosmic energy density, but a theoretical underpinning of their nature and origin is lacking. The Standard Model of particle physics (SM), which describes the sub-atomic particles and fundamental forces of all known matter, only accounts for the other 5% of the Universe. A new species of matter is needed to explain dark matter, with the most promising

candidate being a new fundamental particle beyond the SM. Additionally, answers to open questions about the early Universe – e. g., what drives inflation? – will likely depend on beyond-the-SM (BSM) physics at higher energy scales. A complete cosmological model of the Universe must address the origin and nature of its fundamental ingredients, for which a consistent theory of matter on the smallest microscopic scales and the highest energies is required.

In addition to the dearth of a particle dark matter candidate, there is other observational evidence that the SM is not complete. The SM has been remarkably successful in describing all experimental results to date, with the notable exception of the discovery of neutrino oscillations. Within the SM framework, neutrinos are massless particles; however, neutrino oscillations are only possible if neutrinos have non-zero mass, and thus constitute direct evidence for BSM physics. Massive neutrinos have important cosmological consequences, leaving unique imprints on the expansion rate and structure formation history of the Universe. They contribute to the matter energy budget of the Universe today and thus, in fact, constitute a tiny fraction (less than $\sim 1\%$) of the total dark matter density.

Understanding the nature of dark matter and neutrinos are key open problems at the interface of cosmology and particle physics. As such, major experimental efforts are underway to try to detect dark matter particles and measure the neutrino mass scale. Cosmological observables are promising in this regard and can provide unique insights into the nature of these elusive particles. In this thesis, I present research that highlights the potential of future cosmological probes of dark matter and the complementarity between cosmological observations and terrestrial experiments in inferring the individual neutrino masses and their ordering. This introductory chapter will set the stage for the subsequent chapters: I provide a brief overview of the ΛCDM model in Section 1.1; followed by a review of the astrophysical and cosmological evidence for dark matter, as well as particle candidates and detection methods, in Section 1.2; and finally, a short introduction to neutrino oscillations and the role of massive neutrinos in cosmology is given in Section 1.3.

1.1 The Standard Cosmological Model: ΛCDM

Modern cosmology is built upon a mathematical framework that describes the evolution of the Universe on the largest observable scales. Two cornerstones upon which it rests are Einstein's theory of General Relativity (GR) [4] and *the cosmological principle*. The cosmological principle states that the Universe is

homogeneous and isotropic at sufficiently large scales. Although a fundamental assumption of modern cosmology, there is observational evidence to support it; measurements of the CMB and galaxy surveys show that the Universe is very near isotropic on scales larger than $100\,\mathrm{Mpc}^{-1}$ [5–8] and any possible deviation would be negligible. Homogeneity has also been tested [9–11].

On the other hand, GR has been extensively tested and verified by numerous observations [12–14]. More recently, the detection of gravitational waves from binary black hole and neutron star mergers by the LIGO and Virgo collaborations [15–21] is in spectacular agreement with the predictions of GR. Furthermore, the latest Event Horizon Telescope observations also prove to be consistent with GR [22–24]. To date, no deviation from GR has been detected at the length and energy scales probed.

The publication of Einstein's theory of GR, and the first cosmological solutions of a dynamic Universe found shortly thereafter [25, 26], marked the birth of modern cosmology roughly 100 years ago. Around the same time, the first modern reflecting telescopes began operating at the Mount Wilson Observatory, opening up the exploration of the Universe beyond our own galaxy. Famously, in 1929 Hubble discovered that galaxies were receding from us with a velocity directly proportional to their distance from Earth [27]; more distant galaxies were moving away faster, corresponding to an expanding Universe.[1] Extrapolating the cosmic expansion backwards in time, Lemaître proposed the first idea of a "primeval atom" or singularity as the origin of Universe [28]. Hot Big Bang cosmology flourished with the development of Big-Bang nucleosynthesis (BBN) in the 1940s by Alpher, Bethe and Gamow [29, 30], which correctly predicted the observed abundance of light elements in the Universe and anticipated the existence of a relic radiation left over from the Big Bang, the CMB. The serendipitous discovery of the CMB radiation by Penzias and Wilson [31], and interpretation as such [32] – i. e., relic radiation from the hot, primordial Universe – provided strong support for the Big Bang theory.

While the hot Big Bang model was highly successful, big questions remained regarding the origin and formation of the observed structure in the Universe today. Within the ΛCDM framework, *inflation* and *cold dark matter* provide the answer. A key pillar of modern cosmology is the assumption of inflation, a period of rapid, accelerated expansion in the very early Universe which stretched out initial quantum fluctuations and seeded the large-scale structure observed

[1] In fact, Lemaître already made this connection prior to Hubble's observations; he independently discovered the expanding Universe solution to Einstein's equations and formulated the observational relationship between distance and recessional velocity, providing a first estimate of the Hubble constant based on data available at the time [26].

today. In the simplest models, inflation is driven by a scalar field whose initial quantum fluctuations are blown up to classical scales by the expansion, generating the primordial density perturbations. As the Universe evolves, these primordial density perturbations grow under gravity, eventually forming the galaxies, galaxy clusters, superclusters, filaments and voids that make up the vast cosmic web of structure. While inflation provides the initial conditions, a non-baryonic matter component is needed for these structures to form. Today, a suite of astrophysical and cosmological observations prove that the majority of the matter in the Universe is made up of this invisible dark matter, as we will discuss in detail in Section 1.2.

The first detection of the CMB anisotropies by the COBE collaboration [33] was in agreement with the predictions of inflation and cold dark matter, and ushered in the era of precision cosmology. Later, the discovery of the accelerated expansion of the Universe from observations of SNeIa [34, 35] in the 1990s put in place the last major component of the ΛCDM model: *dark energy*. Dark energy is modelled as a fluid with negative pressure which drives the late-time accelerated expansion and is well-described by a cosmological constant, Λ.[2] Over the last few decades, several notable cosmological observations have been integral in the establishment of the current ΛCDM paradigm. A number of CMB experiments followed after COBE, but none have played as significant a role as the satellite telescopes, WMAP [43, 44], and more recently *Planck* [45], which have provided exquisitely accurate measurements of the CMB anisotropies and furnished us with high precision constraints on the cosmological parameters. Moreover, from the early 2000s galaxy redshift surveys probing the LSS flourished, providing measurements of galaxy clustering and the Baryon Acoustic Oscillations (BAO) scale, as first detected by the SDSS [46] and 2dF [47] collaborations.

These are merely highlights of the seminal research that has firmly established the ΛCDM concordance model, which encapsulates our simplest and most explanatory picture of the Universe. With only six free parameters, the ΛCDM model is able to fit independent high-precision measurements which probe the Universe on vastly different length and time scales; observations of the CMB, $\sim$ 380,000 years after the Big Bang, point to the same values for these cosmological parameters as local measurements of the LSS and cosmic expansion – barring some reported inconsistencies between low- and high-redshift datasets, the most significant being the Hubble tension [45, 48, 49]. More data is needed

[2] Although modified gravity theories have also been proposed, for comprehensive reviews see refs. [36–42].

to confirm if these tensions are signs of new physics rather than systematic effects.

1.1.1 The Expanding Universe

The Einstein field equations describe how the geometrical properties of space-time (gravity) – defined by the metric – relate to the energy and matter content of the Universe. Applying the cosmological principle to the Einstein Equations, the spacetime metric for an isotropic and homogeneous expanding Universe is the Friedman-Lemaître-Robertson-Walker (FLRW) metric [25, 26, 50–52] with the line element

$$\mathrm{d}s^2 = -\mathrm{d}t^2 + a^2(t)\left[\frac{\mathrm{d}r^2}{1-\kappa r^2} + r^2\mathrm{d}\theta^2 + r^2\sin^2\theta\mathrm{d}\phi^2\right], \tag{1.1}$$

where t denotes proper time, r, θ, ϕ are spherical spatial coordinates, $a(t)$ is the scale factor and $\kappa = +1, 0, -1$ describes the geometry for a closed, flat and open Universe respectively. We use Planck units where $c = 1$. The scale factor describes the expansion (or contraction) of space as a function of time only and is normalised such that $a_0 = a(t_0) = 1$ today.

The time evolution of the scale factor describes the Universe's expansion history and is determined by solving the Einstein equations with the FLRW metric. Assuming that the contents of the Universe (e. g. matter, radiation) behave as a perfect fluid with energy density ρ and pressure p, the Einstein equations then reduce to the *Freidmann equations*:

$$\begin{aligned} H^2(a) &= \left(\frac{\dot{a}}{a}\right)^2 = \frac{8\pi G}{3}\rho - \frac{\kappa}{a^2} + \frac{\Lambda}{3}, \\ \dot{H} + H^2 &= \frac{\ddot{a}}{a} = -\frac{4\pi G}{3}(\rho + 3p) + \frac{\Lambda}{3}, \end{aligned} \tag{1.2}$$

where the overdot denotes a time derivative, G is the gravitational constant, and $H = \dot{a}/a$ is the Hubble parameter which describes the expansion rate of the Universe. The value of the Hubble parameter today, H_0, is typically referred to as the Hubble constant. The value of H_0 is also commonly defined via the reduced Hubble constant h as $H_0 = 100\,h\,\mathrm{km\,s^{-1}Mpc^{-1}}$. The Friedmann equations clearly show that the evolution of the Universe (left-hand side) is determined by its contents (right-hand side); therefore, we need to specify the energy-matter content of the Universe to understand its evolution.

The equation of state parameter $w = p/\rho$ specifies the relation between the pressure and energy density of each fluid. A Universe dominated only

by radiation ($w = 1/3$) or non-relativistic matter ($w = 0$) will experience a *decelerated* expansion, i. e. $\ddot{a} < 0$. The cosmological constant, Λ, was initially proposed by Einstein to maintain a static Universe [53]. However, in 1929 Edwin Hubble observed that galaxies were moving away from us at velocities directly proportional to their distance by measuring the spectral emission from distant Cepheid stars [27]. This provided the first concrete evidence that the Universe was not static, as Einstein initially thought, but expanding. In an expanding Universe, the frequency of photons emitted at a source, $\nu_{\rm em}$, is shifted to a lower frequency when observed, $\nu_{\rm obs}$, due to the spacetime expansion; the *redshift* z is defined through $1 + z = \nu_{\rm em}/\nu_{\rm obs}$. The redshift is directly related to the scale factor as $1 + z = 1/a$, and thus $z = 0$ today. Setting $\Lambda = 0$ in Eq. (1.2), the remaining components result in a decelerating expansion, and this was the accepted paradigm until the discovery of the accelerated expansion of the Universe from observations of SNeIa [34, 35] in the 1990s. An accelerated expansion can be modelled by a fluid with negative pressure ($w < -1/3$), which has been termed *dark energy*. According to the latest observations, the late-time cosmic acceleration is well described by a fluid with $w = -1$ and constant energy density, or equivalently a cosmological constant Λ, leading to its re-introduction in the Friedmann equations.

1.1.2 Energy Densities

The *continuity equation*, while not independent of the Friedmann equations above, follows from the conservation of the energy-momentum tensor for a perfect fluid and takes the form

$$\dot{\rho} + 3H(\rho + p) = 0\,, \tag{1.3}$$

where the total energy density ρ and pressure p is summed over different species, each having an equation of state $p = w\rho$. Solving Eq. (1.3), the energy density of each species evolves as a function of the scale factor according to

$$\rho(a) = \rho_0 a^{-3(1+w)}\,, \tag{1.4}$$

where $\rho_0 = \rho(a_0)$. Therefore, the energy densities of the different species of the Universe dilute at different rates, characterised by their equation of state parameter w as follows:

- *Radiation:* photons and relativistic particles (such as neutrinos at early times) have $w = 1/3$, and so $\rho_r(a) \propto a^{-4}$

- *Matter:* non-relativistic matter (baryons and dark matter) are described as a pressureless fluid, i. e. $w = 0$ and $\rho_m(a) \propto a^{-3}$
- *Dark energy*: the cosmological constant Λ is equivalent to a fluid with $w = -1$, such that $\rho_\Lambda = -p = \frac{\Lambda}{8\pi G} = \text{const.}$

The Universe is dominated by each of these components at different times in the cosmic expansion history, defining the domination eras. The early Universe was radiation dominated, but as it expands and a grows, at some point the contribution of the matter to the total energy density becomes equal to that of the radiation marking the *matter-radiation equality*(occurring around $z \sim 3400$). The matter-domination epoch continued until $z + 1 \sim 1.3$, after which the Λ-domination era began which is driving the observed late-time accelerated expansion of the Universe today.

Thus, to know the past, present and future evolution of the Universe, it suffices to know the present energy density of each component and H_0. This is more readily understood by rewriting the Friedmann equation in terms of the present day density parameters of each species. The *critical density* of the Universe is the energy density required for a flat Universe ($\kappa = 0$):

$$\rho_c(a) \equiv \frac{3H(a)^2}{8\pi G}\,, \tag{1.5}$$

with which we can then define the dimensionless *density parameters* of a given species i ($i = r, m, \Lambda$) as

$$\Omega_i = \frac{\rho_i(a_0)}{\rho_c(a_0)}\,. \tag{1.6}$$

Then by definition, the first Friedmann equation at $a = a_0$ reduces to

$$1 = \Omega_r + \Omega_m + \Omega_\Lambda - \frac{\kappa^2}{a_0^2 H_0^2}\,, \tag{1.7}$$

and $\Omega_0 \equiv \sum_i \Omega_i = 1$ if the Universe is flat. The density parameter for a curvature component can be defined as

$$\Omega_\kappa \equiv \frac{-\kappa}{a_0^2 H_0^2}\,. \tag{1.8}$$

Combining these definitions with energy density of each species (Eq. (1.4)), we can rewrite the first Friedmann equation in terms of the relative contribution of each component to the present Universe as

$$H^2(a) = H_0^2(\Omega_r a^{-4} + \Omega_m a^{-3} + \Omega_\kappa a^{-2} + \Omega_\Lambda). \tag{1.9}$$

The determination of the density parameters and H_0 is one of the main goals of observational cosmology. The total matter density can be split into the baryonic matter component, Ω_b, and the dark matter component, $\Omega_{\rm DM}$. Under ΛCDM, the latest cosmological observations measure the relative abundances of the baryons, dark matter and dark energy to be [45]:

$$\Omega_b \sim 0.05, \quad \Omega_{\rm DM} \sim 0.265, \quad \Omega_\Lambda \sim 0.685, \tag{1.10}$$

with a negligible radiation energy density today Ω_r. The cosmological measurements are consistent with a flat Universe [45, 54], and the vast majority of the cosmic energy budget is in dark components. These observations tell us that the mysterious dark energy dominates the Universe and that roughly 85% of the total matter density is made up of non-baryonic, non-luminous dark matter that appears to only interact gravitationally, which we will discuss in more detail in Section 1.2.

1.1.3 The Growth of Structure

Until now, we have described the evolution of a perfectly homogeneous and isotropic expanding Universe. However, the existence of cosmic structure in the form of planets, stars and galaxies make it clear that the cosmological principle does not hold on all scales. ΛCDM assumes that the primordial density perturbations which seed the formation of structure are generated from initial quantum fluctuations that get amplified by inflation. While different inflationary theories propose different mechanisms for this, in general inflation predicts an almost scale-invariant power spectrum of curvature perturbations parameterised in terms of the dimensionless *primordial power spectrum*:

$$P_0(k) = A_s \left(\frac{k}{k_0}\right)^{n_s - 1}, \tag{1.11}$$

where A_s quantifies the amplitude of the primordial power spectrum at the pivot scale k_0 (typically $k_0 \approx 0.05$ Mpc^{-1}), and n_s is the spectral index.

The Friedmann equations describe the background evolution in an expanding Universe; we can perturb them to derive the growth of small primordial density fluctuations into the large structures observed in the Universe today. This is described by the Einstein-Boltzmann equations, a set of coupled differential equations which specify the evolution of the density perturbations of each species in an expanding Universe under GR. Each component is treated as a fluid with overdensity δ_i. The linear growth of these density perturbations

from the primordial perturbations δ_0 is then given by the transfer function $T(k)$: $\delta_i(k,z) = T_i(k,z)\delta_0(k,z)$, where k is the wavenumber. Note that this formalism is valid only in the linear regime, and does not apply on scales where non-linear gravitational collapse dominates the evolution of overdensities. With this, the total matter power spectrum can be related to the power spectrum of primordial density perturbations as follows

$$P_m(k,z) = \left(\sum_i T_i(k,z)\right)^2 P_0(k)\,. \tag{1.12}$$

As we will discuss further in Section 1.2, the success of cosmological structure formation theory relies on the existence of the dark matter component decoupled from the photons which creates the gravitational wells for the baryons to fall into and eventually form the visible galaxies in the present Universe. The observed structure is well-described in terms of a cold, collisionless dark matter particle interacting only via gravity. However, many dark matter models feature some kind of non-gravitational interactions (e. g. scattering or self-interactions) which can manifest as a suppression of the power spectrum on small cosmological scales, as we will consider in Chapter 3.

1.2 Dark Matter

Overwhelming evidence, ranging from galactic to cosmological scales, points to the fact that $\sim 85\%$ of the matter in the Universe is in the form of some unknown, non-luminous component called *dark matter* (DM). Despite the abundance of gravitational evidence for its existence, the fundamental nature of DM remains a mystery. In this section I present the case for particle DM, giving an overview of the observational evidence for DM, what can be inferred about its particle properties, potential candidates, and detection strategies. We begin with a brief historical account of how the evidence for dark matter accumulated and the modern concept of dark matter came to be; for more in-depth historical reviews, the interested reader is referred to refs. [55–60].

1.2.1 A Brief History of Dark Matter

Evidence of some form of unseen, invisible mass in the Universe can be traced back to the early 20$^{\text{th}}$ century. While first attempts to measure the amount of non-luminous mass in our local Galaxy [61–63] concluded that the presence of

a large amount of missing matter was unlikely, these seminal works paved the way for modern measurements of the local DM density.

In the 1930s, the first evidence for the existence of a significant amount of invisible matter came to light. Fritz Zwicky discovered an inconsistency between the observed velocity dispersion of galaxies in the Coma cluster compared to the prediction based on the amount of visible matter alone – which he attributed to the existence of unseen matter [64, 65].[3] Applying the virial theorem, he estimated the amount of non-luminous matter and concluded that it should be much more abundant than the visible matter, finding a mass-to-light ratio of ∼500. Further evidence of missing mass in galaxy clusters was found shortly afterwards in a similar analysis of the Virgo cluster by Sinclair Smith in 1936 [66]. In the decades that followed, evidence of mass discrepancies in different galactic systems continued to accumulate; however, it was not until the 1970s that the significance of these observations – and their interpretation as evidence for dark matter – was fully recognised by the scientific community [59].

The second central piece of gravitational evidence for missing mass came with the discovery of flat galactic rotation curves. Rotation curve diagrams show the orbital velocity of gas and stars in individual galaxies as a function of their distance from the galactic centre. In the 1970s, measurements of such galaxies using optical spectroscopy [67–69] and neutral hydrogen (HI) emission [70–77] showed that rotation curves remain flat out to large radii. Based on the distribution of visible matter, the rotational velocity in the outermost regions of galaxies should fall with radius r as $v(r) \propto 1/\sqrt{r}$. The flat rotation curves – i. e. constant velocity at large radii – indicate that there is more gravitational force than can be accounted for by the visible matter alone, implying the presence of additional non-luminous mass extending to large radii.

At this time, however, there was no clear consensus that these two independent missing mass anomalies – flat galactic rotation curves and the mass discrepancy in galaxy clusters – constituted evidence for the presence of a large fraction of non-luminous matter in the Universe. For the most part, dark matter was not seen as a single solution to these two discrepancies on vastly different astrophysical scales or that they were connected at all. Instead it was the rise of physical cosmology, and its interest in measuring the mass density of the Universe, that finally led to the coalescence of these anomalous observations into the modern dark matter interpretation [59]. The estimated mass density of the Universe based on the visible mass in galaxies alone was found to be two

[3] Zwicky is often credited with the first use of the term "dark matter"; however, he may have been referring to faint stars or gas not visible to us [58].

orders of magnitude below the critical density required to close the Universe. A closed Universe was favoured on theoretical grounds, and thus cosmology was now motivating a search for missing matter. Spurred by this new cosmological focus, in 1974, two landmark papers argued for the existence of an additional dark matter component to resolve both missing mass phenomena while also increasing the matter density of the Universe to achieve the desired critical density [78, 79]. While attempts were made to account for this missing mass within the realm of baryons, the need for a new type of matter to explain observations began to solidify from the 1980s onwards. James Peebles showed that the upper limits on the CMB anisotropies were incompatible with a Universe composed only of baryons; he argued that a new species of massive, weakly interacting particles dominated the matter content of the Universe, whose initial density perturbations would seed the formation of cosmic structures observed today [80–82]. Standard Model neutrinos first appeared to be perfect candidates, being stable and weakly interacting. However, numerical simulations of a Universe dominated by neutrinos predicted a lack of clustering at small scales compared to observations (see Section 1.3.3), ruling them out as the dominant form of dark matter [83]. By the late 1980s, the idea that dark matter must be made up of some new species had become the prevailing paradigm.

1.2.2 Dark Matter Properties

To date, all evidence for DM is gravitational in nature. Nonetheless, the observations that demonstrate the existence of DM also provide ways to constrain its fundamental properties. There is strong evidence that DM must be non-baryonic – and most readily interpreted in terms of a new fundamental particle – as we outline in the following.

CMB anisotropies Today, the most compelling evidence for a non-baryonic DM component comes from the measurements of the anisotropies in the CMB. In cosmology, non-baryonic DM plays a crucial role in the theory of structure formation. Prior to recombination, the baryons are tightly coupled to the photons and radiation pressure prevents the baryon density perturbations from growing until after decoupling. In a Universe without DM, the amplitude of the temperature fluctuations in the CMB would have to be much larger than observed in order for the density perturbations to grow sufficiently from recombination into the observed large-scale structure today. However, in the presence of a non-baryonic DM component decoupled from the photons, matter domination occurs earlier and the DM density perturbations can begin to grow well

before recombination. Following recombination, baryons can then fall into the gravitational potential wells created by the DM and eventually form the visible stars and galaxies we see today. Moreover, detailed analyses of the positions and relative heights of the acoustic peaks in the CMB angular power spectrum give a precise determination of the abundances of the baryonic and DM components [45]. Remarkably, the determination of the baryon density from the CMB ($\Omega_b h^2 \simeq 0.0224$ [45]) is consistent with the independent prediction from BBN. BBN accurately predicts the abundance of light elements created in the primordial Universe which depends on the baryon density, and limits the amount of baryonic matter to $0.021 \leq \Omega_b h^2 \leq 0.024$ [84], further supporting the need for a non-baryonic matter component. Both CMB and BBN measurements can also be used to place limits on the DM particle properties, as we discuss in Section 1.2.4.

Large-scale structure Large-scale structure observations imply that dark matter must be cold, i. e. non-relativistic at matter-radiation equality. Standard Model neutrinos – which first seemed like perfect candidates, being massive and not interacting with light – were ruled out by numerical simulations due to the lack of clustering at small scales compared to observations [83]. Relativistic neutrinos are an example of *hot dark matter* candidates, which erase density perturbations below their free-streaming scale, and predict a *top-down* model of structure formation whereby very large structures form first, which later fragment to form smaller halos. The resulting galaxy distribution is not compatible with observations [60, 85]. In contrast, non-relativistic *cold dark matter* (CDM) predicts a *bottom-up* scenario in which matter first collapses to form the smallest halos, which then merge and form larger structures in a process known as *hierarchical structure formation*. The first numerical simulations of a Universe dominated by CDM correctly reproduced the observed structure [86], and the CDM paradigm soon became well-established. In between these two extremes, *warm dark matter* (WDM) remains a possibility: DM with a mass around the $\sim$ keV scale and a non-negligible free-streaming length, which suppresses the amount of low-mass DM halos [87] compared to a CDM Universe, but is still compatible with the observed structure and N-body simulations. Warm dark matter has been somewhat motivated by the need to resolve a number of small-scale challenges within the CDM framework – known as the *missing satellites* [88, 89], *too-big-to-fail* [90, 91], and *cusp-core* [92] problems. However, these putative issues are still the subject of intense debate in the literature and can potentially be resolved with the inclusion of baryonic physics.

Weak lensing Gravitational lensing is an important result of GR; mass curves spacetime, and so photons travelling from a distance source are deflected by massive objects along their path which act as a lens. If the lens is sufficiently massive, the distorted photons emitted from the background source can be fully resolved and appear as multiple images of the same source or even a ring around the lens, a phenomenon known as *strong lensing*. On the other hand, *weak lensing* is when the lens is not strong enough to produce distinct distorted images of sources visible to the naked eye. However, the small distortions in all images of sources around a given lens are correlated and thus information about the foreground mass can be inferred statistically. Weak gravitational lensing observations of galaxy clusters provide further striking evidence for DM and can be used to map out the matter distribution. Weak lensing observations of the Bullet cluster [93] – a system of two colliding galaxy clusters – reveal that the majority of the mass of the system is dominated by a non-luminous component which is displaced from the hot intra-cluster medium observed in X-ray. As the clusters collide, the two bodies of hot gas interact and form a bow shock formation, but the DM halos of each cluster pass through each other without interacting. As such, DM is often characterised as "collisionless"; analysis of the Bullet cluster places a limit on the self-interaction cross-section of a DM particle of $\sigma/m_\chi \lesssim 1\,\mathrm{cm}^2\,\mathrm{g}^{-1}$ [94].

Efforts to explain DM with modified gravity theories, such as MOND [95], are unable to account for the gravitational lensing of clusters, the CMB and the observed large-scale structure. Other proposals to accommodate DM without the need for a new particle species include Massive Compact Halo Objects (MACHOS) – i. e. compact objects made of baryons which emit negligible radiation such as black holes, neutron stars, dwarf stars and planets. MACHOs can be detected via gravitational microlensing events, but results of microlensing surveys reveal that the abundance of MACHOS is too small to account for the required DM density [96–98]. Moreover, these objects would not be present in the early Universe and so cannot explain CMB and BBN observations. The exception to this is primordial black holes (PBHs), which would behave like a pressureless decoupled fluid and have been proposed as an alternative to particle DM [99, 100]. PBHs face a number of stringent constraints [101], but could still make up some fraction of the DM density. This thesis focus on particle DM candidates, but we refer the reader to refs. [102, 103] for recent reviews on PBH DM.

In short, the seminal research outlined above strongly motivates DM as being

comprised of a cold, collisionless, non-baryonic particle. Further constraints on the particle nature of DM have been gleaned from a multitude of cosmological and astrophysical observations over the last few decades. To summarise, a viable DM particle must be:

- *Neutral*: Very stringent limits exist on charged DM [104–106], and they are effectively ruled out. Models with a fractional electric charge (i. e. millicharged DM) are still allowed, but are severely constrained by a variety of observations and can only constitute a small fraction of the total DM [107–111]
- *Stable*: DM must be stable or very long-lived with respect to the age of the Universe in order to be present today with the observed abundance
- *Collisionless*: The strength of the DM self-interaction cross-section must be within the allowed limits set by, e. g., the Bullet cluster
- *Cold-ish*: DM must be cold enough to reproduce the observed large-scale structure in the Universe today
- Produced in sufficient amounts in the early Universe to be compatible with the observed relic density as measured from the CMB
- Consistent with all other cosmological measurements, such as BBN, and astrophysical bounds (see e. g. ref. [106]).

There is no particle within the SM that possesses all of these properties. If a particle DM candidate is to be found, physics beyond the Standard Model (BSM) is required. At the same time, new particles are required to solve several issues within the SM itself. In the next section, we briefly review several of the most popular DM candidates that arise naturally in solutions to some of the open problems in particle physics.

1.2.3 Particle Dark Matter Candidates

The Standard Model of particle physics (SM) encapsulates our current understanding of the basic structure of matter – the elementary particles and fundamental forces of nature and how they interact. Despite its spectacular experimental success to date, a number of unresolved issues and theoretical shortcomings remain. For example, the SM does not incorporate gravity alongside the other fundamental forces, the origin of the neutrino masses is unknown

(see Section 1.3), and there are several issues related to *fine-tuning* or *naturalness*, such as the hierarchy problem (see e. g. [112]). It turns out that many well-motivated extensions to the SM which aim to resolve one or more of these issues, naturally provide us with a suitable DM candidate. A multitude of DM candidates exist in the literature, and we refer the reader to refs. [113–115] for reviews. Here we provide a brief overview of some of the most theoretically well-motivated particle DM candidates which arise out of BSM theories.

Axions The axion arose as a solution to the strong-CP problem in particle physics. The theory of Quantum Chromodynamics (QCD) – which describes the strong force – permits Charge-Parity (CP) symmetry violation in strong interactions, which would manifest itself as a non-zero neutron electric-dipole moment d_n. However, no CP violation has been observed; current constraints are consistent with a very small or zero electric-dipole moment ($|d_n| < 2.9 \times 10^{-26} e$cm [116], 10 orders of magnitude smaller than expected). As there is no theoretical basis for CP conservation in QCD, this leaves a fine-tuning problem known as the "strong-CP problem". The Peccei-Quinn mechanism provides an elegant solution to the strong-CP problem [117] and generates a new massive particle – the QCD axion [118, 119] – which was later recognised as a viable DM candidate [120–122]. The original (PQWW) QCD axion has been ruled out by particle collider experiments, but alternatives such as the KSVZ [123, 124] and DFSZ [125, 126] QCD axion models are still allowed. Moreover, axions and axion-like particles also arise in other BSM theories, such as string theory – for a review on axion DM, please see [127].

Sterile neutrinos All particles within the SM can have both left- and right-handed chirality. However, only left-handed neutrinos have been observed. The solution is to introduce *sterile neutrinos* with right-handed chirality that do not interact via the weak force, as opposed to their left-handed counterparts which are *active* neutrinos. These sterile neutrinos can act as a DM candidate [128]. Sterile neutrinos can also provide a mechanism for the non-zero neutrino masses (see Section 1.3), which are not accounted for within the SM, via the see-saw mechanism [129–131]. Sterile neutrinos would have mass on the order of $\sim$ keV (for reviews, see refs. [132–134]), and would produce X-rays via radiative decays to active neutrinos – as such, they attracted attention as a potential explanation for the anomalous 3.5 keV X-ray line observed in galaxies and clusters [135, 136] (see also [137]). However, this interpretation is under pressure from other

cosmological and X-ray observations which constrain the allowed parameter space for sterile neutrinos to constitute the DM [138–140].

WIMPs Weakly Interacting Massive Particles (WIMPs) represent a broad category of particle DM candidates with the following properties: weak coupling to SM particles, no direct photon coupling, and thermally produced in the early Universe with their relic density set by their freeze-out abundance. In the early Universe, WIMPs are kept in equilibrium with the thermal plasma via frequent interactions with SM particles. As the Universe cools and the WIMP annihilation rate drops below the Hubble expansion rate, the WIMPs fall out of equilibrium and their number density per comoving volume becomes constant. This process is known as *freeze-out*. In the standard freeze-out scenario, the DM relic density Ω_{DM} observed today directly depends on the annihilation rate as [141]

$$\Omega_{\mathrm{DM}}h^2 \approx \frac{3 \times 10^{-27}\mathrm{cm}^3\,\mathrm{s}^{-1}}{\langle\sigma v\rangle}, \tag{1.13}$$

where is $\langle\sigma v\rangle$ is the WIMP self-annihilation cross-section. To match the observed DM relic density $\Omega_{\mathrm{DM}}h^2 \sim 0.12$ [45], the canonical *thermal relic cross-section* is $\langle\sigma v\rangle \sim 3\times10^{-26}\mathrm{cm}^3\,\mathrm{s}^{-1}$. The fact that massive particles ($\sim$ GeV) with weak-scale interactions naturally produce the correct relic cosmological abundance of DM is known as the *WIMP miracle*. More generally, WIMPs refer to broad class of particles with electroweak scale masses $\mathcal{O}(10\text{ GeV}) - \mathcal{O}(100\text{ TeV})$ and weak-scale interaction cross-sections.

The WIMP paradigm is particularly attractive because new stable particles at the electroweak scale are a generic feature of well-motivated extensions to the SM that seek to address the hierarchy problem. Supersymmetry (SUSY) is the most popular example of such SM extensions, which is able to resolve a number of problems including the hierarchy problem and gauge coupling unification [142]. In SUSY models with R-parity conservation, (typically) the lightest supersymmetric particle – e. g. the *neutralino* – is stable and electrically neutral, making it an ideal WIMP candidate [141, 143]. WIMP candidates also arise in theories of universal extra dimensions, such as Kaluza-Klein particles [144].

Note that the discussion here concentrates on the prototype *standard* or *natural* thermal WIMPs with masses in range from a few GeV to a few TeV. However, specific models can relax this mass range; it is possible to obtain the thermal relic cross-section for a wide range of different masses and coupling strengths [145] (e. g. hidden sector DM). These "non-natural" WIMPs can extend the mass range down to the $\mathcal{O}$(MeV) scale. Additionally, other alternatives

include DM relics produced in the correct abundance by non-thermal production mechanisms, such as FIMPs (or super-WIMPs) [146, 147]. Thus the term WIMP is somewhat ill-defined, and can also generally refer to any particle with the correct relic abundance and some "weak" coupling to SM particles – in this sense, not necessarily referring to the electroweak scale.

1.2.4 Dark Matter Searches

The prevailing WIMP paradigm has motivated an extensive experimental program to search for DM particles with such properties along three broad fronts: direct detection [148, 149], indirect detection [150–152] and collider searches [153, 154].

Collider searches aim to produce DM particles via collisions of SM particles at high energies in particle accelerators such as the large hadron collider [155–157]. DM particles produced in these collisions are expected to escape the detector, leaving an observable signature in terms of missing transverse energy (in combination with a jet of SM particles). Importantly, even if a new stable particle is detected at colliders, corroborating evidence from direct or indirect detection will be required to confirm it as *the* DM in the Universe.

Direct detection experiments search for signals of DM particles scattering with target nuclei in underground detectors, shielded from other radiation such as cosmic rays. State-of-the-art liquid Xenon experiments – such as LUX [158], XENON1T [159], and PandaX-4T [160] – and Cryogenic experiments – e. g. CRESST-III [161] and SuperCDMS [162, 163] – provide some of the strongest constraints on nucleon-DM scattering cross-sections for masses above the $\sim$ GeV scale [164]. Traditional nuclear recoil experiments have limited sensitivity to lighter, sub-GeV DM; strategies for direct detection of sub-GeV DM (e. g. [165–167]) mainly rely on DM-electron recoil experiments. Direct detection of the DM-nucleon scattering cross-section remains a challenge for low mass DM, although novel technologies and experiments are being proposed [168].

Indirect detection refers to searches for the SM particles produced in DM annihilation or decay processes in astrophysical sources with high DM density, such as the Galactic centre, dwarf spheroidal galaxies and galaxy clusters. Space-based experiments such as the *Fermi* Large-Area Telescope (LAT) have provided some of the strongest constraints on DM annihilation to γ-rays [169, 170] in the $\sim \mathcal{O}$(GeV) regime. At the highest energies ($\gtrsim$TeV), constraints from VERITAS [171], MAGIC [172], HAWC [173], H.E.S.S [174] dominate – and will substantially improve with next-generation very high energy gamma-ray experiments such as CTA [175]. A signal of DM decay or annihilation can also be

searched for in high energy cosmic-rays data from, e. g., the Alpha Magnetic Spectrometer (AMS-02) experiment [176–178]. Below the GeV scale, the sensitivity of experiments like *Fermi* and AMS-02 degrade significantly; as we will discuss below, cosmological constraints are very complementary in this regard. There is motivation to explore the 'MeV gap' in gamma-ray astronomy [179]. Observations of the diffuse X-ray sky also places constraints on DM at the keV scale [180, 181].

Despite this comprehensive experimental effort, providing increasingly stronger bounds on the DM properties, a non-gravitational signature of DM is yet to be found. While there is still ample viable parameter space to explore [182, 183], a substantial fraction of the canonical thermal WIMP parameter space has already been excluded [184]. As a result, we are in the midst of a paradigm shift in DM search strategies as the focus broadens to encompass mass and energy scales outwith the conventional WIMP window as well as alternative DM models [185]. Cosmological observations are very promising in this regard, offering a unique and independent probe of DM properties which are highly complementary to the aforementioned methods. Cosmological searches rely on detecting the effects of DM microphysics on the structure formation and thermal history of the Universe. This presents distinct advantages: cosmological probes are often sensitive to complementary regions of parameter space, can avoid the astrophysical backgrounds and modelling uncertainties associated with direct and indirect detection, and can probe dark sector interactions that have no detectable signal in traditional astrophysical or terrestrial experiments.

In the early Universe, DM annihilation or decay via electromagnetic channels injects energy into the photon-baryon plasma, leaving an imprint on the CMB anisotropies [45, 186–188] and spectral distortions [189, 190]. Measurements of the CMB anisotropies provide some of the strongest and most robust constraints on sub-GeV DM, complementary to indirect searches. Furthermore, elastic scattering between DM and SM particles leads to heat and momentum exchange between the DM and baryon fluids which can impact both the thermal history and the growth of cosmological perturbations. Various cosmological observables can probe such effects, and are sensitive to masses and scattering cross-sections outwith the reach of most direct detection experiments (extending down to $\sim$ keV masses). DM-baryon scattering causes a drag force between the two fluids which inhibits DM clustering and smooths out structure on small cosmological scales; the CMB anisotropy measurements provide one of the cleanest probes, and is sensitive to DM scattering with baryons [191–200], electrons [201, 202], photons [203–205], neutrinos [206, 207] and even dark radiation [208–210].

DM-baryon scattering can also drain heat from the photon-baryon plasma affecting the CMB spectral distortions [189, 211], which constrains scattering of light ($\lesssim$ 100 keV) DM. Moreover, the effects of DM-baryon scattering on the matter clustering affects other observables that trace the structure formation throughout cosmic history; the Lyman-α forest, galaxy clustering, and galaxy weak lensing observations as well as near-field cosmology probes such as the Milky Way satellites galaxies, can all be used to constrain DM-baryon scattering (as well as other DM models that modify the matter clustering, see ref. [212] for a comprehensive overview). Finally, different DM models would affect the abundance of light elements created in BBN, which places limits on both coupling to SM particles and new relativistic species [213–219].

In the coming decades, cosmology will play a key role in diversifying the experimental search strategy for DM with next-generation CMB experiments and LSS surveys expected to increase sensitivity to a range of DM models and interactions [220–224]. Moreover, forthcoming measurements of the cosmological 21 cm signal [225, 226] may provide a powerful new probe of DM properties. The redshifted 21 cm emission from neutral hydrogen (HI) offers a unique window on the post-recombination Universe, spanning the cosmic dark ages ($z \sim$ 30–1100) prior to the formation of the stars and the following epochs of cosmic dawn and reionization ($z \sim$ 5–30) after the birth of the first luminous sources. Such observations can bridge the unexplored gap between the last scattering of the CMB in the early Universe and the low-redshift reach of galaxy surveys. The 21 cm signal is highly sensitive to the temperature of the baryon gas, and thus is a promising testbed for exotic DM processes that would alter its thermal properties such as DM decay or annihilation, scattering, and PBHs. Furthermore, the 21 cm line during cosmic dawn is also a probe of structure formation, tracing the formation history of the first stars and galaxies. Various DM processes – including scattering, dark sector interactions and warm DM – suppress clustering at the scales relevant for the DM halos that could host the first galaxies, thereby affecting the abundance of the first luminous objects and the time evolution of 21 cm signal [227–236]. In this thesis, we consider the cosmological consequences of DM decay and annihilation (Chapter 2) and DM-baryon scattering (Chapter 3) and the potential imprint on the 21 cm signal from the dark ages and cosmic dawn. In particular, we do not focus on any specific DM particle or model; instead, assuming some coupling to SM particles within current limits, we aim to study the non-gravitational cosmological signatures of DM interactions relevant to broad classes of DM candidates.

1.3 Massive Neutrinos

Neutrino physics is another compelling example of how the connection between cosmology, particle and astroparticle physics is driving our understanding of fundamental physics. Within the framework of the SM, neutrinos are massless; the discovery of neutrino masses is therefore one of the most compelling cases for physics beyond the SM. At the same time, these light, weakly interacting particles leave unique imprints on cosmological observables which can be used to study their properties. In this section, we give a brief overview of neutrino oscillations from a particle physics perspective and discuss the effects of massive neutrinos in cosmology, highlighting the most relevant aspects in relation to the work presented in Chapter 4.

1.3.1 Discovery

Neutrinos were first postulated in the 1930s by Wolfgang Pauli as a way to preserve energy and momentum conservation in beta decays [237]. His prediction was confirmed almost a quarter of a century later when they were first detected in the 1956 Cowan-Reines neutrino experiment [238]. While the SM predicts neutrinos to be massless, the idea that massive neutrinos would exhibit flavour mixing was first hypothesised by Pontecorvo [239, 240] in 1957. At this time, only the electron neutrino type was known (ν_e), and the idea was that mixing could occur between electron neutrinos and anti-neutrinos. Later, a second neutrino type was discovered – the muon neutrino ν_μ – at the Brookhaven neutrino experiment in 1962 [241]. Following this discovery, theories of neutrino mixing between different flavour eigenstates were further developed [242, 243].

The first experimental indication of this came with the discovery of solar neutrinos [244] in the Homestake experiment of the 1960s. The measured flux of electron neutrinos coming from the sun was found to be ∼2–3 times smaller than the predictions based on the Standard Solar Model [245], a phenomenon known as the *solar neutrino problem* [246]. Pontecorvo has already anticipated the solar neutrino problem, which could be resolved by neutrino oscillations [243]; the experiment was only sensitive to the electron neutrinos produced in the Sun, and if the neutrinos underwent flavour changes as they travelled to Earth, this would explain the discrepancy (as we will discuss below). Finally, the tau neutrino (ν_τ) was discovered in 2000 [247], which completes the standard three-neutrino flavour model predicted in the SM framework [84].

1.3.2 Neutrino Oscillations

Neutrinos come in three (known) flavour eigenstates ν_α ($\alpha = e, \mu, \tau$) which are linear combinations of the mass eigenstates ν_i ($i = 1, 2, 3$), expressed as

$$\nu_\alpha = \sum_i U_{\alpha i} \nu_i \,, \tag{1.14}$$

where U is the Pontecorvo-Maki-Nakagawa-Sakata (PMNS) mixing matrix [240, 242]. Neutrinos are produced at a source in a definite flavour eigenstate but propagate in space as mass eigenstates which evolve at different rates. As a result, there is a non-zero probability that the flavour of the neutrino arriving at a detector some distance from the source will be different from its original flavour. This possibility of flavour change is known as *neutrino oscillations*. For small neutrino masses, flavour oscillations happen over macroscopic scales and can be measured by comparing the measured versus predicted flux of neutrinos from distant sources, e. g. the Sun or the Earth's atmosphere. The probability of flavour change $\nu_\alpha \to \nu_\beta$ over a distance L is given by (see e. g. [248, 249])

$$P(\nu_\alpha \to \nu_\beta) = \sum_{ij} U^*_{\alpha i} U_{\beta j} U_{\alpha i} U^*_{\beta j} e^{-i \frac{\Delta m^2_{ij} L}{2|\mathbf{p}|}} \,, \tag{1.15}$$

where the squared mass splitting $\Delta m^2_{ij} \equiv m^2_i - m^2_i$, and $\mathbf{p}$ is the momentum of the neutrino. If we consider, for example, a simplified case of two-flavour neutrino mixing then the probability becomes

$$P(\nu_\alpha \to \nu_\beta) = \sin^2(2\theta) \sin^2 \left(\frac{\Delta m^2 L}{4E} \right) \,, \tag{1.16}$$

where Δm^2 is the squared mass splitting between the two mass eigenstates, θ is the mixing angle, and E is the neutrino energy. In this form, it is immediately clear that the observation of neutrino oscillations requires that the squared mass splitting be non-zero.

Today there is a strong body of evidence of neutrino oscillations from a variety of experiments. The first conclusive evidence for neutrino oscillations came from the measurement of the flux of atmospheric neutrinos by the Super-Kamiokande experiment in 1998 [250] and the flux of solar neutrinos measured by the Sudbury Neutrino Observatory (SNO) in 2001 [251, 252]. Since then, neutrino oscillations have been further confirmed by other solar [253], atmospheric [254], and reactor [255–258] and accelerator [254, 259] neutrino data.

The neutrino oscillation experiments are sensitive to the difference between

squared neutrino masses only, i. e. $\Delta m^2_{ij} \equiv m^2_i - m^2_i$, and thus are insensitive to the absolute neutrino mass scale (leaving one neutrino mass unconstrained). Current experiments have measured two mass-squared splittings to high precision: the solar mass splitting, Δm^2_{21}, and the atmospheric mass splitting, $|\Delta m^2_{31}|$. Therefore, we know that two of the neutrinos must have non-zero masses. While the magnitudes of the splittings have been measured to exquisite accuracy, the sign of the larger atmospheric mass splitting Δm^2_{31} is currently unknown. This leaves two possibilities for the ordering of the masses, known as the *mass hierarchy*: the normal hierarchy (NH), such that $\Delta m^2_{31} > 0$ and $m_1 < m_2 < m_3$, and the inverted hierarchy (IH), for $\Delta m^2_{31} < 0$ and $m_3 < m_1 < m_2$. If we define the lightest mass m_0, such that $m_0 = m_1$ in the NH and $m_0 = m_3$ in the IH, then the sum of the neutrino masses ($\Sigma m_\nu \equiv \sum_i m_i$) for each ordering can be expressed as:

$$\begin{aligned} \Sigma m_\nu &= m_0 + \sqrt{m_0^2 + \Delta m^2_{21}} + \sqrt{m_0^2 + \Delta m^2_{31}} \quad \text{(NH)}\,, \\ \Sigma m_\nu &= m_0 + \sqrt{m_0^2 + |\Delta m^2_{31}|} + \sqrt{m_0^2 + |\Delta m^2_{31}| + \Delta m^2_{21}} \quad \text{(IH)}\,. \end{aligned} \tag{1.17}$$

This is where cosmological probes become highly relevant. Cosmology is sensitive to the sum of neutrino masses and is thus highly complementary to neutrino oscillation experiments, providing a handle on the absolute neutrino mass scale which can be used to constrain the individual neutrino masses (and hierarchy) in combination with the mass-squared splittings measurements.

The absolute neutrino mass scale can also be probed by beta decay (β-decay) and neutrinoless double-beta decay ($0\nu2\beta$) laboratory experiments. These experiments are sensitive to different combinations of the individual neutrino masses and mixing parameters. Currently, the strongest upper bounds on the effective electron neutrino mass are given by the latest KATRIN Tritium β-decay results, which constrain $m_\beta < 0.8$ eV [260] at 90% confidence level (C.L.). Experimental searches for neutrinoless double-beta decay can also be used to constrain the absolute neutrino mass scale and are sensitive to the effective Majorana mass of the electron neutrino $m_{\beta\beta}$, with the tightest upper limits currently giving $m_{\beta\beta} < 61 - 165$ meV [261] and $m_{\beta\beta} < 79 - 180$ meV [262] (90% C.L. ranges). Oscillation experiments measure the parameters of the mixing matrix U, which together with a measurement of one of the three mass parameters ($\Sigma m_\nu, m_\beta, m_{\beta\beta}$) then uniquely determines the other two. Therefore all these observations probe the absolute neutrino mass scale in a different and synergistic way; combining datasets provides an important consistency check, and can be used to increase the overall sensitivity to the neutrino mass scale.

As we will discuss in the following section, currently cosmological observations provide the tightest constraints on the absolute neutrino mass scale.

1.3.3 Massive Neutrinos in Cosmology

Neutrinos play an important role in cosmic evolution, from the creation of light elements in Big-Bang nucleosynthesis to the large-scale structure formation today. In the early Universe they are ultra-relativistic and contribute to the radiation energy density, but later behave as non-relativistic matter. Here we focus on the effect of massive neutrinos on the evolution of matter perturbations and the imprint on the large-scale structure, which is the key observable to constrain neutrino masses from cosmology. For detailed reviews on the role of neutrinos in cosmology, we refer the reader to refs. [263–266].

In the early Universe, neutrinos are kept in equilibrium with the thermal bath via weak interaction with electrons such as

$$\gamma \leftrightarrow \nu_e + \bar{\nu}_e \leftrightarrow e^+ + e^- \quad \text{and} \quad e^- + \bar{\nu}_e \leftrightarrow e^- + \bar{\nu}_e, \tag{1.18}$$

and likewise for the muon and tau species. As the plasma cools below $T \sim 1$ MeV, the interaction rate drops below the expansion rate of the Universe and neutrinos fall out of thermal equilibrium. After decoupling they have a fixed relic density and freely stream through the Universe without interactions, leaving a relic cosmic neutrino background. After the neutrinos become non-relativistic, they contribute to the matter density of the Universe. The cosmological relic density of neutrinos today is given by

$$\Omega_\nu h^2 \approx \frac{\Sigma m_\nu}{93.14\,\text{eV}}. \tag{1.19}$$

As discussed in Section 1.2, there were early ideas that massive neutrinos could constitute the DM [267–269], and cosmological arguments were used to place upper bounds on absolute neutrino mass scale simply by requiring that neutrinos not be heavy enough to overclose Universe ($\Omega_\nu < 1$) [267, 270], giving $\Sigma m_\nu < 45$ eV (for $h = 0.7$). If we combine with the non-cosmological upper limit on the absolute neutrino mass scale (Section 1.3.2), the tritium β-decay bound $m_\beta < 0.8$ eV can be used to derive a rough upper bound on $\Sigma m_\nu \lesssim 2.4$ eV (assuming $m_\beta \simeq m_0$). This leads to an upper bound on the neutrino relic density of

$$\Omega_\nu h^2 \lesssim 0.0258, \tag{1.20}$$

which, compared to the measurement DM density $\Omega_{\rm DM}h^2 = 0.1197$, is just over one-fifth of it. Moreover, if we include the much stronger cosmological bounds on the mass sum $\Sigma m_\nu < 0.12$ eV (see next section), we can then deduce

$$\Omega_\nu h^2 \lesssim 0.0013. \tag{1.21}$$

Therefore, the SM neutrinos can only contribute at most $\sim 1\%$ of the total DM density.

Despite such a small contribution to the energy density of the Universe, neutrinos have significant cosmological consequences and leave a distinct imprint on both the expansion history and the evolution of cosmological perturbations. Neutrinos were relativistic at decoupling, after which they could freely stream throughout the Universe without interacting much with other species. The mean distance travelled from decoupling until they become non-relativistic defines the *free-streaming scale* below which initial inhomogeneities are washed out. Due to their large velocities, neutrinos cannot be confined in the gravitational potential wells below the free-streaming scale, thereby suppressing the growth of density perturbations at small scales. Once neutrinos become non-relativistic, they behave like standard matter and fall into the potential wells. The comoving free-streaming wavenumber at the non-relativistic transition is defined as

$$k_{\rm nr} \approx 0.018\sqrt{\Omega_m}\left(\frac{\Sigma m_\nu}{1\text{eV}}\right)^{1/2} h\,\text{Mpc}^{-1}\,. \tag{1.22}$$

At scales $k \gg k_{nr}$, the free-streaming damps the neutrino density perturbations which in turn inhibits the clustering of the DM and baryons, while for $k \ll k_{nr}$, the clustering is unaffected and neutrinos effectively behave as cold DM.

Therefore, the matter distribution in the Universe is a powerful tool to constrain the neutrino mass scale and can be probed via measurements of BAO, galaxy lensing, and galaxy clustering [271, 272]. Moreover, the effect of neutrino masses on the large-scale structure also leaves an imprint on the CMB. As CMB photons travel from the last-scattering surface to today, the gravitation potential wells created by the matter clustering generate secondary anisotropies in the CMB [273, 274], providing another probe of neutrino mass scale [275, 276]. Today the strongest constraints on Σm_ν come from a combination of measurements of the CMB anisotropies and BAO from galaxy clustering data, which we discuss below.

1.3.4 Current Constraints and Determining the Mass Hierarchy

Based on the most recent global fit to neutrino oscillations data, the mass splittings are now measured to be $\Delta m^2_{21} \simeq 7.42 \times 10^{-5}\text{eV}^2$ and $|\Delta m^2_{31}| \simeq 2.5 \times 10^{-3}\text{eV}^2$ [277]. Combining these measurements with the definition in Eq. (1.17) and setting $m_0 = 0$, we can obtain a lower limit on the sum of the masses for the two orderings: for the NH, $\Sigma m_\nu^{\text{NH,min}} \simeq 0.06$ eV, while for the IH, $\Sigma m_\nu^{\text{IH,min}} \simeq 0.1$ eV.

As cosmological observations are (at first order) sensitive to Σm_ν, they offer an opportunity to test the neutrino mass hierarchy; if measurements can constrain $\Sigma m_\nu < 0.1$ eV at high statistical significance, the IH would be effectively excluded. Cosmological probes have been providing increasingly stronger bounds on Σm_ν over the past decade(s) and are approaching the minimum bound allowed in the IH. The *Planck* collaboration report an upper limit of $\Sigma m_\nu < 0.12$ eV (95% C.L.) using a combination of CMB data and BAO data from the MGS, 6dFGS and BOSS DR12 galaxy surveys [45]. Even more recently, analysis of a combination of CMB data from *Planck* and LSS data from the eBOSS collaboration (BAO, RSD) obtain an even stronger bound of $\Sigma m_\nu < 0.102$ eV (95% C.L). It is clear that current cosmology constraints are tantalisingly close to $\Sigma m_\nu^{\text{IH,min}}$, putting pressure on the IH scenario (see also Figure 4.1 of Chapter 4). The combination of forthcoming data from LSS surveys and next-generation CMB experiments are expected to reach this bound in the coming decade [220, 221, 278, 279].

Determining the neutrino mass hierarchy is highly important because it will provide insight into the physical mechanism responsible for the neutrino masses, particularly pertaining to the question of whether neutrinos are Dirac or Majorana particles [280]. Moreover, detection of neutrinoless double-beta decay [281] is only possible if neutrinos are Majorana particles. A determination of the hierarchy thus has important implications for experiments aiming to detect this [282]. It is therefore interesting and timely to look at what the current data tells us about the neutrino mass scale and the mass hierarchy, which is the topic of the work presented in Chapter 4.

1.4 Outline of the Thesis

This thesis consists of a collection of original research works carried out during my doctoral studies at the University of Barcelona. The overarching goal of

this research is to study some of the key open questions at the intersection of particle physics and cosmology, in particular the nature of DM and neutrinos, as motivated in the preceding sections. To this end, I present research that highlights the potential of future cosmological observations to explore the nature of DM and the complementarity between cosmological observations and terrestrial experiments in determining the neutrino mass hierarchy.

The thesis is organised as follows. In Chapter 2, we explore the effect of DM decay and annihilation on the thermal and ionization history of the Universe and the observable signatures on the highly redshifted 21 cm line-intensity mapping (LIM) signal from the dark ages. We present forecasted constraints for both forthcoming radio surveys (SKA) and a variety of next-generation experiments. This chapter is based on the original publication [1].

In Chapter 3, we focus on the cosmological consequences of DM models that feature velocity-dependent elastic scattering with baryons. In particular, we study the effect of these interactions on the DM and baryon temperature perturbations and the resulting imprint on the matter clustering at small scales. This chapter is based on the manuscript [2] currently under review.

In Chapter 4, we turn our attention to neutrinos and the role of cosmology in determining the neutrino mass hierarchy. We perform a Bayesian analysis using the latest data from cosmological surveys and neutrino oscillation experiments in order to constrain the neutrino masses and perform a model comparison of the two mass hierarchies considering widely different priors. This chapter is based on the original publication [3].

Finally, in Chapter 5, we summarise the main conclusions and the relevance of the research presented in this thesis and discuss future prospects.

Chapter 2

Dark Matter Annihilation and Decay in the Dark Ages

2.1 Introduction

A vast array of DM candidates predict electromagnetic signatures either through coupling to Standard Model particles via decay, annihilation and scattering, or due to standard astrophysical processes such as primordial black holes [283, 284]. While DM must be predominantly stable over cosmological timescales, it is possible to have particle DM models with a very long yet finite decay lifetime (e. g. sterile neutrinos [134, 285], axinos [286, 287], R-parity violating SUSY models [288]) or where a small fraction of the total DM is decaying (e. g., an excited metastable species [289, 290], atomic DM [291], or some other richer dark sector physics). If the DM consists of a massive particle with weak-scale interactions such as a thermal relic WIMP [292], then we expect coupling to Standard Model particles via DM self-annihilations.

As discussed in Section 1.2, DM candidates with phenomenology beyond the standard cold DM properties are constrained by both astrophysical and cosmological observations [150], as well as direct detection [148, 293] and collider [154] laboratory experiments. Signatures of particle DM in the low-redshift Universe, such as high energy cosmic rays or γ–rays from annihilation or decay of DM in astrophysical sources within our local environment (dwarf galaxies, Galactic centre), have been searched for and used to place stringent bounds on the particle properties (see e. g., [294] and references therein). Non-gravitational effects of particle DM have also been constrained from early Universe observations, such as the CMB power spectrum [45, 186, 188, 295–300] and spectral distortions [188, 301–307], as well as Big-Bang Nucleosynthesis [215, 216, 308].

Probes such as Big-Bang Nucleosynthesis and CMB spectral distortions dominate constraints for DM models with short decay lifetimes ($\tau \lesssim 10^{12}\,\mathrm{s}$), while the CMB angular power spectrum is sensitive to longer lifetimes and

strongly disfavours lifetimes $\tau \lesssim 10^{24} - 10^{25}\,\mathrm{s}$ if all the DM decays [187, 188, 309]. More stringent limits have been set on the decay lifetime in the GeV–TeV mass regime via astrophysical probes; the strongest constraints come from the lack of signal in the Isotropic Gamma-Ray Background above known astrophysical sources [310, 311]. However, these constraints are commonly affected by large uncertainties in the diffuse Galactic background modelling, the Milky Way's DM halo profile, and features of Galactic cosmic-ray propagation. Constraints are typically weaker for light (below $\sim$ GeV) decaying DM. Similarly, measurements of the CMB anisotropies have been used to place constraints on the amount of energy injection due to annihilation of DM particles [45, 186, 295, 300, 312–314]. As in the case of DM decay, indirect detection constraints on DM annihilation can be stronger for masses $\gtrsim$ GeV than those derived from CMB measurements (e. g. [170–172, 315, 316]), but are generally model-dependent and less robust due to the associated astrophysical uncertainties. Despite these constraints, a large portion of viable parameter space for DM decay or annihilation to the visible sector remains unexplored [183].

Future searches must aim to beat and improve these limits, and eventually achieve detection to characterise the nature of DM. However, even with drastically more sensitive future CMB anisotropy instruments, the forecasted constraints on DM annihilation are not expected to drastically improve [317, 318]. It is thus vital that new probes are explored. The advent of line-intensity mapping (LIM) opens up a promising new path for the study of both cosmology and astrophysics [319, 320]. Appropriate analyses of LIM observations will allow to probe cosmology beyond the reach of galaxy surveys (see e. g. [321]), bridging the unexplored epoch of the Universe between redshift $z \sim 3$–5 and the CMB (see e. g. [322, 323]). The 21 cm line [225, 226] offers a direct way to survey the cosmic dark ages, spanning the evolution of the Universe following the end of recombination until the formation of the first luminous objects, with an expected signal in principle reaching up to $z \sim 500$ [324]. Electromagnetic energy injection induced by DM decay or annihilation during the dark ages would alter the thermal and ionisation history of the intergalactic medium (IGM) and leave a potentially detectable imprint in the 21 cm LIM signal and its fluctuations [325–332]. Since the 21 cm LIM signal is sensitive to the late-time behaviour of the Universe and depends on the *thermal* history, not only the ionisation fraction (like CMB), it may provide a powerful complementary cosmological probe of DM with very long lifetimes or low annihilation rates that otherwise evade constraints from the CMB. Furthermore, in contrast to CMB measurements, the onset of structure formation can have an impact on

the DM annihilation rate [297, 333, 334], boosting the effect in the 21 cm signal. Both the global 21 cm signal during reionization and the cosmic dawn and the power spectrum of its fluctuations have been proposed as a probe for exotic DM (see e. g., [188, 328, 330]). However, isolating an unambiguous DM signal in this era, given the uncertainties in the physics of reionization, presents a major challenge [335, 336].

On the other hand targeting the 21 cm signal from the dark ages, although observationally challenging, would circumvent the astrophysical uncertainties related with the cosmic dawn and reionization [337, 338]. Furthermore, matter perturbations remain in the linear regime throughout most of this era [329], which simplifies the modelling of the relevant physics without complications due to galaxy bias and non-linearities in structure formation. Even when departing from the linear regime at $z \gtrsim 30$, corrections remain perturbative [329]. Additionally, the 21 cm temperature fluctuations can be observed at many independent redshift slices, the information from which can be combined to perform a tomographic analysis. This kind of observation would thus provide an uncontaminated window to constrain physics beyond the standard model of cosmology (e. g. inflation [339–341], non-gaussianity [342]), and particularly those involving exotic energy injection from DM [188, 328, 330] or PBH [343, 344].

The forthcoming Square Kilometre Array[1] (SKA) [345] will have the capability to measure the 21 cm LIM signal up to redshifts of $z \sim 30$. Beyond $z \gtrsim 30$, the 21 cm signal is redshifted to low frequencies that the Earth's atmosphere is opaque to and the signal suffers contamination from terrestrial radio interference, rendering detection impossible unless an extremely precise modelling of these contaminants is achieved. As such, the concept of a low-frequency radio array on the lunar far-side is being developed [346–350] in order to study the 21 cm signal up to high enough redshifts to adequately probe the dark ages and take full advantage of the power of 21 cm LIM tomography. A radio telescope on lunar far-side would be shielded from Earth's ionosphere and terrestrial radio interference. However, as we go to higher redshift (lower frequencies), the radio foregrounds become rapidly brighter (reaching several orders of magnitude larger than the expected signal) and will need to be removed with high precision in order to disentangle the cosmological signal in this frequency range from other sources [225].

In this Chapter, we consider the effect of exotic energy injection from DM decay or annihilation on the 21 cm LIM signal during the dark ages. We consider DM with decay lifetimes or annihilation cross-sections that evade current

[1] https://www.skatelescope.org

CMB limits, and model the energy injection in a phenomenological way, without modelling all particle physics properties such as the mass and decay or annihilation channels in detail. The purpose of this work is to evaluate the 21 cm LIM power spectrum from the dark ages as an efficient probe of exotic DM models, estimate its potential, and compare it with existing complementary probes such as the CMB. Therefore, we do not aim for a detailed and comprehensive analysis of the DM contribution depending on the specific underlying particle physics, and leave this study for future work.

This Chapter is organised as follows. We begin in Section 2.2 by reviewing the standard physics of the global 21 cm signal and the angular power spectrum of its fluctuations in the dark ages. In Section 2.3 we introduce the effect of DM decay and annihilation in the physics of the dark ages; we review the thermal and ionisation history of the IGM, including the effect of exotic energy injection, and show how this leads to changes in the global sky-averaged 21 cm signal and the angular power spectrum. Section 2.4 covers the forecasting methodology and the instrumental set-up. In Section 4.3 we present the forecasted detectability of DM decay and annihilation with the forthcoming SKA and different realisations of next-generation radio surveys: a more sensitive "advanced SKA" (aSKA) and a futuristic "Lunar Radio Array" (LRA). Finally, we summarise our findings in Section 2.6.

2.2 Standard 21 cm Line-Intensity Mapping in the Dark Ages

In this section we review the standard physics of the 21 cm signal and set out our notation. Reader experts in this subjects can go directly to Section 2.3.

2.2.1 Global 21 cm signal

The 21 cm line from neutral hydrogen is triggered by the spin-flip transition between the singlet state and triplet state of the hyperfine structure of the $1s$ ground state. The excitation temperature of this transition is called the *spin temperature* T_s, defined via the ratio of the populations in the two hyperfine levels $n_1/n_0 = 3e^{-\frac{T_\star}{T_s}}$ with energy splitting $T_\star = 0.068\,\mathrm{K}$. The spin temperature is driven by: (i) absorption/emission due to Compton scattering with ambient CMB photons, (ii) atomic collisions, relevant at high redshift when the IGM is dense, and (iii) resonant scattering with Lyman-α photons (the

Wouthuysen-Field effect [351–353]). Then, the evolution of the spin temperature follows [354]:

$$T_s = \frac{T_\star + T_{\rm CMB}(z) + y_k T_k(z) + y_\alpha T_\alpha}{1 + y_k + y_\alpha}, \tag{2.1}$$

where $T_{\rm CMB}$ is the CMB temperature, T_k is the mean kinetic temperature of the cosmic gas, T_α the color temperature, and y_k and y_α are the kinetic and Lyman-α coupling terms respectively. The kinetic coupling efficiency y_k is

$$y_k = \frac{T_\star}{A_{10} T_k}(C_H + C_e + C_p), \tag{2.2}$$

with de-excitation rates C_i (of the triplet) due to collisions with neutral hydrogen, free electrons and free protons, respectively. To determine these rates, we adopt the fitting formulas found in [355]:

$$\begin{aligned} C_H &= n_H x_{\rm HI} \kappa, & C_e &= n_H (1 - x_{\rm HI}) \gamma_e, \\ C_p &= 3.2 n_H (1 - x_{\rm HI}) \kappa, \end{aligned} \tag{2.3}$$

where n_H is the comoving number density of hydrogen nuclei and $x_{\rm HI}$ is the fraction of neutral hydrogen, both in units of cm^{-3}, $\kappa = 3.1\times10^{-11} T_k^{0.357} \exp\left(\frac{-32}{T_k}\right)$ $\mathrm{cm}^3\mathrm{s}^{-1}$ and $\log_{10}(\gamma_e/\mathrm{cm}^3\mathrm{s}^{-1}) = -9.607 + 0.5\log_{10}(T_k)\exp[-(\log_{10} T_k)^{4.5}/1800]$ for $T_k \leq 10^4\mathrm{K}$ and otherwise, $\gamma_e(T_k > 10^4\mathrm{K}) = \gamma_e(T_k = 10^4\mathrm{K})$ [356].

Since we focus on the dark ages before the first stars form, in the standard case the Wouthuysen-Field effect can be safely neglected and we set $y_\alpha = 0$. In principle, the injected DM annihilation and decay products may provide a non-negligible Ly-α background intensity which could cause the Ly-α coupling term to become important. We discuss the potential implications of this at the end of Section 2.3.1. We consider the end of the dark ages to be at $z \sim 30$; nonetheless, in some scenarios star formation might begin earlier, hence introducing larger uncertainties in the measurements at $z \sim 30$ due to its effect on the 21 cm signal (see e. g. [335, 336]). We implement a simple stellar reionization model [357] (whose details can be found in Appendix A.1), and find that it has no significant impact in our results.

The observed differential brightness temperature, at some frequency ν, is given by [225, 226, 352],

$$T_{21}^{\rm obs} = \frac{T_s(z) - T_{\rm CMB}(z)}{1+z}(1 - e^{-\tau_{\nu_0}}) \approx$$

$$\approx (27\text{mK})(1+\delta_b)x_{\rm HI}\left(1-\frac{T_{\rm CMB}}{T_s}\right)\left(\frac{\Omega_b h^2}{0.023}\right)\times\left(\frac{1+z}{10}\frac{0.15}{\Omega_m h^2}\right)^{1/2}\frac{1}{1+(1+z)\frac{\partial_r v_r}{H(z)}}, \tag{2.4}$$

where τ_{ν_0} is the optical depth of the IGM for the hyperfine transition frequency $\nu_0 = 1420.4$ MHz, $x_{\rm HI}$ is the fraction of neutral hydrogen, δ_b is the fractional baryon overdensity, Ω_b and Ω_m refer to the baryon and matter density parameters, respectively, $H(z)$ is the Hubble parameter, $h = H_0/100$ is the reduced Hubble constant, and $\partial_r v_r$ is the comoving (peculiar) velocity gradient along the line of sight. Thus, when $T_s < T_{\rm CMB}$, we observe the 21 cm signal in absorption against the CMB spectrum, and in emission for $T_s > T_{\rm CMB}$. Beyond $z \gtrsim 200-500$, collisional coupling is so effective that $T_s = T_k$, while the residual free electron fraction couples the gas to CMB photons via Compton scattering ($T_k = T_{\rm CMB}$), and hence $T_{21}^{\rm obs} \sim 0$. With this in mind, we consider as our science case the interval $30 \lesssim z \lesssim 200$. As we will show, the signal-to-noise is too small beyond $z \sim 200$, so this choice does not affect our results.

2.2.2 Angular Power Spectrum of the 21 cm Fluctuations

Fluctuations in the T_{21} signal are expected to be sourced by perturbations in the density and velocity divergence of the hydrogen clouds (which in turn cause fluctuations in the optical depth and spin temperature). For the purposes of this study, in which we consider the dark ages $z \gtrsim 30$, it suffices to treat the perturbations as linear. Additionally, since we are primarily interested in a signal-to-noise calculation, we neglect fluctuations in other quantities (e. g. the ionisation fraction, gas temperature) which have a sub-dominant effect (see ref. [358] for a full account of these effects up to second-order).

Here we follow the formalism of ref. [329], in which the fluctuations in the 21 cm differential brightness temperature signal to linear order are given by:

$$\delta T_{21}(\vec{x}) = \alpha(z)\delta_b(\vec{x}) + \bar{T}_{21}(z)\delta_v(\vec{x}), \tag{2.5}$$

where $\alpha(z) = \frac{{\rm d}T_{21}}{{\rm d}\delta_b}$, $\delta_v \equiv -(1+z)\delta_r v_r/H(z)$, and we have now dropped the superscript "obs" from Eq. 2.4. Under the assumption of matter domination, and that the baryons follow perfectly the DM distribution, then $\delta_b \propto 1/(1+z)$. Thus, in Fourier space one can write $\delta_v(\mathbf{k}, z) = (\hat{k}\cdot\hat{n})^2\delta_b(\mathbf{k}, z)$ as defined in ref. [329]. Therefore the transfer function of δT_{21} can be defined as:

$$\mathcal{T}_\ell(k,\nu) = \int_0^\infty dx\, W_\nu(x)[\overline{T}_{21}(z)J_\ell(kx) + \alpha(z)j_\ell(kx)], \tag{2.6}$$

where $j_\ell(kx)$ are the spherical Bessel functions, and $J_\ell(kx) \equiv -\partial^2 j_\ell(kx)/(\partial kx)^2$ can be written in terms of spherical Bessel functions[2] [359]. $W_\nu(x)$ is a window function spanning a particular frequency band centred on ν accounting for finite spectral resolution, and x denotes the comoving distance along the line of sight. The window function depends on the details of the experiment; here we have assumed a Gaussian window function of width $\Delta\nu$. The angular power spectrum of the 21 cm fluctuations at a certain frequency ν in terms of the matter power spectrum $P_m(k)$ can then be written as,

$$\mathcal{C}_\ell = \frac{2}{\pi}\int_0^\infty k^2 dk P_m(k)\mathcal{T}_\ell^2(k,\nu). \tag{2.7}$$

In order to speed up computation time, we switch to the Limber approximation [360, 361] at $\ell \geq 10^3$.

2.3 Signatures of Dark Matter on the 21 cm Line-Intensity Mapping Signal

Throughout this work we use the Boltzmann code `CLASS`[3] [362] interfaced with the recombination code `CosmoRec`[4] [363] to solve the evolution equations for x_e and T_k accounting for particle decay or annihilation. In this section we briefly review the standard recombination model plus the additional effects of energy injection from decay or annihilation of DM particles. We then show how the standard 21 cm global signal and angular power spectrum, described in the previous section, is affected by exotic DM energy injection through this dependence on the thermal and ionisation history.

2.3.1 Exotic energy injection: thermal and ionisation history and the global 21 cm signal

Here we follow standard Peebles recombination [364] (further developed in [363, 365–367]). Energy deposited in the medium from an injection of energetic particles, denoted by $\frac{dE}{dVdt}\big|_{\rm dep}$, ionises, excites and heats the medium. The amount of energy going to each of these channels is denoted by the subscripts $c = \{i, \alpha, h\}$, respectively. However, not all the injected energy from the decay and annihilation products is deposited in the medium. The amount of energy deposited

[2] $J_\ell = \frac{-\ell(\ell-1)}{4\ell^2-1} j_{\ell-2}(kx) + \frac{2\ell^2+2\ell-1}{4\ell^2+4\ell-3} j_\ell(kx) + \frac{-(\ell+2)(\ell+1)}{(2\ell+1)(2\ell+3)} j_{\ell+2}$.

[3] https://github.com/lesgourg/class_public

[4] http://www.chluba.de/CosmoRec

depends strongly upon the decay and annihilation channels of the DM particle and its mass (which together determine the energy spectrum of injected particles), and also the redshift of energy injection. Following the approach of refs. [299, 368] the energy deposition rate is commonly parameterised as

$$\left.\frac{dE}{dVdt}\right|_{\rm dep,c}^{\rm dec/ann} = f_c(z)\left.\frac{dE}{dVdt}\right|_{\rm inj}^{\rm dec/ann}, \tag{2.8}$$

where $f_c(z)$ is a dimensionless efficiency function parameterising the amount of energy deposited in the medium in the three different channels $c = \{i, \alpha, h\}$. The function $f_c(z)$ encapsulates the dependence on the energy spectrum of the injected particles and the redshift of injection. A common approximation assumes *on-the-spot* energy deposition, i. e., the energy released from the exotic process is promptly absorbed at the same redshift. A further simplification of this is to approximate the $f_c(z)$ curves by a constant efficiency factor $f_{\rm eff}$ over the entire redshift range, i. e. the fraction of injected energy that is promptly deposited in the IGM stays constant with redshift. This simplification has been shown to be a sufficient approximation in relation to CMB analyses for DM annihilation and long-lived DM decay [187, 295, 357, 368]. We choose to adopt this approximation in our analysis, foregoing a full calculation of the $f_c(z)$ functions, for this initial exploration of the effect of DM energy injection in the 21 cm LIM angular power spectrum. We later discuss the implications of this choice in Appendix A.3.

The evolution of the ionisation fraction (or free electron fraction) x_e is governed by [369],

$$\frac{dx_e}{dz} = \frac{1}{(1+z)H(z)}[R_s(z) - I_s(z) - I_X(z)], \tag{2.9}$$

with the standard recombination and ionisation rates respectively given by,

$$R_s(z) = C\left[\alpha_H x_e^2 n_H\right], \quad I_s(z) = C\left[\beta_H(1-x_e)e^{-\frac{h\nu_\alpha}{k_b T_k}}\right]. \tag{2.10}$$

The coefficient C takes into account the probability that an electron transitions from the $n = 2$ to the $n = 1$ state before being ionised and is given by

$$C = \frac{1 + K_H\Lambda_H n_H(1-x_e)}{1 + K_H(\Lambda_H + \beta_H)n_H(1-x_e)}, \tag{2.11}$$

where $K_H = \lambda_\alpha^3/8\pi H(z)$ describes the cosmological redshifting and escape of the Ly-α photons, and Λ_H is the vacuum decay rate of the metastable $2s$ level

(for a more detailed explanation, refer to Appendix A of ref. [357]).

The final term of Eq. 2.9, $I_X = I_{X_i} + I_{X_\alpha}$, is an effective ionisation rate due to extra injection of energetic particles, split in terms of the direct ionisation rate and the excitation plus ionisation rate following ref. [188] (see also [187, 369]). The contributions to the ionisation rate I_X in terms of the energy deposition rate from the DM decay/annihilation, are

$$\begin{aligned} I_{X_i} &= -\frac{1}{n_H(z) E_i} \frac{dE}{dV dt}\bigg|_{\mathrm{dep},i}, \\ I_{X_\alpha} &= -\frac{1-C}{n_H(z) E_\alpha} \frac{dE}{dV dt}\bigg|_{\mathrm{dep},\alpha}, \end{aligned} \tag{2.12}$$

where $n_H(z)$ is the comoving number density of hydrogen nuclei, and E_i and E_α are the average ionisation energy per hydrogen atom and the Lyman-α energy respectively. Direct ionisations have no inhibition factor C, while extra excitations can only be effective with a probability $1-C$. We neglect the effect of the extra energy injection on Helium ionisation, which has been shown to be sub-dominant [370, 371] and thus should not significantly affect our results.

In turn, the evolution of the kinetic gas temperature T_k follows

$$\frac{dT_k}{dz} = \frac{1}{1+z}\left[2T_k + \gamma(T_k - T_{\mathrm{CMB}})\right] + K_h, \tag{2.13}$$

where γ is a dimensionless parameter defined as [332]

$$\gamma = \frac{8\sigma_T a_R T_{CMB}^4}{3 H m_e c} \frac{x_e}{1 + f_{He} + x_e}. \tag{2.14}$$

Here σ_T is the Thompson cross section, a_R is the radiation constant, m_e the electron mass, c the speed of light and f_{He} is the number of helium nuclei relative to hydrogen nuclei [357, 366]. The additional heating rate term K_h due to the exotic energy injection is given by [332, 357],

$$K_h = -\frac{2}{H(z)(1+z) 3 k_B n_H(z)(1 + f_{He} + x_e)} \frac{dE}{dV dt}\bigg|_{\mathrm{dep},h}, \tag{2.15}$$

where k_B is the Boltzmann constant.

While the formalism described above is general for any exotic source of particles injected to the IGM, we now focus solely on decaying and annihilating DM. The energy injection rates for DM decaying or annihilating into Standard

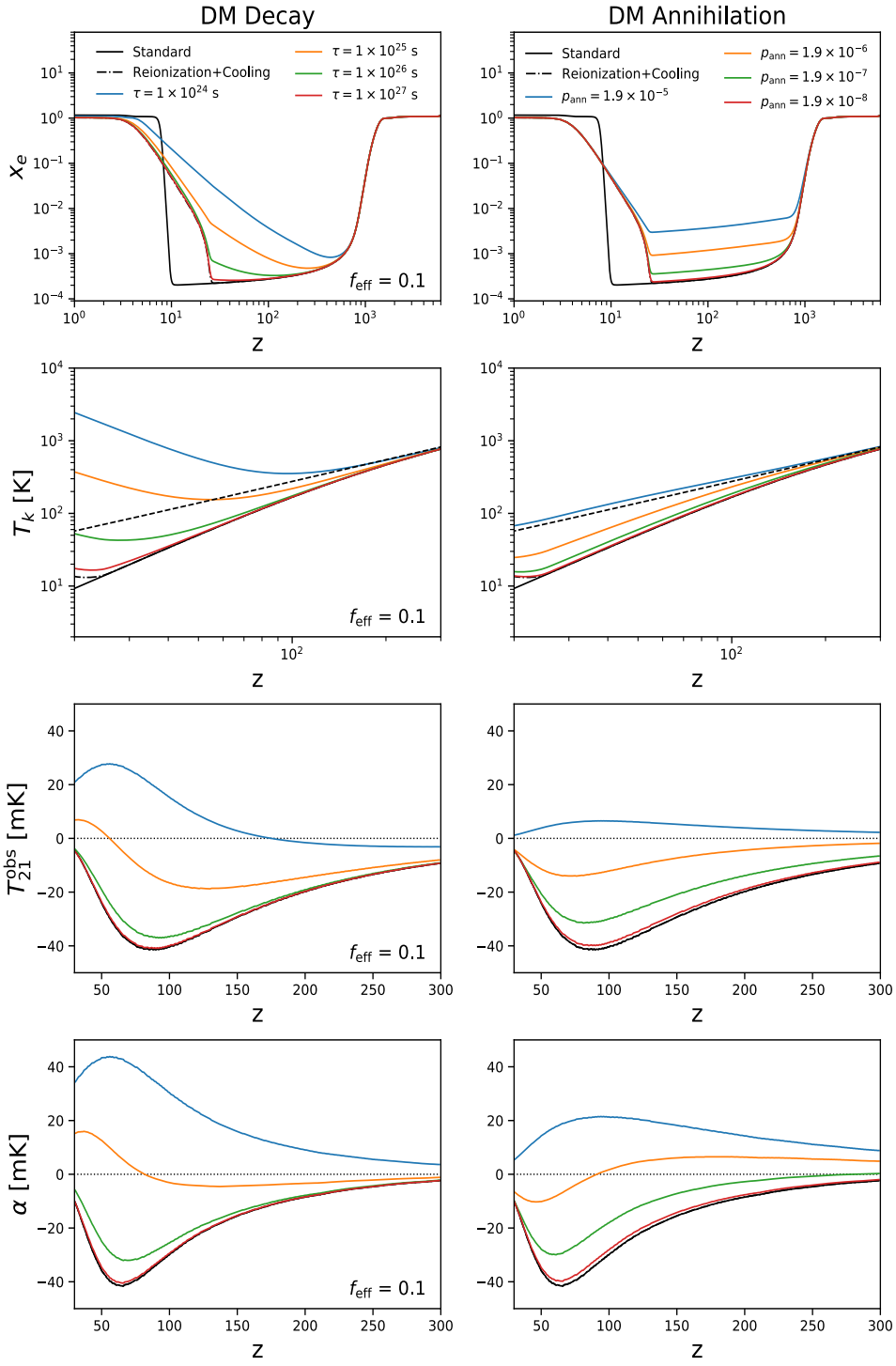

FIGURE 2.1: From top to bottom: Evolution of the free electron fraction x_e, gas kinetic temperature T_k, global 21 cm differential brightness temperature $T_{21}^{\rm obs}$ and $\alpha(z)$ with redshift for DM decay (*left*) and DM annihilation (*right*). The standard ΛCDM prediction is shown for both a single-step reionization (black line) and with a simple stellar reionization model (black dashed) as discussed in Appendix A.1. Black dashed line in the second row represents the CMB temperature. Annihilation efficiency $p_{\rm ann}$ in units of $\mathrm{m^3 s^{-1} kg^{-1}}$.

Model particles are given by, respectively:

$$\left.\frac{dE}{dV\,dt}\right|_{\rm inj}^{\rm dec} = (1+z)^3 f_\chi \Omega_{\rm DM} c^2 \rho_c \frac{e^{-\frac{t}{\tau}}}{\tau}, \qquad \left.\frac{dE}{dV\,dt}\right|_{\rm inj}^{\rm ann} = (1+z)^6 f_\chi^2 \Omega_{\rm DM}^2 c^2 \rho_c^2 \frac{\langle\sigma v\rangle}{m_\chi} \tag{2.16}$$

where f_χ is the fraction of DM that decays/annihilates, $\Omega_{\rm DM}$ is the present-day total abundance of cold DM, ρ_c is the critical density of the Universe today, τ is the lifetime of the decaying particle (related with the decay rate Γ by $\tau \equiv \Gamma^{-1}$), m_χ is the DM particle mass, and $\langle\sigma v\rangle$ is the thermally averaged self-annihilation cross section. As customary, in these equations a smooth cosmological DM distribution is assumed, neglecting structure formation. In this Chapter we consider only cases in which all of the DM decays/annihilates, i. e. $f_\chi = 1$.

For the purposes of this work, for DM decay we choose to set $f_{\rm eff} = 0.1$ in order to explore the implications of this fiducial model on the 21 cm angular power spectrum and the potential to constrain the DM lifetime. We discuss the limitations of this choice and how our results may change quantitatively when considering more detailed injection histories in Appendix A.3. For DM annihilation, we can condense the DM parameters into an effective annihilation efficiency $p_{\rm ann} \equiv f_{\rm eff}\langle\sigma v\rangle/m_\chi$ and so the efficiency factor, if taken to be constant, is already absorbed into the parameter we want to constrain and we do not assume anything for $f_{\rm eff}$. After the first stars form, there are other sources of heating and ionisation. We take this into account by including our simple stellar reionization model, described in Appendix A.1. Unless otherwise stated, the results presented in this Chapter include this stellar reionization prescription.

The effect of DM decay and annihilation on the thermal and ionisation history of the IGM, and the resulting 21 cm differential brightness temperature T_{21}, defined in Eq. 2.4, and corresponding $\alpha(z) = {\rm d}T_{21}/{\rm d}\delta_b$ are shown in Figure 2.1. We show here the standard ΛCDM prediction (without exotic energy injection) both with the stellar reionization model and with the standard hyperbolic tangent transition describing reionization. For decaying DM with the considered lifetimes, the energy injection heats and ionizes the gas, resulting in an increasing ionisation fraction with redshift, slowly reionizing the IGM at high redshift. Additionally, the extra energy injection heats the gas temperature T_k, which then rises above the CMB temperature earlier than in the case of no DM decay. Furthermore, as the DM decay increases the ionisation fraction, Compton scattering becomes more efficient and results in extra heating of the gas (second term of Eq. 2.13) on top of the direct heating term K_h. All of this

has a strong effect in the global T_{21} signal which directly depends on the thermal history, unlike CMB. While $T_k < T_{\rm CMB}$ (and collisional coupling maintains $T_s < T_{\rm CMB}$), we observe the 21 cm signal in absorption. However, due to the heating and ionisation produced by the DM decays, the depth of the absorption signal reduces, even transitioning to a signal in emission for the shortest decay lifetimes considered here.

The effect of annihilating DM on the 21 cm signal is comparable, where greater annihilation efficiency leads to more ionisation and heating of the gas, resulting in a shallower absorption or even emission signal in 21 cm. For annihilating DM however, the energy injection is proportional to the square of the density, hence most of the energy is injected at earlier times (before or around recombination) when the DM density was higher. The ionisation fraction then freezes out at an elevated value relative to the ΛCDM prediction, then decreases very slowly until reionization kicks in. On top of the direct heating of the gas from the energy injected in the annihilation products, the higher x_e can have the effect of delaying hydrogen-CMB decoupling (keeping $T_k \sim T_{\rm CDM}$ for longer) resulting in an increased gas temperature at later times since there has been less time to cool adiabatically. The effect of DM annihilation on gas heating at high-z is much smaller because the majority of energy is injected while Compton scattering is still efficient enough to ensure $T_k \sim T_{\rm CMB}$. Therefore, DM annihilation tends to reduce the variation of T_{21} with redshift.

This work being a proof-of-concept, we do not include second order effects of the extra energy injection from exotic DM in our modelling. Among these, the most important might be the potential advance of reionization, with the first stars forming earlier, due to the impact of DM decays or annihilation. This would increase the redshift at which the dark ages end, hence keeping the observation of the dark ages out of reach for ground-based experiments. However it has been shown [334] that a contribution of more than 10% to reionization is disfavoured for almost all DM decay and annihilation scenarios which are consistent with the CMB constraints. Nevertheless, the backreaction effect of the increased ionisation level due to DM energy injection can lead to greater gas heating, especially near the end of the cosmic dark ages [372] which can in turn modify the global T_{21} signal.

We have also neglected any potential contribution from Ly-α photons injected by the DM decays or annihilations in the IGM. Additional heating of the IGM due to the Ly-α background has been found to be negligible compared to other sources of heating [373–375], and in fact becomes less efficient as the gas temperature rises (e. g. through direct heating from DM annihilations and

decays). However, there may be some consequence due to the Ly-α coupling of T_s to T_k through the Wouthuysen-Field effect. As the IGM cools and expands, collisional coupling becomes inefficient ($z \sim 70$) and T_s tends toward T_{CMB}. If the Ly-α coupling becomes efficient enough to drive T_s toward T_k again, then for DM models in which the IGM temperature remains below T_{CMB}, T_s would be driven towards lower values, resulting in the differential brightness temperature T_{21} curve to drop below that of the standard scenario without DM. Ref. [328] demonstrates this effect for several DM annihilation models, where the additional Ly-α coupling causes the differential brightness temperature to dip slightly below that of the standard scenario at around $z = 30 - 40$ (see their Figure 5). On the other hand, if the IGM is sufficiently heated above the T_{CMB} by the DM energy injection, then we expect the extra Ly-α coupling of T_s to the higher T_k to contribute to an increase in the differential brightness temperature T_{21}; resulting in a shallower absorption signal or earlier emission signal. In either scenario, the effect would result in a larger deviation from the standard (no DM) case, and as such, our projections remain conservative. Further, we expect these deviations to be minor, as Refs. [330, 376] indicate that the Ly-α coupling term is sub-dominant to the collisional coupling/IGM heating in the case of DM energy injection. Given these considerations, we do not expect the inclusion of the Ly-α coupling to alter the results significantly.

We leave the study of these effects to be included in a more detailed analysis in future work. Finally, we do not consider any DM annihilations with velocity-suppressed cross-sections (p–wave annihilation) or models with Sommerfeld enhanced [377] annihilation cross-sections.

2.3.2 Dark matter energy injection on the 21 cm angular power spectrum

We compute the effect of DM decay and annihilation on the 21 cm angular power spectrum during the dark ages. We only consider here the changes in the angular power spectrum due to the modifications of $P_m(k)$, T_{21}, and α. In principle, the extra energy injection would not only affect the global quantities, but also the perturbations and scale dependence of the power spectrum. We leave such study for future more detailed analyses.

Figure 2.2 shows how the 21 cm angular power spectrum at $z = 30$ is modified from the standard ΛCDM signal by electromagnetic energy injection from either decaying or annihilating DM (top left and right panels, respectively), for several values of the decay lifetime or annihilation efficiency. The bottom

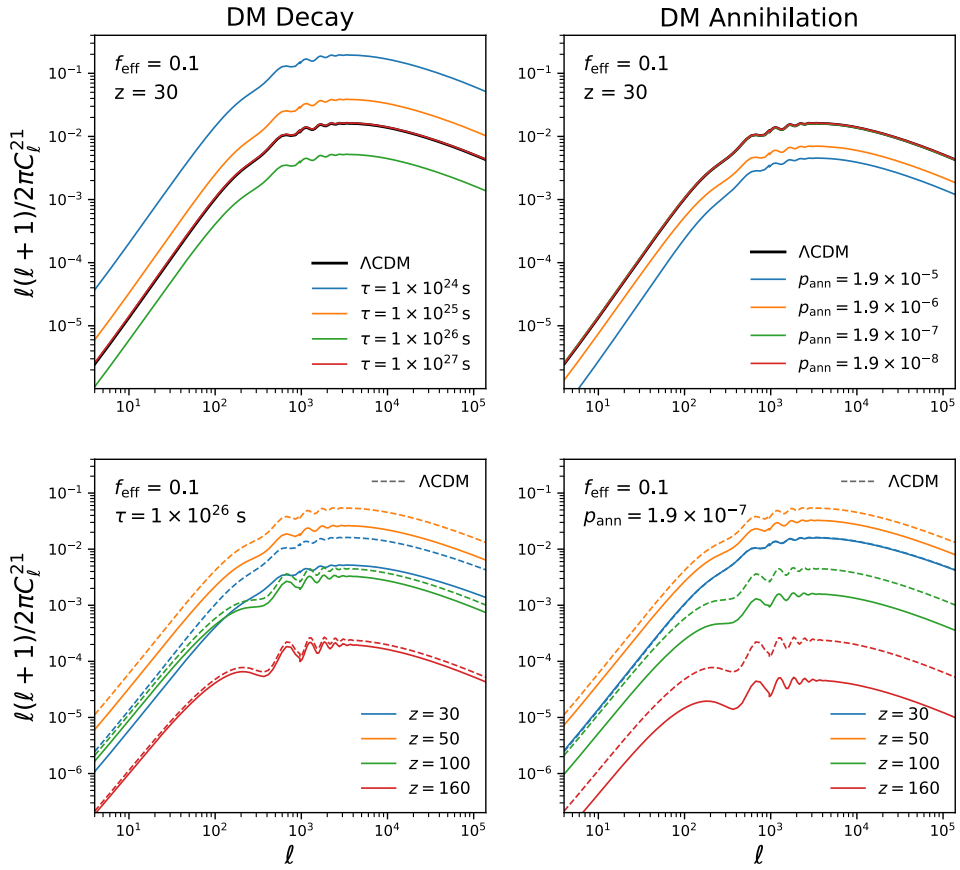

FIGURE 2.2: *Top:* Angular power spectrum of fluctuations in the 21 cm brightness temperature at $z = 30$ with contribution from decaying (left) or annihilating (right) DM of various decay lifetimes or annihilation efficiency. *Bottom:* Angular power spectrum for a fiducial DM decay of $\tau = 1\times10^{26}$ s (left) and fiducial DM annihilation with $p_{\rm ann} = 1.9\times10^{-7}\,{\rm m^3 s^{-1} kg^{-1}}$ (right) in solid lines at various redshifts during the dark ages ($z = 30-180$), compared to the standard ΛCDM power spectrum at each redshift (dashed lines). Annihilation efficiency $p_{\rm ann}$ in units of ${\rm m^3 s^{-1} kg^{-1}}$.

left and right panels of Figure 2.2 show the predicted signal at various redshifts for a single fiducial decay lifetime and annihilation efficiency, respectively. The C_ℓ's depend on the square of the quantities T_{21} and α (eqs. 2.5–2.7), and so the power in the C_ℓ's is enhanced or suppresed accordingly as the absolute value of these quantities changes. In other words, it is the difference in *intensity* of the absorption/emission signal compared to the standard absorption signal that determines the difference on the power spectrum (regardless of whether the global T_{21} signal is in absorption or emission itself).

At $z = 30$, we find an enhancement in the 21 cm fluctuation signal for decay lifetimes $\tau \lesssim 1\times10^{25}$ s, while for $\tau = 1\times10^{26}$ s, the extra energy injection reduces the intensity of the global absorption signal, and so the resulting power spectrum is suppressed compared to the ΛCDM case. For even longer lifetimes, e. g., $\tau = 1\times10^{27}$ s, the global absorption signal is almost as large as the

standard one, and so the power spectrum increases again to close to the ΛCDM line. Within current bounds on the DM annihilation parameter ($p_{\rm ann} < 1.9 \times 10^{-7}\,{\rm m^3 s^{-1} kg^{-1}}$), the deviation from the standard signal in the angular power spectrum is much smaller than for the allowed range of decay lifetimes ($\tau \gtrsim 1 \times 10^{25}$s) at $z = 30$. This is expected due to most of the energy injection occurring at higher redshift for annihilating DM. While the deviation for a fiducial $p_{\rm ann} = 1.9 \times 10^{-7}\,{\rm m^3 s^{-1} kg^{-1}}$ is small at $z = 30$, the difference between the annihilating DM and the standard signal increases with redshift until around $z \sim 50$ (bottom right of Figure 2.2). For the decaying DM lifetime $\tau = 1 \times 10^{26}$s the signal also grows with redshift until around $z \sim 40 - 50$, but then decays faster than for the annihilating DM scenario.

We remind the reader that we demonstrate the effect of each decay lifetime for a fixed $f_{\rm eff} = 0.1$ only, and that the amount of the energy injection for a given lifetime can vary greatly with the particle mass and types of decay channels. We discuss the implications of this, exploring some examples, in Appendix A.3. Due to the sensitivity of the 21 cm signal to the energy injection history, a careful analysis of the effect on the 21 cm LIM signal across all decay masses and channels would allow the possibility to constrain or eventually measure DM particle properties beyond the lifetime, if potential degeneracies can be taken care of. These degeneracies are worth exploring, and we aim to perform such a study in future research.

2.3.3 DM annihilation in halos: the halo-boost

Below $z \sim 100$ the effects of structure formation may become important, enhancing the average square DM density with respect to the smooth background by some boost factor $\mathcal{B}(z)$, such that [297, 357]:

$$\langle \rho^2 \rangle(z) = (1 + \mathcal{B}(z)) \langle \rho \rangle^2(z). \tag{2.17}$$

The energy injected from DM annihilation then becomes,

$$\left. \frac{dE}{dV dt} \right|^{\rm ann}_{\rm inj,smooth+halos} = (1+z)^6 f_\chi^2 \Omega_{\rm DM}^2 c^2 \rho_c^2 \frac{\langle \sigma v \rangle}{m_{\rm DM}} (1 + \mathcal{B}(z)). \tag{2.18}$$

In the halo model framework, adopting the Press-Schechter formalism for the halo mass function, the boost factor is (see Appendix C of ref. [357]),

$$\mathcal{B}(z) = \frac{f_H}{(1+z)^3} {\rm erfc}\left(\frac{1+z}{1+z_H} \right), \tag{2.19}$$

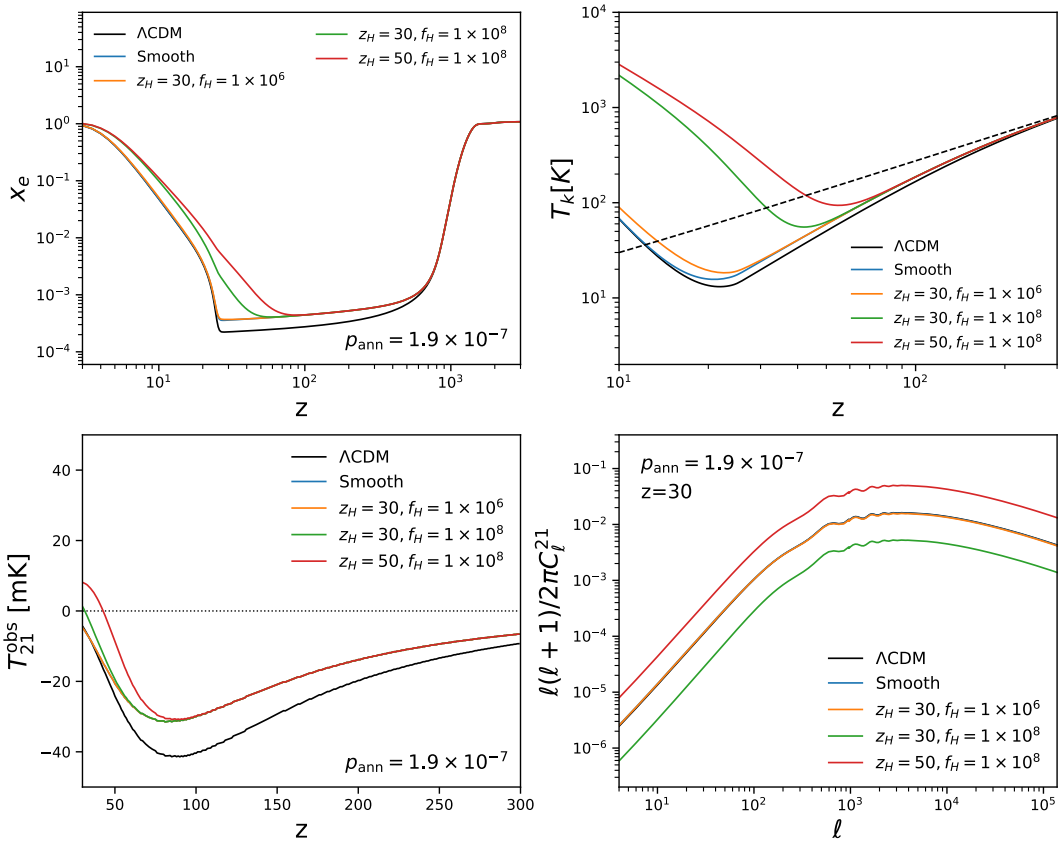

FIGURE 2.3: Evolution of free electron fraction x_e (*top left*), gas temperature T_k (*top right*), and global T_{21} signal (*bottom left*) with redshift, and the angular power spectrum of the 21 cm fluctuations at $z = 30$ (*bottom right*), comparing the effect of energy injection of annihilating DM from the smooth background only and with the effect of various halo boost factors included. For the smallest boost factor considered, the curve (orange) lies on top of the smooth annihilating DM curve (blue) except in the plot of the T_k. The stellar reionization model is included and the annihilation efficiency is fixed at the maximum value allowed by current *Planck* bounds $p_{\rm ann} = 1.9 \times 10^{-7}\,{\rm m^3 s^{-1} kg^{-1}}$.

where z_H is the characteristic redshift at which halos begin to contribute, and f_H is a normalisation set by the amplitude of the boost factor at $z = 0$. According to [357] reasonable values for these parameters lie in the range $z_H \in [20, 30]$ and $\mathcal{B}(z = 0) \in [5 \times 10^4, 10^6]$ (corresponding to $f_H \in [10^6, 10^8]$), however this is still poorly constrained. In Figure 2.3 we show the effect of various halo boost parameterisations on the ionisation fraction and gas temperature compared to a smooth DM distribution, and the resulting evolution of the global 21 cm temperature and its fluctuations (at $z = 30$) for a fixed fiducial $p_{\rm ann} = 1.9 \times 10^{-7}\,{\rm m^3 s^{-1} kg^{-1}}$. Although outside the redshift range of interest here, we find that the stellar reionization model kicks in already before $z = 20$, suppressing the effect of the halo boost choice. For this reason we set $z_H = 30$ and choose different fiducial values of f_H in our analysis.

Once the boost kicks in, it increases DM annihilation efficiency, thereby injecting more energy which in turn induces earlier ionisation and heating of the IGM. For large enough halo boost, this can cause the gas temperature T_k to rise above the CMB temperature T_γ at early redshifts ($z > 30$) and trigger an emission signal in the global 21 cm line during the dark ages. For smaller boost factors, the extra energy injection can result in a smaller absorption or smaller emission signal (in absolute value) at $z = 30$ than for smooth DM, resulting in a suppression of the power spectrum with respect to the smooth DM case.

Here we have only considered the effect of early sub-structure formation boosting the amount of energy injection from DM annihilation. In computing the angular power spectrum we still treat the DM as a continuous background, neglecting a full calculation of the contribution from the 'one-halo' and 'two-halo terms' in the halo model. Additionally, there may be an important Poisson contribution at small scales. It has been shown that when the sub-structure contribution becomes important for DM annihilation, the energy deposition is dominated by $\lesssim 1\,M_\odot$ halos, which can be treated as uniformly distributed on large scales $\gtrsim$ 10Mpc [328, 330]. Assuming ΛCDM with the *Planck* best-fit parameters, at $z = 30$ the multipole $\ell = 10^3$ corresponds to $k \sim 0.1\,{\rm Mpc}^{-1}$ and so up to this scale, we consider our assumption sufficient. At smaller scales (we consider up to $\ell = 10^5$, which corresponds to $k \sim 10\,{\rm Mpc}^{-1}$) however, this assumption may break down as the Poisson contribution may become important. In this case, however, the Poisson-like contribution adds an extra signal (also with its variance) at small scales. Such extra contribution should be accounted for in any realistic analysis but for our proof-of-principle estimate of neglecting it is likely to yield an underestimate of the expected signal to noise.

2.4 Forecasts

We now forecast the detectability of a decaying or annihilating DM contribution to the 21 cm angular power spectrum from the dark ages. We estimate the constraining power of a given experiment using a Fisher information matrix analysis [378, 379]. The Fisher information matrix is defined as

$$\mathcal{F}_{\alpha\beta} = \left\langle -\frac{\partial^2 \ln \mathcal{L}(\theta)}{\partial\theta_\alpha \partial\theta_\beta} \right\rangle, \tag{2.20}$$

where $\mathcal{L}$ is the likelihood and θ_α are the cosmological model parameters. We consider the 21 cm angular power spectrum C_ℓ, measured with a covariance $\sigma^2_{C_\ell}$ (assumed to be diagonal), which will be given by the specific instrumental set-up and presented in Section 2.4.1 and Eq. 2.25. Assuming the C_ℓ's are Gaussian distributed, the Fisher matrix elements corresponding to parameters θ_α and θ_β can be computed from

$$\mathcal{F}^{21\mathrm{cm}}_{\alpha\beta} = \sum_{\ell,z} \frac{\partial C_\ell}{\partial\alpha} \frac{\partial C_\ell}{\partial\beta} \sigma^{-2}_{C_{\ell\ell'}}. \tag{2.21}$$

We assume a standard ΛCDM plus an extra parameter to describe the DM decay or annihilation (lifetime τ and annihilation efficiency p_{ann} respectively) as our fiducial model, considering the following set of free parameters

$$\mathbf{P} \equiv \{\theta_s, \omega_{\mathrm{cdm}}, \omega_{\mathrm{b}}, \ln\left(10^{10} A_s\right), n_s\} + \vartheta, \tag{2.22}$$

where θ_s is the angular size of the sound horizon, $\omega_{\mathrm{cdm}} \equiv \Omega_{\mathrm{cdm}} h^2$ is the cold dark matter abundance, $\omega_{\mathrm{b}} \equiv \Omega_{\mathrm{b}} h^2$ is the baryon abundance, A_s and n_s are the amplitude and spectral index of the primordial power spectrum of scalar modes respectively, and ϑ corresponds either to τ or p_{ann} depending on the DM scenario. We adopt the latest *Planck* 2018 TT, TE, EE + low-E [45] best-fit values for our fiducial ΛCDM cosmology: $\theta_s = 1.04109$, $\omega_{\mathrm{cdm}} = 0.1202$, $\omega_{\mathrm{b}} = 0.02236$, $\ln(10^{10} A_s) = 3.045$, $n_s = 0.9649$. To compute the final constraints we adopt the stellar reionization model discussed in Appendix A.1 , and so we do not fix the redshift of reionization z_{reio} as this is taken care of within the modelling. In our modeling, A_s is completely degenerate with the parameters governing the DM decay or annihilation at each redshift bin (since both control the amplitude of the power spectrum). Therefore, we use a prior on A_s from the *Planck* 2018 TT, TE, EE + low-E [45] results. Nevertheless, this degeneracy would be broken with the use of tomography. We do not include *Planck* priors on other parameters, so beyond A_s, the measurements presented here are

independent of CMB measurements.

We consider several fiducial values for τ and $p_{\rm ann}$ within the current limits set by CMB and Big-Bang Nucleosynthesis analyses, and forecast the errors on the fiducial DM particle parameter of interest. Specifically, we forecast marginalized constraints on the DM decay lifetime for fiducial $\tau = 10^{25} - 10^{27}\,$s and on the annihilation efficiency for fiducial $p_{\rm ann} = 1.9 \times (10^{-7} - 10^{-8})\,{\rm m^3 s^{-1} kg^{-1}}$, still viable ranges for many DM masses and channels. We do so in order to estimate potential detections for 21 cm from the dark ages searches. For DM decay, we assume two cases for a constant $f_{\rm eff}$, with values 0.1 and 0.4, as well as time varying functions mimicking specific DM masses and decay channels. For the annihilating DM case, we consider annihilation with and without the halo boost. Regarding the parameters of the boost, we choose two configurations to bracket the reasonable range described in [357]: Boost 1 $z_{\rm H} = 30$, $f_{\rm H} = 1 \times 10^6$ and Boost 2 $z_{\rm H} = 30$, $f_{\rm H} = 1 \times 10^8$. We do not vary the boost parameters, solely exploring the effect on the constraints for $p_{\rm ann}$ for each fiducial halo boost. Additionally, we fix the fraction of DM that decays/annihilates to $f_\chi = 1$, as varying this fraction would be degenerate with varying the efficiency factor $f_{\rm eff}$.

Finally we consider the case of non-detection, and forecast marginalized upper limits on τ and $p_{\rm ann}$. We do so by assuming a fiducial model with no exotic DM and studying variations around it.

2.4.1 Experimental setup

The power spectrum of the instrumental noise C_ℓ^N of a radio interferometer with uniformly distributed antennas at a given frequency ν can be written as (see e. g. [380–383]),

$$\ell^2 C_{\ell\ell'}^N = \frac{(2\pi)^3 T_{\rm sys}^2(\nu)}{\Delta\nu\, t_o f_{\rm cover}^2} \left(\frac{\ell}{\ell_{\rm cover}(\nu)}\right)^2 \delta_{\ell\ell'}^K, \tag{2.23}$$

where the maximum multipole observable $\ell_{\rm cover}(\nu) \equiv 2\pi D_{\rm base}/\lambda(\nu)$, $D_{\rm base}$ is the largest baseline of the interferometer, $f_{\rm cover}$ is the fraction of this baseline covered with antennas, $t_{\rm obs}$ is the observation time, $T_{\rm sys}$ is the system temperature, and δ^K is the Kronecker delta. Assuming the system temperature to be the synchrotron temperature of the observed sky, we have (extrapolating to lower frequencies the results reported in Ref. [384]):

$$T_{\rm sys}(\nu) = 180 \left(\frac{\nu}{180{\rm MHz}}\right)^{-2.62} {\rm K}. \tag{2.24}$$

Spec	SKA	aSKA	LRA1	LRA2	LRA3
$D_{\rm base}$ (km)	6	100	30	100	300
$f_{\rm cover}$	0.02	0.2	0.1	0.5	0.75
$t_{\rm obs}$ (years)	5	10	5	5	5
$l_{\rm cover}\frac{1+z}{31}$	5790	96515	28954	96515	289547

TABLE 2.1: Instrument specifications for the forthcoming SKA, an advanced ground-based SKA-like experiment (aSKA), and three realisations of a futuristic lunar radio array (LRA).

Therefore, the uncertainty in the measured 21 cm C_ℓ at a given multipole ℓ including cosmic-variance is then given by

$$\sigma_{C_{\ell\ell'}} = \sqrt{\frac{2(C_\ell + C^N_{\ell\ell'})^2}{f_{\rm sky}(2\ell+1)}}\delta^K_{\ell\ell'}, \tag{2.25}$$

where $f_{\rm sky}$ is the fraction of sky coverage of the survey (we assume all-sky surveys, i. e., $f_{\rm sky} = 0.75 \sim 30,000\,{\rm deg}^2$). In addition, we consider for all cases a frequency band $\Delta\nu = 1\,{\rm MHz}$. We consider both the forthcoming SKA experiment, and different realisations of more advanced, futuristic earth- and lunar-based radio interferometers. The instrument specifications for each survey we consider are summarised in Table 2.1. Ground-based experiments (SKA and aSKA) will be limited to observe at $z = 30$, while the three realisations of the LRA will be able to perform a tomographic analysis over the redshift range $30 \lesssim z \lesssim 200$. By considering both, we examine how much improvement in detection capabilities for a DM decay or annihilation signal is possible for different types of next-generation experiments measuring the 21 cm LIM power spectrum. Following the arguments of Ref. [342], we consider 39 independent (i. e. uncorrelated) redshift bins between $z = 30$ and $z = 180$, equally spaced in frequency with $\Delta\nu = 1\,{\rm MHz}$.

2.5 Results

We present forecasted constraints and lower (upper) limits on τ ($p_{\rm ann}$) for DM decay (annihilation), from the 21 cm LIM power spectrum as observed by the experimental setups described in Section 2.4.1, for different versions of the SKA and Lunar radio arrays. To obtain comprehensive results, we consider two representative values of the effective efficiency parameter $f_{\rm eff} = 0.1, 0.4$ for decays, and both a smooth background and halo-boosted annihilations for the

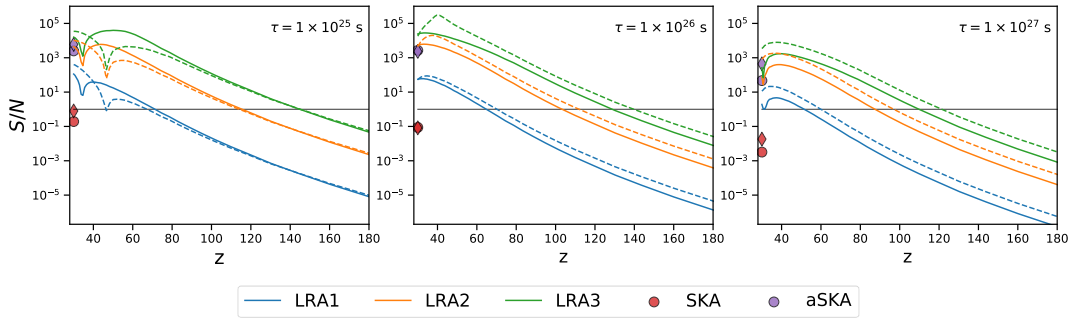

FIGURE 2.4: Evolution of the signal-to-noise ratio (S/N) with redshift between the 21 cm angular power spectrum with decaying DM lifetimes $\tau = 1 \times (10^{25} - 10^{27})$ s compared to the ΛCDM case (no decaying DM) as measured by SKA, an advanced SKA-like instrument (aSKA) and 3 realisations of a futuristic lunar radio array (LRA). Instrument specifications can be found in Table 2.1. For SKA and aSKA ($z = 30$), the circles represent $f_{\rm eff} = 0.1$ and diamonds represent $f_{\rm eff} = 0.4$. For LRA, solid lines represent an efficiency factor $f_{\rm eff} = 0.1$ and dashed lines represent $f_{\rm eff} = 0.4$. Solid black line represents an S/N of unity. We define $S/N = \sum_\ell (\Delta C_\ell / \sigma_{C_\ell})$, and the lines connect the S/N in each redshift bin into a curve.

annihilating DM scenario. We summarize our results in this section, and report all cases in detail in Tables A.1, A.2 and A.3 in Appendix A.2.

We find that the forecasted errors are largely insensitive to the adopted stellar reionization model (Appendix A.1) as expected, given that the reionization effect kicks in below $z = 30$. Hence, all results are reported with the stellar reionization prescription included, and we do not expect reasonable changes to the reionization model to affect our results.

Figures 2.4 and 2.5 show the evolution of the signal-to-noise ratio (S/N) with redshift of the 21 cm angular power spectrum for the fiducial decaying and annihilating DM models, respectively, as measured by SKA, aSKA ($z = 30$) and LRA. As most of the energy injection occurs at earlier times for DM annihilation when the background DM density is higher, the S/N tends to peak at higher redshift than for decaying DM. The dip in the S/N that is observed e. g. for $\tau = 1 \times 10^{25}$ s is due to the crossing from absorption into emission of the global T_{21} signal, resulting in a drop in signal in the C_ℓ's. Figures 2.6 and 2.7 summarise the marginalised forecasted *relative errors* around each fiducial decay lifetime and annihilation efficiency respectively, for all 5 experimental set-ups measuring the 21 cm power spectrum.

Our results demonstrate that SKA alone is unlikely to precisely constrain DM decay even for the shortest viable decay lifetimes. There is no case within the allowed lifetimes for which the SKA reaches a signal-to-noise ratio S/N of unity, except for decay channels with much larger energy injection, see Appendix A.3. Even under the optimistic assumption that SKA can observe up to

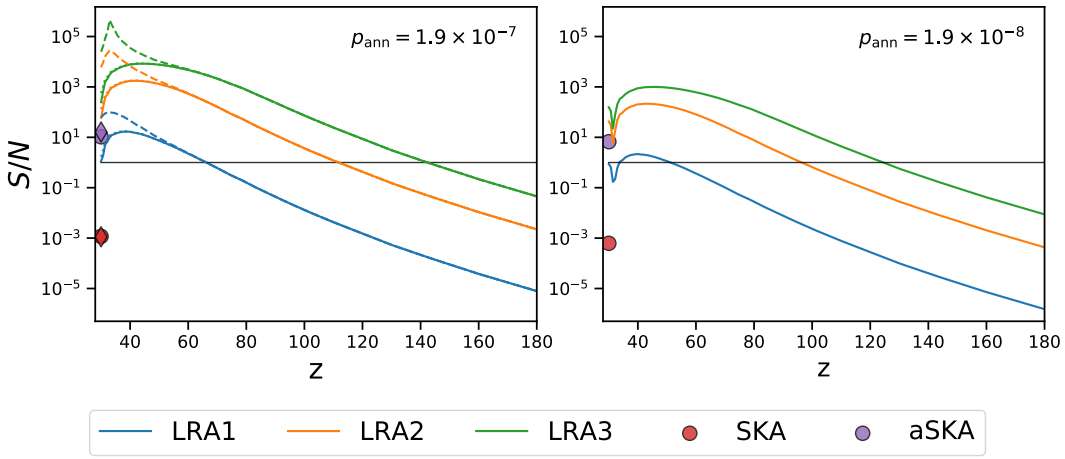

FIGURE 2.5: Evolution of the difference in signal-to-noise ratio (S/N) with redshift between 21 cm power spectrum with annihilating DM with $p_{\rm ann} = 1.9 \times (10^{-7} - 10^{-8})\mathrm{m^3 s^{-1} kg^{-1}}$ in smooth background (solid), with halo boost 1 (dotted) and halo boost 2 (dashed), with respect to the ΛCDM case (no DM energy injection). For SKA and aSKA ($z = 30$), the circles represent smooth DM distribution and diamonds represent with halo boost 1. Solid black line represents a S/N of unity. S/N defined as in Figure 2.4.

$z \sim 35$, we found the constraints do not improve dramatically enough to enable a precise detection. With a more sensitive earth-based instrument like aSKA, it would be possible to constrain lifetimes of up to $\tau = 1 \times 10^{26}$s with close to percent-level precision observing at $z = 30$ only. Due to its large baseline, aSKA measuring the power spectrum at $z = 30$ could better constrain the DM lifetime than LRA1 even taking advantage of the full redshift range. Therefore, having a large enough baseline with enough angular resolution to resolve the information at small scales will be critical in providing precise measurements of the DM parameters.

However, only a tomographic analysis would allow the possibility to constrain the DM lifetime down to the sub-percent level. The information gain from probing higher redshifts significantly boosts the detection capabilities. While in general the S/N decreases with redshift, the maximum S/N appears at $z > 30$ for various parameters configurations, especially as the experiment improves (see Figure 2.4). Even with a much more sensitive instrument like LRA3 (with a much larger baseline and $f_{\rm cover}$), the measurement errors at $z = 30$ alone do not improve much over what is attainable with aSKA (an improvement of around a factor of ~ 1.3 at $z = 30$ compared with a factor ~ 11 using the range $30 < z < 200$). As such, a lot of information is lost if these higher redshifts cannot be reached.

With LRA2, it would be possible to constrain lifetimes of up to $\tau = 1 \times$

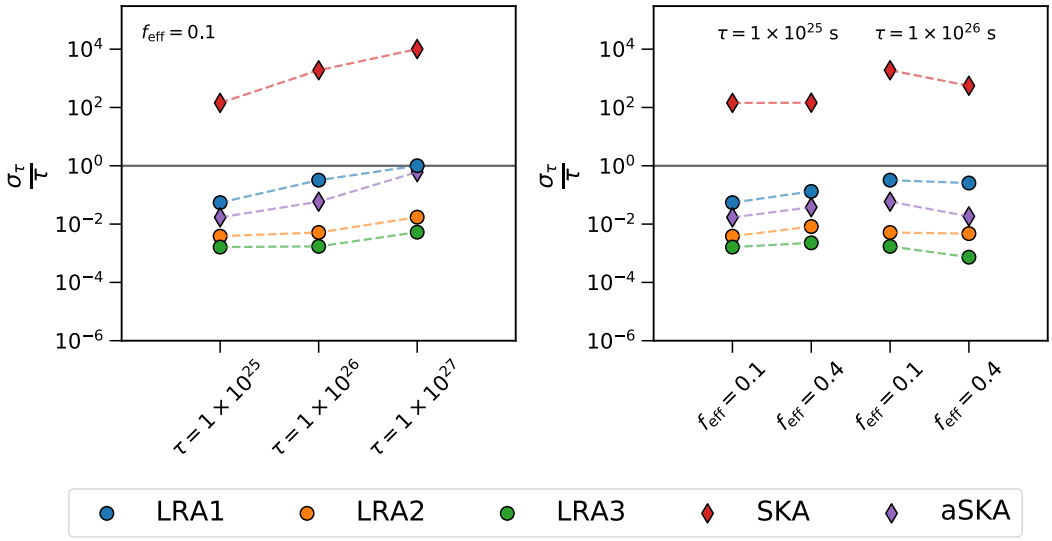

FIGURE 2.6: Marginalised 68% confidence level forecast *relative errors* around each fiducial decay lifetime $\tau = 1 \times (10^{25} - 10^{26})$ s (left panel) and comparing the errors around two fiducial lifetimes with both $f_{\rm eff} = 0.1, 0.4$ (right panel), for SKA, an advanced SKA-like instrument (aSKA) and 3 realisations of a futuristic lunar radio array (LRA). For SKA and aSKA, the constraints are based on a measurement of the 21 cm at $z = 30$ only while LRA utilises tomography of the 21 cm LIM in $30 \leq z \leq 200$. Solid black line represents a relative error of unity.

10^{26} s at the sub-percent level, already ~ 1 order of magnitude below general bounds on the DM lifetime from CMB [187]. LRA3 could reach sub-percent level precision even for $\tau = 1 \times 10^{27}$s, two orders of magnitude longer lifetimes than current CMB limits (given an energy injection of $f_{\rm eff} = 0.1$). For decay scenarios with larger energy injection, even longer lifetimes could be probed.

We also use the Fisher matrix formalism to forecast a lower limit on the decay lifetime in case of non-detection, assuming $f_{\rm eff} = 0.1$. For aSKA, we project a lower limit at $\tau > 1.9 \times 10^{27}$ s at 95% C.L. With a lunar-based instrument, we can reach a forecasted lower bound on the lifetime of $\tau > 2.21 \times 10^{29}$ s at 95% C.L for LRA3, improving upon the current bounds from CMB measurements by more than 4 orders of magnitude ($\tau > 1 \times 10^{25}$ s [187]). A detailed report of forecasted limits for each experiment can be found in Table A.3 in Appendix A.2.

We emphasise that the forecasts discussed above corresponding to DM decay are for two representative cases of the energy injection history, $f_{\rm eff} = 0.1, 0.4$. In Figure 2.6 we can see that the relative forecasted errors do not change significantly when assuming $f_{\rm eff} = 0.4$; hinting that the constraining power does not depend strongly on the value of $f_{\rm eff}$ while it is constant. Still, we explore some specific particle decay cases (e. g. DM particles of 100 MeV decaying into electron-positron pairs ($\chi \to e^+e^-$) and 100 GeV decay to photons ($\chi \to \gamma\gamma$))

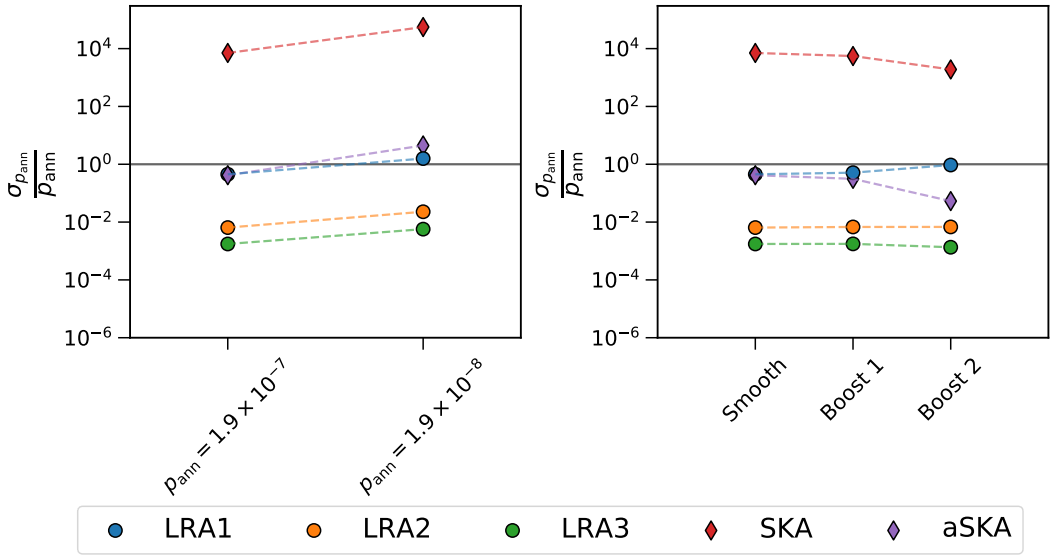

FIGURE 2.7: As in Figure 2.6, but here forecasted constraints are shown for the fiducial values of $p_{\rm ann} = 1.9 \times (10^{-7} - 10^{-8}) {\rm m}^3 {\rm s}^{-1} {\rm kg}^{-1}$ for a smooth DM distribution (left panel) and errors around a fixed $p_{\rm ann} = 1.9 \times 10^{-7} {\rm m}^3 {\rm s}^{-1} {\rm kg}^{-1}$ assuming a smooth background DM distribution only compared to adding a halo boost factor to account for early structure formation (right panel). Solid black line represents a relative error of unity.

for a lifetime of $\tau = 1 \times 10^{26}$ s and discuss the implications for the forecasted constraints in Appendix A.3. We find that the constraints on τ can vary by up to an order of magnitude for the specific decay models considered. The main case studied here, $f_{\rm eff} = 0.1$ describes reasonably well a 100 GeV decay $\chi \to e^+ e^-$. In any case, observations of the 21 cm power spectrum at $z = 30$ alone are unlikely to yield a S/N of unity for DM decay, except in decay cases where the energy injection is near maximal, e. g. MeV-scale particle decaying to electron–position pairs, or with an instrument with extremely good resolution like aSKA. Nonetheless, 21 cm LIM tomography with LRA will have the power to improve upon CMB constraints by orders of magnitude.

As in the case of decaying DM, SKA will not reach the required sensitivity to detect an annihilating DM signal in the 21 cm angular power spectrum. Even at the upper limit set by *Planck* CMB measurements of $p_{\rm ann} = 1.9 \times 10^{-7} {\rm m}^3 {\rm s}^{-1} {\rm kg}^{-1}$ and with the largest considered halo boost, the S/N for SKA remains well below unity. aSKA may have the potential to detect a DM annihilation signal if the annihilation rate (or boost factor) is sufficiently high. In order to reach (sub-)percent level precision measurements or probe weaker annihilation rates it will be necessary to use tomographic observations of the 21 cm LIM. An instrument like LRA2 (LRA3) has the capability to constrain the DM annihilation parameter at the level of $p_{\rm ann} = 1.9 \times 10^{-8} {\rm m}^3 {\rm s}^{-1} {\rm kg}^{-1}$ with percent

(sub-percent) precision, allowing for a very accurate measurement, at least one order of magnitude below the current limit set by *Planck* CMB measurements.

The importance of measuring the 21 cm power spectrum beyond $z > 30$ to perform tomography is even more pronounced in the case of annihilating dark matter. Since the majority of energy injection occurs earlier, the contribution from exotic DM at $z = 30$ is generally significantly less than its maximum at around $z \sim 50$. This results in a huge improvement in the forecasted measurement errors when comparing LRA constraints at $z = 30$ versus using tomography (up to 3 orders of magnitude improvement, e. g. for LRA3 measuring an annihilation rate $p_{\rm ann} = 1.9 \times 10^{-8} \mathrm{m^3 s^{-1} kg^{-1}}$).

Including the effect of sub-structure in the DM distribution with the halo boost enhances the DM annihilation efficiency at low redshift, thereby boosting the S/N at later times (see Figure 2.5). For the most conservative boost factor we chose, Boost 1, the impact in the constraints is negligible. However with the larger Boost 2, the effect in the constraints at $z = 30$ can be significant (see right panel Figure 2.7). For example, there is a factor of ~ 8 improvement for aSKA, and over an order of magnitude stronger constraints with LRA3 at $z = 30$. When performing tomography with LRA, the effect in the constraints is negligible. However, when including the effects of structure formation, the effective on-the-spot approximation may break down and the energy deposition curves can change substantially at low redshifts [368]. Therefore, a full calculation of the redshift-dependent $f(z)$ (or $p_{\rm ann}(z)$) curves once precision 21 cm measurements are made possible should be taken into account when including halo boost effects.

Regarding the upper limit on the annihilation efficiency $p_{\rm ann}$ for cases of non-detection, we can compare it with the forecast from an ideal Cosmic Variance limited (CVl) CMB experiment, reported to be $p_{\rm ann} < 5 \times 10^{-8} \mathrm{m^3 s^{-1} kg^{-1}}$ at 95% C.L. in Ref. [295]. Figure 2.8 shows the forecasted upper limits on the annihilation efficiency for each experimental set-up, compared to the latest *Planck* bounds and the aforementioned CVl experiment forecast. Exploiting the power of tomography of the 21 cm LIM signal, LRA could detect or exclude values of $p_{\rm ann}$ up to 1–3 orders of magnitude smaller than current CMB bounds (based on LRA1–LRA3 upper limit). Even with an earth-based instrument like aSKA, measurement of the 21 cm power spectrum can achieve 20–fold improvement over current *Planck* bounds with a projected upper limit of $p_{\rm ann} < 9.3 \times 10^{-9} \mathrm{m^3 s^{-1} kg^{-1}}$ at 95% C.L.

Assuming a thermal relic cross-section of $\langle \sigma v \rangle \sim 3 \times 10^{-26} \, \mathrm{cm^3 s^{-1}}$ and a

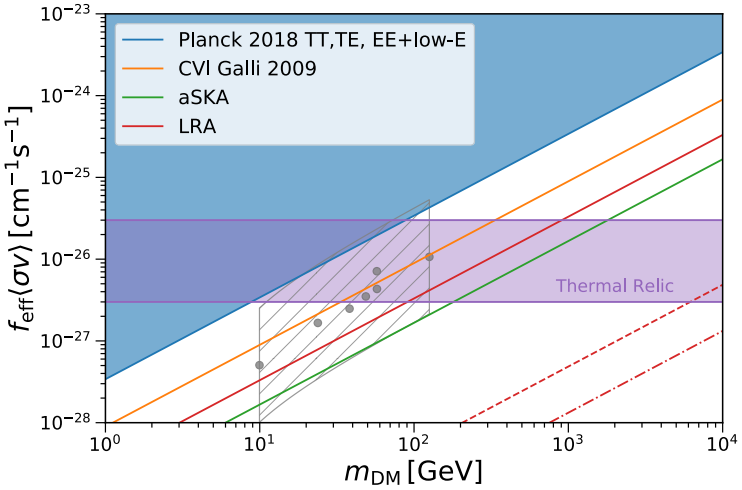

FIGURE 2.8: Projected upper limits (95% C.L.) are shown in green for aSKA and red for LRA (solid, dashed, and dot-dashed represent LRA1–LRA3 respectively), compared to a forecasted Cosmic Variance limited CMB bound (95% C.L.) from Ref. [295] (orange). Blue shaded exclusion region is the 95% C.L. *Planck* 2018 TT,TE,EE+lowE bound [45]. Purple horizontal band represents the thermal relic cross section of $\langle\sigma v\rangle = 3\times10^{-26}\,{\rm cm}^3{\rm s}^{-1}$ multiplied by a range of $f_{\rm eff}$ values for different annihilation channels, from $f_{\rm eff} = 1$ (top) to $f_{\rm eff} = 0.2$ (bottom). The grey circles show the best-fit DM models that are compatible with the *Fermi*-LAT Galactic centre excess found in Ref. [385], and the hatched area represents the factor ~ 5 uncertainty in the best-fit cross-section due to Milky Way halo parameters.

perfect absorption efficiency of $f_{\rm eff} = 1$, then a non-detection of a DM annihilation signal with LRA3 would exclude a thermal WIMP of $\mathcal{O}(10^5)\,{\rm GeV}$ mass. For a more conservative choice of $f_{\rm eff} = 0.2$ (relevant for many annihilation channels [317]), LRA3 would have the potential to probe the region of the thermal relic annihilation cross-section for $\mathcal{O}(10^4)\,{\rm GeV}$ WIMP masses. Even less powerful instruments such as aSKA and LRA1 would permit the possibility to probe a thermal relic WIMP of mass $\mathcal{O}(10^2 - 10^3)\,{\rm GeV}$, allowing to explore much of the parameter space often invoked if DM annihilations are to explain the observed *Fermi*-LAT Galactic centre gamma-ray excess [385] and the AMS anti-proton excess [386]. With more sensitive instruments like LRA2 or LRA3, this region could be decisively excluded. We leave for future work a detailed computation of the energy injection histories in order to forecast constraints on the cross-section in terms of specific annihilation channels.

2.6 Conclusions

In this chapter, we have proposed the use of the 21 cm line-intensity mapping angular power spectrum from the dark ages to constrain decaying and

annihilating dark matter through its exotic energy injection. While remaining agnostic about the specifics of the microscopic description of the DM particles (i. e. mass, branching ratios), we modelled generic energy injection from DM on the thermal and ionisation history of the intergalactic medium, and computed how this in turn modifies the global T_{21} and the angular power spectrum of its fluctuations during the cosmic dark ages, the epoch following the last scattering of the CMB until the formation of the first stars and galaxies.

In particular, we estimated the potential of next-generation and futuristic radio arrays to detect signatures of decaying or annihilating DM. Considering several fiducial cases for the DM parameters allowed by current bounds, we forecasted the observational errors and limits (in the case of non-detection) on the decay lifetime τ or annihilation efficiency $p_{\rm ann}$ with the forthcoming SKA, an idealised earth-based SKA-like instrument (aSKA), and three realisations of a futuristic radio array on the lunar far-side (LRA). We have found that a dramatic improvement upon current and maximal constraints from other probes, such as the CMB power spectrum, can be achieved for experiments beyond SKA. This is especially true for the LRA realisations, which will allow tomographic analyses of the 21 cm LIM power spectra from the dark ages.

Ground-based experiments will need exquisite angular resolution to access very small scales and be able to efficiently constrain these DM models. However, the real boost in constraining power comes from the tomographic analyses; in many cases the S/N remains larger than unity over a large redshift range. The information available thanks to observations at $z > 30$ is most apparent for the annihilating DM case since the majority of the energy injection occurs earlier, boosting the S/N at higher redshift. In addition, measuring the signal across a wide redshift range will also be important for understanding the evolution of the signal, which may prove to be crucial for constraining the precise particle properties and breaking otherwise degenerate signals at a single redshift.

Since the 21 cm signal is sensitive to both the thermal and ionisation history of the IGM, it holds great promise, and has the potential to constrain much smaller or later-time energy injection from DM than the CMB, even when considering next generation (e. g. CMB-S4 [220]) or a Cosmic Variance limited CMB experiment, which is sensitive only to the ionisation fraction around the time of recombination. Our results demonstrate that an instrument like LRA3 could be sensitive to annihilation efficiencies up to $p_{\rm ann} = 7.4 \times 10^{-11} \mathrm{m^3 s^{-1} kg^{-1}}$ (95% C.L.), reaching over 2 orders of magnitude greater sensitivity than what is ultimately accessible with an idealised CMB experiment, and over 3 orders of magnitude more than current *Planck* bounds, allowing to probe the thermal

relic cross-section for $\sim \mathcal{O}(10^4)$ GeV WIMP masses. In the case that all of the DM decays, the proposed instruments (aSKA–LRA3) could probe lifetimes up to $\tau \sim 10^{27} - 10^{29}$ s, improving by 2–4 orders of magnitude the current bounds on DM lifetime from CMB measurements. This represents an interesting region of parameter space for certain light decaying DM models (e. g. sterile nuetrinos, axinos) which are expected to have a lifetime on the order of $\sim 10^{27}$ s if they are to explain the 3.5 keV photon line observed in several galaxy clusters [387–391].

Given the proof-of-concept character of this work, our modelling presents several caveats due to some simplifying assumptions which should be taken into consideration. First, we assume that the extra energy injection does not accelerate the process of formation of the first stars, and that the end of the dark ages is fixed at $z \sim 30$, no matter the lifetime or annihilation rate of the DM. However, in order to remain consistent with CMB measurements, it has been shown that DM decay or annihilation cannot be a dominant contribution to cosmic reionization [334, 357]. Further, neglecting the backreaction effect of the increased ionisation level on the evolution of the thermal and ionisation history may not be a valid assumption at the end of the cosmic dark ages [372]. Including this effect leads to greater energy deposition in heating the gas temperature T_k, which can result in 10%-50% stronger constraints from the global T_{21} signal [372]. Hence by ignoring this effect we expect our forecasts to be more conservative. Second, we neglect any effect of the exotic energy injection on the spatial perturbations of the 21 cm signal, beyond its effect on the global T_{21}, as well as any potential coupling to the gas through the Wouthuysen-Field effect. In addition, for most of our results we assume no knowledge of the particle decay (or annihilation) process, and adopt a constant on-the-spot energy injection efficiency. The actual energy injection history is highly dependent on the particle mass and decay channel, as well as the lifetime, and so the DM lifetime forecasts presented here may change quantitatively when taking this into account. Likewise, the use of a constant efficiency factor $f_{\rm eff}$ may not be a sufficient assumption during the redshift range of interest. We explore more realistic scenarios in Appendix A.3, and find that in these cases the significant improvement on exotic DM constraints from 21 cm LIM during the dark ages with respect to any other probe holds true. The fact that the results are sensitive to the precise energy injection history demonstrates that the 21 cm power spectrum from the dark ages holds promise of being a powerful tool to not only detect a decay or annihilation signal, but to probe the precise microscopic nature of the DM particle. A more detailed analysis, computing the corresponding

$f(z)$ functions over the whole redshift range to specific microscopic DM descriptions (using e. g. `DarkHistory` [372] or `ExoCLASS` [392]), ascertaining whether different options could be distinguishable, is left for future work. Finally, the forecasted constraints presented here assume that the relevant foregrounds can be characterised and subtracted perfectly well, and we consider only the cosmic variance and instrumental noise in our final forecasted uncertainties in order to evaluate the potential reach of future 21 cm observations.

Observing a deviation from the standard ΛCDM signal in the 21 cm global sky-averaged brightness temperature or its fluctuations during the dark ages would be strongly indicative of exotic physics, as there is no known astrophysical process which could mimic such a signal. However, in this work we have not considered alternative sources of exotic energy injection during the dark ages other than DM decays or annihilations, which could be degenerate with the studied DM models. Nevertheless, the signature from decaying and annihilating DM on the 21 cm angular power spectrum are qualitatively rather different from that expected due to e. g. a population of primordial black holes [343] which enhances the power spectrum significantly at small scales only during the dark ages. At lower redshifts there may be some effects at large scales also [344]. Similarly, models with DM-baryon scattering are expected to have a distinct effect in the 21 cm signal [393, 394]; we will explore this topic further in Chapter 3.

Another important effect to consider is that of massive neutrinos, which suppress the growth of perturbations (at small scales) in a scale-dependent and redshift dependent manner, in turn affecting the 21 cm power spectrum of fluctuations. The 21 cm window promises to be highly complementary to the CMB and LSS windows used thus far to constrain neutrino properties, due to the different redshift range and the sheer number of modes accessible. Hence, the observational efforts examined in this work may at the same time provide a powerful probe of neutrino properties.

In summary, if DM is coupled to the visible sector beyond gravitational interactions, then the 21 cm LIM signal will be very sensitive to exotic energy injection from its interactions with Standard Model particles. Measuring the signal during the cosmic dark ages can provide a clean and robust measurement of the DM properties, free from complication due to astrophysical processes. In this Chapter, we have shown how the 21 cm angular power spectrum will be an extremely powerful probe of the DM decay and annihilation rate, with the potential to measure orders of magnitude weaker signals than those accessible with current or even idealised CMB experiments. At the same time, the potential

constraints are complementary to indirect detection probes (or even stronger, e. g. MeV–GeV mass particles decaying to e^+e^- pairs), while being more robust to uncertainties in the astrophysical modelling (especially at $z > 30$). Our results highlight the power of 21 cm LIM in the dark ages to measure DM annihilation and decay; however, opening a window to this unexplored epoch in cosmic history will undoubtedly bring other major findings and will be highly complementary to forthcoming experiments aiming to measure the global 21 cm signal and the power spectrum from the later epoch of reionization and cosmic dawn.

Chapter 3

Dark Matter-Baryon Scattering and Implications for Cosmic Dawn

3.1 Introduction

Many well-motivated particle candidates for DM, including weakly-interacting massive particle (WIMP) models [113, 395], predict elastic scattering between the DM and baryons which has cosmological consequences. While direct detection experiments are highly sensitive to DM-nucleon interactions for DM masses larger than a few GeV, cosmological probes cover complementary regions of parameter space and are particularly sensitive to scattering of sub-GeV DM with baryons [189, 191–202, 211, 222, 396–399]. In a cosmological context, the interaction between DM and baryons leads to transfer of heat and momentum between the two fluids which can affect a range of physical scales and leave imprints on cosmological observables throughout cosmic history. A key signature of the interactions is a suppression of power in cosmological perturbations on small physical scales.

In cosmology, DM-baryon scattering is often characterised by a power law dependence of the momentum-transfer cross section on the relative particle velocity, $\sigma(v) = \sigma_0 v^n$, with a power law index n and an unknown coefficient σ_0 that quantifies the strength of the interaction at hand. If the dependence of the scattering cross section on the relative velocity is steep enough ($n < -2$), its effect is larger later on in cosmic history, thus impacting late-time observables more than the cosmic microwave background (CMB) anisotropy. Moreover, the impact of the interactions on the baryon temperature and matter clustering at small scales is expected to affect the formation of the first stars.

Upcoming cosmological probes, in particular line-intensity mapping, will provide new avenues to investigate the nature of DM. While post-reionization measurements are promising in this regard (see, e. g., [400, 401]), the 21 cm-HI intensity mapping signal from cosmic dawn is expected to be especially sensitive

to the DM microphysics. In general, any model with clustering suppression at small scales delays the collapse of the first halos and therefore the formation of the first stars, affecting the time evolution of cosmic dawn and reionization [228–236]. Furthermore, since the HI signal is highly sensitive to the gas temperature through the HI spin temperature, any modification to the gas temperature (either due to energy injection or heat transfer) is expected to greatly modify the HI signal [1, 107, 330, 343, 344, 402–405]. This has motivated studies of the signatures of DM-baryon scattering in the HI intensity mapping from the dark ages and cosmic dawn [107–109, 198, 393, 394, 404–406], especially in attempts to explain the anomalous EDGES measurement [407]. Experiments such as EDGES [407], SARAS [408], and LEDA [409], which measure the sky-averaged brightness temperature of the HI line at cosmic dawn, and HERA [410] and SKA [411], which will provide measurements of its power spectrum, are thus expected to return invaluable insight on the nature of the dark matter.

However, the direct contribution from DM-baryon scattering to the gas temperature perturbations and the actual dark matter temperature perturbations have been thus far ignored. Temperature perturbations are usually negligible for CMB observations [412] but are critical for signals like the HI intensity mapping, and they may affect the clustering of the first stars. Furthermore, temperature perturbations appear in the sound speed terms of the DM and baryon fluid evolution equations, modifying the clustering at scales below the corresponding Jeans scales. Therefore, we deem the inclusion of these contributions and variables in the evolution equations critical for a detailed assessment of the effects of DM-baryon scattering at low redshift.

In this Chapter, we compute for the first time the effects of DM-baryon elastic scattering in the baryon temperature and ionization fraction perturbations, as well as considering the DM temperature perturbations. We implement this derivation in a modified version of the linear Boltzmann solver `CLASS`[1] [362], developed for DM-baryon scattering cosmologies in ref. [196], and self-consistently evolve the perturbation equations up to the beginning of cosmic dawn (which we consider to be at $z \sim 30$).[2] We show numerical results for the $n = -4$ case with cross section values set to the 95% confidence level (C.L.) upper limits from CMB analyses when all the dark matter interacts with baryons [196, 197]. As expected, we find significant changes in the gas temperature and ionization fraction perturbations due to the additional terms sourced by DM-baryon scattering. Furthermore, there is an increased suppression of the baryon and total

[1] https://github.com/lesgourg/class_public

[2] The specific start of cosmic dawn depends on the cosmological and astrophysical model. However, this does not affect our main conclusions.

matter power spectra relative to ΛCDM when compared to the prediction for DM-baryon scattering models neglecting the newly-derived contributions to the temperature perturbations. We argue that these changes are large enough to have a sizeable impact in the beginning of cosmic dawn and must be taken into account when setting the initial conditions for cosmic dawn. Once the first stars form, the heating of the gas will be dominated by these sources and a dedicated study, beyond the scope of this work, is required to follow the evolution of the gas and dark matter temperature perturbations coherently with the effects of the scattering in the matter clustering. As an example of the impact of the new terms in an observable, we compute the HI power spectrum from the dark ages.

This Chapter is organised as follows. In Section 3.2, after reviewing the modified Boltzmann equations for DM-baryon scattering cosmologies, we present the main result of this work: we derive the evolution of the temperature and ionization fraction perturbations sourced by the DM-baryon interactions. In Section 3.3 we present our numerical results, quantifying the effects on the DM and baryon temperature and ionization fraction perturbations and the consequent effect on the baryon and total matter power spectra. Finally, in Section 3.4 we discuss the phenomenological impact of the new temperature perturbation contributions on cosmological observables and as a case example, we compute the effects on the HI line-intensity mapping signal during the dark ages. We discuss and conclude in Section 3.5. Hereinafter we focus on the power spectrum at $z = 30$, but relevant results at $z = 50$ can be found in Appendix B.1, while the effects of varying the scattering cross section and the fraction of interacting DM are discussed in Appendix B.2.

3.2 Evolution of perturbations with DM-baryon scattering

In this section, we derive the contributions to the perturbed DM and baryon temperatures and ionization fraction arising from the DM-baryon collision term, and incorporate these contributions into the modified Boltzmann equations for DM-baryon interacting cosmologies. We consider DM-baryon scattering of the form $\sigma(v) = \sigma_0 v^n$, where v is the relative velocity between scattering particles.

Perturbations in the ionization fraction during recombination and the dark ages affect the evolution of the baryon temperature and density perturbations, which has a direct impact on the HI signal and structure formation. Here

we follow the nomenclature introduced by ref. [412] and refer to this effect as "perturbed recombination".

3.2.1 Modified Boltzmann equations

We review the modified Boltzmann equations accounting for scattering between the DM and baryons, following the treatment presented in ref. [196]. Note that here we work in the Newtonian gauge, but the equations in the synchronous gauge are identical up to terms involving the metric perturbations. The evolution equations for the DM and baryon density perturbations, δ_χ and δ_b, and velocity divergences, θ_χ and θ_b, respectively, are given by

$$\begin{aligned}
\dot{\delta_\chi} &= -\theta_\chi + 3\dot{\phi} \\
\dot{\delta_b} &= -\theta_b + 3\dot{\phi} \\
\dot{\theta_\chi} &= -\frac{\dot{a}}{a}\theta_\chi + c_\chi^2 k^2 \left(\delta_\chi + \delta_{T_\chi}\right) + k^2\psi + \widetilde{R}_\chi\left(\theta_b - \theta_\chi\right) \\
\dot{\theta_b} &= -\frac{\dot{a}}{a}\theta_b + c_b^2 k^2 \left(\delta_b + \delta_{T_b}\right) + k^2\psi + R_\gamma\left(\theta_\gamma - \theta_b\right) + \frac{\rho_\chi}{\rho_b}\widetilde{R}_\chi\left(\theta_\chi - \theta_b\right),
\end{aligned} \tag{3.1}$$

where k is the wave number of a given Fourier mode; a is the scale factor; ϕ and ψ are the Newtonian scalar metric potentials; c_χ and c_b are the DM and baryon sound speeds, respectively; ρ_χ and ρ_b are their energy densities; R_γ is the momentum-transfer rate for baryon-photon coupling due to Compton scattering; and $\widetilde{R}_\chi$ is the (modified) momentum-transfer rate arising from the DM-baryon interactions. The overdot denotes a derivative with respect to conformal time. We have added the temperature perturbations δ_{T_χ} and δ_{T_b} ($\delta_{T_{\chi,b}} \equiv \delta T_{\chi,b}/\bar{T}_{\chi,b}$, where $\bar{T}_{\chi,b}$ denotes the mean temperatures) of the DM and baryon gas to the sound speed terms in the momentum equations, as is done for the baryons in refs. [413, 414]. Previously the DM temperature perturbations δ_{T_χ} have been neglected entirely; in this work, as will become clear in the following, we include it for the first time. As we will see below, accounting for the DM temperature perturbations will not only change the gas temperature power spectrum but also the growth of matter overdensities at small scales, due to this additional contribution to the DM sound speed.

At early times ($z > 10^4$), the DM-baryon relative bulk velocity is small compared to the relative thermal velocity dispersion, and the momentum-transfer coefficient R_χ is approximately independent of the velocity divergences such that

$$R_\chi = a\rho_b \frac{Y_H \sigma_o}{m_\chi + m_b} \mathcal{N}_n \bar{v}_{\rm th}^{(n+1)}, \tag{3.2}$$

where $\mathcal{N}_n \equiv 2^{(5+n)/2}\Gamma(3+n/2)/(3\sqrt{2})$, $\bar{v}_{\rm th}^2 = T_\chi/m_\chi + T_b/m_b$ is the relative thermal velocity dispersion squared, T_χ (m_χ) and T_b (m_b) are the DM and baryon temperatures (masses), respectively, Y_H is the mass fraction of hydrogen, and we neglect helium scattering. This approximation breaks down at lower redshifts for $n \leq -2$ as the relative bulk velocity becomes non-negligible, resulting in non-linear Boltzmann equations and mode-coupling. In order to restore linearity to the evolution equations, we follow the prescription of ref. [196] in which a modified momentum-transfer rate is introduced to include the effects of mode mixing. Defining

$$\begin{aligned} V_{\rm flow}^2 &\equiv \int_0^k \frac{dk'}{k'}\Delta_\zeta^2\left[\frac{\theta_b(k',z)-\theta_\chi(k',z)}{k'}\right]^2 \\ V_{\rm RMS}^2 &\equiv \int_k^\infty \frac{dk'}{k'}\Delta_\zeta^2\left[\frac{\theta_b(k',z)-\theta_\chi(k',z)}{k'}\right]^2, \end{aligned} \tag{3.3}$$

where Δ_ζ^2 is the primordial curvature perturbation variance per $\ln k$, the modified momentum-transfer rate is given by

$$\widetilde{R}_\chi = R_\chi\left[1+\frac{V_{\rm RMS}^2(k,z)/3}{\bar{v}_{\rm th}^2}\right]^{(n+1)/2} \times {}_1F_1\left(-\frac{n+1}{2},\frac{5}{2},-\frac{V_{\rm flow}^2(k,z)}{2[\bar{v}_{\rm th}^2+V_{\rm RMS}^2(k,z)/3]}\right), \tag{3.4}$$

where ${}_1F_1$ is the confluent hypergeometric function of the first kind. In the limit where $\langle V_{\chi b}^2\rangle \equiv V_{\rm flow}^2 + V_{\rm RMS}^2 \ll \bar{v}_{\rm th}^2$,[3] we recover $\widetilde{R}_\chi = R_\chi$, as desired.

Before recombination, supersonic relative velocities between the DM and baryons are generated, leading to a root-mean-square (rms) velocity of ~ 29 km s^{-1} at kinematic decoupling. This supersonic relative velocity permits the baryons to freely stream out of the DM potential wells, suppressing density perturbations at scales below the characteristic advection scale over a Hubble time at the time of decoupling ($k \sim 40\,{\rm Mpc}^{-1}$) [414–417]. The relative velocity is coherent over scales much smaller than $k \sim 0.3\,{\rm Mpc}^{-1}$, which allows the use of moving-background perturbation theory to account for a formally non-linear term, by perturbing around a local background value of the relative bulk velocity within coherent patches. Following ref. [415], the evolution of small-scale perturbations ($k \gtrsim 10\,{\rm Mpc}^{-1}$) after recombination in the presence of a

[3] $\langle V_{\chi b}^2\rangle$ is the full variance of the relative bulk velocity, integrated over all k.

local relative bulk velocity $\boldsymbol{v}_{\chi b}^{\rm bg}$ can be written to first order as[4]

$$\begin{aligned}
\dot{\delta}_\chi &= i(\boldsymbol{v}_{\chi b}^{\rm bg}\cdot\boldsymbol{k})\,\delta_\chi - \theta_\chi \\
\dot{\theta}_\chi &= i(\boldsymbol{v}_{\chi b}^{\rm bg}\cdot\boldsymbol{k})\theta_\chi - \frac{\dot{a}}{a}\theta_\chi + k^2\phi + c_\chi^2 k^2(\delta_\chi+\delta_{T_\chi}) + \widetilde{R}_\chi(\theta_b-\theta_\chi) \\
\dot{\delta}_b &= -\theta_b \\
\dot{\theta}_b &= -\frac{\dot{a}}{a}\theta_b + k^2\phi + c_b^2 k^2(\delta_b+\delta_{T_b}) + \frac{\rho_\chi}{\rho_b}\widetilde{R}_\chi(\theta_\chi-\theta_b) \\
\text{with}\quad \frac{k^2}{a^2}\phi &= -\frac{3}{2}\frac{H_0^2}{a^3}(\Omega_b^0\delta_b + \Omega_\chi^0\delta_\chi)\,.
\end{aligned} \tag{3.5}$$

In this regime, we are considering scales much smaller than the horizon and times after recombination, and so we neglect the relativistic contributions to the evolution equations and the baryon-photon coupling term. For small scales, $V_{\rm RMS}^2 \to 0$ and $V_{\rm flow}^2 \to \langle V_{\chi b}^2\rangle$ in Eq. (3.4); moreover, we replace $\langle V_{\chi b}^2\rangle$ by the local relative velocity $V_{\chi b}^2$ (where $V_{\chi b} = |\boldsymbol{v}_{\chi b}^{\rm bg}|$) in each patch. We assume that $\boldsymbol{v}_{\chi b}^{\rm bg}$ follows an 3-dimensional Gaussian distribution with variance given by $\langle V_{\chi b}^2\rangle$ and place ourselves in the local baryon rest frame.

The small-scale patches with coherent relative velocities are correlated as a relic of the correlation of the relative velocities after recombination. Therefore, the small-scale fluctuations modulated by the relative velocities also affect the large-scale fluctuations through uncorrelated, additive quadratic terms [414, 416]. The quadratic terms at small scales are averaged over regions of the size of the coherence scale of the relative velocity and contribute to large-scale perturbations, following the correlation function of the local relative velocities. Throughout this work, unless otherwise stated, we refer to $k \gtrsim 10\,{\rm Mpc}^{-1}$ and $k \lesssim 1\,{\rm Mpc}^{-1}$ as small and large scales respectively.

3.2.2 Temperature and ionization fraction perturbations

To derive the evolution equations for the DM and baryon temperature perturbations, we begin from the first law of thermodynamics

$$\frac{3}{2}dT_{\chi,b} - T_{\chi,b}d\log\rho_{\chi,b} = dQ_{\chi,b}, \tag{3.6}$$

where $dQ_{\chi,b}$ is the heating rate per particle. In the absence of DM-baryon interactions, the only relevant source of heating is the standard Compton collision

[4]Note that, contrary to ref. [415], we use derivatives with respect to conformal time and use the standard definition of θ as the velocity divergence with respect to comoving space.

heating rate for baryons scattering with CMB photons, given by

$$\dot{Q}_C = 3\frac{\mu_b}{m_e}R_\gamma(T_\gamma - T_b) = \frac{4a\sigma_T\rho_\gamma x_e}{m_e(1+x_{\rm He}+x_e)}(T_\gamma - T_b) \tag{3.7}$$

where $\mu_b = m_H(1+4x_{\rm He})/(1+x_{\rm He}+x_e)$ is the mean molecular weight of the baryons, m_e is the electron mass, T_γ is the photon temperature, $x_e = n_e/n_{\rm H}$ is the free electron fraction, $x_{\rm He} = n_{\rm He}/n_{\rm H}$ is the constant helium to hydrogen number density ratio, $\rho_\gamma = a_r T_\gamma^4$ is the photon energy density with radiation constant a_r, and σ_T is the Thompson cross section.

In our case, there is an additional contribution sourced by DM-baryon interactions $\dot{Q}^{\rm iDM}$, for both the baryons and DM. Scattering of the baryons with the colder DM leads to heat exchange between the two species, cooling down the baryons and heating the DM. Moreover, the non-negligible relative bulk velocity induces a drag force between the two fluids which generates an additional temperature-independent heating term that dominates over the baryon cooling at high redshift for masses $m_\chi \gtrsim 1$ GeV [393]. The heat exchange rates due to DM-baryon interactions, accounting for a non-negligible relative bulk velocity, were generalised for all $n > -5$ in ref. [196]. Let us define the following rates

$$\begin{aligned}
\Gamma_\chi &\equiv 2\frac{\bar{\rho}_b}{\rho_b}R'_\chi\left[{}_1F_1\left(-\frac{n+3}{2},\frac{3}{2},-\frac{V_{\chi b}^2}{2\bar{v}_{\rm th}^2}\right) - \frac{V_{\chi b}^2}{3\bar{v}_{\rm th}^2}{}_1F_1\left(-\frac{n+1}{2},\frac{5}{2},-\frac{V_{\chi b}^2}{2\bar{v}_{\rm th}^2}\right)\right], \\
\Gamma_b &\equiv \frac{2\mu_b}{m_\chi}\frac{\bar{\rho}_\chi}{\rho_b}R'_\chi\left[{}_1F_1\left(-\frac{n+3}{2},\frac{3}{2},-\frac{V_{\chi b}^2}{2\bar{v}_{\rm th}^2}\right) - \frac{V_{\chi b}^2}{3\bar{v}_{\rm th}^2}{}_1F_1\left(-\frac{n+1}{2},\frac{5}{2},-\frac{V_{\chi b}^2}{2\bar{v}_{\rm th}^2}\right)\right], \\
\mathcal{H}_\chi &\equiv 2\frac{\bar{\rho}_b}{\rho_b}R'_\chi\frac{m_b}{3}V_{\chi b}^2{}_1F_1\left(-\frac{n+1}{2},\frac{5}{2},-\frac{V_{\chi b}^2}{2\bar{v}_{\rm th}^2}\right), \\
\mathcal{H}_b &\equiv \frac{2\mu_b}{m_\chi}\frac{\bar{\rho}_\chi}{\rho_b}R'_\chi\frac{m_\chi}{3}V_{\chi b}^2{}_1F_1\left(-\frac{n+1}{2},\frac{5}{2},-\frac{V_{\chi b}^2}{2\bar{v}_{\rm th}^2}\right),
\end{aligned} \tag{3.8}$$

where the heat-transfer rate coefficient is given by $R'_\chi = R_\chi m_\chi/(m_\chi+m_b)$. The heating rates due to DM-baryon interactions may then be written as

$$\dot{Q}_\chi^{\rm iDM} = \frac{3}{2}\left(\Gamma_\chi\frac{\rho_b}{\bar{\rho}_b}(T_b - T_\chi) + \mathcal{H}_\chi\frac{\rho_b}{\bar{\rho}_b}\right), \qquad \dot{Q}_b^{\rm iDM} = \frac{3}{2}\left(\Gamma_b\frac{\rho_\chi}{\bar{\rho}_\chi}(T_\chi - T_b) + \mathcal{H}_b\frac{\rho_\chi}{\bar{\rho}_\chi}\right). \tag{3.9}$$

Combining Eqs. (3.6), (3.7) and (3.9), we obtain the full evolution equations for the DM and baryon temperatures

$$\begin{aligned}\dot{T}_\chi - \frac{2}{3}\frac{\dot{\rho}_\chi}{\rho_\chi}T_\chi &= \Gamma_\chi \frac{\rho_b}{\bar{\rho}_b}(T_b - T_\chi) + \mathcal{H}_\chi \frac{\rho_b}{\bar{\rho}_b}\,,\\ \dot{T}_b - \frac{2}{3}\frac{\dot{\rho}_b}{\rho_b}T_b &= \Gamma_b \frac{\rho_\chi}{\bar{\rho}_\chi}(T_\chi - T_b) + \mathcal{H}_b \frac{\rho_\chi}{\bar{\rho}_\chi} + \frac{2\mu_b}{m_e}R_\gamma\,(T_\gamma - T_b)\,.\end{aligned} \tag{3.10}$$

Expanding Eq. (3.10) and linearising using $\dot{\rho}_i/\rho_i = -3\dot{a}/a + \dot{\delta}_i$ for species i, we find the homogeneous part gives the evolution of the background temperatures

$$\begin{aligned}\dot{\bar{T}}_\chi + 2\frac{\dot{a}}{a}\bar{T}_\chi &= \Gamma_\chi(\bar{T}_b - \bar{T}_\chi) + \mathcal{H}_\chi\,,\\ \dot{\bar{T}}_b + 2\frac{\dot{a}}{a}\bar{T}_b &= \Gamma_b(\bar{T}_\chi - \bar{T}_b) + \mathcal{H}_b + \frac{2\mu_b}{m_e}R_\gamma\left(\bar{T}_\gamma - \bar{T}_b\right)\,,\end{aligned} \tag{3.11}$$

which matches the results found in previous work [196, 393]. The background temperature evolution depends on the DM-baryon relative velocity $V_{\chi b}$ through the rates in Eqs. (3.8). Therefore, they are coupled with an equation for the evolution of the relative velocity [196, 393]

$$\dot{V}_{\chi b} + \frac{\dot{a}}{a}V_{\chi b} = -a\frac{(\rho_b + \rho_\chi)\sigma_0}{m_\chi + m_b}\mathcal{N}_n \bar{v}_{\rm th}^{(n+1)} V_{\chi b}\,{}_1F_1\left(-\frac{n+1}{2}, \frac{5}{2}, -\frac{V_{\chi b}^2}{2\bar{v}_{\rm th}^2}\right)\,, \tag{3.12}$$

assuming interactions with a baryon fluid comprised of a single species. Following the prescription first set out in ref. [393], we evolve this system of equations simultaneously (together with the ionization fraction, see below) for an array of different initial relative velocities $V_{\chi b,0}$ to obtain the background evolution $\bar{T}_i = \bar{T}_i(z, V_{\chi b,0})$. The average temperature evolution is then found by averaging over the Maxwell-Boltzmann initial-velocity probability distribution $\mathcal{P}(V_{\chi b,0})$, with rms value σ_{3d}, according to

$$\begin{aligned}\langle \bar{T}_i(z)\rangle &= \int dV_{\chi b,0}\bar{T}_i(V_{\chi b,0})\mathcal{P}(V_{\chi b,0})\,,\\ \mathcal{P}(V_{\chi b,0}) &= 4\pi V_{\chi b,0}^2 e^{-3V_{\chi b,0}^2/2\sigma_{3d}^2}/(2\pi\sigma_{3d}^2/3)^{3/2}.\end{aligned} \tag{3.13}$$

Figure 3.1 shows the evolution of the averaged background temperatures, and the ionization fraction (with respect to ΛCDM), as function of redshift for different DM masses and $n = -4$ when setting σ_0 to current 95% C.L. upper limits from CMB power spectrum analyses as reported in Table 3.1.

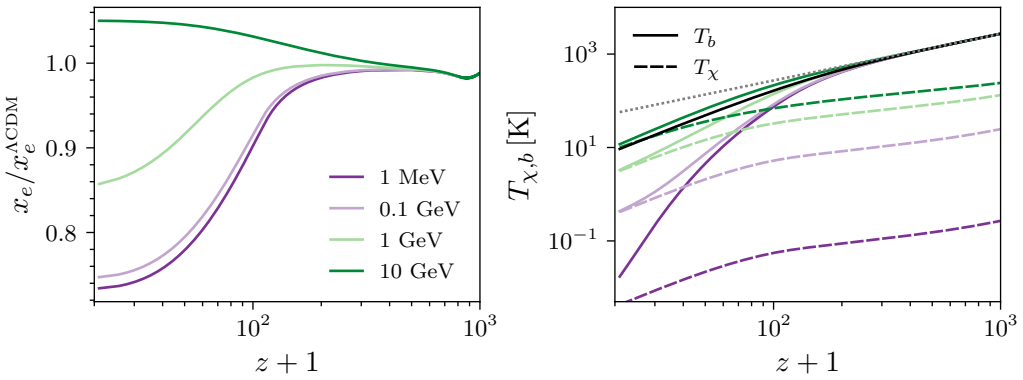

FIGURE 3.1: Evolution of the mean free-electron fraction over the ΛCDM prediction (left) and the mean baryon and DM temperatures (right) as a function of redshift for several DM masses for $n = -4$ (averaged over relative velocities). The ΛCDM mean baryon temperature is shown in black, and the CMB temperature is shown in dotted grey. For each DM mass, the coefficient of the momentum-transfer cross section σ_0 can be found in Table 3.1, consistent with 95% C.L. upper limits derived in refs. [196, 197].

After expanding Eq. (3.10) to first order in the perturbations $\delta_{T_i} = (T_i - \bar{T}_i)/\bar{T}_i$, we find the perturbed DM and gas temperatures evolve according to

$$\dot{\delta}_{T_\chi} - \frac{2}{3}\dot{\delta}_\chi = \Gamma_\chi \left[\left(\frac{\bar{T}_b - \bar{T}_\chi}{\bar{T}_\chi} \right) \delta_b + \frac{\bar{T}_b}{\bar{T}_\chi}(\delta_{T_b} - \delta_{T_\chi}) \right] + \mathcal{H}_\chi \left(\frac{\delta_b - \delta_{T_\chi}}{\bar{T}_\chi} \right) + \delta_{\Gamma_\chi} + \delta_{\mathcal{H}_\chi} \tag{3.14}$$

$$\begin{aligned} \dot{\delta}_{T_b} - \frac{2}{3}\dot{\delta}_b = {} & \Gamma_b \left[\left(\frac{\bar{T}_\chi - \bar{T}_b}{\bar{T}_b} \right) \delta_\chi + \frac{\bar{T}_\chi}{\bar{T}_b}(\delta_{T_\chi} - \delta_{T_b}) \right] + \mathcal{H}_b \left(\frac{\delta_\chi - \delta_{T_b}}{\bar{T}_b} \right) + \delta_{\Gamma_b} + \delta_{\mathcal{H}_b} \\ & + \frac{2\mu_b}{m_e} R_\gamma \left[\left(\frac{\bar{T}_\gamma}{\bar{T}_b} - 1 \right) \left\{ \delta_{x_e} - \frac{\bar{x}_e \delta_{x_e}}{1 + x_{\mathrm{He}} + \bar{x}_e} + \delta_\gamma \right\} - \frac{\bar{T}_\gamma}{\bar{T}_b}(\delta_{T_b} - \delta_{T_\gamma}) \right], \end{aligned} \tag{3.15}$$

where δ_{T_γ} is the photon temperature fluctuation, $\delta_\gamma = 4\delta_{T_\gamma}$ is the photon density fluctuation, $\delta_{x_e} \equiv \delta x_e/\bar{x}_e$ is free electron fraction fluctuation, and helium fraction perturbations are neglected. The terms $\delta_{\Gamma_i}, \delta_{\mathcal{H}_i}$ denote the perturbation terms that result from the dependence of the rates on the temperatures through the thermal velocity $\bar{v}_{\mathrm{th}}^2$. These terms are sub-dominant to the other contributions; therefore, we decide not to include them explicitly here for clarity. The interested reader can find them in Appendix B.3. In the above equations the first line corresponds to the contributions from the DM-baryon scattering, while the contributions from Compton heating are encoded in the second line of the baryon temperature perturbation equation. A detailed derivation of the

fluctuations sourced by the standard Compton heating term can be found in, e. g., refs. [412, 413, 418]. Eqs. (3.14) and (3.15) are the main theoretical result of this work, and we study the effects of including the temperature perturbations in the following sections. Note that here the temperatures $\bar{T}_i$ and rates Γ_i, $\mathcal{H}_i$ are still functions of the relative velocity. Therefore, the perturbations are evolved as a function of the relative velocity in different patches of the sky, as described for Eqs. (3.11), and averaged over the distribution of initial relative velocities.

At small scales ($k \gtrsim 10\,\mathrm{Mpc}^{-1}$) and after recombination, where the supersonic relative velocities between DM and baryons are coherent and the growth of perturbations is affected, we solve the system using the moving-background perturbation theory as described in Eq. (3.5). The temperature (and ionization fraction, see below) perturbations are affected by the coherent bulk velocities indirectly through the DM and baryon perturbations, hence we need to take this into account. Furthermore, we neglect the photon temperature perturbations in this regime as they are negligible.

Ionization fraction fluctuations

The evolution of the ionization fraction perturbations is modified by DM-baryon interactions indirectly through the dependence on the gas temperature fluctuations. After recombination, the ionization fraction obeys

$$\dot{x}_e \approx -C\mathcal{A}_\mathrm{B} n_\mathrm{H} x_e^2, \tag{3.16}$$

where C is the Peebles factor [364] and $\mathcal{A}_\mathrm{B}(T_b, T_\gamma)$ is the effective case-B recombination coefficient [419, 420]. The linear ionization fraction perturbations then evolve as

$$\dot{\delta}_{x_e} = \frac{\dot{\bar{x}}_e}{\bar{x}_e}(\delta_{x_e} + \delta_b + \delta_{\mathcal{A}_\mathrm{B}} + \delta_C), \tag{3.17}$$

where $\delta_{n_\mathrm{H}} \approx \delta_b$ up to very small corrections, and

$$\delta_{\mathcal{A}_\mathrm{B}} = \frac{\partial \ln \mathcal{A}_\mathrm{B}}{\partial \ln T_b}\delta_{T_b} \quad \delta_C = \frac{\partial \ln C}{\partial \ln R_{\mathrm{Ly}\alpha}}\left(\frac{\theta_b}{3H} - \delta_b\right). \tag{3.18}$$

Here the Lyman-α escape rate is modified to account for the local baryon expansion rate, i. e.,

$$R_{\mathrm{Ly}\alpha} \equiv \frac{8\pi(H + \theta_b/3)}{3\lambda_{\mathrm{Ly}\alpha}^3(1 - x_e)n_\mathrm{H}} \tag{3.19}$$

following refs. [412, 418].

Large-scale enhancement of temperature and ionization perturbations

At small scales, the relative velocities only affect the temperature and ionization perturbations indirectly through their effect on the matter. Over large scales, the small-scale relative velocities have no dynamical effect on the growth of overdensities, since the non-linear terms are full divergences that integrate to zero. However, the quadratic cooling of temperatures at small scales is non-adiabatic and therefore the temperature and ionization fraction need to be evolved as a coupled system up to second order, which affects the large-scale temperature and ionization perturbations differently [329].

Perturbing the temperature evolution equations (3.10) to second order – i. e., $T_i = \bar{T}_i(1 + \delta^{\rm I}_{T_i} + \delta^{\rm II}_{T_i})$ – we find

$$\dot{\delta}^{\rm II}_{T_\chi} = \frac{2}{3}\dot{\delta}_\chi(\delta^{\rm I}_{T_\chi} - \delta_\chi) + \Gamma_\chi\left[\frac{\bar{T}_b}{\bar{T}_\chi}\left(\delta^{\rm II}_{T_b} - \delta^{\rm II}_{T_\chi} + \delta^{\rm I}_{T_b}\delta_b\right) - \delta^{\rm I}_{T_\chi}\delta_b\right] + \mathcal{H}_\chi\frac{\delta^{\rm II}_{T_\chi}}{\bar{T}_\chi} \tag{3.20}$$

$$\begin{aligned}\dot{\delta}^{\rm II}_{T_b} = {}& \frac{2}{3}\dot{\delta}_b(\delta^{\rm I}_{T_b} - \delta_b) + \Gamma_b\left[\frac{\bar{T}_\chi}{\bar{T}_b}\left(\delta^{\rm II}_{T_\chi} - \delta^{\rm II}_{T_b} + \delta^{\rm I}_{T_\chi}\delta_\chi\right) - \delta^{\rm I}_{T_b}\delta_\chi\right] + \mathcal{H}_b\frac{\delta^{\rm II}_{T_b}}{\bar{T}_b} \\ & + \frac{2\mu_b}{m_e}R_\gamma\left[\frac{\bar{T}_\gamma - \bar{T}_b}{\bar{T}_b}\delta^{\rm II}_{x_e} - \delta^{\rm I}_{x_e}\delta^{\rm I}_{T_b} - \frac{\bar{T}_\gamma}{\bar{T}_b}\delta^{\rm II}_{T_b}\right],\end{aligned} \tag{3.21}$$

where we have neglected photon temperature fluctuations and assumed $1+x_{\rm He}+x_e \approx 1+x_{\rm He}$ to be locally homogeneous, valid at small (sub-horizon) scales. As was the case at first order, here there are also additional perturbation terms resulting from the dependence of the rates on the temperatures through the thermal velocity $\bar{v}^2_{\rm th}$; these terms are sub-dominant to the other contributions shown here, and we choose to neglect them.

The second-order perturbations to the ionization fraction $\delta^{\rm II}_{x_e}$ evolve according to [329]

$$\dot{\delta}^{\rm II}_{x_e} = \frac{\dot{x}_e}{\bar{x}_e}\left(\delta^{\rm II}_{x_e} + \frac{\partial \ln \mathcal{A}_B}{\partial \ln T_b}\delta^{\rm II}_{T_b} + \delta^{\rm II}_{\dot{x}_e}\right), \tag{3.22}$$

where $\delta^{\rm II}_{\dot{x}_e}$ represents the part of $\delta\dot{x}_e/\dot{\bar{x}}_e$ quadratic in the perturbations. Each of the source terms in the above equations are previously smoothed over the small volumes with coherent relative velocities.

3.3 Numerical results

We solve the perturbation equations in different regimes, accounting for all new terms in the temperature perturbations sourced by DM-baryon scattering, and also for the coherent relative velocities at small scales and the consequent quadratic contributions at large scales, as required in each regime. Therefore, we use a different approach in each case.

We have implemented the new contributions to the perturbed recombination arising from DM-baryon interactions derived in Section 3.2.2 (see Eqs. (3.14)–(3.15)) into a modified version of the linear Boltzmann solver `CLASS` that has been developed for DM-baryon scattering models in ref. [196]. We use this version of `CLASS` to evolve the linear perturbation equations at all scales before recombination, extract the initial conditions at $z = 1010$, and then evolve the perturbation equations in each regime as described in Section 3.2 until $z = 20$.[5] At large scales ($k \lesssim 10$ Mpc^{-1}), the perturbation equations are a function of the magnitude $V_{\chi b}$ only, and we average the power spectrum by integrating over the Maxwell-Boltzmann distribution $\mathcal{P}(V_{\chi b,0})$. The small-scale perturbations (Eqs. (3.5)) are a function of $\boldsymbol{v}_{\chi b}^{\rm bg} \cdot \boldsymbol{k}$, hence the power spectrum is first averaged isotropically over the direction of $\boldsymbol{k}$ with respect to $\boldsymbol{v}_{\chi b}^{\rm bg}$, and then over $\mathcal{P}(V_{\chi b,0})$. With these results, we follow ref. [329] to compute the quadratic corrections at large scales, using the smoothed perturbations at small scales and the solution of the system in Eqs. (3.20), (3.21), and (3.22). For $z \lesssim 50$, non-linear effects become important at the several percent level at high-k. Due to this, we restrict our $k_{\rm max} = 500\,{\rm Mpc}^{-1}$ when computing the large-scale modulation of small-scale perturbations at these redshifts, which should result in a conservative estimate.

For all results presented in this work we consider DM-baryon interactions with $n = -4$ velocity dependence and adopt the best-fit *Planck* 2018 [45] values for the ΛCDM cosmological parameters. We show results for selected masses in the range 1 MeV–10 GeV, setting σ_0 for each DM mass to the corresponding 95% C.L. upper limit found in ref. [196] where available. The mass-scaling relationship $\sigma_0 \propto (m_\chi + m_H)$ of refs. [197, 198] is used to obtain our benchmark 10 GeV limit. For reference these values are reported in Table 3.1. As anticipated in the introduction, the perturbed recombination – even with the new contributions derived in the previous section – has no significant effect on the CMB power spectra.

[5] At $z \lesssim$ 40–30 we expect the first stars to form, triggering cosmic dawn, which will then dominate the temperature perturbations; the effects of DM-baryon scattering on the temperature perturbations during cosmic dawn are beyond the scope of this study and left for future work.

DM mass m_χ	σ_0 [cm^2]
1 MeV	1.7×10^{-41}
0.1 GeV	1.9×10^{-41}
1 GeV	3.5×10^{-41}
10 GeV	2.0×10^{-40}

TABLE 3.1: Benchmark values of the momentum-transfer cross section coefficient σ_0 for each DM mass used in all of our numerical results. Consistent with the 95% C.L. upper limits found in refs. [196–198].

3.3.1 Temperature and ionization fraction perturbations

We first focus on the perturbations of the baryon temperature and ionization fraction. We compare the results considering DM-baryon scattering with respect to that of ΛCDM, both when including and neglecting the DM-baryon interactions contribution to the perturbed recombination (in the latter case, this amounts to setting $\Gamma_b = \mathcal{H}_b = 0$ in Eq. (3.15) and ignoring δ_{T_χ}). We refer to these two cases as $\delta^{\rm iDM}$ and $\delta^{\rm std}$ and represent them in figures with solid (or dark) and dashed (or light), respectively, unless otherwise stated.

The evolution of the baryon temperature and ionization fraction perturbations as a function of redshift for $k = 1$ Mpc^{-1} is shown in Figure 3.2, for an initial relative velocity equal to the rms value. In the bottom panels, we explicitly show the relative contributions of each term in Eq. (3.15) to the evolution of the perturbations, with each term labelled by its rate coefficient respectively: R_γ, Γ_b, or $\mathcal{H}_b$. For $m_\chi \gtrsim 1$ GeV, the drag heating term ($\mathcal{H}_b$) dominates at early times, increasing temperature fluctuations and therefore indirectly enhancing the standard Compton heating term through its dependence on δ_{T_b}, analogous to the effect on the mean temperatures. These two terms have opposite impact in the evolution of δ_{T_b}, but their balance results in enhanced temperature perturbations for all redshifts considered. On the other hand, the ionization fraction fluctuations are suppressed relative to ΛCDM, as recombination is less efficient in the overdensities due to the higher gas temperature, i.e. there are more free electrons. A similar effect – albeit with smaller amplitude – is seen for $m_\chi = 1$ GeV, with the exception that the contribution from the cooling term (Γ_b) becomes important at later times, and δ_{T_b} is suppressed for $50 \lesssim z \lesssim 100$, then enhanced again $z \lesssim 50$. For $m_\chi < 1$ GeV, while the $\mathcal{H}_b$ contribution can enhance temperature perturbations at $z \sim 10^3$, the cooling term dominates at late times; this results first in suppressed temperature fluctuations for $100 \lesssim z \lesssim 200$, and later enhanced negative fluctuations $z \lesssim 100$ compared to ΛCDM. For 0.1–1 GeV, the dominant contribution to the cooling term becomes

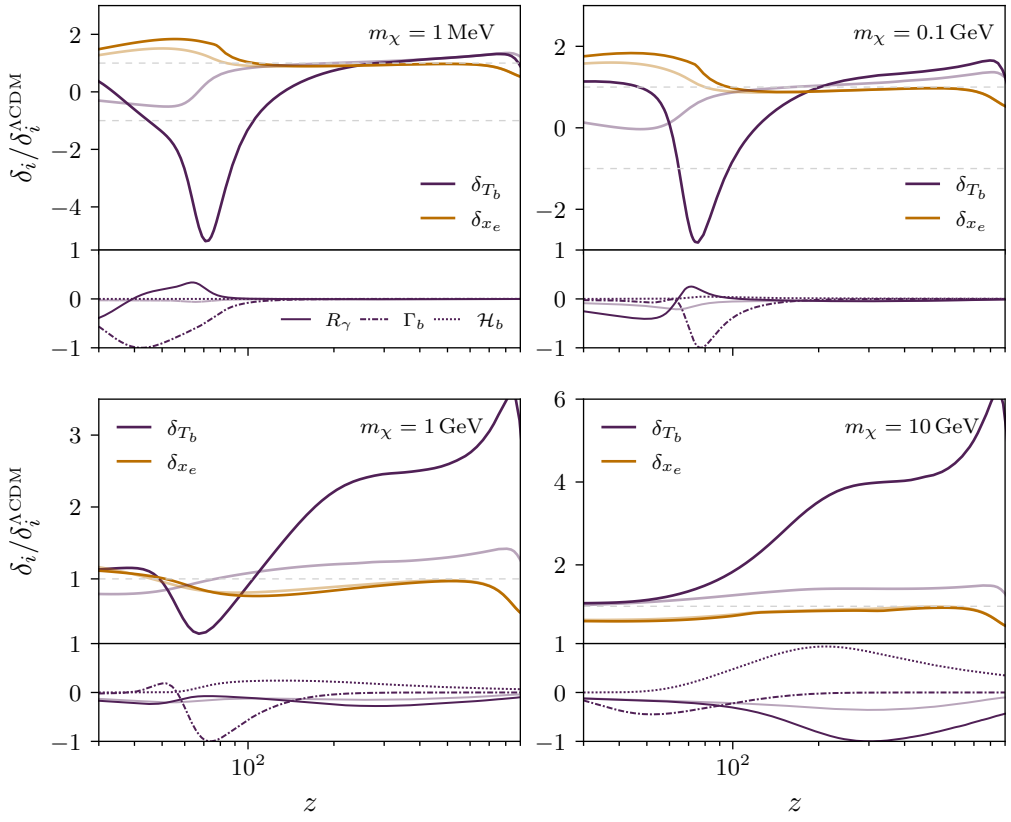

FIGURE 3.2: The evolution of the gas temperature and ionization fraction fluctuations at $k = 1\,\mathrm{Mpc}^{-1}$ as a fraction of the respective fluctuation in ΛCDM, including (dark) and neglecting (light) the new temperature perturbations sourced by DM-baryon interactions. In the bottom panel of each figure, we show the relative contribution of each of the three terms in Eq. (3.15) (labelled by its coefficient) to the temperature fluctuations, scaled to the range $[-1, 1]$. When neglecting the fluctuations from DM-baryon scattering, there is only a contribution from the term proportional to R_γ. Note the change of scale in the y-axis of each panel. Here we show the evolution for the case $V_{\chi b,0} = \sigma_{3d} \sim 29\,\mathrm{kms}^{-1}$.

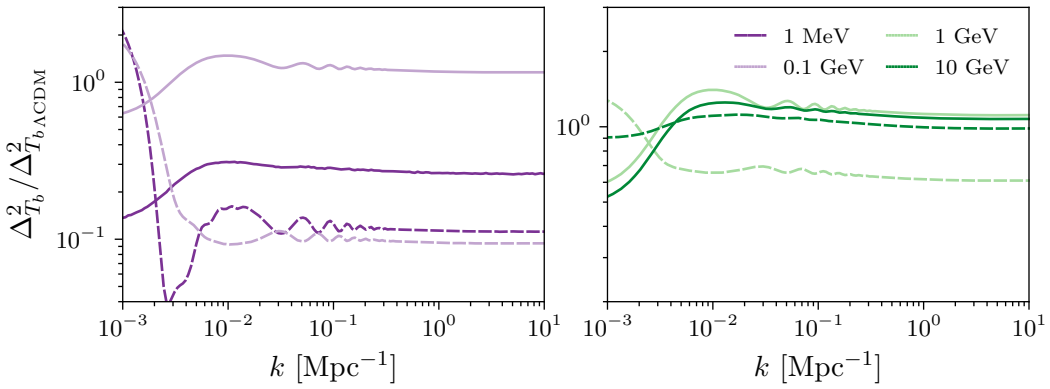

FIGURE 3.3: Ratio of the linear power spectra (with respect to ΛCDM) of gas temperature fluctuations at $z = 30$ for several DM masses, including (solid) and neglecting (dashed) fluctuations sourced by DM-baryon interactions, shown until $k = 10\,\mathrm{Mpc}^{-1}$. At smaller scales, other effects become important, which are considered in Section 3.3.2.

small at $z \lesssim 70$ as the DM and baryon temperatures approach equilibrium; the remaining terms add up to increase the temperature perturbations, and hence the gas temperature grows again in over-dense regions. For $m_\chi = 1$ MeV, the DM and baryon temperatures approach equilibrium later, at $z \lesssim 30$. Finally, for sub-GeV masses, the lower temperature in overdensities results in an enhancement of the (negative) ionization fraction fluctuations, due to more efficient recombination. In all cases, the interdependence of the three contributions to the temperature perturbations results in a richer redshift evolution of the perturbed temperatures with respect to neglecting the terms sourced by DM-baryon scattering.

In Figure 3.3, we demonstrate how the baryon temperature power spectrum changes due to the DM-baryon interactions and in particular, the importance of the new terms derived in the previous section. We plot the ratio of the baryon temperature power spectrum for different DM masses with respect to the ΛCDM prediction at $z = 30$. The contributions from the DM-baryon scattering to the baryon temperature power spectrum modify the amplitude by a factor of a few up to several tens in a roughly scale-independent manner. We find that the power spectrum is always larger than the standard prediction (Compton only, dashed lines) at the end of the dark ages ($z \sim 30$–50). Moreover, we see that including the DM-baryon scattering contributions to the perturbed recombination can enhance or suppress the baryon acoustic oscillation (BAO) feature in the temperature power spectrum. This is a result of the changes, with respect to considering Compton scattering only, in the terms that dominate the baryon temperature perturbations and their dependence on the density

perturbations.

These results depend on the strength of the interacting cross section, which we explore for a DM mass of 1 GeV in Appendix B.2. Interestingly, the change in amplitude of the gas temperature power spectrum does not necessarily decrease with the scattering cross section; reducing the cross section alters the balance of competing terms on the right-hand side of Eq. (3.15), which can result in more or less enhancement or suppression of the temperature perturbations depending on the redshift.

3.3.2 Small-scale effects

In addition to the almost scale-independent enhancement of the temperature fluctuations, there are several effects that alter the power spectra only at scales $k \gtrsim 10\ \mathrm{Mpc}^{-1}$. First, there is the averaged effect due to the relative bulk velocities; the effect of the $\boldsymbol{v}_{\chi b}^{\mathrm{bg}} \cdot \boldsymbol{k}$ term is qualitatively similar to ΛCDM cosmologies, suppressing fluctuations at wave numbers higher than the characteristic advection scale ($k \gtrsim 40\,\mathrm{Mpc}^{-1}$). However, DM-baryon interactions lead to a further suppression of power and a series of damped oscillations at very small scales. We find that averaging over relative bulk velocities can modify the shape of this oscillatory feature. Moreover, in the presence of DM-baryon interactions, the baryon sound speed c_b depends on the relative velocity through $\bar{T}_b(V_{\chi b})$; smaller values of $V_{\chi b}$ result in a lower sound speed, and therefore an enhancement of power around the baryonic Jeans scale. This effect is independent of the new contributions to the temperature fluctuations, and therefore is present for both δ^{iDM} and δ^{std} cases. Due to this, the velocity-averaged baryon power spectrum features an increase in power around the baryon Jeans scale, which is most pronounced for the 10 GeV case.

Second, the changes to the temperature fluctuations sourced by DM-baryon interactions are imprinted on the small-scale density fluctuations through the sound speed terms. The dark matter fluid sound speed term now has an additional contribution due to the presence of δ_{T_χ}, which acts to suppress the DM density perturbations at small scales for all cases since δ_{T_χ} is always positive. Similarly, δ_{T_b} has new contributions, which modify the baryon fluid sound speed term: the cooler (hotter) baryon temperature in overdensities for sub-GeV masses ($m_\chi \gtrsim 1$ GeV) tends to enhance (suppress) the baryon density power spectrum. However, due to the coupling of the two fluids, the suppressing effect on the DM due to δ_{T_χ} dominates in all cases; we find that the baryon power spectrum is increasingly suppressed due to the contributions to perturbed recombination from DM-baryon scattering for all masses considered. The effect

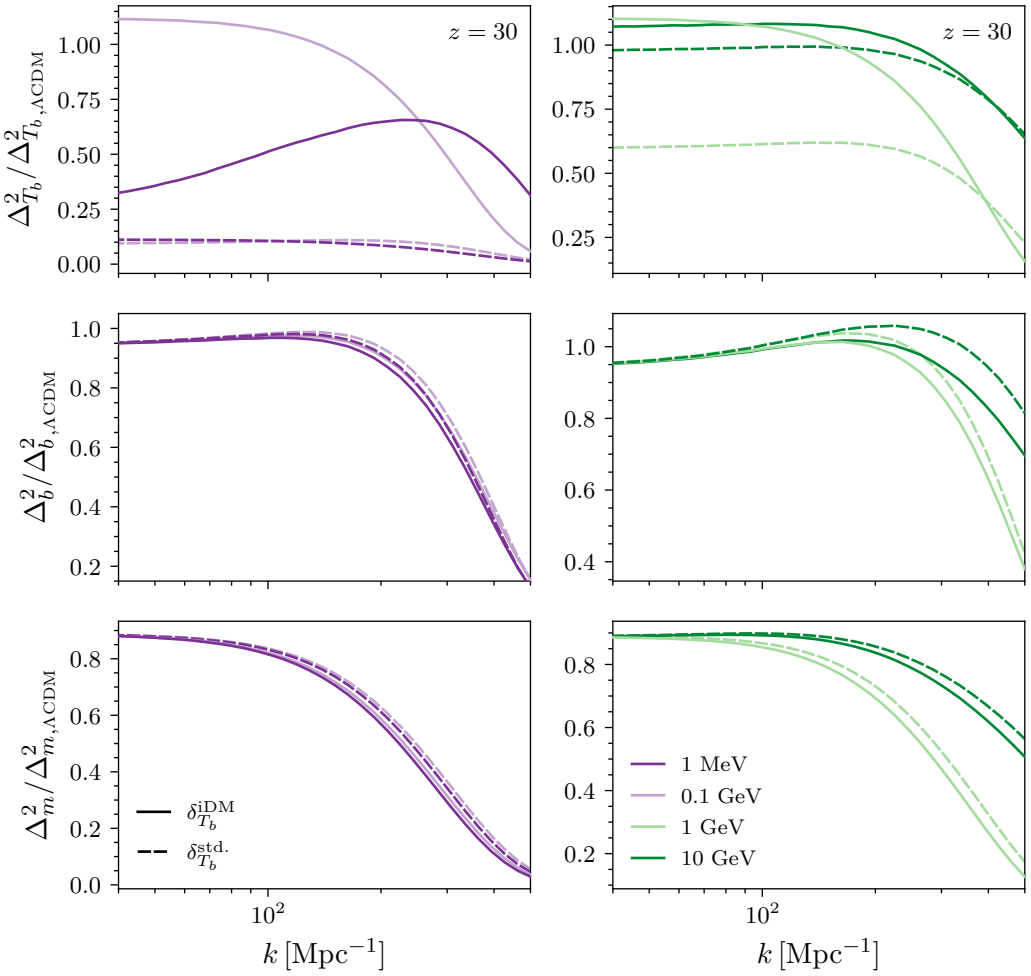

FIGURE 3.4: Ratio (with respect to ΛCDM) of the small-scale power spectra of baryon temperature (top), baryon density (middle) and matter density (bottom) fluctuations at $z = 30$ for scales $k = 40$–$500\,\mathrm{Mpc}^{-1}$. We compare the result when including (solid) and neglecting (dashed) the novel contributions to perturbed recombination from DM-baryon interactions for each DM mass, finding additional suppression of small-scale baryon and matter density perturbations in the former case.

is smaller for sub-GeV masses because of the opposite trends in the effects of δ_{T_b} and δ_{T_χ} described above. Of course, the new contributions to the sound speed terms result in a larger suppression of the small-scale total matter power spectrum, too. Consequently, the temperature power spectrum is also affected at small scales through its dependence on the density perturbations.

We illustrate this effect in Figure 3.4, showing the ratio of the small-scale baryon temperature, baryon density and total matter density power spectra with respect to ΛCDM at $z = 30$, comparing the predictions for DM-baryon scattering cosmologies with (solid) and without (dashed) including the new contributions to perturbed recombination. For $k \lesssim 100$ Mpc^{-1} we find a similar scale-independent enhancement of the baryon temperature power spectrum as demonstrated in Figure 3.3. However, this power spectrum drops at higher k due to the DM-baryon interactions. This suppression is faster when all the terms in the temperature perturbations are included, since the contributions to the sound speed terms increase. This can be seen comparing the panels corresponding to the baryon temperature and the baryon density power spectra. The relative suppression of baryon density perturbations, including all contributions to perturbed recombination, is greater for DM masses $\gtrsim 1$ GeV due to the combined effect of increased contributions to both the DM and baryon sound speed terms (e. g., for a 10 GeV DM, there is a further $\sim$ 5–10% suppression of the baryon power spectrum for $k \sim 200$–300 Mpc^{-1}, compared a few % for sub-GeV masses at the same scales.)

On the other hand, the DM temperature perturbations δ_{T_χ} are larger for lighter DM masses; this results in a greater suppression of the DM density perturbations, and therefore the total matter power spectrum, at small scales. For sub-GeV masses, we find that the total matter power spectrum is suppressed by $\sim$ 10–15% over scales $k \sim 200$–300 Mpc^{-1} relative to the case when neglecting the temperature perturbations sourced by DM-baryon scattering. For heavier DM, the small-scale suppression is less steep; over the same scales, the matter power suppression ranges from $\sim$ 5–10% for $m_\chi = 1$ GeV and from $\sim$ few–5% for $m_\chi = 10$ GeV, compared to neglecting the new contributions.

Overall, depending on the DM mass, we find that including the terms sourced by DM-baryon scattering in the perturbed recombination leads to an additional $\sim$ 5–10% suppression of the total matter power spectrum relative to ΛCDM for scales $k \gtrsim 200$ Mpc^{-1}. These results will also depend on the strength of the interaction cross section σ_0. We discuss the effect varying σ_0 for a 1 GeV mass in Appendix B.2. As one might expect, the additional small-scale suppression that results from our full treatment of the perturbed recombination scales

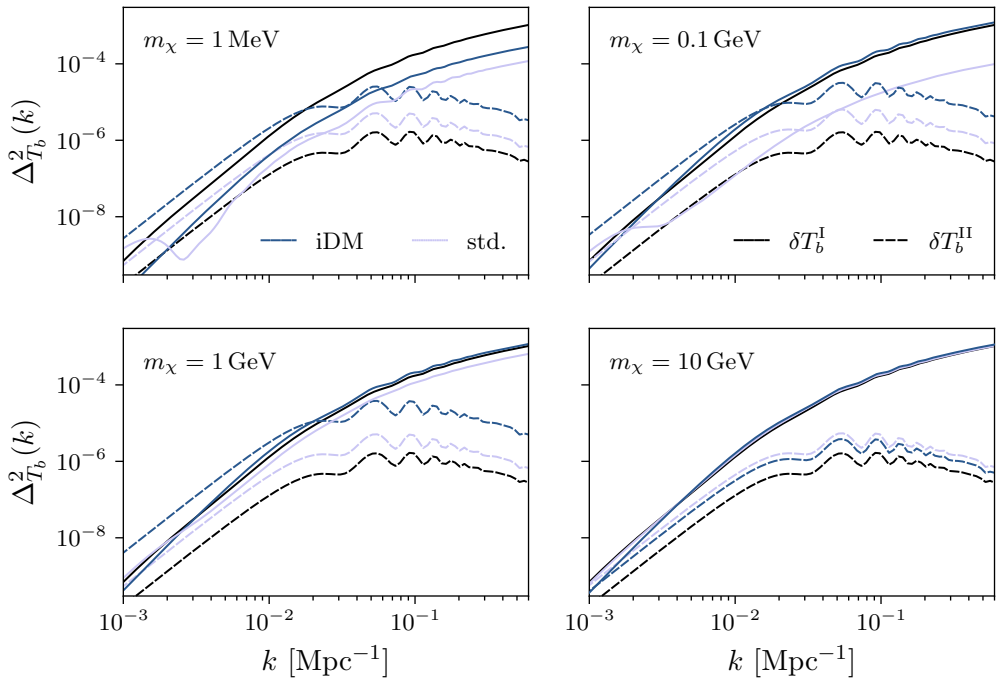

FIGURE 3.5: Quadratic correction to large-scale gas temperature fluctuations at $z = 30$, including the DM-baryon scattering contribution to perturbed recombination (iDM) and neglecting them (std.). We show the ΛCDM prediction in black for reference. Note that for $m_\chi \leq 1$ GeV, the temperature fluctuations δ_{T_b} can change sign from negative to positive at certain values of z; this explains the "dip" feature in the monopole evident for the 1 MeV case. For each DM mass we set the momentum-transfer cross section to the values found in Table 3.1.

inversely with the scattering cross section, and the effect is less pronounced as the interaction strength weakens. However, there is still an extra suppression at the few percent level even for a value of σ_0 one order of magnitude below current limits.

3.3.3 Large-scale enhancement of baryon temperature power spectrum

Finally, we study the large-scale quadratic corrections to the baryon temperature power spectrum. In the case of ΛCDM, this correction amounts to a $\sim 10\%$ enhancement of power at $k \lesssim 0.01\,\mathrm{Mpc}^{-1}$ for $z = 30$ [329]. Scattering between DM and baryons can enhance the quadratic contribution to the large-scale temperature fluctuations (both in absolute terms and relative to the linear power spectrum), as we illustrate in Figure 3.5. We find that for $m_\chi = 1$ MeV–1 GeV, this contribution to the large-scale temperature fluctuations can become larger than the standard, linear contribution for scales $k \lesssim 0.01\,\mathrm{Mpc}^{-1}$. Neglecting the temperature fluctuations sourced by DM-baryon interactions not

only significantly mis-estimates the linear power spectrum, but the second order contribution at large scales as well.

3.4 Consequences of temperature perturbations in the presence of DM-baryon scattering

In the previous sections, we have derived the new contributions to perturbed recombination arising from DM-baryon scattering and their direct effects on the evolution of cosmological perturbations, with special attention to the temperature and density power spectra. While the newly-derived contributions do not have an impact on CMB power spectra, the modified baryon temperature and growth of structure at small scales may have sizable signatures in other observables that are sensitive to the abundance of light collapsed structures and the baryonic gas.

It is expected that the first stars form at $z \sim 30$–40 in the densest volumes of the Universe where gas collapses into dark matter halos and cools. As discussed above, accounting for the temperature perturbations arising from the DM-baryon scattering results in a $\sim 10\%$ suppression of the baryon and matter density power spectra with respect to the (already suppressed) previous predictions. This suppression occurs at the scales of interest for the formation of the dark matter halos that could host the first stars. Therefore, the DM-baryon interactions may delay cosmic dawn even more than originally predicted by first estimates that neglected the contributions to the temperature perturbations, which should have a very strong impact in the HI line-intensity mapping observables during cosmic dawn [228–236]. Moreover, the modified temperature perturbations may induce additional spatial correlations in the clustering of the first stars. At the very least, our results show that the inclusion of all relevant sources of temperature perturbations is very likely to modify the initial conditions at the onset of cosmic dawn. Nonetheless, it will arguably still play an important role once sources of radiation switch on, modifying the predicted evolution of the cosmic dawn and the epoch of reionization. Given the complexity of such processes and the expected highly non-trivial interplay between the effects of the DM-baryon scattering (both on densities and temperature) and astrophysical processes, we leave a dedicated study of this to future work. In any case, we anticipate that these contributions will increase the sensitivity of experiments targeting both the high-redshift HI power spectrum – such as HERA [410] and SKA [411] – and the sky-averaged measurements –

e. g. EDGES [407], SARAS [408] and LEDA [409] – to DM-baryon scattering models.

As an example, we study the effect on the HI line-intensity mapping from the dark ages, before the formation of the first stars, which can be computed from the evolution equations in Section 3.2. We first briefly review the computation of the HI line-intensity mapping observables from the dark ages, drawing heavily from refs. [329, 421]; we refer the interested reader to these works for further details. Then, we show the predicted power spectra. We note that for $z \lesssim 50$, non-linearities become important in the HI fluctuations and can affect the small-scale power spectrum at the many percent level [421]. However, we emphasise that the aim of this work is to demonstrate the importance of including DM-baryon interactions in the temperature perturbations (not just the background) when evaluating the HI signal for these models. For this purpose it is sufficient to limit ourselves to a linear treatment, but non-linear effects should be included for a high-precision prediction of the signal and comparison with data.

3.4.1 HI line intensity and fluctuations

The spin temperature T_s of the baryon gas is defined through the ratio of the populations of neutral hydrogen in triplet to singlet state, and can be computed, in the limit $T_\star \ll T_b, T_\gamma$, as

$$T_s = T_\gamma + (T_b - T_\gamma)\frac{C_{10}}{C_{10} + A_{10}\frac{T_b}{T_\star}}, \tag{3.23}$$

where C_{01} and C_{10} are the upward and downward collision transition rates, respectively [421], $A_{10} \approx 2.85 \times 10^{-15}\,\mathrm{s}^{-1}$ is the spontaneous Einstein decay rate of the HI transition, and $T_\star \approx 0.068\mathrm{K}$ is the energy difference between the two spin states.

The HI brightness temperature T_{HI}, defined as the difference between the brightness of the HI radiation field and the background CMB radiation field, is equivalent to the line intensity. The observed brightness temperature (redshifted to today) of the HI radiation emitted at redshift z is given by

$$T_{\mathrm{HI}} = \frac{(T_s - T_\gamma)(1 - e^{-\tau})}{1+z} \approx \frac{(T_s - T_\gamma)}{1+z}\tau, \tag{3.24}$$

where we have used the optically thin limit, valid during all of the dark ages, and τ is the optical depth for the HI radiation. Since the gas temperature depends on the DM-baryon relative velocity, so do the spin temperature and the HI brightness temperature.

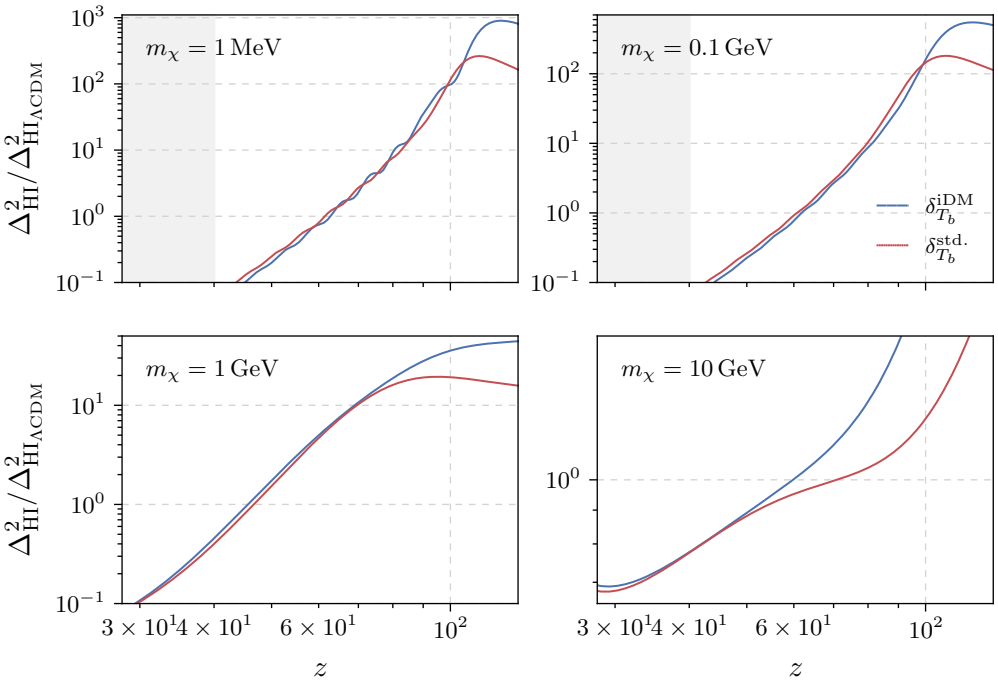

FIGURE 3.6: Ratio (with respect to ΛCDM) of the HI power spectrum as a function of redshift at $k = 1\,\mathrm{Mpc}^{-1}$. We show the result when including the additional temperature fluctuations due to DM-baryon interactions (blue, iDM) compared to neglecting them (red, std.) For each DM mass, the value of the cross section σ_0 is found in Table 3.1. Note that for sub-GeV masses, there is effectively no HI absorption line $z \lesssim 40$, indicated by the shaded region.

We compute the HI brightness temperature fluctuations to second order in the hydrogen density, temperature perturbations, and ionization fraction, neglecting fluctuations in the photon temperature. Accounting for redshift-space distortions, the observed brightness temperature fluctuations to second order are

$$\begin{aligned}\delta T^{\mathrm{obs}}_{\mathrm{HI}} = & -\overline{T}_{\mathrm{HI}}\delta_v + \mathcal{T}_H\delta_b + \mathcal{T}_T\delta_{T_b} + \mathcal{T}_x\delta_{x_e} \\ & + \mathcal{T}_{HH}\delta_b^2 + \mathcal{T}_{TT}\delta_{T_b}^2 + \mathcal{T}_{xx}\delta_{x_e}^2 + \mathcal{T}_{HT}\delta_b\delta_{T_b} + \mathcal{T}_{Hx}\delta_{x_e}\delta_b + \mathcal{T}_{Tx}\delta_{T_b}\delta_{x_e},\end{aligned} \tag{3.25}$$

where $\overline{T}_{\mathrm{HI}}(V_{\chi b})$ is the mean brightness temperature, $\delta_v \equiv \partial_\parallel v_\parallel / H$ is a dimensionless small quantity (where $\partial_\parallel v_\parallel$ is the line-of-sight gradient in proper space of the component of the peculiar velocity along the line of sight), and we assume $\delta_H \approx \delta_b$. The coefficients $\mathcal{T}_i$ are also functions of redshift *and* the relative velocity (for explicit expressions see ref. [358]).

The monopole source can be defined as

$$\delta_s \equiv \frac{\mathcal{T}_H \delta_b + \mathcal{T}_T \delta^{\rm I}_{T_b}}{\overline{T}_{\rm HI}} \tag{3.26}$$

and the total contribution of quadratic terms (recalling that $\delta_{T_b} = \delta^{\rm I}_{T_b} + \delta^{\rm II}_{T_b}$ contains quadratic terms itself) is defined as

$$\delta T^{\rm II}_{\rm HI} \equiv \mathcal{T}_{HH} \Delta\delta_b^2 + \mathcal{T}_{TT} \Delta\delta^2_{T_b} + \mathcal{T}_{HT} \Delta\delta_b \delta_{T_b} + \mathcal{T}_T \delta^{\rm II}_{T_b} \,, \tag{3.27}$$

where we have neglected terms involving the ionization fraction perturbations because they are much smaller, $\Delta\delta^2$ is the fluctuation around the mean of δ^2, and relativistic terms are neglected. Therefore, the perturbations of the observed brightness temperature are

$$\delta T^{\rm obs}_{\rm HI} = \overline{T}_{\rm HI}(\delta_s - \delta_v) + \delta T^{\rm II}_{\rm HI} = \overline{T}_{\rm HI}(\delta_s - \frac{\mu^2 \theta_b}{H}) + \delta T^{\rm II}_{\rm HI} \,, \tag{3.28}$$

where $\mu = \hat{\boldsymbol{n}} \cdot \hat{\boldsymbol{k}}$. At small scales we only consider the first term, while at large scales the quadratic corrections are uncorrelated with the linear terms. Finally, we compute the HI power spectrum averaged over the initial relative velocity distribution.

In Figure 3.6, we illustrate the effect of DM-baryon scattering on the HI power spectrum as a function of redshift for each DM mass. We show the ratio of the power spectra sourced by the monopole at $k = 1$ Mpc^{-1} with respect to ΛCDM, comparing the result when including (blue) and neglecting (red) the new contributions to the gas temperature fluctuations from DM-baryon scattering. The primary effect of including the additional gas temperature fluctuations is to modify the overall amplitude of the HI power spectrum over a wide range of scales and redshifts. This is not surprising, since this was also the main effect at large scales for the baryon gas temperature power spectrum which is one of the leading contributions to $\delta T_{\rm HI}$ at linear order. However, the coefficient $\mathcal{T}_T$ decreases with redshift, which can diminish the impact of the enhanced temperature perturbations δ_{T_b} at low-redshift.

For $m_\chi < 1$ GeV, we find an enhancement of the HI power spectrum by up to a factor of a few for $z \gtrsim 100$ compared to neglecting the effects of DM-baryon interactions in the perturbed recombination; at lower redshift, the HI power spectrum is modified at the tens of percent level. Note that for sub-GeV masses, the cooling of the baryon gas temperature drives the mean brightness temperature $\overline{T}_{\rm HI} \to 0$ much faster, and there is effectively no HI absorption

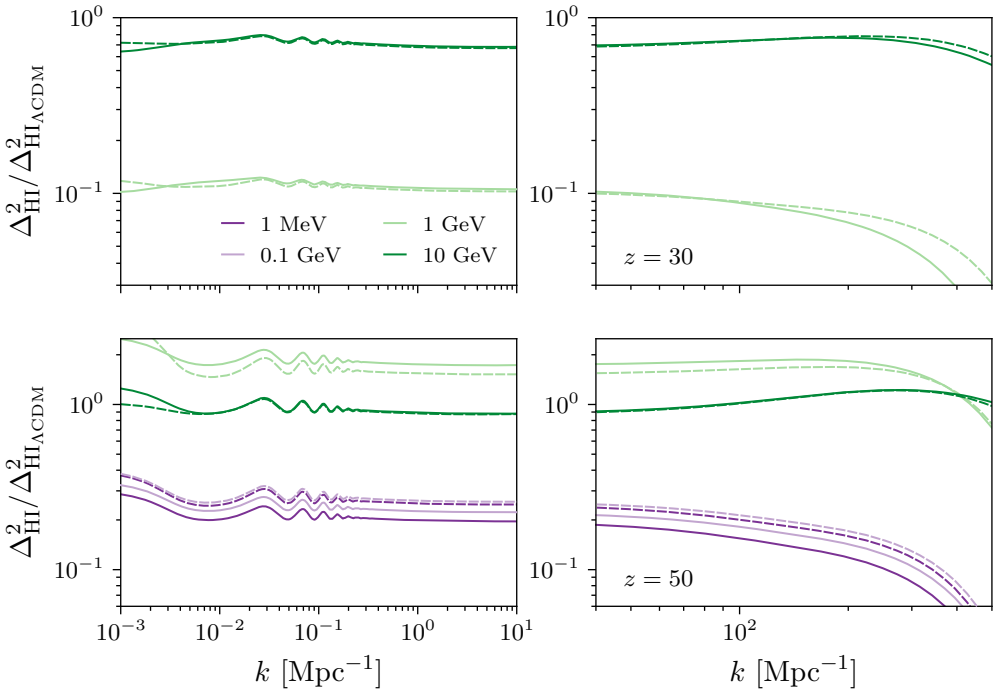

FIGURE 3.7: Ratio (with respect to ΛCDM) of the power spectrum of HI fluctuations at $z = 30$ (top panels) and $z = 50$ (bottom panels). On the left, we show the large-scale power spectrum both including (solid) and neglecting (dashed) the DM-baryon scattering contributions to perturbed recombination until $k = 10\,\mathrm{Mpc}^{-1}$. On the right, we show the same for scales $k = 40$–$500\,\mathrm{Mpc}^{-1}$.

line below $z \sim 40$. Similarly for $m_\chi \gtrsim 1$ GeV, the amplitude of the HI power spectrum is enhanced by up to a factor $\sim$ few for $z \gtrsim 70$; below this redshift, even while the baryon temperature fluctuations may be enhanced, there is a closer cancellation of the monopole terms and the enhancement of the HI power spectrum is lessened. The undulating behaviour in the upper panels is an artefact of averaging over a finite number of relative velocity patches, in which some coefficients $\mathcal{T}_i(V_{\chi b})$ in Eq. (3.25) cross from positive to negative at different times for different relative velocities.

In the left panels of Figure 3.7 we show the ratio of the large-scale HI power spectrum relative to ΛCDM at $z = 30$ and 50 up to $k = 10\,\mathrm{Mpc}^{-1}$. At $z = 50$, the amplitude of HI power spectrum for $m_\chi = 1$ GeV is enhanced by $\sim$ 10% compared to the case when considering standard Compton scattering only in the temperature perturbations. Moreover, the additional gas temperature fluctuations from DM-baryon interactions can modify the BAO feature in the power spectrum depending on which term in Eq. (3.25) dominates. Observing this feature could help to distinguish a DM-baryon scattering signal from other exotic physics which might modify the amplitude of the HI power spectrum. The right panels of Figure 3.7 show the ratio of the HI power spectrum relative

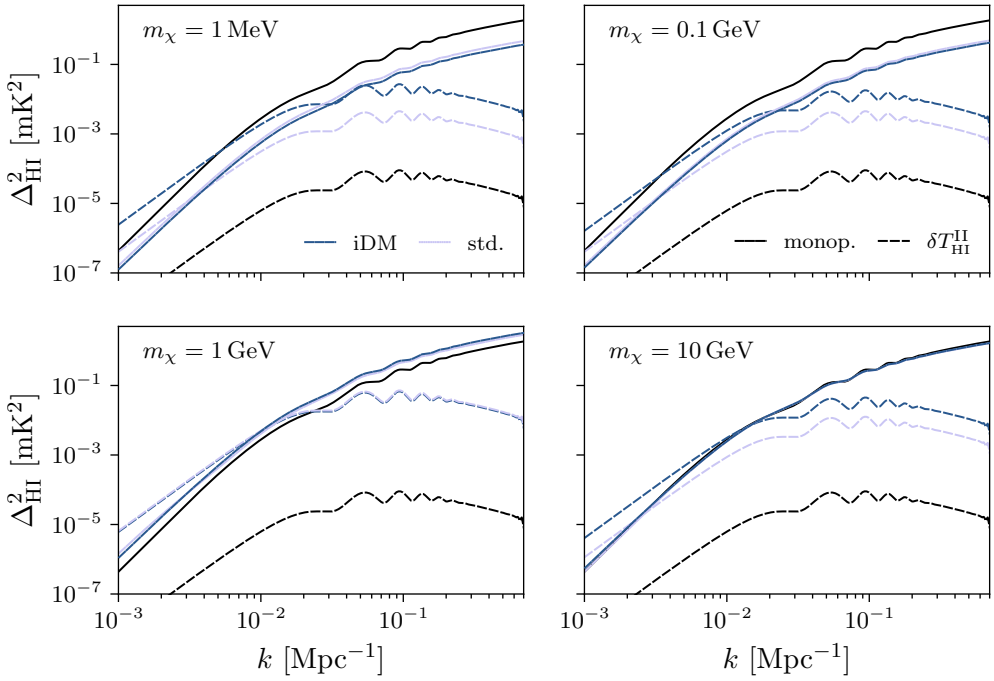

FIGURE 3.8: Power spectrum of HI fluctuations at $z = 50$ comparing the standard monopole term (solid) and the quadratic contribution (dashed). We compare our full calculation (iDM), to the result when ignoring the fluctuations sourced by DM-baryon scattering (std.), and to ΛCDM (black). The interaction cross section σ_0 for each DM mass is set to the values found in Table 3.1.

to ΛCDM at $z = 30$ and 50 for scales $k \geq 40\,\mathrm{Mpc}^{-1}$. The effects on smaller scales are a combination of the results at larger scales (i.e., maintaining the amplitude change shown in Figure 3.6) and the suppression of temperatures and densities at scales smaller than the Jeans scale. However, for the $m_\chi = 10$ GeV case, the HI power spectrum can become enhanced around the baryonic Jeans scale due to the enhanced baryon density perturbations (see Figure 3.4).

Finally, in Figure 3.8 we show the power spectrum of the quadratic terms $\delta T^{\mathrm{II}}_{\mathrm{HI}}$ compared to the monopole fluctuations for both the ΛCDM and DM-baryon scattering cases at $z = 50$. In ΛCDM, the relative contribution of quadratic terms is maximal around $z \sim 30$, contributing greater than $\sim 10\%$ of the monopole fluctuations for $k \lesssim 0.01\,\mathrm{Mpc}^{-1}$. In the presence of interactions between the DM and baryons, however, we find a considerable enhancement of the absolute and relative amplitudes of the quadratic contributions. For all masses considered, this contribution becomes comparable to or larger than the monopole signal for scales $k \lesssim 0.01\ \mathrm{Mpc}^{-1}$ at $z = 50$. The relative contribution is similar at $z = 30$ for 1–10 GeV masses (not shown). In almost all cases, neglecting the new contributions from DM-baryon interactions in the temperature fluctuations significantly underestimates the amplitude of the quadratic

correction to the HI power spectrum.

3.5 Conclusions

In this Chapter, we have considered the cosmological effects of dark matter that features velocity-dependent elastic interaction with protons, where the momentum-transfer cross section is parameterised as a power law of the relative particle velocity, $\sigma(v) = \sigma_0 v^n$. In particular, we focused on understanding the effects of the perturbed baryon and dark matter temperatures, deriving for the first time the contributions arising directly from the DM-baryon collision term and studying their effects on the evolution of cosmological perturbations. We presented numerical results for Coulomb-like scattering with $n = -4$. Such interactions have been previously invoked to explain the anomalous HI signal reported by the EDGES collaboration, but are also well-motivated from a theoretical standpoint within millicharged models for dark matter.

While the effect of DM-baryon scattering on the background DM and baryon temperatures has been well-studied in the literature, this is the first time the impact at the level of the perturbations has been explicitly considered. We derived the modified perturbed recombination equations for the temperatures and the ionization fraction and evolved them self-consistently with the linear Boltzmann equations appropriate for DM-baryon scattering cosmologies until the end of the dark ages ($z \sim 30$). By doing so, we also computed how the modified DM and baryon temperature perturbations affect the growth of structure by properly accounting for their contribution to the sound speed terms in the momentum evolution of each fluid respectively.

We found that the baryon temperature (and ionization fraction) perturbations are enhanced by up to an order of magnitude when including the novel DM-baryon scattering contributions to perturbed recombination, for scattering cross sections within current CMB bounds. These changes are significant over a wide redshift throughout the dark ages, and largely scale-independent for $k \lesssim 100\,\mathrm{Mpc}^{-1}$. Moreover, the DM-baryon interactions result in non-negligible DM temperature perturbations as well. These additional contributions to the DM and baryon temperature perturbations also affect the growth of density perturbations at the Jeans scale through the sound speed terms in the Boltzmann equations; we found a further $\sim 5\%$–10% suppression of the baryon and matter power spectra at scales $k \sim 200\,\mathrm{Mpc}^{-1}$ relative to ΛCDM at $z = 30$, compared to the prediction without including these effects (depending on the DM mass and scattering cross section).

The effects of DM-baryon scattering on the temperature perturbations, and the resulting suppression of small-scale structures, have important implications for the modelling and interpretation of cosmological observables sensitive to the gas temperature and the abundance of light collapsed objects. The evolution of cosmic dawn and reionization is highly sensitive to the early-time star formation history, which in turn depends upon the fraction of gas collapsed into halos where it can sufficiently cool and form stars. Therefore, our results will be critical to accurately predict the initial conditions of cosmic dawn and we anticipate this to have a significant impact on the reionization history, delaying the milestone epochs of cosmic dawn, X-ray heating and reionization. This will provide future observations with additional sensitivity to DM-baryon scattering models. One example of such an observable is HI intensity mapping. To illustrate this point, we computed the HI power spectrum from the dark ages including the newly derived contributions to the temperature perturbations from DM-baryon scattering. We found that the amplitude of the HI power spectrum is modified by tens of percent at $z = 30$, and up to factor of a few at higher redshifts. The effect of the interactions is also expected to alter the global HI signal [422].

We have considered the end of the cosmic dark ages to be at $z \sim 30$. However, if cosmic dawn begins earlier, our main conclusions still hold; the novel effects of DM-baryon scattering on the temperature perturbations and the matter power spectra are significant at higher redshift, which is shown explicitly for $z = 50$ in Appendix B.1. We emphasise that the (previously neglected) temperature perturbations sourced by DM-baryon scattering derived in this work are required to model the initial conditions for cosmic dawn properly. Once the first stars form, their radiation will become the dominant heating source over the Compton or DM-baryon scattering contributions, and a dedicated study of the interplay of these different effects is necessary to predict the evolution of the cosmic dawn signal. Our results strongly motivate further investigation into how these effects would impact the cosmic dawn signal beyond $z = 30$, which are likely to further improve the constraining power of forthcoming probes of the high-redshift Universe to DM-baryon interactions.

Chapter 4

Inferring the Neutrino Mass Hierarchy with Cosmology

4.1 Introduction

Solar, atmospheric, accelerator and reactor neutrino experiments have observed neutrino flavor conversion driven by neutrino masses, but the observable effects of neutrino oscillations are sensitive only to mass-squared splittings among eigenstates and thus can only constrain the neutrino mass square differences. Matter effects have allowed the sign of the small mass splitting to be determined, leaving two possible mass orderings: the normal hierarchy (NH) and the inverted hierarchy (IH). Determining the precise values of the three mass states, and the mass ordering (i.e., the hierarchy) or, equivalently, the precise determination of the sum of the masses (or the absolute mass scale) and the hierarchy, remains an open challenge.

The absolute neutrino mass scale can be probed using beta decay; the best current bound is provided by the KATRIN experiment with an upper limit on the beta decay effective neutrino mass of $m_\beta < 0.8$ eV, i. e., the sum of neutrinos masses $\Sigma m_\nu < 2.4$ eV [260] at 90% C.L., which improves dramatically upon the previous limit of $\Sigma m_\nu < 6.9$ eV at 95% C.L. [423]. Yet, despite these spectacular improvements, this bound is still about an order of magnitude less stringent than state-of-the-art cosmology constraints.

This is where cosmological observations become of relevance (see, e. g., [271, 424–428] and references therein). Cosmological surveys can provide crucial information on the absolute masses of neutrinos, as massive neutrinos influence both the expansion history and growth of structure in the Universe. Over the past five years the cosmological limits on the sum of neutrino masses, Σ (now dropping the m_ν to clarify notation), have become increasingly tighter, and are getting tantalizingly close to the lower limit for the sum of the masses allowed by the inverted hierarchy $\Sigma_{\mathrm{IH},low} = 0.0982 \pm 0.0010$ eV (68% C.L.) [429, 430],

implying the volume of parameter space available for the IH is becoming heavily restricted. In this chapter, we revisit the question originally asked in ref. [431]: "Given the current knowledge about mass-squared splittings and cosmological constraints on the total mass, can anything be said about the neutrino mass hierarchy?"

Whether the electron neutrino is mainly composed by the lightest mass state (as in the NH) or not (IH) has important implications on the theoretical upper limit of the neutrinoless double-beta decay half life [432], in the case that neutrinos are Majorana fermions and obtain the Majorana mass through the three light neutrinos mechanism. Therefore, the fraction of the neutrino parameter space to be explored by future ton-scale double-beta decay experiments [282, 433, 434] is greatly influenced by the type of neutrino mass hierarchy. As such, determining the hierarchy has important implications for the future technologies and resources needed to lead to a potential discovery.

In cosmology we cannot perform experiments; we only observe the sky. As such, we always test a model of the observations that we gather from the sky with our detectors. Given this constraint, the most natural choice to make inference in cosmology and astronomy is Bayesian statistics: we want to infer the parameters of the model given some data. This takes the following, extremely well known, mathematical form

$$P(\alpha|D,M) = \frac{P(D|\alpha,M)P(\alpha|M)}{P(D|M)}\,, \tag{4.1}$$

where D stands for data (observations), M for model (hypothesis) and α denotes the parameters of the model; $P(\alpha|D,M)$ is the posterior, used for parameter inference, and $P(D|\alpha,M)$ is the likelihood which is usually provided along with the data. $P(\alpha|M)$ is the prior, the so-called prior knowledge, which has provoked abundant literature for centuries on its choice and value and an ongoing debate between Bayesian and frequentist approaches to probability. All Bayesian inference depends on the choice of the prior, which is *always* a subjective choice. It is true that for parameter inference, in the limit of precision measurements – i. e., if the likelihood is very localised – the likelihood can overcome (most reasonable choices of) the prior.

The question we set out to address, however, falls under "model selection" or "model comparison" and therefore it is useful to employ Bayesian evidence methods [435], which have gained attention in cosmology over the past couple of decades [436–438]. The evidence can be written as a function of the likelihood and the prior, being the integral of the likelihood over the (full range of the)

prior integrated over the values of the parameters α:

$$P(D|M) = \int P(D|\alpha, M)P(\alpha|M)d\alpha\,. \tag{4.2}$$

The evidence quantifies the probability of obtaining the data given the full model, not just a specific set of parameters values. What we really want to infer is the probability of a particular model given the data, i. e.,

$$P(M|D) = \frac{P(D|M)P(M)}{P(D)}\,. \tag{4.3}$$

Thus when considering two models, each of them with the same a priori probability $P(M)$ for the same data, model comparison can be done by taking the evidence ratio for the two models. It is important to note that the evidence, and hence also the evidence ratio, will *always* depend on the choice of the prior $P(\alpha|M)$ even for very localised likelihoods.

In light of this limitation, it is important to fully understand the motivation for and implications of a given prior choice, the impact of the prior choice on the inferred result, or alternatively, how to choose the prior depending on the context or the question at hand.

> Historically, Bayesian analysis has been accompanied by methods to work out the "right" prior for a problem, for example, the principles of insufficient reason and maximum entropy. The modern Bayesian, however, does not take a fundamentalist attitude to assigning the "right" priors - many different priors can be tried; each particular prior corresponds to a different hypothesis about the way the world is. We can compare these alternative hypotheses in the light of the data by evaluating the evidence. The answer to this question can be reached by performing Bayesian model comparison. - *DJC MacKay* [439].

Choosing an appropriate prior in the context of inferring the odds of one mass hierarchy over the other has been discussed at length in the literature [431, 440–446]. The results of ref. [431] elicited strong reactions and stimulated a vivid discussion on the hierarchical nature of neutrinos. Many different sets of priors have been explored which have yielded a wide range of conclusions. The disparities in the findings of these works further highlights the fact that the evidence *always* depends on the prior choice. Yet very few have followed MacKay's advice regarding how the prior choice encompasses our *a priori* views

about the way the world is – in this case which set of prior is supported by our knowledge of e. g., physics, and how that informs model selection.

For example, ref. [445] argues that the prior choice should be motivated by fundamental physical principles and chooses to specify the prior directly at the level of the neutrino mass matrix, obtaining odds of the order of ∼100:1 for the NH, using the constraints available in 2018. Ref. [431] on the other hand, tries to be more generic and argues that the prior should describe our state of belief before we have constraints, i. e. before the measurement of neutrino oscillations and thus before having information about the mass-squared splittings, when each of the neutrino masses has an uncertainty that spans many orders of magnitude. In this case, ref. [431] argues, a logarithmic prior on each of the masses naturally incorporates this uncertainty. More precisely, rather than using a single pre-determined prior, ref. [431] adopted a family of priors described by hyper-parameters, which yields a hierarchical prior (see Appendix C.1) and obtained odds of 40:1 for the NH. Such a choice of prior reflects the fact that the three masses are indistinguishable before the data arrives, and specifies the prior on each mass before any ordering takes place. This prior is well known in the particle physics community. It is based on the construction of the Standard Model mass mechanisms, which generally assume a common mechanism (usually at a high energy scale) for the origin of the three neutrino masses. In perspective, this prior is behind the rise of neutrino oscillation experiments. The additional ingredient of adopting a hierarchical prior (see Appendix C.1) means that effectively rather than one given prior, a family of priors – described by hyperparameters – is adopted, and the hyperparameter values are marginalized over.

A completely different approach to the same question, which comes from the alternative school of thought that is "Objective Bayesianism", is taken in ref. [440]. The idea is to construct a prior that is as uninformative as possible from a mathematical point of view. To do so the likelihood is used and in particular the likelihood provided by oscillation data. The adopted prior, for precision experiments where the likelihood achieves asymptotic normality, uses as information measure the Fisher information. This choice of prior depends on the experimental set up. In particular, in the case of the neutrino hierarchy, it does not enclose any *a priori* information about the fact that e. g., we believe there to be a single mechanism that gives rise to the three neutrino masses and that their masses can span many orders of magnitude (as ref. [431] does). Still it is important to note that this prior choice reflects the fact the three masses are indistinguishable before the data arrives, and thus does not favour

one hierarchy over the other.[1] This *objective* prior does need to be updated for every different experiment that is performed. For the experimental data considered in ref. [440], this approach yielded odds of 5:1 for the NH.

In addition, as MacKay points out, the very same framework that we use to compare the normal hierarchy to the inverted hierarchy – the Bayesian evidence ratio – can also be used to identify which set of priors is favoured by the data. This can be explicitly explored in the hierarchical prior case, where the distribution of the hyper-parameters quantifies exactly this (see Appendix C.1).

In this work, we revisit this issue – which has remained somewhat dormant since 2018 – in light of the latest cosmological constraints and global fits to neutrino oscillation experiments. We follow MacKay in considering two generic type of priors: the logarithmic-hierarchical prior used in ref. [431] (which we abbreviate by 'SJPV' from the author's initials), and the objective Bayesian ('HS') used in ref. [440]. We perform a Bayesian model comparison under each of these approaches, computing the evidence for NH and IH, as well as computing the posterior distributions for the individual neutrino masses and the sum of the masses under each hierarchy. We speculate on the implications of these results for double-beta decay experiments. While other prior choices have been considered in the literature, we do not consider them here because they are either not physically motivated, or adopt different prior distributions for the different mass eigenstates, or would return odds in between the HS and the SJPV cases. This Chapter is organised as follows: in Section 4.2, we introduce the datasets used in our analysis and set out our notation and methodology; in Section 4.3 we present our numerical results and discuss their interpretation with regard to each prior; in Section 4.4 we perform a sensitivity analysis, reporting results for different variations of our baseline dataset, and finally we discuss and conclude in Section 4.5.

4.2 Data and Methodology

Following standard practice we denote the three neutrino mass eigenstates as m_1, m_2, and m_3 such that there are two independent neutrino mass-squared differences and two possible hierarchies only. Here we adopt the convention where $m_1 < m_2$ and m_1, m_2 refers to the smaller mass-squared difference. Hence

[1] Note that conversely, it is possible to set up a prior that does not distinguish between the hierarchies yet does not satisfy exchangeability (the three masses are not drawn from a common prior, see for example the priors adopted in refs. [447–449] and other references therein). This choice implies that the three masses do not share a common origin and therefore that there are different physical mechanisms that give neutrinos the different masses. We do not consider this case.

in the so-called normal mass hierarchy (NH), m_1, m_2, and m_3 are defined in ascending order such that $m_1 \leq m_2 \leq m_3$. In the inverted hierarchy (IH) the ordering is instead $m_3 \leq m_1 \leq m_2$. The hierarchy is given by the sign of the square mass splitting involving m_3. When needed, we might refer to the three masses as $m_{\rm L}$, $m_{\rm M}$ and $m_{\rm H}$ (for "low", "medium" and "high" respectively). In the NH then $m_{\rm L} \lesssim m_{\rm M} \ll m_{\rm H}$, while in the IH instead $m_{\rm L} \ll m_{\rm M} \lesssim m_{\rm H}$.

We will use the following constraints on the squared mass splitting, derived from a global fit to observations of neutrino oscillations using NuFIT v5.1 (2021)[2] [277]

$$\begin{aligned} \Delta m^2_{21} &= m_2^2 - m_1^2 = 7.42\,(\pm 0.21) \times 10^{-5}\text{eV}^2 \quad (68.4\%\text{CL}) \\ \Delta m^2_{3\ell} &= m_3^2 - m_\ell^2 = \begin{cases} 2.510\,(\pm 0.027) \times 10^{-3}\text{eV}^2 & (\text{NH}) \\ -2.490\,(\pm 0.027) \times 10^{-3}\text{eV}^2 & (\text{IH}) \end{cases} \quad (68.4\%\text{CL})\,, \end{aligned} \tag{4.4}$$

where m_ℓ denotes m_1 and m_2 for the normal (NH) and inverted (IH) hierarchies respectively, and we approximate the uncertainty distribution as a Gaussian. In particular we have symmetrized the error bars for simplicity as this has a completely negligible effect on the final results. Compared to refs. [431, 440] the error bars have increased by ∼10% on Δm^2_{21} but decreased by ∼30% on $\Delta m^2_{3\ell}$. This provides (a Gaussian approximation to) the likelihood $P(D|\alpha, M)$ where α denotes the mass-squared splittings of Eq. (4.4).

It is important to note that, as discussed extensively in ref. [277], the three flavour oscillation parameters from the fit to global data yields the best fit for the normal ordering, with the solution for the inverted ordering having a worse fit by $\Delta\chi^2 = 7\,(2.6)$ when including (not including) the Super-Kamiokande atmospheric data (SK-atm). Moreover, there is a small tension between T2K and NOvA data, where the normal ordering option preferred by NOvA is in tension with the combination of T2K and reactor neutrino data. Although the inclusion of Super-Kamiokande data in the analysis of ref. [277] is sub-optimal, we see no reason to exclude this data set, and hence our baseline results will always include SK-atm. For our purposes the mild tension with NOvA data and the sub-optimal inclusion of SK-atm primarily affect the $\Delta\chi^2$ values, which generally underestimate the power of disentangling the neutrino parameter space when the tension is resolved.

[2]The original reference reports slightly asymmetric error bars: $^{+0.21}_{-0.20}$ for Δm^2_{21} and $^{+0.026}_{-0.028}$ for Δm^2_{32} IH, which we have symmetrized here as Gaussianity is a key assumption of ref. [440].

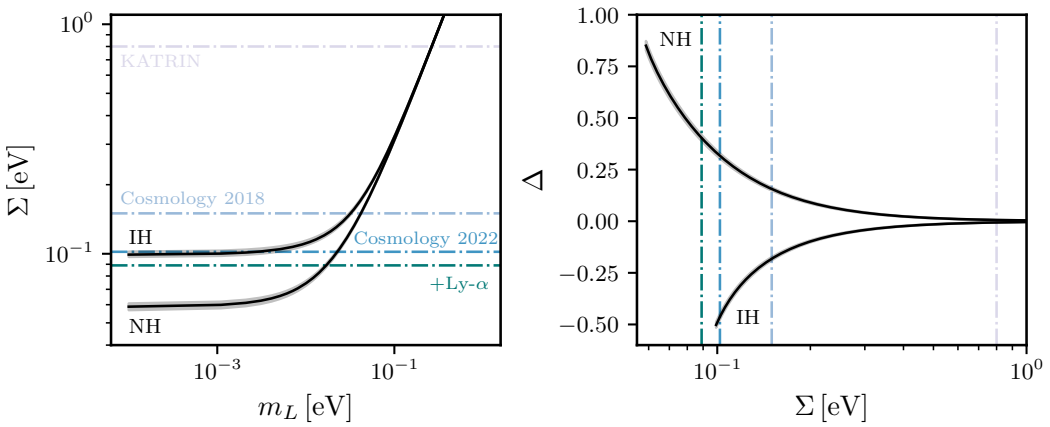

FIGURE 4.1: Visualization of the neutrino oscillation experiment constraints (Eq. (4.4)) and Σ_β KATRIN sensitivity limit and $\Sigma_{\rm cosmo}$ constraints (95% C.L.) in the $m_{\rm L}$-Σ plane and Δ-Σ plane. The grey bands represent 5σ uncertainties on the oscillations measurements.

The oscillation constraints of Eq. (4.4) can be visualized in Figure 4.1 where we show the allowed region in the $m_{\rm L}$-Σ plane, and in the Δ-Σ plane where Δ is defined as the ratio of the largest mass splitting to the total mass [427],

$$\Delta_{\rm NH} \equiv (m_{\rm H} - m_{\rm L})/\Sigma \;\text{ and }\; \Delta_{\rm IH} \equiv (m_{\rm L} - m_{\rm H})/\Sigma. \tag{4.5}$$

The bound on the sum of the masses $\Sigma = m_1 + m_2 + m_3$ derived from beta decay has significantly improved recently from $\Sigma < 6.9$ eV (95% C.L.) from the Mainz experiment [423] to $\Sigma < 3.3$ eV (90% C.L.) from the first KATRIN campaign [450] and even further to $\Sigma < 2.4$ eV (90% C.L.) from the combination of the first and second KATRIN campaigns [260]. The estimated sensitivity of KATRIN is $\Sigma < 0.8$ eV (95% C.L.) Meanwhile, over the past two decades cosmological surveys have yielded increasingly stronger constraints on the sum of the masses: $\Sigma_{\rm cosmo} < 1.8$ eV in 2002 [451], $\Sigma_{\rm cosmo} < 0.44$ in 2012 [452], $\Sigma_{\rm cosmo} < 0.25$ eV [453] in 2013, $\Sigma_{\rm cosmo} < 0.18$ eV [300] in 2015 and $\Sigma_{\rm cosmo} < 0.13$ eV [454] in 2016 (all quoted at 95% C.L.). The latest constraints provided by the eBOSS collaboration from the joint analysis of cosmic microwave background and large-scale structure data obtain an upper limit of $\Sigma_{\rm cosmo} = 0.102$ eV (95% C.L.) for the combination of *Planck* CMB data with BAO and redshift space distortions (RSD) from e-BOSS (CMB+BAO+RSD) and $\Sigma_{\rm cosmo} = 0.099$ eV (95% C.L.) for the combination CMB+BAO+RSD+SNeIa (including Type Ia supernovae data) [429]. Finally in combination with the Lyman-α forest 1D flux power spectrum, ref. [430] obtains an even stronger bound of $\Sigma_{\rm cosmo} < 0.089$ eV (95% C.L.). We illustrate a few of these cosmological constraints in Figure 4.1.

In what follows, as is commonly done, we assume Gaussianity in all the reported constraints. The upper limit on $\Sigma_{\rm cosmo}$ can in principle be interpreted in two ways: either as a (one-sided) Gaussian distribution centered at $\Sigma = 0$ or as a Gaussian distribution extrapolated to $\Sigma < 0$ and centered at the (interpolated or extrapolated) maximum of the posterior (even if that happens to be at $\Sigma < 0$) and truncated at $\Sigma = 0$. Since the data show no indication of a detection of Σ and negative masses are unphysical, we adopt the first interpretation. However, we explore the sensitivity of the results to this assumption for a few select cases.

The priors and evidences for logarithmic hierarchical SJPV and objective Bayesian HS are computed following refs. [431] and [440] respectively, using the updated constraints. In the case of the HS prior, the interpretation of the mass splittings and the naming conventions of the individual masses are slightly different from that of ref. [440] to make them consistent with the treatment of SJPV and ref. [277]. Details are reported in Appendices C.1 and C.2.

Different sources are responsible for different contributions to the final evidence ratio. We denote the final evidence ratio for the NH over the IH by $K_{\rm HS/SJPV}$ with subscript indicating the choice of prior. Partial results towards the full K, obtained including only some of the different contributions, are denoted by κ_i (where the subscript i specifies the different contributions considered or excluded). In particular, the contribution to K due to the $\Delta\chi^2$ of the global fit is a multiplicative factor: $\kappa_{\Delta\chi^2} = \exp(\Delta\chi^2/2)$. For completeness and a more transparent comparison with previous work, we also report the partial results excluding the $\kappa_{\Delta\chi^2}$ contribution. However, we stress here that we see no reason to exclude it.

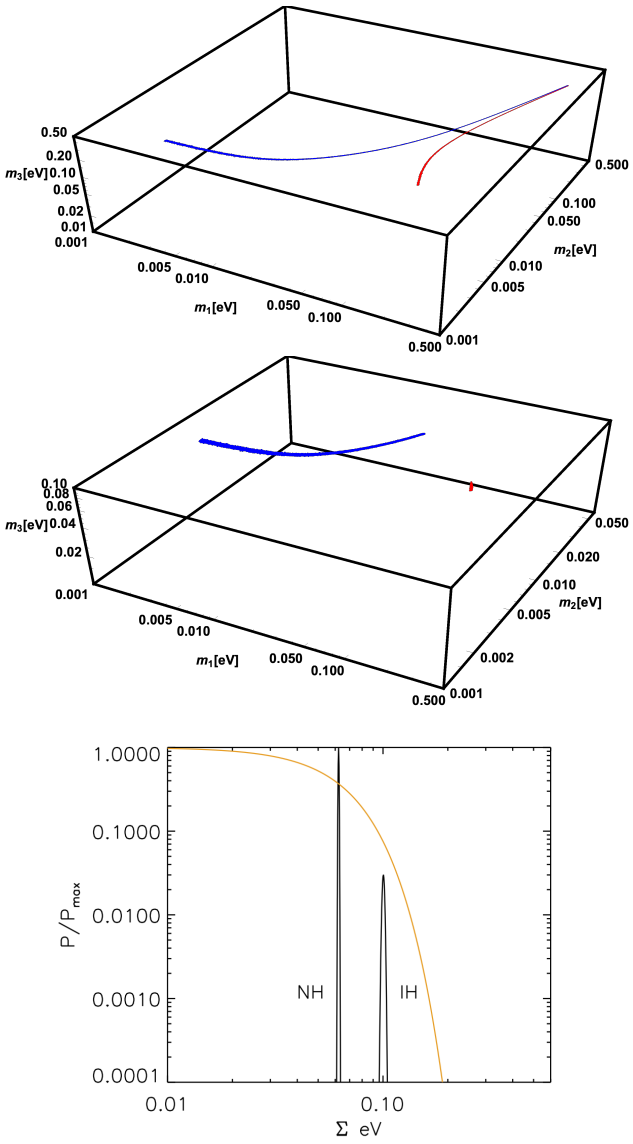

FIGURE 4.2: Visualization of current constraints. On the top two panels, the two thin (blue, NH and red, IH) ridges in the 3D space of m_1, m_2, m_3 represent the mass splitting constraints (95% CL) from oscillation experiments in Eq. (4.4). For the NH (m_1, m_2, m_3) corresponds to $(m_\mathrm{L}, m_\mathrm{M}, m_\mathrm{H})$, while for the IH it corresponds to $(m_\mathrm{M}, m_\mathrm{H}, m_\mathrm{L})$. For visualization purposes the NH ridge is shown only for $m_\mathrm{L} > 10^{-3}$ eV. In the uppermost panel only oscillation constraints are used, while in the middle panel a cosmology constraints of $\Sigma < 0.1$ eV is imposed; note the significant decrease of the allowed IH region and the different z-axis range. The bottom panel shows the normal and inverted hierarchy oscillations likelihood probability distributions (P/P_max) for the sum of the masses, keeping the mass of the lightest neutrino fixed at $m_\mathrm{L} = 3 \times 10^{-3}$ eV and cosmology constraint $\Sigma_\mathrm{cosmo} < 0.089$ eV (95% C.L., orange).

4.3 Results

We begin by presenting a visualization of the parameter space available for the two hierarchies, given the updated constraints illustrated in Figure 4.1 where the

probability distribution for the sum of the masses Σ is shown on the right panel. The black lines correspond to the oscillation constraints for the normal and inverted hierarchies, as indicated in the labels, and the grey bands represent the 5σ uncertainty regions. The vertical lines show the various $\Sigma_{\rm cosmo}$ constraints.

However, the (e.g., 95% C.L.) regions allowed by the oscillation experiments are actually in the 3D space of (m_1, m_2, m_3); recall that for the NH this corresponds to $(m_{\rm L}, m_{\rm M}, m_{\rm H})$ and for the IH this corresponds to $(m_{\rm M}, m_{\rm H}, m_{\rm L})$. Therefore, in Figure 4.2 we show the 3D locus of the hierarchies as allowed by current oscillation data (top panel) and after imposing a cosmological constraint of $\Sigma < 0.1$ eV (middle panel); note the significant decrease of the allowed region for the IH. The bottom panel shows the probability distribution of the sum of the masses given the oscillations measurements for both the NH and IH and fixing the lightest neutrino to $m_{\rm L} = 3 \times 10^{-3}$ eV, and the effect of the cosmological constraint (orange line) at further decreasing the allowed region for the IH.

It is very illustrative to visualize the priors of the two different approaches and compare them. In Figure 4.3, the top panels show the logarithmic hierarchical (SJPV) prior probability density, $P(\mathbf{m})$, in the $m_{\rm L}$-$m_{\rm M}$ plane for a fixed $m_{\rm H} = 1\,$eV and before considering the oscillations data. We show this for a representative choice of hyper-parameters $\log\mu = -1.5$, $\sigma = 1.0$, noting that while this is a somewhat low value of σ (see discussion in Appendix C.1), a higher value would be less illustrative as the distribution on the right panel would look very uniform. The specific choice of value for $m_{\rm H}$ does not affect the distribution, provided that $m_{\rm H} \geq m_{\rm M}$. The prior distributions are shown with axes in both linear (left) and logarithmic (right) scales. The bottom row panels show the corresponding probability density for the objective Bayesian (HS) prior. In this case, changing the value of $m_{\rm H}$ simply rescales the values on the $m_{\rm L}$ and $m_{\rm M}$ axes. The HS prior decreases for smaller values of $m_{\rm M}$ and $m_{\rm L}$ and, for a fixed value of $m_{\rm L}$, is minimal when $m_{\rm M} = m_{\rm L}$. On the other hand, the SJPV prior (before any oscillation data) does exactly the opposite; it increases for low $m_{\rm M}$ and $m_{\rm L}$ and, for a fixed value of $m_{\rm L}$, is maximal when $m_{\rm M} = m_{\rm L}$.

In Figure 4.4 we demonstrate how the SJPV hyperprior changes once the hyper-parameters are constrained by the inclusion of the oscillations data. It is evident that once oscillation constraints are taken into account, the resulting hierarchical prior becomes drastically different. The oscillations-informed hyperprior heavily favors either $m_{\rm L} \simeq m_{\rm M}$ (NH, diagonal ridge) or $m_{\rm L} \ll m_{\rm M}$ (IH). Even along these directions this prior favors low masses and the smooth

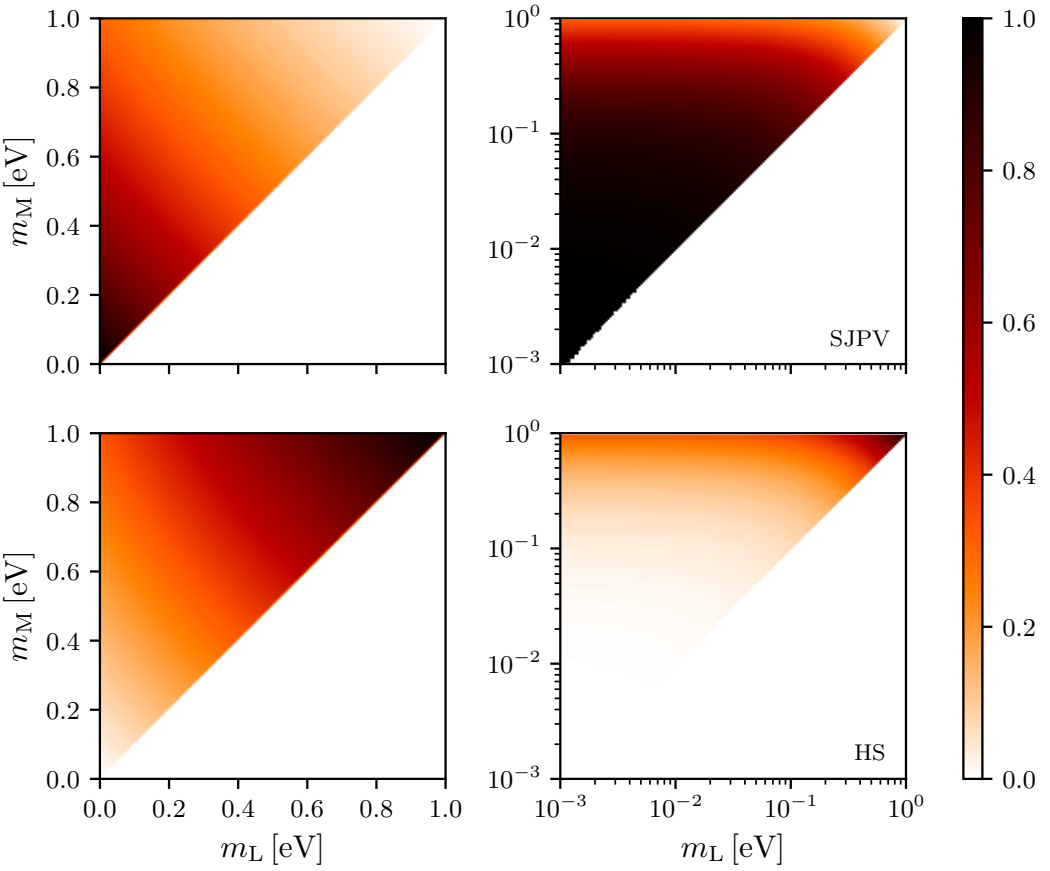

FIGURE 4.3: Comparison of the SJPV (logarithmic hierarchical) and HS (objective Bayesian) prior density $P(\mathbf{m})$: top panels show the SJPV prior probability before imposing oscillations constraints for an illustrative choice of hyper-parameters $\log\mu = -1.5$, $\sigma = 1$ in the $m_{\rm L}$-$m_{\rm M}$ plane, for a fixed $m_{\rm H}$, while bottom panels show the corresponding probability density for the HS prior. Shown for axes in linear (left) or logarithmic (right) scale. The color scale is linear with black at the maximum ($P/P_{\rm max} = 1$) and white at the minimum. The lower triangle is excluded by the condition $m_{\rm L} \leq m_{\rm M} \leq m_{\rm H}$. The HS prior decreases for low $m_{\rm M}$ and $m_{\rm L}$ and, for a fixed value of $m_{\rm L}$, is minimal when $m_{\rm M} = m_{\rm L}$; for the SJPV prior, the opposite is true.

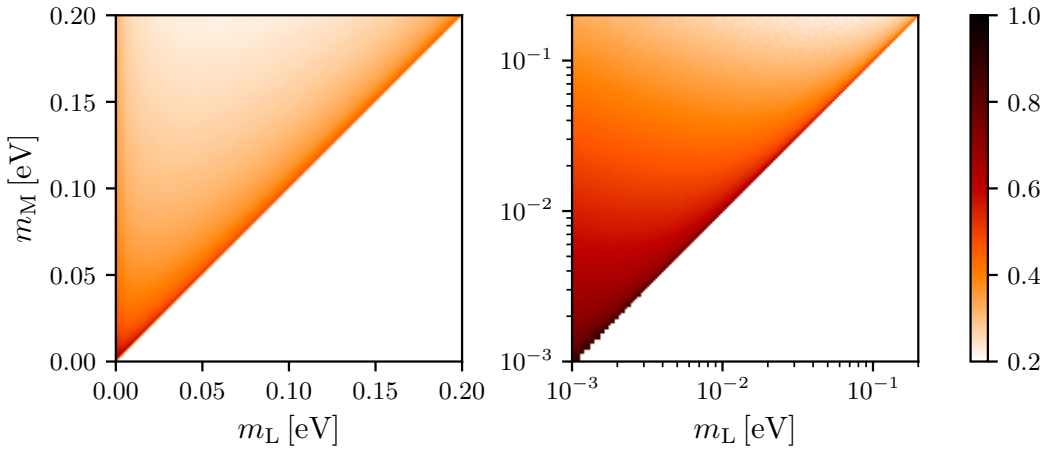

FIGURE 4.4: SJPV hyperprior density $P(\mathbf{m})$ once constraints from oscillation data are included, marginalized over the hyper-parameters μ and σ and over $m_{\rm H}$; no constraints on Σ are imposed. Axes in linear (left) and logarithmic (right) scale, with linear color-scale artificially cut at 0.2 to increase contrast. Here it is evident that the SJPV hierarchical prior, which encodes information from oscillations, differs drastically from HS, favoring low masses.

cutoff at high masses becomes more stringent with subsequent improvements on the Σ limits.

The probability density of the hyper-parameters μ and σ for the logarithmic hierarchical SJPV prior is shown in Figure 4.5 for the normal (left) and inverted (right) hierarchies after imposing cosmological constraints. A direct comparison with Figures 2 and 3 of ref. [431] shows how the hyper-parameter values change as the bound on Σ becomes more stringent, progressively disfavoring the hyper-parameter space for the IH more than for the NH.

We are now ready to interpret the Bayesian evidence results presented in Table 4.1 for both the SJPV and HS priors as a function of the Σ upper limit, assuming a zero-centered Gaussian distribution truncated at $\Sigma = 0$. The error in the calculation of the log-evidence values is estimated to be around 0.05–0.1, hence negligible for our purposes. Results with or without the Super-Kamiokande atmospheric (SK-atm) data are reported in Section 4.4 for completeness. However, we see no reason to exclude this data set, hence our baseline results discussed here always include it.

The new oscillation constraints do not significantly alter the evidence compared to the 2018 situation. In the HS case, compared with ref. [440], the major effect is due to the increased $\Delta\chi^2$ between the two hierarchies which has risen from $\Delta\chi^2 = 0.83$ in 2018 to $\Delta\chi^2 = 7.0$ now, increasing the contribution to the HS evidence ratio from the $\Delta\chi^2$ alone (which is an overall multiplicative normalization factor) from $\kappa_{\Delta\chi^2} = 1.5$ to $\kappa_{\Delta\chi^2} = 33$. Ref. [431], using the SJPV

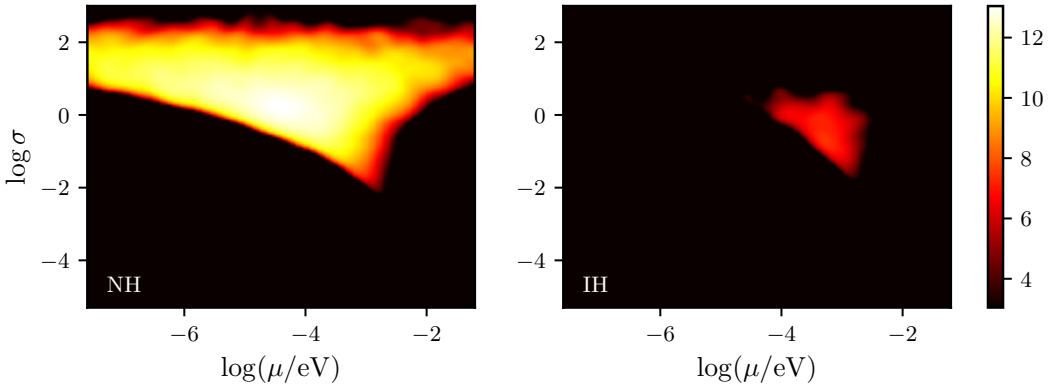

FIGURE 4.5: Normal (left) and Inverted (right) hierarchy marginal log-likelihood distributions for the hyper-parameters of the hierarchical prior for a cosmology mass limit of $\Sigma_{\rm cosmo} < 0.089$ eV (95% C.L.). The colorbar convention used here matches that of Ref. [431], for easier comparison.

	SJPV		HS	
	$\kappa_{\rm no\Delta_{\chi^2}}$	$K_{\rm SJPV}$ (w/ Δ^2_χ)	$\kappa_{\rm no\Delta_{\chi^2}}$	$K_{\rm HS}$ (w/ Δ^2_χ)
$\Sigma < 2.85$ eV (95%) [A]	3.8	124	1.0	33.1
$\Sigma < 0.8$ eV (95%) [B]	5.3	175	1.2	38.1
$\Sigma < 0.12$ eV (95%) [C]	49	1607	3.6	118
$\Sigma < 0.102$ eV (95%) [D]	87	2861	4.3	143
$\Sigma < 0.099$ eV (95%) [E]	88	2890	4.7	156
$\Sigma < 0.089$ eV (95%) [F]	138	4553	7.4	244

TABLE 4.1: Bayesian evidence ratios for the NH vs IH with SJPV and HS priors. The Σ constraints assume zero-centred Gaussian distributions and 95% C.L. limits as follows: A=KATRIN (current) [260], B=KATRIN (sensitivity) [260], C=*Planck*+BAO [429], D=*Planck*+BAO+RSD [429], E=*Planck*+BAO+RSD+SNeIa [429] F=*Planck*+BAO+Ly-α [430]. The sensitivity to the interpretation of the $\Sigma_{\rm cosmo}$ constraints is explored in Table 4.4.

K	Strength of evidence
1–3.2	Not worth more than a bare mention
3.2–10	Substantial
10–100	Strong
>100	Decisive

TABLE 4.2: Kass and Rafetry 1995 [455] qualitative interpretation of Bayesian evidence ratios. K is a osterior Bayesian odds ratio, the relative plausibility of two models in light of the data, and should not be interpreted as number of sigmas or a p-value.

prior, reported evidence ratios neglecting the contribution from the $\Delta\chi^2$ as it had a negligible effect for the oscillations measurements adopted in that work. One can also appreciate that the increasingly stringent mass limits have only a mild effect on the evidence ratio for the HS prior choice, but a much more significant effect for the SJPV prior.

By construction both priors, in the absence of oscillations data, do not favour one hierarchy over the other.[3] Once the oscillations data are taken into account, but before considering any constraint on Σ, both priors give very similar posterior odds, which now are driven by the $\Delta\chi^2$. Recall that the oscillation experiment measurements of the mass-squared splittings in Eq. (4.4) have not changed dramatically since 2018, although the value of the $\Delta\chi^2$ has. As long as the constraints on the sum of the masses are weak – e.g. $\Sigma_\beta < 6.9$ eV (adopted in SJPV) or $\Sigma_{\rm cosmo} < 1.5$ eV (adopted in HS) – as in 2018, the evidence ratio $\kappa_{{\rm no}\Delta\chi^2}$ is inconclusive (< 3) for both prior choices, although the $\kappa_{\Delta\chi^2}$ contribution now boosts the overall posterior odds for the NH by a factor 33. However, the situation changes drastically as the bounds on Σ tighten: in the SJPV case, the evidence is much more sensitive to the Σ constraints and the evidence for the NH increases much more dramatically once the total mass limit crosses $\Sigma < 0.1$ eV. Regardless of the prior choice, the odds ratio for NH is always $\gtrsim 100$ when including the latest cosmological constraints $\Sigma_{\rm cosmo}$ which disfavour values of Σ above 0.1 eV.

The Bayesian evidence ratio values or odds can be interpreted qualitatively according to e.g. the Kass and Raftery [455] scale reported in Table 4.2, which indicates that in all cases for both choices of priors the evidence ratio is always "Strong" or "Decisive" when including the $\kappa_{\Delta\chi^2}$ normalization. Independently of the prior choice the evidence for the NH is now "Decisive". For the HS prior,

[3] See related discussion in refs. [431, 440]. In short, the priors do not distinguish the three mass eigenstates – a feature called *exchangeability*, see Appendix C.1 – and hence do not favour one hierarchy over the other before the data arrives.

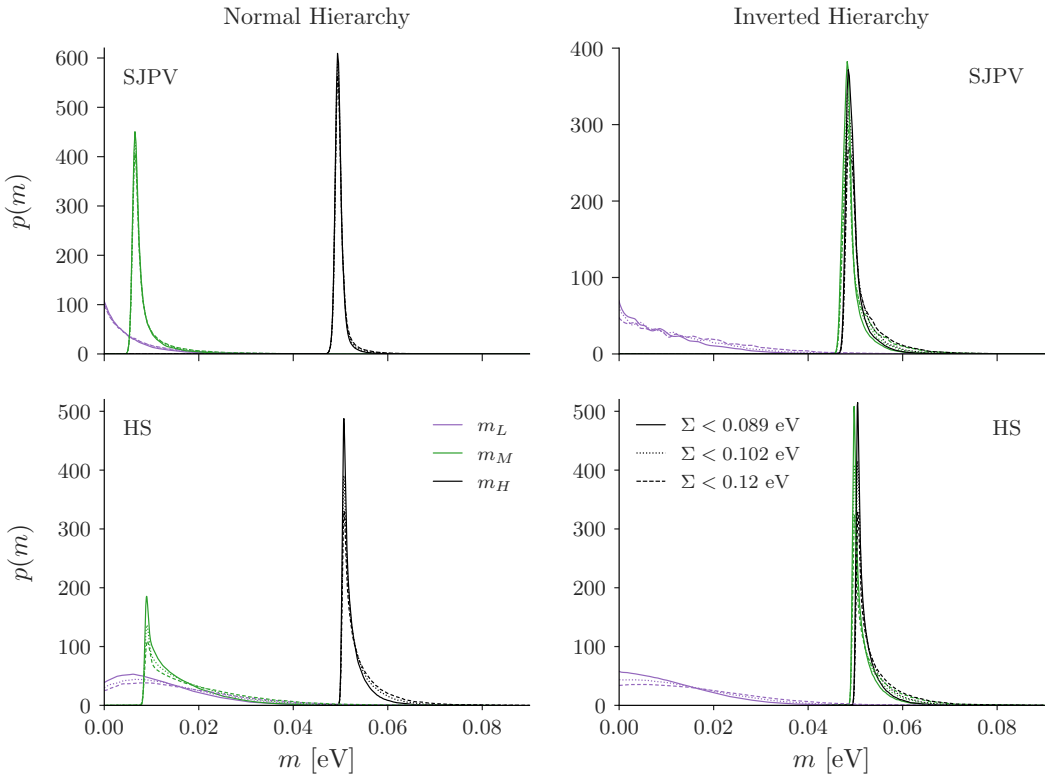

FIGURE 4.6: Posterior distributions $p(m_i) = P(m_i|D, M)$ for the individual masses and sensitivity to the adopted Σ limit for the NH (left) and the IH (right). Upper panels show the result with the SJPV prior, bottom panels the HS prior.

compared to the results from 2018 when the evidence was weak, this is driven by the $\Delta\chi^2$ obtained from the global fit of oscillations data. For the SJPV prior the evidence moves from "Strong" to "Decisive" even without accounting for the $\Delta\chi^2$ contribution, and is driven by the improved cosmological limit on the sum of the masses.

Finally, we report the posterior distributions for the individual masses and the sum of the masses for both NH and IH according to the two prior choices in Figures 4.6 and 4.7. The distributions of the individual masses are very similar for the two prior choices: once a hierarchy is chosen and the degenerate regime (where all the masses are much bigger than the splittings) is excluded by the constraints on Σ, the individual masses are determined by the oscillations constraints on the mass splittings (Eq. (4.4)). The probability distribution for the sum of the masses of course differs under NH or IH assumptions, but when taking the weighted sum of the two components the combined probability distribution for Σ is virtually indistinguishable from that for the NH for either prior choice. This reflects the fact that the evidence prefers the NH over the IH with odds greater than 100:1. The effect of the stronger Σ limit can be

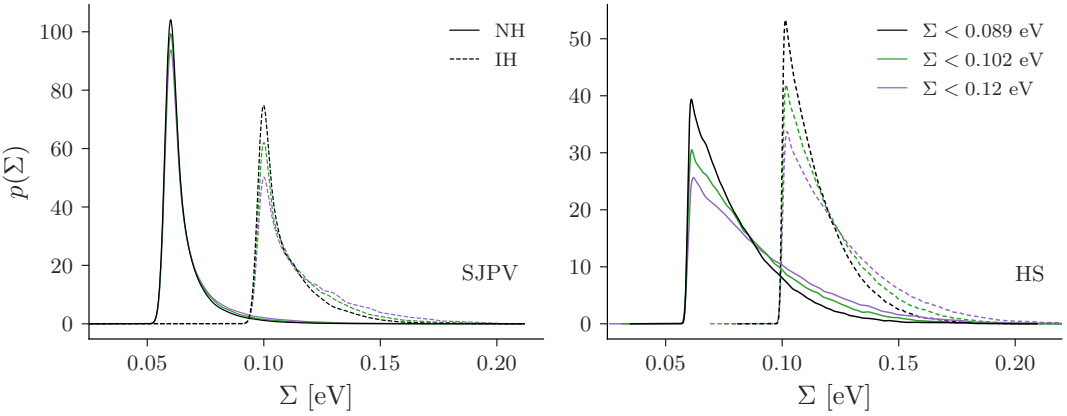

FIGURE 4.7: Comparison of the posterior distributions for the sum of the masses with the SJPV prior (left) and the HS prior (right). Dashed lines denote the IH, solid lines the NH. The weighted combined distribution for the two hierarchies is indistinguishable from that of the NH, because of the overwhelming odds.

appreciated by comparing our Figure 4.7 with Figure 8 of ref. [431], where a limit of $\Sigma < 6.9$ eV was adopted.

4.4 Sensitivity analysis

The above results are quite robust to variations over the baseline setup of Section 4.3; in a few cases these variations affect the results quantitatively but not qualitatively, which we discuss below. In ref. [277] results are also reported without the SK-atm constraints, in which case the constraints on $\Delta m^2_{3\ell}$ in Eq. (4.4) become

$$\Delta m^2_{3\ell} = m^2_3 - m^2_\ell = \begin{cases} 2.515\,(\pm 0.028) \times 10^{-3}\text{eV}^2, & \text{(NH)} \\ -2.498\,(\pm 0.029) \times 10^{-3}\text{eV}^2, & \text{(IH)} \end{cases} \quad (68.4\%\text{CL})\,. \quad (4.6)$$

The evidence ratios both with and without inclusion of SK-atm data for both prior choices are reported in Table 4.3. For each case, we report the resulting odds before and after including the $\Delta\chi^2$ normalisation from oscillations data. While the SK-atm data does not affect much the $\kappa_{\text{no}\Delta\chi^2}$, the effect on the $\kappa_{\Delta\chi^2}$ is major, ranging from 3.7 (no SK-atm) to 33 (with SK-atm). Both cases are reported for completeness, but we see no reason to exclude the SK-atm data set or the $\Delta\chi^2$ normalisation, and hence our baseline results include it.

The sensitivity of the posterior odds to the choice of interpretation of the cosmological constraints on Σ is presented in Table 4.4. Clearly, for a fixed 95% C.L. limit, there is some sensitivity to the assumed shape (i.e., location of the peak) of the probability distribution, but the evidence is always "Strong"

	NuFITv5.1 (no SK-atm)		NuFITv5.1 (SK-atm)	
SJPV	$\kappa_{\mathrm{no}\Delta_{\chi^2}}$	$K_{\mathrm{SJPV}}\,(\Delta^2_\chi = 2.6)$	$\kappa_{\mathrm{no}\Delta_{\chi^2}}$	$K_{\mathrm{SJPV}}\,(\Delta^2_\chi = 7.0)$
$\Sigma < 0.8$ eV (95%) [A]	4.9	18.1	5.3	174.8
$\Sigma < 0.12$ eV (95%) [B]	50.2	219.4	48.7	1607.4
$\Sigma < 0.102$ eV (95%) [C]	87.3	322.9	86.7	2861.5
$\Sigma < 0.099$ eV (95%) [D]	91.2	337.6	87.5	2888.6
$\Sigma < 0.089$ eV (95%) [E]	131.2	485.3	138.0	4553.8
HS	$\kappa_{\mathrm{no}\Delta_{\chi^2}}$	$K_{\mathrm{HS}}\,(\Delta^2_\chi = 2.6)$	$\kappa_{\mathrm{no}\Delta_{\chi^2}}$	$K_{\mathrm{HS}}\,(\Delta^2_\chi = 7.0)$
$\Sigma < 0.8$ eV (95%) [A]	1.1	4.0	1.2	38.1
$\Sigma < 0.12$ eV (95%) [B]	3.4	12.4	3.6	118.4
$\Sigma < 0.102$ eV (95%) [C]	4.1	15.2	4.3	143.4
$\Sigma < 0.099$ eV (95%) [D]	4.6	16.8	4.7	156.1
$\Sigma < 0.089$ eV (95%) [E]	6.4	23.3	7.4	244.2

TABLE 4.3: Bayesian evidence ratios with the SJPV and HS priors. As ref. [277] present results with and without including Super-Kamiokande atmospheric constraints, here we also report both cases for completeness. The upper limits on Σ are follows: A=KATRIN sensitivity limit [260], B=*Planck*+BAO [429], C=*Planck*+BAO+RSD [429], D=*Planck*+BAO+RSD+SNeIa [429] E=*Planck*+BAO+Ly-α [430].

Dataset	$\kappa_{\rm SJPV}$ ($\rm K_{SJPV}$)	$\rm K_{HS}$
Splitting constraints ($\Sigma < 6.9$ eV)	2.6 (85.8)	33
$\Sigma < 0.8$ zero-centred Gaussian	5.3 (175)	38
$\Sigma < 0.102$ Gaussian centred at -0.026 eV	74 (2442)	138
$\Sigma < 0.102$ zero-centred Gaussian	87 (2860)	143
$\Sigma < 0.099$ zero-centred Gaussian	88 (2900)	156
$\Sigma < 0.099$ Gaussian centered at 0.04 eV	43 (1419)	92
$\Sigma < 0.089$ zero-centred Gaussian	138 (4550)	244

TABLE 4.4: Bayesian evidence ratios for the baseline case but using different interpretations of the $\Sigma_{\rm cosmo}$ constraints (in eV, 95% C.L.). The rationale for centering the distribution at -0.026 eV is that this is suggested by ref. [429]; the other plausible alternative to centering the distribution at zero is to center the distribution at the minimum value allowed by oscillations $\Sigma \sim 0.04$ eV.

or "Decisive" once the $\Delta\chi^2$ is included. Excluding SK-atm on the other hand lowers the $\kappa_{\Delta\chi^2}$ by almost a factor of 10, from 33 to 3.7, but still larger than the 2018 (HS adopted) value of $\kappa_{\Delta\chi^2} = 1.5$.

4.5 Conclusions

Adopting the latest constraints on the sum of neutrino masses from cosmological observations and on the mass-squared splittings from ground-based oscillation experiments, we have computed the Bayesian evidence for the normal and inverted hierarchies in order to determine whether the current data shows a preference for a given neutrino mass ordering. Additionally, we have estimated the posterior distributions of the individual neutrino masses and the sum of the masses under each hierarchy. Our main conclusion is that new data prefer "Strongly" if not "Decisively" the normal hierarchy, with odds over 100:1 (ranging from 140:1 to over 2000:1 depending on the prior choice). Compared to similar analyses presented with older oscillation experiments constraints, this result is driven by two main effects: the increased $\Delta\chi^2$ from global fits to neutrino oscillations data; and the more stringent limits on the sum of neutrino masses from cosmology (obtained under the assumption of a ΛCDM model).

It is well known that the evidence calculation is sensitive to the prior choice. To demonstrate the robustness of this result we have considered two widely different priors: (i) a set of hyperpriors in logarithmic space on the individual neutrino masses, adopted in ref. [431] and (ii) the so-called "Objective Bayesian"

reference prior, linear in the individual masses, motivated in ref. [440] in order to make the prior as minimally informative as possible to the oscillations measurements. These two cases are at the extreme of possibilities for prior choices, and therefore bracket the range of results achievable with other (physical) choices of priors. While the exact numerical value for the evidence depends on the specific choice of prior and the adopted limit on the sum of the masses, we find that for the latest cosmological constraints[4] on the sum of the masses the evidence remains "Decisive" across these very different prior choices. For the HS prior, the cosmological constraints on the sum of the masses are crucial to push the Bayesian evidence above the "Decisive" threshold. It is important to bear in mind that cosmological constraints are well known to be model dependent; the quoted constraints on Σ degrade for non-standard cosmological models. There are examples in the literature (see e. g. [447–449] and references therein) where the choice of the prior leads to an evidence for the normal hierarchy weaker than reported here. This is achieved at the cost of having different prior distributions for the different individual masses. Physically this would imply that the three masses do not share a common origin and therefore that there are three different (yet undiscovered) mechanisms of mass generation for the different mass eigenstates.

Our findings update and corroborate the previous results of ref. [431] and significantly increase the Bayesian evidence for the normal hierarchy. This has important consequences for neutrino physics and experiments that search for neutrinoless double-beta decay. Current efforts aim at the ton-scale active material experiments, which are sensitive to the 10 meV scale in the effective neutrino mass of this decay. In light of the results of this work, the motivation for covering the inverted hierarchy scenario is diminished and the focus should shift to maximising the fraction of the normal hierarchy parameter space covered by a given experiment. Moreover, our results increase the incentive for future neutrinoless double-beta decay experiments that would further cover the parameter space for the NH, either due to their ability to scale up the mass of the decaying nucleus or because the choice of nucleus is favoured by a smaller decay half-life.

[4] In an otherwise standard ΛCDM cosmological model.

Chapter 5

Conclusions

Our understanding of the Universe has grown immensely in the last few decades, and much of this progress has been driven by the ever-increasing collaboration between the fields of cosmology, particle and astroparticle physics. Answers to the fundamental open questions that remain – such as the nature of dark energy, dark matter, and the origin of the Universe – will likewise be guided by a collective approach. Once considered a science with errors in the exponents [456], cosmology has reached an astonishing level of precision thanks to a suite of high accuracy measurements of the CMB anisotropies, the large-scale structure and distance measures from Type Ia supernovae. It is a remarkable feat of modern cosmology that observations of the Universe on the largest physical scales can be used to constrain the microscopic properties of fundamental particles such as neutrinos and dark matter. With this in mind, the research presented in this thesis motivates the potential of current and future cosmological data in providing insight into the nature of these elusive particles, which are key indicators of new physics beyond the SM and ΛCDM paradigms.

In the following, we summarise the main conclusions of these works and examine their relevance in the broader context of current developments in the field. We also discuss future prospects and potential avenues to follow up on these lines of research. To this end, we group our discussion along two main themes: DM and 21 cm LIM observations, and neutrino cosmology.

Dark matter and 21 cm cosmology

In the first part of this thesis, we studied the cosmological signatures of non-gravitational DM interactions – such as decay, annihilation, and scattering – relevant to broad classes of particle DM candidates that feature some coupling to SM particles. In particular, we explored the effects of such interactions on the thermal and ionization history of the Universe and the resulting impact on cosmological observables such as the 21 cm LIM signal from the dark

ages and cosmic dawn. The 21 cm signal offers a unique window to the post-recombination Universe, probing the cosmic dark ages prior to the formation of the first luminous objects ($z \sim 30$–1100) and the period directly following, once the first stars and galaxies have begun to form, known as cosmic dawn and the Epoch of Reionization (EoR) ($z \sim 5$–30).

In Chapter 2 (based on ref. [1]), we computed the effects of electromagnetic energy injection from DM decay and annihilation on the intergalactic medium during the cosmic dark ages and the resulting impact on the global 21 cm brightness temperature and the angular power spectrum of the 21 cm fluctuations from this epoch. We then estimated the potential to detect such a DM signature with future 21 cm LIM experiments, forecasting constraints for fiducial decay lifetimes and annihilation cross-sections allowed by current limits for the forthcoming SKA, an improved terrestrial SKA-like instrument (aSKA), and different realisations of a futuristic radio array on the lunar far-side (LRA). Our results show that while SKA may have some limited sensitivity, more advanced next-generation 21 cm LIM experiments will be an extremely powerful probe of DM decay and annihilation, with the potential to detect (or constrain) a signal many orders of magnitude weaker than current or maximal constraints from next-generation probes such as CMB-S4 [220]. Ground-based experiments' ability to observe the dark ages is limited, and are incapable of accessing redshifts much farther than $z \sim 30$. On the other hand, including observations of the 21 cm line fluctuations well beyond the end of the dark ages $z \gtrsim 30$ dramatically boosts the sensitivity; for the fiducial cases considered, we find huge constraining power comes from the ability to perform tomography utilising the information from many independent redshift slices. Such observations are only possible with an LRA-type experiment, located outside the Earth's ionosphere. Interestingly, we demonstrate that such an experiment would be able to explore much of the remaining viable parameter space for a thermal relic WIMP with mass up to $\sim \mathcal{O}(10^4)$ GeV. Moreover, this would also cover (almost all of) the parameter space invoked for the DM annihilation interpretation of the *Fermi*-LAT Galactic Centre γ-ray excess [385, 457–463], potentially settling the ongoing debate on the millisecond pulsar versus DM origin of this signal.

The results of Chapter 2 strongly motivate the science case for more advanced 21 cm LIM experiments that could observe deep into the dark ages prior to the formation of the first stars. While ambitious, the discovery potential of such experiments is huge; free from astrophysical contamination, the 21 cm signal from the dark ages is an extremely sensitive and pristine probe of exotic physics such as DM interactions and PBHs [343, 344, 464]. Moreover,

the highly redshifted 21 cm fluctuations provide access to orders of magnitude more modes of the matter density field than other observables [465] and probes the early Universe when small-scale perturbations remain mostly in the linear regime. This supports precision tests of fundamental cosmology such as the inflationary paradigm [339–341, 466] and non-gaussianity [342, 467, 468], isotropy and homogeneity [469], and cosmological parameters constraints on, e. g., curvature and neutrino masses [466]. Targeting the 21 cm LIM signal from the dark ages is extremely challenging, however. The signal from the dark ages is redshifted to low frequencies at which the Galactic synchrotron foregrounds are many orders of magnitude brighter. Moreover, the Earth's ionosphere is opaque to low-frequency radio waves ($\lesssim$ 45 MHz) which necessitates observations made from space, with the radio-quiet lunar far-side being the most promising option. Therefore, future work is crucially needed to overcome the technical challenges of foreground removal as well as developing the theoretical modelling and computational techniques (e. g. simulation, data analysis) to fully exploit the cosmological information from 21 cm measurements. The forecasts presented in Chapter 2 assume a comprehensive characterisation of the relevant foregrounds is possible; a more realistic assessment of how the foreground subtraction may affect the detectability is thus an important point for future work. The arrival of data from the current generation of 21 cm experiments targeting the EoR and cosmic dawn is an essential step in this direction, which will help characterise the low-frequency radio sky and improve foreground modelling, allowing for better exploration of cosmological constraints. Furthermore, extending our analysis to lower redshift ranges would be interesting for these experiments happening on a shorter timescale, although added complications due to astrophysics and degeneracy with other signals would arise. Finally, it could be interesting to evaluate the effect of DM decay and annihilation on the temperature perturbations, as we do in Chapter 3 for DM-baryon scattering models.

In Chapter 3 (based on ref. [2]), we considered the cosmological effects of velocity-dependent elastic scattering between DM and baryons in the post-recombination Universe. Such interactions received a lot of attention in wake of the anomalous EDGES 21 cm measurement [407], which exhibits a much larger than expected absorption signal and could be explained by a small fraction of millicharged DM [107, 198, 404]. However, strong constraints have been placed on the millicharged DM interpretation [107–109] and the EDGES measurement

awaits confirmation from other experiments.[1] Nonetheless, many DM models predict elastic scattering with baryons which imprints signatures on the thermal history of the Universe and the matter clustering at small scales, and is expected to modify the 21 cm signal from the dark ages and cosmic dawn [107–109, 198, 393, 394, 404–406]. However, the direct contribution of the DM-baryon interactions on the perturbed baryon gas and DM temperatures had previously been neglected. The 21 cm intensity mapping signal directly depends on the gas temperature perturbations, so it is critical to understand these effects.

In this work we derived these contributions for the first time, evolved the cosmological perturbations until the end of the dark ages and show that they may have a significant impact at the beginning of cosmic dawn. In particular, we found that the amplitude of the temperature power spectrum at large scales can change by an order of magnitude and that the matter power spectrum is further suppressed with respect to ΛCDM by $\sim$ 5–10% at $k \sim 200\,\mathrm{Mpc}^{-1}$ compared to the computation ignoring these contributions, for scattering cross sections at current CMB limits. These results have important implications for cosmological observables sensitive to the gas temperature and the abundance of light collapsed objects. The modified temperature perturbations and the suppression of small-scale density perturbations can affect both the amplitude and time evolution of the 21 cm signal during cosmic dawn. The further suppression of the matter clustering occurs at the scales of interest for the formation of the DM halos that could host the first stars and thus may delay the cosmic dawn even more than originally predicted by first estimates that neglected these effects, which should have a strong impact in the 21 cm LIM signal. As such, the inclusion of the novel temperature perturbations derived in this work is required to properly model the initial conditions for cosmic dawn in the presence of DM-baryon scattering, and may provide forthcoming 21 cm observations with additional sensitivity to these models. As a case example, we computed the 21 cm power spectrum from the dark ages and found that the new contributions can modify the amplitude of the power spectrum by up to a factor of a few at high redshift ($z > 30$), which further promotes the science case for next-generation LIM experiments targeting this epoch.

The 21 cm fluctuations from cosmic dawn and EoR are expected to be especially sensitive to DM microphysics, both to DM-baryon interactions as well as other exotic models such as warm DM, fuzzy DM or dark sector interactions. Thus, an accurate and complete modelling of all relevant effects in each

[1] The latest measurements from the SARAS experiment is inconsistent with the EDGES signal, disfavouring the interpretation in terms of new physics [470].

case is of the utmost importance to potentially distinguish between different DM models. The results of our work must be taken into account when setting the initial conditions for cosmic dawn in the context of DM-baryon scattering models, and strongly motivate further investigation into how these effects would impact the evolution of the cosmic dawn signal at lower redshift ($z < 30$) in anticipation of coming measurements of the 21 cm signal from this epoch. Once the first stars switch on they will dominate the heating of the medium, and a detailed study of the non-trivial interplay between the DM-baryon scattering effects and astrophysical processes is needed. This is a future research direction we are already pursuing, with the aim of implementing the novel contributions to the temperature perturbations in `21cmFAST`[2] [471, 472] in order to model the effects on the 21 cm signal during cosmic dawn and examine the sensitivity of upcoming measurements of the 21 cm power spectrum (HERA [410], SKA [411]) and the global signal (EDGES [407], LEDA [409], SARAS [473]) to constrain DM-baryon scattering. A significant challenge will be to separate the astrophysics of cosmic dawn and reionization from the cosmological information. Several promising strategies are being developed in this regard, including improved theoretical modelling of the complex astrophysics [474, 475], more flexible parameterisation in semi-numerical codes [476] as well as machine learning techniques [477]. Additionally, small-scale effects of DM on the matter power spectrum may be probed through their imprint on large scales which are expected to be more robust to astrophysical uncertainties [232, 416, 478–480].

The highly-redshifted cosmological 21 cm signal represents just one of the promising avenues to identify the fundamental nature of DM with cosmology in the coming decade. Cosmological observations offer a way to probe DM properties on a vast range of physical scales and throughout cosmic history; as such, they can offer insight into processes relevant at energy, time and length scales inaccessible from Earth. The next-generation of LSS and CMB data will significantly increase the sensitivity to a wide range of DM interactions and models, both interactions with SM particles (annihilation, decay, or scattering) and within the dark sector itself (self-interactions, dark radiation) as well as other beyond-CDM models such as warm DM, fuzzy DM and PBHs. The arrival of these even higher precision cosmological observations will complement the ongoing searches for DM in other astrophysical probes and terrestrial experiments. All strategies must be fully exploited in the hunt for DM, which has thus far evaded all pursuit. The synergy between all these different experimental avenues to search for DM will be the keystone for the eventual discovery of

[2] `https://github.com/21cmfast/21cmFAST`

DM and characterisation its properties.

Neutrino masses and the mass hierarchy

In Chapter 4 (based on ref. [3]), we performed a Bayesian analysis using the latest constraints on the sum of neutrino masses from cosmology and the squared mass splittings from global fits to neutrino oscillations data. We sought to answer the question of whether the current data shows a preference for one of the neutrino mass hierarchies. To do so, we performed a Bayesian model comparison study, computing the Bayesian evidence for each mass ordering. The topic of a suitable prior choice in the context of the mass hierarchy has been the subject of much debate in the literature [431, 440–446]; therefore, we chose to perform our analysis considering two priors at opposite ends of this debate. Firstly, we followed ref. [431] and adopted a hierarchical prior which previously found evidence in favour of the NH with odds of 40:1. On the other hand, we compared this to the so-called "Objective Bayesian" prior used in ref. [440]; the 2018 analysis performed in this work showed no strong preference for the NH under this prior. In light of more recent data, we re-analysed the evidence for the NH and found that – while the numerical value for the evidence depends on the choice of prior – the Bayesian odds now remain greater than 100:1 across these very different prior choices. This is driven by two factors: (i) stronger preference for the NH has arisen from the latest global fit to neutrino oscillations data, giving an increased $\Delta\chi^2$ value and (ii) tighter cosmological constraints on Σm_ν have been obtained, which are critical in pushing the evidence for NH above the "Strong" or "Decisive" threshold in the case of the Objective Bayesian prior.

Our results demonstrate that even under widely different priors, the current combination of data now shows strong (or even decisive) Bayesian evidence for the NH (as foreseen by ref. [431]). Regardless of the ongoing debate on prior choices, it appears clear that the data is converging towards the NH. Forthcoming cosmology surveys are expected to reach the sensitivity for a guaranteed detection of the absolute neutrino mass scale. If the NH is really the true one, as our analysis suggests, then it should be possible to decisively exclude the IH with cosmological data in the coming decade. However, our results have immediate implications for the discovery potential of planned and future neutrinoless double-beta decay ($0\nu2\beta$) experiments and strongly motivate experimental design targeting the parameter space available for the normal mass ordering [433].

Currently, cosmological data provides the strongest upper limits on the absolute neutrino mass scale but is as yet unable to provide a categorical detection of Σm_ν. However, this is likely to change with next-generation experiments

which are expected to provide the first definitive measurement of Σm_ν. Combinations of next-generation CMB lensing data (CMB-S4, Simons Observatory) with forthcoming data from LSS surveys (DESI-BAO) are projected to reach a sensitivity of $\sigma(\Sigma m_\nu) \sim 0.03$ eV, assuming the current measurements of the reionization optical depth τ [220, 221]. Moreover, future LSST galaxy clustering and lensing data can reach a similar precision [481]. This would correspond to a 2σ detection of the minimum mass sum allowed from oscillation experiments ($\Sigma m_\nu = 0.06$eV). However, a better determination of τ – possible with experiments targeting the large-angular scale CMB E-modes, such as CLASS [482], BFORE [483], LiteBIRD [484] and PICO [485] – would greatly improve the sensitivity, enabling a $\sim 3\sigma$ detection of $\Sigma m_\nu = 0.06$ eV (or a $\sim 6\sigma$ detection of $\Sigma m_\nu = 0.01$ eV, the minimum mass allowed in the IH). Furthermore, 21 cm measurements can also be very powerful for cosmological parameter estimation; ref. [466] forecasts a neutrino mass sum measurement to within ~ 0.007 eV.

The current and forecasted constraints assume the ΛCDM model. While data are consistent with a cosmological constant ($w = -1$) and a flat Universe, departures from ΛCDM such as dynamical dark energy (time-varying w) models or non-zero curvature are not excluded [486] and can have a degenerate effect on the expansion rate of the Universe and the matter clustering as massive neutrinos. It has been shown that when allowing for a time-varying dark energy equation of state, cosmological constraints on Σm_ν can degrade significantly [276] (and vice-versa, allowing Σm_ν to be a free parameter loosens the constraints on w [481]). These degeneracies can be alleviated with combinations of future CMB and LSST data [487]. Ref. [488] provides a comprehensive study of the forecasted sensitivity of a large number of different combinations of future CMB and LSS datasets, finding that a high significance measurement of the neutrino mass sum is still very likely under both minimal ΛCDM and its typical extensions with forthcoming surveys.

A concrete measurement of the neutrino mass sum from cosmology would have deep implications for particle physics and would be highly complementary to laboratory experiments targeting the absolute neutrino mass scale (which are sensitive to different combinations for individual masses and mixing parameters). The results of our work indicate a strong preference for the NH, and a definitive confirmation of this from a measurement of $\Sigma m_\nu < 0.1$ from future surveys would decisively exclude the IH. Determining Σm_ν and the hierarchy will inform both the fundamental theory behind the neutrino mass generation as well as the discovery prospects of current and planned $0\nu2\beta$ experiments [282,

433, 434]. Future $0\nu2\beta$ experiments may achieve a discovery sensitivity competitive with cosmology [282], while the ongoing KATRIN β-decay experiment is projected to reach a sensitivity of $m_\beta < 0.2$ eV ($m_\beta < 0.04$ eV projected for the final phase of Project8 [489]). Furthermore, future long-baseline oscillations experiments such as DUNE [490–492] aim to determine the sign of the atmospheric mass splitting and therefore the mass ordering. The complementarity between these different datasets will provide an important consistency check; if significant tensions arise between cosmological data and the other probes, it may signify new physics and can be an important guidepost for cosmology beyond ΛCDM.

Appendix A

Supplementary Results: Dark Matter Decay and Annihilation

A.1 Reionization modelling

In Chapter 2 we focus on the dark ages before the formation of the first stars, but given the large uncertainties around the reionization epoch, we consider how the modelling of the reionization might affect the 21 cm signal at $z \gtrsim 30$ and thereby our results. While the physics of reionization is poorly constrained, a new generation of upcoming experiments such as the Hydrogen Epoch of Reionization Array (HERA [410]), James Webb Space Telescope (JWST [493]) and the Dark Ages Radio Explorer (DARE [494]) will soon start to explore this period of the cosmos. To date we have only weak upper limits on the redshift of reionization and its physical processes. Nevertheless, we know the low-redshift Universe is fully ionized (by around $z \sim 8$), and this process is thought to be mostly due to the astrophysical processes of the first luminous sources.

The standard procedure (e. g., widely assumed for CMB power spectra analyses) is to model the transition to a fully ionized Universe with a single-step half-hyperbolic tangent function. This is unrealistic, and only modifies x_e while leaving the evolution of the inter-galactic medium temperature unchanged without any treatment of how the astrophysical sources of reionization also heat the kinetic gas temperature T_k. We follow the approach of ref. [357], adopting their simple model of stellar reionization and implementing it into `CosmoRec`. A source term is added to the x_e evolution equation (Eq. 2.9 in Section 2.3.1) that accounts for Lyman continuum photons from UV sources in star-forming galaxies, thought to be a primary source of reionization. In addition to the ionizing radiation, a source term is added to the kinetic gas temperature evolution equation (Eq. 2.13 in Section 2.3.1) to account for the extra heating of the intergalactic medium due to e. g. X-rays from the stellar population. We refer

the reader to ref. [357] for a detailed description. Additional collisional cooling terms are added following ref. [495].

Unless otherwise stated, all results shown in Chapter 2 are computed assuming this stellar reionization model. We found no significant change in our results from using the standard `CLASS` prescription for reionization, indicating that the 21 cm signal measured from the dark ages should be largely insensitive to the reionization process. Nonetheless, the extra ionization and heating of the IGM might advance the formation of the first stars, increasing the redshift at which the dark ages would end. We leave the exploration of the impacts of this relation for future work. However it has been shown that DM annihilation cannot be a dominant contribution to cosmic reionization if it is to be consistent with CMB results [357], requiring an overly large annihilation rate or halo boost. It is shown in Ref. [334] that for the most part DM cannot contribute by more than 10% to reionization.

A.2 21 cm forecast results

A.2.1 Decaying DM

Experiment	Redshift range	Efficiency factor	Relative Error σ_τ/τ		
			$\tau = 1\times10^{25}$	$\tau = 1\times10^{26}$	$\tau = 1\times10^{27}$
SKA	$z = 30$	$f_{\rm eff} = 0.1$	1.43×10^{2}	1.89×10^{3}	1.01×10^{4}
		$f_{\rm eff} = 0.4$	1.45×10^{2}	5.56×10^{2}	2.3×10^{3}
aSKA	$z = 30$	$f_{\rm eff} = 0.1$	1.70×10^{-2}	5.88×10^{-2}	6.07×10^{-1}
		$f_{\rm eff} = 0.4$	3.79×10^{-2}	1.84×10^{-2}	1.11×10^{-1}
LRA1	$z = 30$	$f_{\rm eff} = 0.1$	2.42×10^{-1}	2.89	1.65×10^{1}
		$f_{\rm eff} = 0.4$	2.75×10^{-1}	8.63×10^{-1}	3.62
	$30 < z < 200$	$f_{\rm eff} = 0.1$	5.46×10^{-2}	3.21×10^{-1}	1.0
		$f_{\rm eff} = 0.4$	1.32×10^{-1}	2.56×10^{-1}	1.11
LRA2	$z = 30$	$f_{\rm eff} = 0.1$	1.52×10^{-2}	3.17×10^{-2}	4.04×10^{-1}
		$f_{\rm eff} = 0.4$	3.52×10^{-2}	1.04×10^{-2}	7.19×10^{-2}
	$30 < z < 200$	$f_{\rm eff} = 0.1$	3.84×10^{-3}	5.15×10^{-3}	1.73×10^{-2}
		$f_{\rm eff} = 0.4$	8.24×10^{-3}	4.71×10^{-3}	1.18×10^{-2}
LRA3	$z = 30$	$f_{\rm eff} = 0.1$	1.41×10^{-2}	1.34×10^{-2}	2.60×10^{-1}
		$f_{\rm eff} = 0.4$	3.18×10^{-2}	5.55×10^{-3}	4.70×10^{-2}
	$30 < z < 200$	$f_{\rm eff} = 0.1$	1.63×10^{-3}	1.72×10^{-3}	5.28×10^{-3}
		$f_{\rm eff} = 0.4$	2.27×10^{-3}	7.32×10^{-4}	2.91×10^{-3}

TABLE A.1: Forecasted 68% C.L. relative errors on the lifetime τ for each fiducial parameterisation and experimental set-up measuring the 21 cm angular power spectrum.

A.2.2 Annihilating DM

Experiment	Redshift range	Boost Factor	Relative Error $\sigma_{p_{\rm ann}}/p_{\rm ann}$	
			$p_{\rm ann} = 1.9 \times 10^{-7}$	$p_{\rm ann} = 1.9 \times 10^{-8}$
SKA	$z = 30$	Smooth	7.07×10^{3}	5.57×10^{4}
		$f_h = 1 \times 10^{6}$	5.54×10^{3}	-
		$f_h = 1 \times 10^{8}$	1.9×10^{3}	-
aSKA	$z = 30$	Smooth	4.18×10^{-1}	4.47
		$f_h = 1 \times 10^{6}$	3.13×10^{-1}	-
		$f_h = 1 \times 10^{8}$	5.32×10^{-2}	-
LRA1	$z = 30$	Smooth	11.33	9.35×10^{1}
		$f_h = 1 \times 10^{6}$	8.82	-
		$f_h = 1 \times 10^{8}$	2.93	-
	$30 < z < 200$	Smooth	4.50×10^{-1}	1.58
		$f_h = 1 \times 10^{6}$	5.11×10^{-1}	-
		$f_h = 1 \times 10^{8}$	9.42×10^{-1}	-
LRA2	$z = 30$	Smooth	2.91×10^{-1}	3.39
		$f_h = 1 \times 10^{6}$	2.41×10^{-1}	-
		$f_h = 1 \times 10^{8}$	2.65×10^{-2}	-
	$30 < z < 200$	Smooth	6.45×10^{-3}	2.28×10^{-2}
		$f_h = 1 \times 10^{6}$	6.78×10^{-3}	-
		$f_h = 1 \times 10^{8}$	6.80×10^{-3}	-
LRA3	$z = 30$	Smooth	2.15×10^{-1}	2.37
		$f_h = 1 \times 10^{6}$	1.54×10^{-1}	-
		$f_h = 1 \times 10^{8}$	7.88×10^{-3}	-
	$30 < z < 200$	Smooth	1.75×10^{-3}	5.70×10^{-3}
		$f_h = 1 \times 10^{6}$	1.76×10^{-3}	-
		$f_h = 1 \times 10^{8}$	1.35×10^{-3}	-

TABLE A.2: Forecasted 68% C.L. relative errors on the annihilation efficiency $p_{\rm ann}$ for each fiducial parameterisation and experimental set-up measuring the 21 cm angular power spectrum.

A.2.3 Non-detection limits

The upper limits for the decay lifetime are only valid for an energy injection of $f_{\rm eff} = 0.1$ (which roughly corresponds to 100 GeV decay to electron-positrons).

Experiment	τ (95% C.L.)	$p_{\rm ann}$ (95% C.L.)
SKA	$> 9.7 \times 10^{22}$ s	$< 1.9 \times 10^{-4}\,\mathrm{m^3 s^{-1} kg^{-1}}$
aSKA	$> 1.9 \times 10^{27}$ s	$< 9.3 \times 10^{-9}\,\mathrm{m^3 s^{-1} kg^{-1}}$
LRA1	$> 1.3 \times 10^{27}$ s	$< 1.9 \times 10^{-8}\,\mathrm{m^3 s^{-1} kg^{-1}}$
LRA2	$> 7.4 \times 10^{28}$ s	$< 2.7 \times 10^{-10}\,\mathrm{m^3 s^{-1} kg^{-1}}$
LRA3	$> 2.2 \times 10^{29}$ s	$< 7.4 \times 10^{-11}\,\mathrm{m^3 s^{-1} kg^{-1}}$

TABLE A.3: Forecasted 95% C.L. lower (upper) bounds on the DM decay lifetime (annihilation efficiency) for each experimental set-up measuring the 21 cm angular power spectrum.

A.3 Comparison to specific decay channels

We compare our generic approach of a constant effective efficiency parameter using the on-the-spot treatment to a more precise energy injection history for a few specific decay masses and channels. For the chosen decay channels and masses, we fit $f_{\rm eff}(z)$ to the predictions from Ref. [368].

As exemplified in Figure A.1, the amount of energy injection can vary greatly for a given lifetime, when the DM mass or decay channel is varied. For the three cases explored here, we find around ~ 1 order of magnitude variation in the forecasted relative errors for LRA, see Table A.4. The forecasted errors at $z = 30$ can vary by almost 3 orders of magnitude between the most extreme cases. The results we found for $f_{\rm eff} = 0.1$ correspond roughly to 100 GeV decay to electron–positron pairs ($\chi \to e^+e^-$). However, for a 100 GeV particle decaying to photons only, the projected sensitivity is significantly weaker. Yet even in this case with minimal energy injection, LRA3 could reach almost percent-level precision constraints. On the other hand, there are decay scenarios which can inject much more energy than what our fiducial $f_{\rm eff} = 0.1$ describes e. g. 100 MeV $\chi \to e^+e^-$, and so 21 cm LIM will be even more powerful to constrain certain cases. Therefore, our choice remains as a conservative assumption, not too optimistic nor pessimistic, given the different predictions across the available parameter space. Nevertheless, the main conclusions still hold: observations of the 21 cm power spectrum at $z = 30$ alone are unlikely to yield a S/N of unity for DM decay, except in decay cases where the energy injection is near maximal. In most cases, and especially to probe the longest decay lifetimes, reaching percent or sub-percent precision will require a lunar radio array with the ability to perform tomography during the cosmic dark ages. 21 cm LIM tomography with LRA will have the power to improve upon CMB constraints by several orders of magnitude - and for some decay channels, by even more than

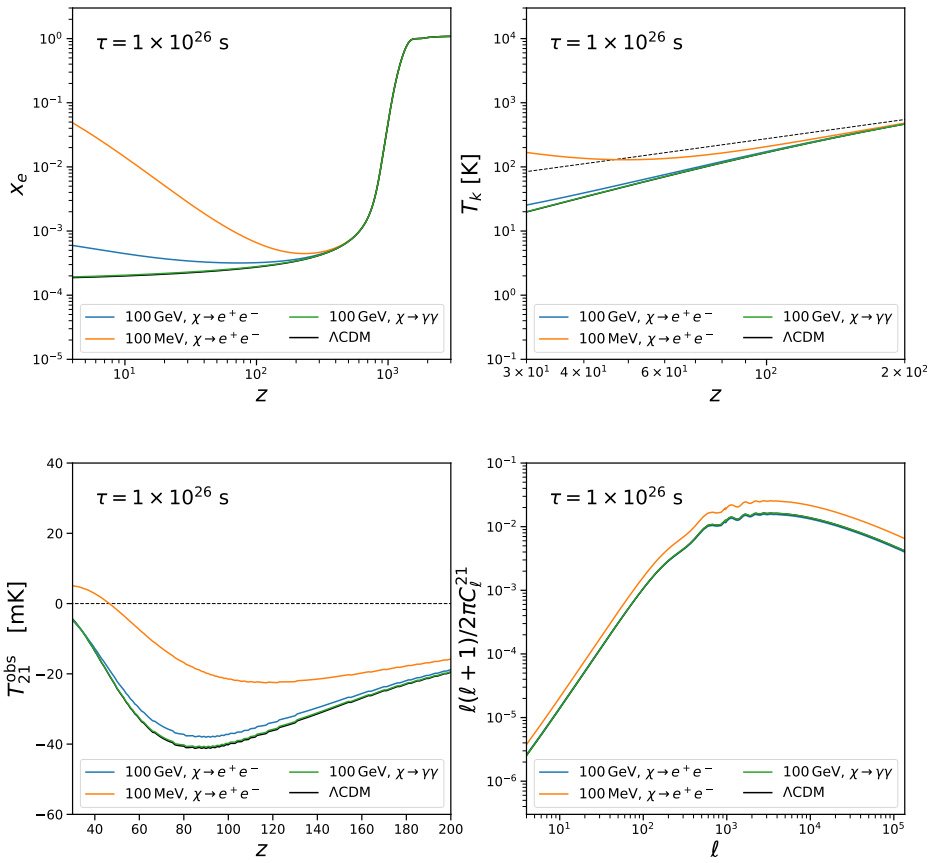

FIGURE A.1: Evolution of free electron fraction x_e (*top left*), gas temperature T_k (*top right*), and global T_{21} signal (*bottom left*) with redshift, and the angular power spectrum of the 21 cm fluctuations at $z = 30$ (*bottom right*), for 3 example DM decay channels with a decay lifetime $\tau = 1 \times 10^{26}$ s.

shown in our main results. The fact that the results are sensitive to the precise energy injection history demonstrates that the 21 cm power spectrum could be a powerful tool not only to detect a decay signal, but also constrain the DM particle properties, provided that potential degeneracies can be accounted for. A more detailed analysis, computing the $f(z)$ functions over the whole redshift range (using e. g. `DarkHistory` [372] or `ExoCLASS` [392]) will be necessary once 21 cm data is realised in order to determine constraints on specific decay channels and masses.

In the case of annihilating DM, we do not assume a value for the efficiency factor f_{eff}, as all the model-dependence of the energy injection rate is condensed into the annihilation efficiency parameter p_{ann}. While it has been shown that a constant energy injection rate can capture with high precision the effect of DM annihilation on the CMB [186, 298, 312, 317, 496], whether this approach is sufficient to describe the impact on the 21 cm fluctuations during the dark

ages needs to be evaluated. Given the proof-of-concept nature of this work, we expect the uncertainties introduced by this assumption to be sub-dominant, but the validity of this approach should be revisited with a calculation of the redshift-dependent $f(z)$ (or $p_{\rm ann}(z)$) curves once precision 21 cm measurements are made possible. This is especially important at low redshifts when including the effects of structure formation where the energy deposition curves can change substantially [368].

Experiment	Redshift	Relative Error σ_τ/τ : $\tau = 1 \times 10^{26}$ s		
		100 MeV $\chi \to e^+e^-$	100 GeV $\chi \to e^+e^-$	100 GeV $\chi \to \gamma\gamma$
SKA	$z = 30$	1.14×10^{2}	4.10×10^{3}	1.04×10^{5}
aSKA	$z = 30$	1.15×10^{-2}	2.42×10^{-1}	2.90
LRA1	$z = 30$	1.90×10^{-1}	6.56	1.70×10^{2}
	$30 < z < 200$	6.19×10^{-2}	6.07×10^{-1}	5.06
LRA2	$z = 30$	1.05×10^{-2}	1.59×10^{-1}	1.23
	$30 < z < 200$	4.23×10^{-3}	8.28×10^{-3}	7.15×10^{-2}
LRA3	$z = 30$	1.01×10^{-2}	1.05×10^{-1}	3.67×10^{-1}
	$30 < z < 200$	1.60×10^{-3}	2.12×10^{-3}	1.80×10^{-2}

TABLE A.4: Forecasted 68% C.L. relative errors for 3 example decay channels with a lifetime $\tau = 1 \times 10^{26}$ s for each experimental set-up measuring the 21 cm angular power spectrum.

Appendix B

Supplementary Results: Dark Matter-Baryon Scattering

Here we present some additional results which supplement the main results of Chapter 3. Our main results are shown at $z = 30$, which we assume to be the end of the dark ages, but here we include results also at $z = 50$. Moreover, in our main results we set the scattering cross-section to the current limits allowed by CMB measurements, and always assume that 100% of the DM scatters with baryons; here we explore the effects of varying these parameters.

B.1 Results at $z = 50$

In the main body of Chapter 3 we show results at $z = 30$ which we consider to mark the end of the dark ages and the beginning of cosmic dawn. However, as demonstrated in Figure 3.2, there are significant changes to the temperature and ionization fraction perturbations during much of the redshift range of the dark ages. We highlight here that there are important effects beyond $z > 30$ which, given the astrophysical uncertainties surrounding early stellar formation, may be relevant for modelling the initial conditions of cosmic dawn at higher redshift. Figures B.1 and B.2 are analogous to figures 3.3 and 3.4, but shown for $z = 50$.

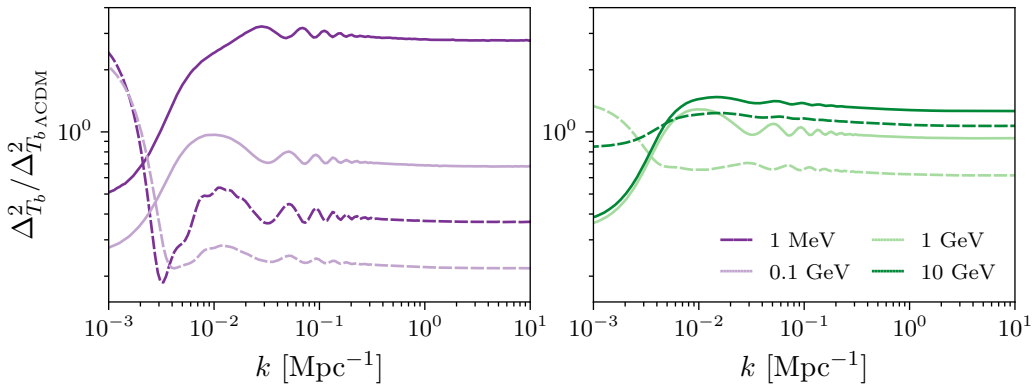

FIGURE B.1: Ratio of the linear power spectra (with respect to ΛCDM) of the gas temperature fluctuations at $z = 50$ for several DM masses, including (solid) and neglecting (dashed) fluctuations sourced by DM-baryon interactions, shown until $k = 10\,\mathrm{Mpc}^{-1}$.

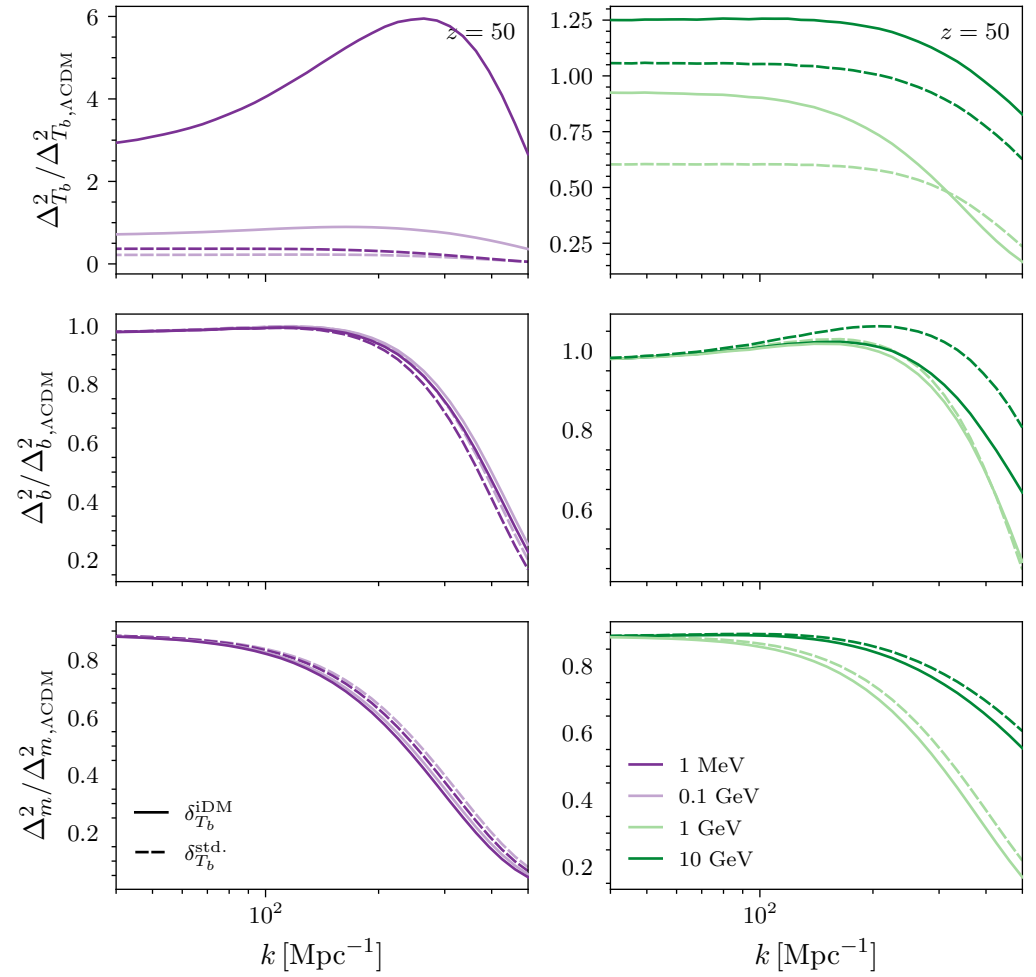

FIGURE B.2: Ratio (with respect to ΛCDM) of small-scale power spectra of baryon temperature (top), baryon density (middle) and matter density (bottom) fluctuations at $z = 50$ for scales $k = 40$–$500\,\mathrm{Mpc}^{-1}$. We compare the result when including (solid) and neglecting (dashed) additional contributions to perturbed recombination from DM-baryon interactions for each DM mass.

B.2 Varying scattering cross-section and the fraction of interacting DM

Throughout Chapter 3 we show results for the case where all of the dark matter interacts with baryons and adopt a benchmark value of σ_0 for each DM mass, consistent with the 95% C.L. upper limits derived in refs. [196–198]. In this appendix we vary these parameters, considering different values of σ_0 and small fractions of strongly interacting DM f_χ. Note that the results here are obtained assuming the background temperature evolution computed in CLASS, without averaging the thermal history over the full initial relative velocity distribution, as was done for our main results. Therefore these results may differ quantitatively from that when taking into account this effect; however, this limited example reveals qualitative trends when varying σ_0 or f_χ. We leave a more accurate and complete exploration of this case for future work.

In Figure B.3 we show how results change when reducing the strength of the interaction cross section by a numerical factor below the current upper limit for $m_\chi = 1$ GeV. We find that as we reduce σ_0, there is an intermediate range where the change in the amplitude of the temperature power spectrum at $z = 30$, with respect to neglecting temperature perturbations sourced by DM-baryon scattering, actually increases significantly before decreasing again. This is due to how the evolution of the temperature perturbations δ_{T_b} depends on the different contributions in eq. (3.15); varying the cross section alters the balance of these competing terms and can result in either more or less enhancement or suppression of the temperature perturbations, depending on the redshift. For example, for an interaction cross section set at 80% of our benchmark σ_0, we find that the temperature power spectrum is suppressed by almost an order of magnitude at $z = 30$. This also has an impact in the large-scale HI power spectrum; the amplitude of the HI signal becomes suppressed by $\sim 25\%$ at $z = 30$ relative to neglecting the DM-baryon scattering effects on the temperature perturbations (compared to $\sim 15\%$ for our benchmark σ_0).

On the other hand, the amount of extra suppression in the total matter power spectrum due to the DM-baryon interaction contribution to the perturbations scales inversely with σ_0. For a cross section one order of magnitude weaker than current limits, there is an additional suppression of a ∼few % in the total matter power spectrum at $k = 200\,\mathrm{Mpc}^{-1}$.

Lastly, we also consider how our results change when only a fraction f_χ of the total DM density is interacting; in this regime larger values of the cross section are allowed for small interacting fractions. In Figure B.4 we show results for

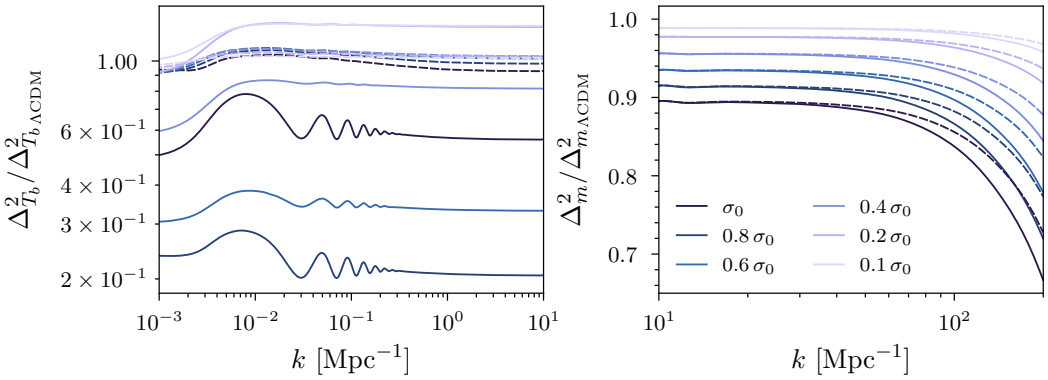

FIGURE B.3: Effect of varying the scattering cross section for a DM mass of 1 GeV on the large-scale baryon temperature power spectrum (left) and the small-scale total matter power spectrum (right) at $z = 30$. We compare the result when including (solid) and neglecting (dashed) the additional contributions to perturbed recombination resulting from the DM-baryon interactions for several values of σ_0 below the 95% C.L. upper limit given in Table 3.1.

various fractions with σ_0 set to the corresponding 95% C.L. upper limit derived in ref. [196] for a mass of 1 MeV (reported in Table B.1).

For $f_\chi \gtrsim 2\%$ the limit on σ_0 roughly scales with f_χ. In this regime, we find that the amount of extra suppression in the matter power spectrum declines with smaller f_χ. On the other hand, the amplification of the temperature perturbations can be substantially increased; e. g., for $f_\chi = 0.1$, the large-scale temperature power spectrum is enhanced by almost an order of magnitude at $z = 30$ when fully accounting for all contributions to perturbed recombination. The difference in scale of the impact on the baryon temperature and the matter power spectra can be explained as follows. As shown in Figure 3.2, each contribution to the gas temperature depends indirectly on the rest and the evolution with redshift is much richer than when only Compton heating is considered. Therefore, even if only a small part of the DM interacts, the change can be very large. However, the effect on the total matter density decreases significantly because the temperature of the (interacting) dark matter now only affects a small fraction of the total dark matter.

The sensitivity of CMB constraints to DM-baryon interactions degrades significantly for very small interacting fractions (below $f_\chi \sim 0.4\%$ [196]), and large values of σ_0 are permitted for which the interacting sub-component of DM is tightly coupled to the baryons. In this regime, we find there can still be considerable modifications to the baryon temperature perturbations (for $f_\chi = 0.3\%$, suppressed by almost a factor of ~ 100 at $z = 30$), while the BAO feature is markedly enhanced. Moreover, for such small tightly coupled fractions, the

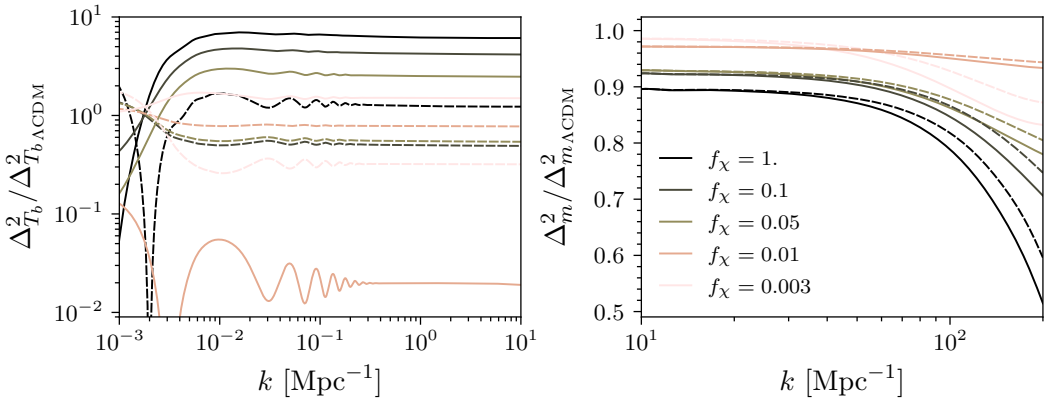

FIGURE B.4: Effect of varying the interacting fraction of DM f_χ for a DM mass of 1 MeV, with σ_0 set to the respective 95% C.L. upper limits derived in ref. [196] (see Table B.1). We show the large-scale baryon temperature power spectrum (left) and the small-scale total matter power spectrum (right) at $z = 30$, comparing the result when including (solid) and neglecting (dashed) the additional contributions to perturbed recombination resulting from the DM-baryon interactions.

f_χ	σ_0 [cm^2]
1	1.7×10^{-41}
0.1	1.9×10^{-40}
0.05	6.0×10^{-40}
0.01	5.5×10^{-39}
0.003	5.0×10^{-35}

TABLE B.1: Benchmark values of the momentum-transfer cross section coefficient σ_0 for various interacting DM fractions f_χ for $m_\chi = 1$ MeV, consistent with 95% C.L. upper limits derived in ref. [196].

additional suppression in the small-scale matter power spectrum can increase again.

These results motivate further investigation and modelling of the effects of these contributions to the full cosmic dawn signal, especially in the context of millicharged DM models invoked to explain the EDGES measurement.

B.3 Thermal velocity perturbation terms

In Section 3.2.2 we derived the new terms in the perturbed DM and baryon temperature evolution equations (eqs. (3.14) and (3.15)) resulting from the DM-baryon interactions. Here we report the full expressions for the terms $\delta_{\Gamma_i}, \delta_{\mathcal{H}_i}$

appearing in these equations, resulting from the dependence of the rates on the thermal velocity $\bar{v}_{\rm th}^2$, for the case $n = -4$:

$$\begin{aligned}\delta_{\Gamma_\chi} &\equiv \frac{\partial \Gamma_\chi}{\partial \bar{v}_{\rm th}^2}\left(\frac{\bar{T}_b - \bar{T}_\chi}{\bar{T}_\chi}\right)\left(\frac{\bar{T}_\chi \delta_{T_\chi}}{m_\chi} + \frac{\bar{T}_b \delta_{T_b}}{m_b}\right) \\ &= \Gamma_\chi\left(-\frac{3}{2\bar{v}_{\rm th}^2} + \frac{V_{\chi b}^2}{2\bar{v}_{\rm th}^4}\right)\left(\frac{\bar{T}_b - \bar{T}_\chi}{\bar{T}_\chi}\right)\left(\frac{\bar{T}_\chi \delta_{T_\chi}}{m_\chi} + \frac{\bar{T}_b \delta_{T_b}}{m_b}\right)\end{aligned} \tag{B.1}$$

and

$$\begin{aligned}\delta_{\mathcal{H}_\chi} &\equiv \frac{\partial \mathcal{H}_\chi}{\partial \bar{v}_{\rm th}^2}\frac{1}{\bar{T}_\chi}\left(\frac{\bar{T}_\chi \delta_{T_\chi}}{m_\chi} + \frac{\bar{T}_b \delta_{T_b}}{m_b}\right) \\ &= \frac{\mathcal{H}_\chi}{\bar{T}_\chi}\left(-\frac{1}{\sqrt{2\pi}}\frac{r^3 e^{-r^2/2}}{F(r)}\frac{1}{\bar{v}_{\rm th}^2}\right)\left(\frac{\bar{T}_\chi \delta_{T_\chi}}{m_\chi} + \frac{\bar{T}_b \delta_{T_b}}{m_b}\right)\end{aligned} \tag{B.2}$$

where

$$F(r) \equiv \mathrm{erf}\left(\frac{\mathrm{r}}{\sqrt{2}}\right) - \sqrt{\frac{2}{\pi}}\mathrm{e}^{-\mathrm{r}^2/2} \tag{B.3}$$

and we have defined $r \equiv V_{\chi b}/\bar{v}_{\rm th}$. The expressions for δ_{Γ_b} and $\delta_{\mathcal{H}_b}$ are obtained by simply substituting $\chi \leftrightarrow b$ in eqs. (B.1) and (B.2) respectively.

Appendix C

Interpretation of Neutrino Mass Priors

C.1 Bayesian hierarchical modelling

A key difference between the analysis of ref. [431] and other works is that the prior is hierarchical in nature. Hierarchical priors were first explored in the 1960s, but their impact was not fully realised until the 21st century. This is mostly due to the increase in computing power, as computing the evidence from these priors is computationally expensive. Rather than adopting a single predetermined prior of fixed position and breadth, one adopts instead a *hyperprior* – that is, one introduces an entire family of priors and effectively marginalises over them. This process is called *Bayesian hierarchical modelling*. Without repeating the arguments presented in ref. [431], the rational can be summarised as follows: hyperpriors are more flexible and as a result of marginalizing over the hyper-parameters describing this family of priors, the posterior is less sensitive to the prior itself.

To appreciate how hierarchical priors can help improve measurements, consider the following scenario: Alice and Bob are the first astronauts ever to set foot on an exoplanet. Upon exiting their spacecraft, they soon come across a new life form, a species they call snargs. In order to collect data on the nature of snargs, Alice and Bob perform various measurements on the individual creatures. One by one, Alice and Bob begin measuring how much each adult snarg weighs. The first specimen weighs 9.8 kg, while the second is found to weigh 9.7 kg. For these measurements, the accuracy of the weighing device is one part in a thousand, and the uncertainties in the separate measurements can be assumed to be statistically independent (i. e., not due to a calibration error in the weighing device). After some time, Alice and Bob have successfully measured the masses of 99 different snargs. The mean mass of the snargs they have sampled so far is 9.6 kg, with a standard deviation of 0.2 kg. However, they are

not so fortunate with the 100$^{\text{th}}$ snarg. Activity from a nearby star causes an electrical storm to engulf the planet, resulting in both of their weighing devices to malfunction when measuring the 100$^{\text{th}}$ snarg. The weighing device returns a measurement of 25 kg, along with an uncertainty of 20 kg. What is the true mass of the 100$^{\text{th}}$ snarg? Alice and Bob are both Bayesians, but they adopt different priors on their snarg masses. Alice adopts independent uniform priors on each of the snargs. Her posterior belief on the mass of the 100$^{\text{th}}$ snarg is therefore 25 kg with a standard error of 20 kg. Bob adopts a different approach. Bob assumes that the mass of every snarg (including the 100$^{\text{th}}$ they weigh) comes from the same underlying distribution, and adopts a hyerarchical prior which is described by two hyperparameters: the mean and the standard deviation. Bob marginalizes over the hyperparameters values, in the usual way. The precise measurements on the first 99 snargs effectively constrain the values of the hyperparameters. By using a hierarchical model on the mass of the snargs, Bob's posterior belief is that the mass of the 100$^{\text{th}}$ snarg is 9.6 kg with a standard error of 0.2 kg. Alice's and Bob's beliefs in the mass of the 100$^{\text{th}}$ snarg differ in their precision by a factor of one hundred.

Hyperpriors are more flexible than standard priors and make the posterior less sensitive to the prior itself. Following ref. [431], we work in a five-dimensional parameter space, consisting of the three neutrino masses indicated by the vector $\mathbf{m} = m_1, m_2, m_3$, and two hyperparameters μ and σ. This takes the form

$$P(D, \mathbf{m}, \mu, \sigma|M) = P(D|\mathbf{m}, M)P(\mathbf{m}|\mu, \sigma, M)\pi(\mu, \sigma|M)\,, \tag{C.1}$$

where D represents the data vector and M the Model or hypothesis i. e., the normal or inverted hierarchy, and $\pi(\mu, \sigma|M)$ is the hyperprior.

The prior must reflect our state of belief *before* the data arrived. As the three masses are indistinguishable before the (oscillation) data arrives, our prior must (and does by construction, as the three masses are drawn from a common prior) reflect this symmetry. This feature is also known as *exchangeability*, which naturally arises if the three masses share a common origin – a hypothesis that is adopted in most particle physics models for the neutrino masses. The relationship between exchangeability and hierarchical priors is further explored in refs. [497–499], but we will not dwell on this here. Following ref. [431] we adopt a hierarchical log-normal prior $P(\log \mathbf{m}|\mu, \sigma, M) \sim \mathcal{N}(\log \mu, \sigma)$, where $\mathcal{N}$ denotes the Normal (Gaussian) distribution with mean and standard deviation controlled by the two hyperparameters μ and σ. Here μ represents

the median mass value associated with the log-normal distribution, while σ denotes the standard deviation of the Gaussian in logarithmic space. The hyperprior imposed on our hyperparameters is given by $\pi(\log\mu, \log\sigma|M) \sim \mathcal{U}(\log\mu_{\rm min}, \log\mu_{\rm max})\mathcal{U}(\log\sigma_{\rm min}, \log\sigma_{\rm max})$, where $\mathcal{U}$ denotes a uniform distribution between the maximum and minimum bounds of $\mu_{\rm min} = 5 \times 10^{-4}$ eV, $\mu_{\rm max} = 0.3$ eV and $\sigma_{\rm min} = 5 \times 10^{-3}$ eV, $\sigma_{\rm max} = 20$ eV.

C.2 Objective Bayesian prior

For completeness, we report here the details of our implementation of the HS prior from ref. [440]. The approach in ref. [440] is to construct a prior that contributes minimal information to the analysis – or, in other words, the prior that maximises the expected information gain from the data. To do so a *reference prior* (see e. g. [500]) is used, which maximises the missing information between the posterior and prior as data arrives, in a mathematically well-defined sense. In the case of the neutrino hierarchy problem, where the likelihood has achieved asymptotic normality, the reference prior corresponds to the Jeffreys prior and thus uses the Fisher information as information measure.

The natural parameters to use then are the small and large squared mass splittings, ϕ and ψ respectively,[1] and the sum of the masses Σ. With the precision of current measurements, all three parameters (ϕ, ψ, Σ) can be treated as linear and the standard deviation as constant, which results in uniform Jeffreys priors for each of the parameters (ϕ, ψ, Σ). Due to the independence of the datasets, the total reference prior is the product of the three reference priors for ϕ, ψ, Σ. Hence these are taken to be uniform, excluding non-physical values. This prior is improper so a maximum value for Σ must be imposed, which HS take to be 1.5 eV. This prior can then be transformed to the reference prior in the ($m_{\rm L}$, $m_{\rm M}$, $m_{\rm H}$) parameterisation using the Jacobian, such that

$$\begin{aligned} J(m_{\rm L}, m_{\rm M}, m_{\rm H}) &= \left|\left| \frac{\partial(\phi, \psi, \Sigma)}{\partial(m_{\rm L}, m_{\rm M}, m_{\rm H})} \right|\right| \\ &= 4(m_{\rm L}m_{\rm M} + m_{\rm L}m_{\rm H} + m_{\rm M}m_{\rm H})\,, \end{aligned} \tag{C.2}$$

is the resulting reference prior on the neutrino masses.

The implicit approximation adopted here, as discussed in ref. [440], is that there is translational invariance of the likelihood – i. e., the likelihood does not

[1] Ref. [440] uses an alternative definition for the large mass splitting, but this is unimportant for this application.

change shape or width as a function of each parameter. While this is approximately (although certainly not exactly) true for Σ, it is interesting to consider the case for the squared mass splittings. This approximation implies that the error on ϕ (the small squared mass splitting) and ψ (the large one) do not depend on the value of the splitting (ϕ or ψ) itself. We know that this holds around the maximum likelihood for each mass splitting: the sensitivity to the mass splitting goes roughly like $\sim \sin^2(\Delta m^2_{ij} L/E)$ where L denotes the distance traveled by the neutrinos and E their energy and the L/E range explores more than 2π in the argument of sin. However, the experimental design is very different for the large versus the small splitting. In particular, the large splitting constraints rely on accelerators and the small splitting constraints rely on nuclear reactors, which have different energies and spread physics.

As eq. (4.4) indicates, ϕ is about an order of magnitude smaller than ψ (a factor 30 to be precise) and the error on ϕ is about an order of magnitude smaller than ψ, suggesting that experimental design might have been tuned to reach roughly the same relative errors in each of the splittings. On the other hand, if it can be stated that the small mass splitting would have an error of $\sim 10^{-6}$ eV^2 and the large one an error of $\sim 10^{-5}$ eV^2 even if the two mass spitting were of the same order of magnitude, then the likelihood is truly transationally invariant.

It is beyond the scope of this work to find a firm answer to this, but we believe these considerations might help the reader to appreciate the subtle but important role of priors and their relation to the physics and the mathematics underlying the issue at hand.

Bibliography

[1] K. Short et al., *Enlightening the dark ages with dark matter*, J. Cosmology Astropart. Phys. **2020**, 020, 020 (2020), arXiv:1912.07409 [astro-ph.CO].

[2] K. Short et al., *Dark matter-baryon scattering effects on temperature perturbations and implications for cosmic dawn*, submitted to: J. Cosmology Astropart. Phys. (2022), arXiv:2203.16524 [astro-ph.CO].

[3] R. Jimenez et al., *Neutrino masses and mass hierarchy: evidence for the normal hierarchy*, J. Cosmology Astropart. Phys. **2022**, 006 (2022), arXiv:2203.14247 [hep-ph].

[4] A. Einstein, *Die Grundlage der allgemeinen Relativitätstheorie*, Annalen der Physik **354**, 769 (1916).

[5] A. Hajian and T. Souradeep, *Measuring the Statistical Isotropy of the Cosmic Microwave Background Anisotropy*, ApJ **597**, L5 (2003), arXiv:astro-ph/0308001 [astro-ph].

[6] C. Marinoni, J. Bel, and A. Buzzi, *The scale of cosmic isotropy*, J. Cosmology Astropart. Phys. **2012**, 036, 036 (2012), arXiv:1205.3309 [astro-ph.CO].

[7] P. A. R. Ade et al., *Planck 2015 results. XVI. Isotropy and statistics of the CMB*, Astron. Astrophys. **594**, A16 (2016), arXiv:1506.07135 [astro-ph.CO].

[8] N. S. Sugiyama, M. Shiraishi, and T. Okumura, *Limits on statistical anisotropy from BOSS DR12 galaxies using bipolar spherical harmonics*, MNRAS **473**, 2737 (2018), arXiv:1704.02868 [astro-ph.CO].

[9] A. F. Heavens, R. Jimenez, and R. Maartens, *Testing homogeneity with the fossil record of galaxies*, J. Cosmology Astropart. Phys. **2011**, 035, 035 (2011), arXiv:1107.5910 [astro-ph.CO].

[10] B. Hoyle et al., *Testing Homogeneity with Galaxy Star Formation Histories*, ApJ **762**, L9, L9 (2013), arXiv:1209.6181 [astro-ph.CO].

[11] R. S. Gonçalves et al., *Cosmic homogeneity: a spectroscopic and model-independent measurement*, MNRAS **475**, L20 (2018), arXiv:1710.02496 [astro-ph.CO].

[12] S. G. Turyshev, *Experimental Tests of General Relativity*, Annual Review of Nuclear and Particle Science **58**, 207 (2008), arXiv:0806.1731 [gr-qc].

[13] C. M. Will, *The Confrontation between General Relativity and Experiment*, Living Rev. Rel. **17**, 4 (2014), arXiv:1403.7377 [gr-qc].

[14] E. Berti et al., *Testing General Relativity with Present and Future Astrophysical Observations*, Class. Quant. Grav. **32**, 243001 (2015), arXiv:1501.07274 [gr-qc].

[15] B. P. Abbott et al., *GW151226: Observation of Gravitational Waves from a 22-Solar-Mass Binary Black Hole Coalescence*, Phys. Rev. Lett. **116**, 241103, 241103 (2016), arXiv:1606.04855 [gr-qc].

[16] B. P. Abbott et al., *Observation of Gravitational Waves from a Binary Black Hole Merger*, Phys. Rev. Lett. **116**, 061102, 061102 (2016), arXiv:1602.03837 [gr-qc].

[17] B. P. Abbott et al., *GW170104: Observation of a 50-Solar-Mass Binary Black Hole Coalescence at Redshift 0.2*, Phys. Rev. Lett. **118**, 221101, 221101 (2017), arXiv:1706.01812 [gr-qc].

[18] B. P. Abbott et al., *GW170608: Observation of a 19 Solar-mass Binary Black Hole Coalescence*, ApJ **851**, L35, L35 (2017), arXiv:1711.05578 [astro-ph.HE].

[19] B. P. Abbott et al., *GW170814: A Three-Detector Observation of Gravitational Waves from a Binary Black Hole Coalescence*, Phys. Rev. Lett. **119**, 141101, 141101 (2017), arXiv:1709.09660 [gr-qc].

[20] B. P. Abbott et al., *GW170817: Observation of Gravitational Waves from a Binary Neutron Star Inspiral*, Phys. Rev. Lett. **119**, 161101, 161101 (2017), arXiv:1710.05832 [gr-qc].

[21] B. P. Abbott et al., *Multi-messenger Observations of a Binary Neutron Star Merger*, ApJ **848**, L12, L12 (2017), arXiv:1710.05833 [astro-ph.HE].

[22] Event Horizon Telescope Collaboration et al., *First M87 Event Horizon Telescope Results. I. The Shadow of the Supermassive Black Hole*, ApJ **875**, L1, L1 (2019), arXiv:1906.11238 [astro-ph.GA].

[23] Event Horizon Telescope Collaboration et al., *First Sagittarius A* Event Horizon Telescope Results. I. The Shadow of the Supermassive Black Hole in the Center of the Milky Way*, ApJ **930**, L12, L12 (2022).

[24] Event Horizon Telescope Collaboration et al., *First Sagittarius A* Event Horizon Telescope Results. VI. Testing the Black Hole Metric*, ApJ **930**, L17, L17 (2022).

[25] A. Friedmann, *Über die Krümmung des Raumes*, Zeitschrift fur Physik **10**, 377 (1922).

[26] G. Lemaître, *Un Univers homogène de masse constante et de rayon croissant rendant compte de la vitesse radiale des nébuleuses extra-galactiques*, Annales de la Société Scientifique de Bruxelles **47**, 49 (1927).

[27] E. Hubble, *A Relation between Distance and Radial Velocity among Extra-Galactic Nebulae*, Proceedings of the National Academy of Science **15**, 168 (1929).

[28] G. Lemaître, *The Beginning of the World from the Point of View of Quantum Theory*. Nature **127**, 706 (1931).

[29] R. A. Alpher, H. Bethe, and G. Gamow, *The Origin of Chemical Elements*, Physical Review **73**, 803 (1948).

[30] R. A. Alpher and R. Herman, *Evolution of the Universe*, Nature **162**, 774 (1948).

[31] A. A. Penzias and R. W. Wilson, *Measurement of the Flux Density of CAS a at 4080 Mc/s*. ApJ **142**, 1149 (1965).

[32] R. H. Dicke et al., *Cosmic Black-Body Radiation*. ApJ **142**, 414 (1965).

[33] G. F. Smoot et al., *Structure in the COBE Differential Microwave Radiometer First-Year Maps*, ApJ **396**, L1 (1992).

[34] A. G. Riess et al., *Observational Evidence from Supernovae for an Accelerating Universe and a Cosmological Constant*, AJ **116**, 1009 (1998), arXiv:astro-ph/9805201 [astro-ph].

[35] S. Perlmutter et al., *Measurements of* Ω *and* Λ *from 42 High-Redshift Supernovae*, ApJ **517**, 565 (1999), arXiv:astro-ph/9812133 [astro-ph].

[36] J. A. Frieman, M. S. Turner, and D. Huterer, *Dark energy and the accelerating universe*. ARA&A **46**, 385 (2008), arXiv:0803.0982 [astro-ph].

[37] T. Clifton et al., *Modified gravity and cosmology*, Phys. Rep. **513**, 1 (2012), arXiv:1106.2476 [astro-ph.CO].

[38] A. Joyce et al., *Beyond the cosmological standard model*, Phys. Rep. **568**, 1 (2015), arXiv:1407.0059 [astro-ph.CO].

[39] K. Koyama, *Cosmological tests of modified gravity*, Reports on Progress in Physics **79**, 046902, 046902 (2016), arXiv:1504.04623 [astro-ph.CO].

[40] A. Joyce, L. Lombriser, and F. Schmidt, *Dark Energy Versus Modified Gravity*, Annual Review of Nuclear and Particle Science **66**, 95 (2016), arXiv:1601.06133 [astro-ph.CO].

[41] L. Heisenberg, *A systematic approach to generalisations of General Relativity and their cosmological implications*, Phys. Rep. **796**, 1 (2019), arXiv:1807.01725 [gr-qc].

[42] M. Ishak, *Testing general relativity in cosmology*, Living Reviews in Relativity **22**, 1, 1 (2019), arXiv:1806.10122 [astro-ph.CO].

[43] C. L. Bennett et al., *Nine-year Wilkinson Microwave Anisotropy Probe (WMAP) Observations: Final Maps and Results*, ApJS **208**, 20, 20 (2013), arXiv:1212.5225 [astro-ph.CO].

[44] G. Hinshaw et al., *Nine-year Wilkinson Microwave Anisotropy Probe (WMAP) Observations: Cosmological Parameter Results*, ApJS **208**, 19, 19 (2013), arXiv:1212.5226 [astro-ph.CO].

[45] N. Aghanim et al., *Planck 2018 results. VI. Cosmological parameters*, Astron. Astrophys. **641**, [Erratum: Astron.Astrophys. 652, C4 (2021)], A6 (2020), arXiv:1807.06209 [astro-ph.CO].

[46] D. J. Eisenstein et al., *Detection of the Baryon Acoustic Peak in the Large-Scale Correlation Function of SDSS Luminous Red Galaxies*, ApJ **633**, 560 (2005), arXiv:astro-ph/0501171 [astro-ph].

[47] S. Cole et al., *The 2dF Galaxy Redshift Survey: power-spectrum analysis of the final data set and cosmological implications*, MNRAS **362**, 505 (2005), arXiv:astro-ph/0501174 [astro-ph].

[48] A. G. Riess et al., *Large Magellanic Cloud Cepheid Standards Provide a 1% Foundation for the Determination of the Hubble Constant and Stronger Evidence for Physics beyond ΛCDM*, ApJ **876**, 85, 85 (2019), arXiv:1903.07603 [astro-ph.CO].

[49] A. G. Riess et al., *Cosmic Distances Calibrated to 1% Precision with Gaia EDR3 Parallaxes and Hubble Space Telescope Photometry of 75 Milky Way Cepheids Confirm Tension with ΛCDM*, ApJ **908**, L6, L6 (2021), arXiv:2012.08534 [astro-ph.CO].

[50] A. Friedmann, *Über die Möglichkeit einer Welt mit konstanter negativer Krümmung des Raumes*, Zeitschrift fur Physik **21**, 326 (1924).

[51] H. P. Robertson, *Kinematics and World-Structure*, ApJ **82**, 284 (1935).

[52] A. G. Walker, *On Milne's Theory of World-Structure*, Proceedings of the London Mathematical Society **42**, 90 (1937).

[53] A. Einstein, *Kosmologische Betrachtungen zur allgemeinen Relativitätstheorie*, Sitzungsberichte der Königlich Preußischen Akademie der Wissenschaften (Berlin, 142 (1917).

[54] S. Alam et al., *Completed SDSS-IV extended Baryon Oscillation Spectroscopic Survey: Cosmological implications from two decades of spectroscopic surveys at the Apache Point Observatory*, Phys. Rev. D **103**, 083533 (2021), arXiv:2007.08991 [astro-ph.CO].

[55] V. Trimble, *Existence and Nature of Dark Matter in the Universe*, Annual Review of Astronomy and Astrophysics **25**, 425 (1987).

[56] R. H. Sanders, *The Dark Matter Problem: A Historical Perspective* (2010).

[57] J. Einasto, *Dark Matter and Cosmic Web Story* (2014).

[58] G. Bertone and D. Hooper, *History of dark matter*, Reviews of Modern Physics **90**, 10.1103/revmodphys.90.045002 (2018).

[59] J. G. de Swart, G. Bertone, and J. van Dongen, *How dark matter came to matter*, Nature Astronomy **1**, 0059, 0059 (2017), arXiv:1703.00013 [astro-ph.CO].

[60] C. S. Frenk and S. D. M. White, *Dark matter and cosmic structure*, Annalen der Physik **524**, 507 (2012), arXiv:1210.0544 [astro-ph.CO].

[61] J. C. Kapteyn, *First Attempt at a Theory of the Arrangement and Motion of the Sidereal System*, The Astrophysical Journal **55**, 302 (1922).

[62] J. H. Jeans, *The Motions of Stars in a Kapteyn-Universe*, Monthly Notices of the Royal Astronomical Society **82**, 122 (1922).

[63] J. H. Oort, *Observational evidence confirming Lindblad's hypothesis of a rotation of the galactic system*, Bull. Astron. Inst. Netherlands **3**, 275 (1927).

[64] F. Zwicky, *Die Rotverschiebung von extragalaktischen Nebeln*, Helvetica Physica Acta **6**, 110 (1933).

[65] F. Zwicky, *On the Masses of Nebulae and of Clusters of Nebulae*, The Astrophysical Journal **86**, 217 (1937).

[66] S. Smith, *The Mass of the Virgo Cluster*, The Astrophysical Journal **83**, 23 (1936).

[67] V. C. Rubin and J. F. W. Kent, *Rotation of the Andromeda Nebula from a Spectroscopic Survey of Emission Regions*, The Astrophysical Journal **159**, 379 (1970).

[68] V. C. Rubin, N. Thonnard, and J. F. W. K., *Extended rotation curves of high-luminosity spiral galaxies. IV - Systematic dynamical properties, SA through SC*, The Astrophysical Journal **225**, L107 (1978).

[69] V. C. Rubin, N. Thonnard, and J. F. W. K., *Rotational properties of 21 SC galaxies with a large range of luminosities and radii, from NGC 4605 /R = 4kpc/ to UGC 2885 /R = 122 kpc/*, The Astrophysical Journal **238**, 471 (1980).

[70] G. S. Shostak and D. H. Rogstad, *Aperture synthesis study of neutral hydrogen in NGC 2403 and NGC 4236. I. Observations.* A&A **24**, 405 (1973).

[71] D. H. Rogstad, G. S. Shostak, and A. H. Rots, *Aperture synthesis study of neutral hydrogen in the galaxies NGC 6946 and IC 342.* A&A **22**, 111 (1973).

[72] G. A. Seielstad and M. C. H. Wright, *Neutral-hydrogen aperture-synthesis maps of IC 2574 and NGC 7640.* ApJ **184**, 343 (1973).

[73] D. H. Rogstad, I. A. Lockhart, and M. C. H. Wright, *Aperture-synthesis observations of H I in the galaxy M83.* ApJ **193**, 309 (1974).

[74] W. K. Huchtmeier, *Rotation-curves of galaxies from 21-cm-line observations.* A&A **45**, 259 (1975).

[75] M. S. Roberts and R. N. Whitehurst, *The rotation curve and geometry of M31 at large galactocentric distances.* ApJ **201**, 327 (1975).

[76] M. S. Roberts, *The Rotation Curves of Galaxies*, Comments on Astrophysics **6**, 105 (1976).

[77] A. Bosma, *The distribution and kinematics of neutral hydrogen in spiral galaxies of various morphological types*, PhD thesis (University of Groningen, Netherlands, Mar. 1978).

[78] J. P. Ostriker, P. J. E. Peebles, and A. Yahil, *The Size and Mass of Galaxies, and the Mass of the Universe*, ApJ **193**, L1 (1974).

[79] J. Einasto, A. Kaasik, and E. Saar, *Dynamic evidence on massive coronas of galaxies*, Nature **250**, 309 (1974).

[80] P. J. E. Peebles, *Primeval adiabatic perturbations - Constraints from the mass distribution*, ApJ **248**, 885 (1981).

[81] P. J. E. Peebles, *Primeval adiabatic perturbations - Effect of massive neutrinos*, ApJ **258**, 415 (1982).

[82] P. J. E. Peebles, *Large-scale background temperature and mass fluctuations due to scale-invariant primeval perturbations*, ApJ **263**, L1 (1982).

[83] S. D. M. White, C. S. Frenk, and M. Davis, *Clustering in a neutrino-dominated universe*, ApJ **274**, L1 (1983).

[84] P. A. Zyla et al., *Review of Particle Physics*, PTEP **2020**, 083C01 (2020).

[85] M. Davis et al., *A survey of galaxy redshifts. II. The large scale space distribution.* ApJ **253**, 423 (1982).

[86] M. Davis et al., *The evolution of large-scale structure in a universe dominated by cold dark matter*, ApJ **292**, 371 (1985).

[87] M. R. Lovell et al., *The haloes of bright satellite galaxies in a warm dark matter universe*, MNRAS **420**, 2318 (2012), arXiv:1104.2929 [astro-ph.CO].

[88] B. Moore et al., *Dark Matter Substructure within Galactic Halos*, ApJ **524**, L19 (1999), arXiv:astro-ph/9907411 [astro-ph].

[89] A. Klypin et al., *Where Are the Missing Galactic Satellites?*, ApJ **522**, 82 (1999), arXiv:astro-ph/9901240 [astro-ph].

[90] J. I. Read et al., *The importance of tides for the Local Group dwarf spheroidals*, MNRAS **367**, 387 (2006), arXiv:astro-ph/0511759 [astro-ph].

[91] M. Boylan-Kolchin, J. S. Bullock, and M. Kaplinghat, *Too big to fail? The puzzling darkness of massive Milky Way subhaloes*, MNRAS **415**, L40 (2011), arXiv:1103.0007 [astro-ph.CO].

[92] B. Moore, *Evidence against dissipation-less dark matter from observations of galaxy haloes*, Nature **370**, 629 (1994).

[93] D. Clowe et al., *A Direct Empirical Proof of the Existence of Dark Matter*, ApJ **648**, L109 (2006), arXiv:astro-ph/0608407 [astro-ph].

[94] M. Markevitch et al., *Direct Constraints on the Dark Matter Self-Interaction Cross Section from the Merging Galaxy Cluster 1E 0657-56*, ApJ **606**, 819 (2004), arXiv:astro-ph/0309303 [astro-ph].

[95] M. Milgrom, *A modification of the Newtonian dynamics as a possible alternative to the hidden mass hypothesis.* ApJ **270**, 365 (1983).

[96] C. Alcock et al., *The MACHO Project: Microlensing Results from 5.7 Years of Large Magellanic Cloud Observations*, ApJ **542**, 281 (2000), arXiv:astro-ph/0001272 [astro-ph].

[97] T. Lasserre et al., *Not enough stellar mass Machos in the Galactic halo*, A&A **355**, L39 (2000), arXiv:astro-ph/0002253 [astro-ph].

[98] P. Tisserand et al., *Limits on the Macho content of the Galactic Halo from the EROS-2 Survey of the Magellanic Clouds*, A&A **469**, 387 (2007), arXiv:astro-ph/0607207 [astro-ph].

[99] G. F. Chapline, *Cosmological effects of primordial black holes*, Nature **253**, 251 (1975).

[100] P. Meszaros, *Primeval black holes and galaxy formation.* A&A **38**, 5 (1975).

[101] B. Carr et al., *Constraints on primordial black holes*, Rept. Prog. Phys. **84**, 116902 (2021), arXiv:2002.12778 [astro-ph.CO].

[102] B. Carr and F. Kühnel, *Primordial Black Holes as Dark Matter: Recent Developments*, Annual Review of Nuclear and Particle Science **70**, 355 (2020), arXiv:2006.02838 [astro-ph.CO].

[103] P. Villanueva-Domingo, O. Mena, and S. Palomares-Ruiz, *A brief review on primordial black holes as dark matter*, Frontiers in Astronomy and Space Sciences **8**, 87, 87 (2021), arXiv:2103.12087 [astro-ph.CO].

[104] A. De Rujula, S. L. Glashow, and U. Sarid, *CHARGED DARK MATTER*, Nucl. Phys. B **333**, 173 (1990).

[105] S. Dimopoulos et al., *Getting a charge out of dark matter*, Phys. Rev. D **41**, 2388 (1990).

[106] M. Taoso, G. Bertone, and A. Masiero, *Dark matter candidates: a ten-point test*, J. Cosmology Astropart. Phys. **2008**, 022, 022 (2008), arXiv:0711.4996 [astro-ph].

[107] E. D. Kovetz et al., *Tighter limits on dark matter explanations of the anomalous EDGES 21 cm signal*, Phys. Rev. D **98**, 103529 (2018), arXiv:1807.11482 [astro-ph.CO].

[108] R. Barkana et al., *Strong constraints on light dark matter interpretation of the EDGES signal*, Phys. Rev. **D98**, 103005 (2018), arXiv:1803.03091 [hep-ph].

[109] A. Berlin et al., *Severely Constraining Dark Matter Interpretations of the 21-cm Anomaly*, Phys. Rev. Lett. **121**, 011102 (2018), arXiv:1803.02804 [hep-ph].

[110] A. Caputo et al., *Constraints on millicharged dark matter and axionlike particles from timing of radio waves*, Phys. Rev. D **100**, 063515, 063515 (2019), arXiv:1902.02695 [astro-ph.CO].

[111] R. Plestid et al., *New Constraints on Millicharged Particles from Cosmic-ray Production*, arXiv e-prints, arXiv:2002.11732, arXiv:2002.11732 (2020), arXiv:2002.11732 [hep-ph].

[112] C. Csáki and P. Tanedo, *Beyond the Standard Model*, in 2013 European School of High-Energy Physics (2015), pp. 169–268, arXiv:1602.04228 [hep-ph].

[113] G. Bertone, D. Hooper, and J. Silk, *Particle dark matter: evidence, candidates and constraints*, Physics Reports **405**, 279 (2005).

[114] J. L. Feng, *Dark Matter Candidates from Particle Physics and Methods of Detection*, ARA&A **48**, 495 (2010), arXiv:1003.0904 [astro-ph.CO].

[115] L. Bergstrom, *Dark Matter Candidates*, New J. Phys. **11**, 105006 (2009), arXiv:0903.4849 [hep-ph].

[116] C. A. Baker et al., *Improved Experimental Limit on the Electric Dipole Moment of the Neutron*, Phys. Rev. Lett. **97**, 131801, 131801 (2006), arXiv:hep-ex/0602020 [hep-ex].

[117] R. D. Peccei and H. R. Quinn, *CP conservation in the presence of pseudoparticles*, Phys. Rev. Lett. **38**, 1440 (1977).

[118] S. Weinberg, *A new light boson?*, Phys. Rev. Lett. **40**, 223 (1978).

[119] F. Wilczek, *Problem of strong P and T invariance in the presence of instantons*, Phys. Rev. Lett. **40**, 279 (1978).

[120] J. Preskill, M. B. Wise, and F. Wilczek, *Cosmology of the invisible axion*, Physics Letters B **120**, 127 (1983).

[121] L. Abbott and P. Sikivie, *A cosmological bound on the invisible axion*, Physics Letters B **120**, 133 (1983).

[122] M. Dine and W. Fischler, *The not-so-harmless axion*, Physics Letters B **120**, 137 (1983).

[123] J. E. Kim, *Weak-Interaction Singlet and Strongmml:math xmlns:mml="http://www.w3.org/199 display="inline"mml:miCP/mml:mi/mml:mathInvariance*, Physical Review Letters **43**, 103 (1979).

[124] M. Shifman, A. Vainshtein, and V. Zakharov, *Can confinement ensure natural CP invariance of strong interactions?*, Nuclear Physics B **166**, 493 (1980).

[125] M. Dine, W. Fischler, and M. Srednicki, *A simple solution to the strong CP problem with a harmless axion*, Physics Letters B **104**, 199 (1981).

[126] A. R. Zhitnitsky, *On Possible Suppression of the Axion Hadron Interactions. (In Russian)*, Sov. J. Nucl. Phys. **31**, 260 (1980).

[127] D. J. Marsh, *Axion cosmology*, Physics Reports **643**, 1 (2016).

[128] S. Dodelson and L. M. Widrow, *Sterile neutrinos as dark matter*, Phys. Rev. Lett. **72**, 17 (1994), arXiv:hep-ph/9303287 [hep-ph].

[129] P. Minkowski, $\mu \to e\gamma$ *at a Rate of One Out of* 10^9 *Muon Decays?*, Phys. Lett. B **67**, 421 (1977).

[130] R. N. Mohapatra and G. Senjanovic, *Neutrino Mass and Spontaneous Parity Nonconservation*, Phys. Rev. Lett. **44**, 912 (1980).

[131] T. Yanagida, *Horizontal gauge symmetry and masses of neutrinos*, Conf. Proc. C **7902131**, edited by O. Sawada and A. Sugamoto, 95 (1979).

[132] M. Drewes, *The Phenomenology of Right Handed Neutrinos*, International Journal of Modern Physics E **22**, 1330019-593, 1330019 (2013), arXiv:1303.6912 [hep-ph].

[133] R. Adhikari et al., *A White Paper on keV sterile neutrino Dark Matter*, J. Cosmology Astropart. Phys. **2017**, 025, 025 (2017), arXiv:1602.04816 [hep-ph].

[134] A. Boyarsky et al., *Sterile Neutrino Dark Matter*, Prog. Part. Nucl. Phys. **104**, 1 (2019), arXiv:1807.07938 [hep-ph].

[135] E. Bulbul et al., *Detection of an Unidentified Emission Line in the Stacked X-Ray Spectrum of Galaxy Clusters*, ApJ **789**, 13, 13 (2014), arXiv:1402.2301 [astro-ph.CO].

[136] A. Boyarsky et al., *Unidentified Line in X-Ray Spectra of the Andromeda Galaxy and Perseus Galaxy Cluster*, Phys. Rev. Lett. **113**, 251301, 251301 (2014), arXiv:1402.4119 [astro-ph.CO].

[137] O. Ruchayskiy et al., *Searching for decaying dark matter in deep XMM-Newton observation of the Draco dwarf spheroidal*, MNRAS **460**, 1390 (2016), arXiv:1512.07217 [astro-ph.HE].

[138] V. Iršič et al., *New constraints on the free-streaming of warm dark matter from intermediate and small scale Lyman-α forest data*, Phys. Rev. D **96**, 023522, 023522 (2017), arXiv:1702.01764 [astro-ph.CO].

[139] J. Baur et al., *Constraints from Ly-α forests on non-thermal dark matter including resonantly-produced sterile neutrinos*, J. Cosmology Astropart. Phys. **2017**, 013, 013 (2017), arXiv:1706.03118 [astro-ph.CO].

[140] K. Perez et al., *Almost closing the ν MSM sterile neutrino dark matter window with NuSTAR*, Phys. Rev. D **95**, 123002, 123002 (2017), arXiv:1609.00667 [astro-ph.HE].

[141] G. Jungman, M. Kamionkowski, and K. Griest, *Supersymmetric dark matter*, Phys. Rep. **267**, 195 (1996), arXiv:hep-ph/9506380 [hep-ph].

[142] S. P. Martin, *A Supersymmetry Primer*, in *Perspectives on Supersymmetry. Edited by KANE GORDON L. Published by World Scientific Publishing Co. Pte. Ltd* (1998), pp. 1–98.

[143] J. Ellis et al., *Supersymmetric relics from the big bang*, Nuclear Physics B **238**, 453 (1984).

[144] H.-C. Cheng, K. T. Matchev, and M. Schmaltz, *Radiative corrections to Kaluza-Klein masses*, Phys. Rev. D **66**, 036005, 036005 (2002), arXiv:hep-ph/0204342 [hep-ph].

[145] J. L. Feng and J. Kumar, *Dark-Matter Particles without Weak-Scale Masses or Weak Interactions*, Phys. Rev. Lett. **101**, 231301, 231301 (2008), arXiv:0803.4196 [hep-ph].

[146] L. J. Hall et al., *Freeze-in production of FIMP dark matter*, Journal of High Energy Physics **2010**, 80, 80 (2010), arXiv:0911.1120 [hep-ph].

[147] N. Bernal et al., *The dawn of FIMP Dark Matter: A review of models and constraints*, International Journal of Modern Physics A **32**, 1730023-274, 1730023 (2017), arXiv:1706.07442 [hep-ph].

[148] M. Schumann, *Direct Detection of WIMP Dark Matter: Concepts and Status*, J. Phys. **G46**, 103003 (2019), arXiv:1903.03026 [astro-ph.CO].

[149] J. Billard et al., *Direct Detection of Dark Matter – APPEC Committee Report*, (2021), arXiv:2104.07634 [hep-ex].

[150] J. M. Gaskins, *A review of indirect searches for particle dark matter*, Contemporary Physics **57**, 496 (2016).

[151] J. Conrad and O. Reimer, *Indirect dark matter searches in gamma and cosmic rays*, Nature Phys. **13**, 224 (2017), arXiv:1705.11165 [astro-ph.HE].

[152] C. Pérez de los Heros, *Status, Challenges and Directions in Indirect Dark Matter Searches*, Symmetry **12**, 1648 (2020), arXiv:2008.11561 [astro-ph.HE].

[153] F. Kahlhoefer, *Review of LHC Dark Matter Searches*, Int. J. Mod. Phys. A **32**, 1730006 (2017), arXiv:1702.02430 [hep-ph].

[154] A. Boveia and C. Doglioni, *Dark Matter Searches at Colliders*, Ann. Rev. Nucl. Part. Sci. **68**, 429 (2018), arXiv:1810.12238 [hep-ex].

[155] G. Aad et al., *Search for dark matter candidates and large extra dimensions in events with a jet and missing transverse momentum with the ATLAS detector*, JHEP **04**, 075 (2013), arXiv:1210.4491 [hep-ex].

[156] V. Khachatryan et al., *Search for dark matter, extra dimensions, and unparticles in monojet events in proton–proton collisions at* $\sqrt{s} = 8$ *TeV*, Eur. Phys. J. C **75**, 235 (2015), arXiv:1408.3583 [hep-ex].

[157] S. Rappoccio, *The experimental status of direct searches for exotic physics beyond the standard model at the Large Hadron Collider*, Rev. Phys. **4**, 100027 (2019), arXiv:1810.10579 [hep-ex].

[158] D. S. Akerib et al., *Results from a Search for Dark Matter in the Complete LUX Exposure*, Phys. Rev. Lett. **118**, 021303, 021303 (2017), arXiv:1608.07648 [astro-ph.CO].

[159] E. Aprile et al., *Dark Matter Search Results from a One Ton-Year Exposure of XENON1T*, Phys. Rev. Lett. **121**, 111302, 111302 (2018), arXiv:1805.12562 [astro-ph.CO].

[160] Y. Meng et al., *Dark Matter Search Results from the PandaX-4T Commissioning Run*, Phys. Rev. Lett. **127**, 261802, 261802 (2021), arXiv:2107.13438 [hep-ex].

[161] CRESST Collaboration et al., *First results from the CRESST-III low-mass dark matter program*, arXiv e-prints, arXiv:1904.00498, arXiv:1904.00498 (2019), arXiv:1904.00498 [astro-ph.CO].

[162] R. Agnese et al., *Search for Low-Mass Weakly Interacting Massive Particles with SuperCDMS*, Phys. Rev. Lett. **112**, 241302 (2014), arXiv:1402.7137 [hep-ex].

[163] R. Agnese et al., *Results from the Super Cryogenic Dark Matter Search Experiment at Soudan*, Phys. Rev. Lett. **120**, 061802 (2018), arXiv:1708.08869 [hep-ex].

[164] D. S. Akerib et al., *Snowmass2021 Cosmic Frontier Dark Matter Direct Detection to the Neutrino Fog*, arXiv e-prints, arXiv:2203.08084, arXiv:2203.08084 (2022), arXiv:2203.08084 [hep-ex].

[165] R. Essig, J. Mardon, and T. Volansky, *Direct detection of sub-GeV dark matter*, Phys. Rev. D **85**, 076007, 076007 (2012), arXiv:1108.5383 [hep-ph].

[166] P. W. Graham et al., *Semiconductor Probes of Light Dark Matter*, Phys. Dark Univ. **1**, 32 (2012), arXiv:1203.2531 [hep-ph].

[167] S. Derenzo et al., *Direct Detection of sub-GeV Dark Matter with Scintillating Targets*, Phys. Rev. D **96**, 016026 (2017), arXiv:1607.01009 [hep-ph].

[168] R. Essig et al., *Snowmass2021 Cosmic Frontier: The landscape of low-threshold dark matter direct detection in the next decade*, arXiv e-prints, arXiv:2203.08297, arXiv:2203.08297 (2022), arXiv:2203.08297 [hep-ph].

[169] M. Ackermann et al., *Searching for Dark Matter Annihilation from Milky Way Dwarf Spheroidal Galaxies with Six Years of Fermi Large Area Telescope Data*, Phys. Rev. Lett. **115**, 231301 (2015), arXiv:1503.02641 [astro-ph.HE].

[170] A. Albert et al., *Searching for Dark Matter Annihilation in Recently Discovered Milky Way Satellites with Fermi-LAT*, Astrophys. J. **834**, 110 (2017), arXiv:1611.03184 [astro-ph.HE].

[171] S. Archambault et al., *Dark Matter Constraints from a Joint Analysis of Dwarf Spheroidal Galaxy Observations with VERITAS*, Phys. Rev. **D95**, 082001 (2017), arXiv:1703.04937 [astro-ph.HE].

[172] M. L. Ahnen et al., *Limits to Dark Matter Annihilation Cross-Section from a Combined Analysis of MAGIC and Fermi-LAT Observations of Dwarf Satellite Galaxies*, JCAP **1602**, 039 (2016), arXiv:1601.06590 [astro-ph.HE].

[173] A. Albert et al., *Dark Matter Limits from Dwarf Spheroidal Galaxies with the HAWC Gamma-Ray Observatory*, ApJ **853**, 154, 154 (2018), arXiv:1706.01277 [astro-ph.HE].

[174] H. Abdallah et al., *Search for dark matter signals towards a selection of recently detected DES dwarf galaxy satellites of the Milky Way with H.E.S.S.* Phys. Rev. D **102**, 062001, 062001 (2020), arXiv:2008.00688 [astro-ph.HE].

[175] B. S. Acharya et al., *Science with the Cherenkov Telescope Array* (WSP, Nov. 2018), arXiv:1709.07997 [astro-ph.IM].

[176] J. Kopp, *Constraints on dark matter annihilation from AMS-02 results*, Phys. Rev. D **88**, 076013, 076013 (2013), arXiv:1304.1184 [hep-ph].

[177] A. Cuoco, M. Krämer, and M. Korsmeier, *Novel Dark Matter Constraints from Antiprotons in Light of AMS-02*, Phys. Rev. Lett. **118**, 191102, 191102 (2017), arXiv:1610.03071 [astro-ph.HE].

[178] A. Reinert and M. W. Winkler, *A precision search for WIMPs with charged cosmic rays*, J. Cosmology Astropart. Phys. **2018**, 055, 055 (2018), arXiv:1712.00002 [astro-ph.HE].

[179] M. Tavani et al., *Science with e-ASTROGAM: A space mission for MeV–GeV gamma-ray astrophysics*, JHEAp **19**, edited by A. De Angelis et al., 1 (2018), arXiv:1711.01265 [astro-ph.HE].

[180] R. Essig et al., *Constraining light dark matter with diffuse X-ray and gamma-ray observations*, Journal of High Energy Physics **2013**, 193, 193 (2013), arXiv:1309.4091 [hep-ph].

[181] T. E. Jeltema and S. Profumo, *Dark matter detection with hard X-ray telescopes*, MNRAS **421**, 1215 (2012), arXiv:1108.1407 [astro-ph.HE].

[182] M. van Beekveld et al., *Supersymmetry with dark matter is still natural*, Phys. Rev. D **96**, 035015, 035015 (2017), arXiv:1612.06333 [hep-ph].

[183] R. K. Leane et al., *GeV-scale thermal WIMPs: Not even slightly ruled out*, Phys. Rev. **D98**, 023016 (2018), arXiv:1805.10305 [hep-ph].

[184] G. Arcadi et al., *The waning of the WIMP? A review of models, searches, and constraints*, European Physical Journal C **78**, 203, 203 (2018), arXiv:1703.07364 [hep-ph].

[185] G. Bertone and T. Tait M. P., *A new era in the search for dark matter*, Nature **562**, 51 (2018), arXiv:1810.01668 [astro-ph.CO].

[186] T. R. Slatyer, *Indirect dark matter signatures in the cosmic dark ages. I. Generalizing the bound on s-wave dark matter annihilation from Planck results*, Phys. Rev. **D93**, 023527 (2016), arXiv:1506.03811 [hep-ph].

[187] T. R. Slatyer and C.-L. Wu, *General Constraints on Dark Matter Decay from the Cosmic Microwave Background*, Phys. Rev. **D95**, 023010 (2017), arXiv:1610.06933 [astro-ph.CO].

[188] V. Poulin, J. Lesgourgues, and P. D. Serpico, *Cosmological constraints on exotic injection of electromagnetic energy*, JCAP **1703**, 043 (2017), arXiv:1610.10051 [astro-ph.CO].

[189] Y. Ali-Haïmoud, *Testing dark matter interactions with CMB spectral distortions*, Phys. Rev. D **103**, 043541 (2021), arXiv:2101.04070 [astro-ph.CO].

[190] B. Bolliet, J. Chluba, and R. Battye, *Spectral distortion constraints on photon injection from low-mass decaying particles*, MNRAS **507**, 3148 (2021), arXiv:2012.07292 [astro-ph.CO].

[191] X.-l. Chen, S. Hannestad, and R. J. Scherrer, *Cosmic microwave background and large scale structure limits on the interaction between dark matter and baryons*, Phys. Rev. D **65**, 123515 (2002), arXiv:astro-ph/0202496.

[192] K. Sigurdson et al., *Dark-matter electric and magnetic dipole moments*, Phys. Rev. D **70**, [Erratum: Phys.Rev.D 73, 089903 (2006)], 083501 (2004), arXiv:astro-ph/0406355.

[193] C. Dvorkin, K. Blum, and M. Kamionkowski, *Constraining Dark Matter-Baryon Scattering with Linear Cosmology*, Phys. Rev. D **89**, 023519 (2014), arXiv:1311.2937 [astro-ph.CO].

[194] V. Gluscevic and K. K. Boddy, *Constraints on Scattering of keV–TeV Dark Matter with Protons in the Early Universe*, Phys. Rev. Lett. **121**, 081301 (2018), arXiv:1712.07133 [astro-ph.CO].

[195] K. K. Boddy and V. Gluscevic, *First Cosmological Constraint on the Effective Theory of Dark Matter-Proton Interactions*, Phys. Rev. D **98**, 083510 (2018), arXiv:1801.08609 [astro-ph.CO].

[196] K. K. Boddy et al., *Critical assessment of CMB limits on dark matter-baryon scattering: New treatment of the relative bulk velocity*, Phys. Rev. **D98**, 123506 (2018), arXiv:1808.00001 [astro-ph.CO].

[197] W. L. Xu, C. Dvorkin, and A. Chael, *Probing sub-GeV Dark Matter-Baryon Scattering with Cosmological Observables*, Phys. Rev. D **97**, 103530 (2018), arXiv:1802.06788 [astro-ph.CO].

[198] T. R. Slatyer and C.-L. Wu, *Early-Universe constraints on dark matter-baryon scattering and their implications for a global 21 cm signal*, Phys. Rev. D **98**, 023013 (2018), arXiv:1803.09734 [astro-ph.CO].

[199] Z. Li et al., *Disentangling Dark Physics with Cosmic Microwave Background Experiments*, Phys. Rev. D **98**, 123524 (2018), arXiv:1806.10165 [astro-ph.CO].

[200] J. Ooba, H. Tashiro, and K. Kadota, *Cosmological constraints on the velocity-dependent baryon-dark matter coupling*, JCAP **09**, 020 (2019), arXiv:1902.00826 [astro-ph.CO].

[201] D. V. Nguyen et al., *Observational constraints on dark matter scattering with electrons*, Phys. Rev. D **104**, 103521 (2021), arXiv:2107.12380 [astro-ph.CO].

[202] M. A. Buen-Abad et al., *Cosmological constraints on dark matter interactions with ordinary matter*, Phys. Rept. **961**, 1 (2022), arXiv:2107.12377 [astro-ph.CO].

[203] C. Bœhm et al., *Interacting dark matter disguised as warm dark matter*, Phys. Rev. D **66**, 083505, 083505 (2002), arXiv:astro-ph/0112522 [astro-ph].

[204] R. J. Wilkinson, J. Lesgourgues, and C. é. Bœhm, *Using the CMB angular power spectrum to study Dark Matter-photon interactions*, J. Cosmology Astropart. Phys. **2014**, 026, 026 (2014), arXiv:1309.7588 [astro-ph.CO].

[205] J. Stadler and C. Bœhm, *Constraints on γ-CDM interactions matching the Planck data precision*, J. Cosmology Astropart. Phys. **2018**, 009, 009 (2018), arXiv:1802.06589 [astro-ph.CO].

[206] R. J. Wilkinson, C. Bœhm, and J. Lesgourgues, *Constraining dark matter-neutrino interactions using the CMB and large-scale structure*, J. Cosmology Astropart. Phys. **2014**, 011, 011 (2014), arXiv:1401.7597 [astro-ph.CO].

[207] A. Olivares-Del Campo et al., *Dark matter-neutrino interactions through the lens of their cosmological implications*, Phys. Rev. D **97**, 075039, 075039 (2018), arXiv:1711.05283 [hep-ph].

[208] F.-Y. Cyr-Racine et al., *ETHOS—an effective theory of structure formation: From dark particle physics to the matter distribution of the Universe*, Phys. Rev. D **93**, 123527, 123527 (2016), arXiv:1512.05344 [astro-ph.CO].

[209] M. Archidiacono et al., *Linear scale bounds on dark matter–dark radiation interactions and connection with the small scale crisis of cold dark matter*, JCAP **11**, 010 (2017), arXiv:1706.06870 [astro-ph.CO].

[210] M. Archidiacono et al., *Constraining Dark Matter-Dark Radiation interactions with CMB, BAO, and Lyman-α*, J. Cosmology Astropart. Phys. **2019**, 055, 055 (2019), arXiv:1907.01496 [astro-ph.CO].

[211] Y. Ali-Haïmoud, J. Chluba, and M. Kamionkowski, *Constraints on Dark Matter Interactions with Standard Model Particles from Cosmic Microwave Background Spectral Distortions*, Phys. Rev. Lett. **115**, 071304 (2015), arXiv:1506.04745 [astro-ph.CO].

[212] K. K. Boddy et al., *Astrophysical and Cosmological Probes of Dark Matter*, in 2022 Snowmass Summer Study (Mar. 2022), arXiv:2203.06380 [hep-ph].

[213] M. Kawasaki et al., *Revisiting Big-Bang Nucleosynthesis Constraints on Dark-Matter Annihilation*, Phys. Lett. B **751**, 246 (2015), arXiv:1509.03665 [hep-ph].

[214] M. Escudero, *Neutrino decoupling beyond the Standard Model: CMB constraints on the Dark Matter mass with a fast and precise N_{eff} evaluation*, J. Cosmology Astropart. Phys. **2019**, 007, 007 (2019), arXiv:1812.05605 [hep-ph].

[215] V. Poulin and P. D. Serpico, *Nonuniversal BBN bounds on electromagnetically decaying particles*, Phys. Rev. **D91**, 103007 (2015), arXiv:1503.04852 [astro-ph.CO].

[216] F. Iocco et al., *Primordial Nucleosynthesis: from precision cosmology to fundamental physics*, Phys. Rept. **472**, 1 (2009), arXiv:0809.0631 [astro-ph].

[217] C. Brust, D. E. Kaplan, and M. T. Walters, *New light species and the CMB*, Journal of High Energy Physics **2013**, 58, 58 (2013), arXiv:1303.5379 [hep-ph].

[218] C. Giovanetti et al., *Joint Cosmic Microwave Background and Big Bang Nucleosynthesis Constraints on Light Dark Sectors with Dark Radiation*, Phys. Rev. Lett. **129**, 021302, 021302 (2022), arXiv:2109.03246 [hep-ph].

[219] K. M. Nollett and G. Steigman, *BBN and the CMB constrain neutrino coupled light WIMPs*, Phys. Rev. D **91**, 083505, 083505 (2015), arXiv:1411.6005 [astro-ph.CO].

[220] K. N. Abazajian et al., *CMB-S4 Science Book, First Edition*, (2016), arXiv:1610.02743 [astro-ph.CO].

[221] P. Ade et al., *The Simons Observatory: Science goals and forecasts*, JCAP **02**, 056 (2019), arXiv:1808.07445 [astro-ph.CO].

[222] K. Bechtol et al., *Dark Matter Science in the Era of LSST*, (2019), arXiv:1903.04425 [astro-ph.CO].

[223] K. K. Boddy et al., *Astrophysical and Cosmological Probes of Dark Matter*, arXiv e-prints, arXiv:2203.06380, arXiv:2203.06380 (2022), arXiv:2203.06380 [hep-ph].

[224] M. Valluri et al., *Snowmass2021 Cosmic Frontier White Paper: Prospects for obtaining Dark Matter Constraints with DESI*, arXiv e-prints, arXiv:2203.07491, arXiv:2203.07491 (2022), arXiv:2203.07491 [astro-ph.CO].

[225] S. Furlanetto, S. P. Oh, and F. Briggs, *Cosmology at Low Frequencies: The 21 cm Transition and the High-Redshift Universe*, Phys. Rept. **433**, 181 (2006), arXiv:astro-ph/0608032 [astro-ph].

[226] J. R. Pritchard and A. Loeb, *21-cm cosmology*, Rept. Prog. Phys. **75**, 086901 (2012), arXiv:1109.6012 [astro-ph.CO].

[227] M. Sitwell et al., *The Imprint of Warm Dark Matter on the Cosmological 21-cm Signal*, Mon. Not. Roy. Astron. Soc. **438**, 2664 (2014), arXiv:1310.0029 [astro-ph.CO].

[228] S. Das et al., *On dark matter - dark radiation interaction and cosmic reionization*, JCAP **08**, 045 (2018), arXiv:1712.03976 [astro-ph.CO].

[229] M. Escudero et al., *A fresh look into the interacting dark matter scenario*, JCAP **06**, 007 (2018), arXiv:1803.08427 [astro-ph.CO].

[230] M. Safarzadeh, E. Scannapieco, and A. Babul, *A limit on the warm dark matter particle mass from the redshifted 21 cm absorption line*, Astrophys. J. Lett. **859**, L18 (2018), arXiv:1803.08039 [astro-ph.CO].

[231] L. Lopez-Honorez, O. Mena, and P. Villanueva-Domingo, *Dark matter microphysics and 21 cm observations*, Phys. Rev. D **99**, 023522 (2019), arXiv:1811.02716 [astro-ph.CO].

[232] J. B. Muñoz, C. Dvorkin, and F.-Y. Cyr-Racine, *Probing the Small-Scale Matter Power Spectrum with Large-Scale 21-cm Data*, Phys. Rev. D **101**, 063526 (2020), arXiv:1911.11144 [astro-ph.CO].

[233] J. B. Muñoz et al., *ETHOS - an effective theory of structure formation: Impact of dark acoustic oscillations on cosmic dawn*, Phys. Rev. D **103**, 043512 (2021), arXiv:2011.05333 [astro-ph.CO].

[234] D. Jones et al., *Fuzzy Dark Matter and the 21 cm Power Spectrum*, Astrophys. J. **913**, 7 (2021), arXiv:2101.07177 [astro-ph.CO].

[235] S. K. Giri and A. Schneider, *Imprints of fermionic and bosonic mixed dark matter on the 21-cm signal at cosmic dawn*, (2022), arXiv:2201.02210 [astro-ph.CO].

[236] D. Sarkar, J. Flitter, and E. D. Kovetz, *Exploring delaying and heating effects on the 21-cm signature of fuzzy dark matter*, (2022), arXiv:2201.03355 [astro-ph.CO].

[237] W. Pauli, *Dear radioactive ladies and gentlemen*, Phys. Today **31N9**, 27 (1978).

[238] J. Cowan C. L. et al., *Detection of the Free Neutrino: A Confirmation*, Science **124**, 103 (1956).

[239] B. Pontecorvo, *Mesonium and anti-mesonium*, Sov. Phys. JETP **6**, 429 (1957).

[240] B. Pontecorvo, *Inverse beta processes and nonconservation of lepton charge*, Zh. Eksp. Teor. Fiz. **34**, 247 (1957).

[241] G. Danby et al., *Observation of High-Energy Neutrino Reactions and the Existence of Two Kinds of Neutrinos*, Physical Review Letters **9**, 36 (1962).

[242] Z. Maki, M. Nakagawa, and S. Sakata, *Remarks on the unified model of elementary particles*, Prog. Theor. Phys. **28**, 870 (1962).

[243] B. Pontecorvo, *Neutrino Experiments and the Problem of Conservation of Leptonic Charge*, Zh. Eksp. Teor. Fiz. **53**, 1717 (1967).

[244] R. Davis, D. S. Harmer, and K. C. Hoffman, *Search for Neutrinos from the Sun*, Physical Review Letters **20**, 1205 (1968).

[245] J. N. Bahcall, N. A. Bahcall, and G. Shaviv, *Present Status of the Theoretical Predictions for the ^{36}Cl Solar-Neutrino Experiment*, Phys. Rev. Lett. **20**, 1209 (1968).

[246] W. C. Haxton, *The Solar Neutrino Problem*, ARA&A **33**, 459 (1995), arXiv:hep-ph/9503430 [hep-ph].

[247] K. Kodama et al., *Observation of tau neutrino interactions*, Phys. Lett. B **504**, 218 (2001), arXiv:hep-ex/0012035.

[248] A. de Gouvea, *TASI lectures on neutrino physics*, in Theoretical Advanced Study Institute in Elementary Particle Physics: Physics in D $\geqq$ 4 (Nov. 2004), pp. 197–258, arXiv:hep-ph/0411274.

[249] P. Hernandez, *Neutrino physics*, in 5th CERN - Latin American School of High-Energy Physics (Oct. 2010), arXiv:1010.4131 [hep-ph].

[250] Y. Fukuda et al., *Evidence for oscillation of atmospheric neutrinos*, Phys. Rev. Lett. **81**, 1562 (1998), arXiv:hep-ex/9807003.

[251] Q. R. Ahmad et al., *Measurement of the rate of $\nu_e + d \rightarrow p + p + e^-$ interactions produced by ^8B solar neutrinos at the Sudbury Neutrino Observatory*, Phys. Rev. Lett. **87**, 071301 (2001), arXiv:nucl-ex/0106015.

[252] Q. R. Ahmad et al., *Direct evidence for neutrino flavor transformation from neutral current interactions in the Sudbury Neutrino Observatory*, Phys. Rev. Lett. **89**, 011301 (2002), arXiv:nucl-ex/0204008.

[253] C. Arpesella et al., *Direct Measurement of the Be-7 Solar Neutrino Flux with 192 Days of Borexino Data*, Phys. Rev. Lett. **101**, 091302 (2008), arXiv:0805.3843 [astro-ph].

[254] D. G. Michael et al., *Observation of muon neutrino disappearance with the MINOS detectors and the NuMI neutrino beam*, Phys. Rev. Lett. **97**, 191801 (2006), arXiv:hep-ex/0607088.

[255] K. Eguchi et al., *First Results from KamLAND: Evidence for Reactor Antineutrino Disappearance*, Phys. Rev. Lett. **90**, 021802, 021802 (2003), arXiv:hep-ex/0212021 [hep-ex].

[256] F. P. An et al., *Observation of electron-antineutrino disappearance at Daya Bay*, Phys. Rev. Lett. **108**, 171803 (2012), arXiv:1203.1669 [hep-ex].

[257] J. K. Ahn et al., *Observation of Reactor Electron Antineutrino Disappearance in the RENO Experiment*, Phys. Rev. Lett. **108**, 191802 (2012), arXiv:1204.0626 [hep-ex].

[258] Y. Abe et al., *Indication of Reactor $\bar{\nu}_e$ Disappearance in the Double Chooz Experiment*, Phys. Rev. Lett. **108**, 131801 (2012), arXiv:1112.6353 [hep-ex].

[259] K. Abe et al., *Evidence of Electron Neutrino Appearance in a Muon Neutrino Beam*, Phys. Rev. D **88**, 032002 (2013), arXiv:1304.0841 [hep-ex].

[260] M. Aker et al., *Direct neutrino-mass measurement with sub-electronvolt sensitivity*, Nature Phys. **18**, 160 (2022), arXiv:2105.08533 [hep-ex].

[261] A. Gando et al., *Search for Majorana Neutrinos near the Inverted Mass Hierarchy Region with KamLAND-Zen*, Phys. Rev. Lett. **117**, [Addendum: Phys.Rev.Lett. 117, 109903 (2016)], 082503 (2016), arXiv:1605.02889 [hep-ex].

[262] M. Agostini et al., *Final Results of GERDA on the Search for Neutrinoless Double-β Decay*, Phys. Rev. Lett. **125**, 252502 (2020), arXiv:2009.06079 [nucl-ex].

[263] J. Lesgourgues and S. Pastor, *Massive neutrinos and cosmology*, Phys. Rep. **429**, 307 (2006), arXiv:astro-ph/0603494 [astro-ph].

[264] J. Lesgourgues and S. Pastor, *Neutrino mass from Cosmology*, arXiv e-prints, arXiv:1212.6154, arXiv:1212.6154 (2012), arXiv:1212.6154 [hep-ph].

[265] Y. Y. Y. Wong, *Neutrino mass in cosmology: status and prospects*, Ann. Rev. Nucl. Part. Sci. **61**, 69 (2011), arXiv:1111.1436 [astro-ph.CO].

[266] M. Lattanzi and M. Gerbino, *Status of neutrino properties and future prospects - Cosmological and astrophysical constraints*, Front. in Phys. **5**, 70 (2018), arXiv:1712.07109 [astro-ph.CO].

[267] R. Cowsik and J. McClelland, *An Upper Limit on the Neutrino Rest Mass*, Phys. Rev. Lett. **29**, 669 (1972).

[268] R. Cowsik and J. McClelland, *Gravity of Neutrinos of Nonzero Mass in Astrophysics*, ApJ **180**, 7 (1973).

[269] A. S. Szalay and G. Marx, *Neutrino rest mass from cosmology.* A&A **49**, 437 (1976).

[270] S. S. Gershtein and Y. B. Zel'dovich, *Rest Mass of Muonic Neutrino and Cosmology*, ZhETF Pisma Redaktsiiu **4**, 174 (1966).

[271] W. Hu, D. J. Eisenstein, and M. Tegmark, *Weighing Neutrinos with Galaxy Surveys*, Phys. Rev. Lett. **80**, 5255 (1998), arXiv:astro-ph/9712057 [astro-ph].

[272] K. N. Abazajian et al., *Cosmological and astrophysical neutrino mass measurements*, Astroparticle Physics **35**, 177 (2011), arXiv:1103.5083 [astro-ph.CO].

[273] N. Aghanim, S. Majumdar, and J. Silk, *Secondary anisotropies of the CMB*, Reports on Progress in Physics **71**, 066902, 066902 (2008), arXiv:0711.0518 [astro-ph].

[274] A. Lewis and A. Challinor, *Weak gravitational lensing of the CMB*, Phys. Rep. **429**, 1 (2006), arXiv:astro-ph/0601594 [astro-ph].

[275] R. de Putter, O. Zahn, and E. V. Linder, *CMB lensing constraints on neutrinos and dark energy*, Phys. Rev. D **79**, 065033, 065033 (2009), arXiv:0901.0916 [astro-ph.CO].

[276] R. Allison et al., *Towards a cosmological neutrino mass detection*, Phys. Rev. D **92**, 123535, 123535 (2015), arXiv:1509.07471 [astro-ph.CO].

[277] M. C. Gonzalez-Garcia, M. Maltoni, and T. Schwetz, *NuFIT: Three-Flavour Global Analyses of Neutrino Oscillation Experiments*, arXiv e-prints, arXiv:2111.03086, arXiv:2111.03086 (2021), arXiv:2111.03086 [hep-ph].

[278] A. Font-Ribera et al., *DESI and other Dark Energy experiments in the era of neutrino mass measurements*, J. Cosmology Astropart. Phys. **2014**, 023, 023 (2014), arXiv:1308.4164 [astro-ph.CO].

[279] T. Sprenger et al., *Cosmology in the era of Euclid and the Square Kilometre Array*, J. Cosmology Astropart. Phys. **2019**, 047, 047 (2019), arXiv:1801.08331 [astro-ph.CO].

[280] X. Qian and P. Vogel, *Neutrino mass hierarchy*, Progress in Particle and Nuclear Physics **83**, 1 (2015), arXiv:1505.01891 [hep-ex].

[281] S. Dell'Oro et al., *Neutrinoless double beta decay: 2015 review*, Adv. High Energy Phys. **2016**, 2162659 (2016), arXiv:1601.07512 [hep-ph].

[282] M. Agostini, G. Benato, and J. Detwiler, *Discovery probability of next-generation neutrinoless double- β decay experiments*, Phys. Rev. D **96**, 053001 (2017), arXiv:1705.02996 [hep-ex].

[283] A. Kashlinsky et al., *Electromagnetic probes of primordial black holes as dark matter*, (2019), arXiv:1903.04424 [astro-ph.CO].

[284] V. Gluscevic et al., *Cosmological Probes of Dark Matter Interactions: The Next Decade*, (2019), arXiv:1903.05140 [astro-ph.CO].

[285] K. N. Abazajian et al., *Light Sterile Neutrinos: A White Paper*, (2012), arXiv:1204.5379 [hep-ph].

[286] H. B. Kim and J. E. Kim, *Late decaying axino as CDM and its lifetime bound*, Physics Letters B **527**, 18 (2002).

[287] K. Hamaguchi, K. Nakayama, and Y. Tang, *Gravitino/Axino as Decaying Dark Matter and Cosmological Tensions*, Phys. Lett. **B772**, 415 (2017), arXiv:1705.04521 [hep-ph].

[288] V. Berezinsky, A. Masiero, and J. Valle, *Cosmological signatures of supersymmetry with spontaneously broken R parity*, Physics Letters B **266**, 382 (1991).

[289] D. P. Finkbeiner and N. Weiner, *Exciting Dark Matter and the INTEGRAL/SPI 511 keV signal*, Phys. Rev. **D76**, 083519 (2007), arXiv:astro-ph/0702587 [astro-ph].

[290] D. P. Finkbeiner and N. Weiner, *X-ray line from exciting dark matter*, Phys. Rev. **D94**, 083002 (2016), arXiv:1402.6671 [hep-ph].

[291] D. E. Kaplan et al., *Atomic Dark Matter*, JCAP **1005**, 021 (2010), arXiv:0909.0753 [hep-ph].

[292] G. Jungman, M. Kamionkowski, and K. Griest, *Supersymmetric dark matter*, Phys. Rept. **267**, 195 (1996), arXiv:hep-ph/9506380 [hep-ph].

[293] T. Lin, *Dark matter models and direct detection*, PoS **333**, 009 (2019), arXiv:1904.07915 [hep-ph].

[294] T. R. Slatyer, *TASI Lectures on Indirect Detection of Dark Matter*, arXiv e-prints, arXiv:1710.05137, arXiv:1710.05137 (2017), arXiv:1710.05137 [hep-ph].

[295] S. Galli et al., *CMB constraints on Dark Matter models with large annihilation cross-section*, Phys. Rev. **D80**, 023505 (2009), arXiv:0905.0003 [astro-ph.CO].

[296] T. R. Slatyer, N. Padmanabhan, and D. P. Finkbeiner, *CMB Constraints on WIMP Annihilation: Energy Absorption During the Recombination Epoch*, Phys. Rev. **D80**, 043526 (2009), arXiv:0906.1197 [astro-ph.CO].

[297] G. Huetsi, A. Hektor, and M. Raidal, *Constraints on leptonically annihilating Dark Matter from reionization and extragalactic gamma background*, Astron. Astrophys. **505**, 999 (2009), arXiv:0906.4550 [astro-ph.CO].

[298] S. Galli et al., *Updated CMB constraints on Dark Matter annihilation cross-sections*, Phys. Rev. **D84**, 027302 (2011), arXiv:1106.1528 [astro-ph.CO].

[299] D. P. Finkbeiner et al., *Searching for Dark Matter in the CMB: A Compact Parameterization of Energy Injection from New Physics*, Phys. Rev. **D85**, 043522 (2012), arXiv:1109.6322 [astro-ph.CO].

[300] P. A. R. Ade et al., *Planck 2015 results. XIII. Cosmological parameters*, Astron. Astrophys. **594**, A13 (2016), arXiv:1502.01589 [astro-ph.CO].

[301] J. R. Ellis, J. E. Kim, and D. V. Nanopoulos, *Cosmological Gravitino Regeneration and Decay*, Phys. Lett. **145B**, 181 (1984).

[302] S. Sarkar and A. M. Cooper-Sarkar, *Cosmological and experimental constraints on the tau neutrino*, Phys. Lett. **148B**, [,I.362(1984)], 347 (1984).

[303] W. Hu and J. Silk, *Thermalization constraints and spectral distortions for massive unstable relic particles*, Phys. Rev. Lett. **70**, 2661 (1993).

[304] P. McDonald, R. J. Scherrer, and T. P. Walker, *Cosmic microwave background constraint on residual annihilations of relic particles*, Phys. Rev. **D63**, 023001 (2001), arXiv:astro-ph/0008134 [astro-ph].

[305] J. Chluba and R. A. Sunyaev, *The evolution of CMB spectral distortions in the early Universe*, Mon. Not. Roy. Astron. Soc. **419**, 1294 (2012), arXiv:1109.6552 [astro-ph.CO].

[306] J. Chluba, *Distinguishing different scenarios of early energy release with spectral distortions of the cosmic microwave background*, Mon. Not. Roy. Astron. Soc. **436**, 2232 (2013), arXiv:1304.6121 [astro-ph.CO].

[307] J. Chluba and D. Jeong, *Teasing bits of information out of the CMB energy spectrum*, Mon. Not. Roy. Astron. Soc. **438**, 2065 (2014), arXiv:1306.5751 [astro-ph.CO].

[308] M. Pospelov and J. Pradler, *Big Bang Nucleosynthesis as a Probe of New Physics*, Ann. Rev. Nucl. Part. Sci. **60**, 539 (2010), arXiv:1011.1054 [hep-ph].

[309] M. Lucca et al., *The synergy between CMB spectral distortions and anisotropies*, (2019), arXiv:1910.04619 [astro-ph.CO].

[310] T. Cohen et al., *Gamma-ray Constraints on Decaying Dark Matter and Implications for IceCube*, Phys. Rev. Lett. **119**, 021102 (2017), arXiv:1612.05638 [hep-ph].

[311] C. Blanco and D. Hooper, *Constraints on Decaying Dark Matter from the Isotropic Gamma-Ray Background*, JCAP **1903**, 019 (2019), arXiv:1811.05988 [astro-ph.HE].

[312] G. Giesen et al., *CMB photons shedding light on dark matter*, JCAP **1212**, 008 (2012), arXiv:1209.0247 [astro-ph.CO].

[313] L. Lopez-Honorez et al., *Constraints on dark matter annihilation from CMB observations before Planck*, JCAP **1307**, 046 (2013), arXiv:1303.5094 [astro-ph.CO].

[314] M. Kawasaki, K. Nakayama, and T. Sekiguchi, *CMB Constraint on Dark Matter Annihilation after Planck 2015*, Phys. Lett. **B756**, 212 (2016), arXiv:1512.08015 [astro-ph.CO].

[315] A. Abramowski et al., *Search for dark matter annihilation signatures in H.E.S.S. observations of Dwarf Spheroidal Galaxies*, Phys. Rev. **D90**, 112012 (2014), arXiv:1410.2589 [astro-ph.HE].

[316] M. Ackermann et al., *Searching for Dark Matter Annihilation from Milky Way Dwarf Spheroidal Galaxies with Six Years of Fermi Large Area Telescope Data*, Phys. Rev. Lett. **115**, 231301 (2015), arXiv:1503.02641 [astro-ph.HE].

[317] M. S. Madhavacheril, N. Sehgal, and T. R. Slatyer, *Current Dark Matter Annihilation Constraints from CMB and Low-Redshift Data*, Phys. Rev. **D89**, 103508 (2014), arXiv:1310.3815 [astro-ph.CO].

[318] D. Green, P. D. Meerburg, and J. Meyers, *Aspects of Dark Matter Annihilation in Cosmology*, JCAP **1904**, 025 (2019), arXiv:1804.01055 [astro-ph.CO].

[319] E. D. Kovetz et al., *Line-Intensity Mapping: 2017 Status Report*, (2017), arXiv:1709.09066 [astro-ph.CO].

[320] E. D. Kovetz et al., *Astrophysics and Cosmology with Line-Intensity Mapping*, (2019), arXiv:1903.04496 [astro-ph.CO].

[321] J. L. Bernal et al., *A User's Guide to Extracting Cosmological Information from Line-Intensity Maps*, (2019), arXiv:1907.10067 [astro-ph.CO].

[322] J. L. Bernal, P. C. Breysse, and E. D. Kovetz, *The Cosmic Expansion History from Line-Intensity Mapping*, (2019), arXiv:1907.10065 [astro-ph.CO].

[323] J. B. Muñoz, *Standard Ruler at Cosmic Dawn*, Phys. Rev. Lett. **123**, 131301 (2019), arXiv:1904.07868 [astro-ph.CO].

[324] P. C. Breysse, Y. Ali-Hamoud, and C. M. Hirata, *Ultimate frontier of 21-cm cosmology*, Phys. Rev. **D98**, 043520 (2018), arXiv:1804.10626 [astro-ph.CO].

[325] S. R. Furlanetto, S. P. Oh, and E. Pierpaoli, *The Effects of Dark Matter Decay and Annihilation on the High-Redshift 21 cm Background*, Phys. Rev. **D74**, 103502 (2006), arXiv:astro-ph/0608385 [astro-ph].

[326] Y. A. Shchekinov and E. O. Vasiliev, *Particle decay in the early universe: predictions for 21 cm*, Mon. Not. Roy. Astron. Soc. **379**, 1003 (2007), arXiv:astro-ph/0604231 [astro-ph].

[327] M. Valdes et al., *Constraining DM through 21 cm observations*, Mon. Not. Roy. Astron. Soc. **377**, 245 (2007), arXiv:astro-ph/0701301 [astro-ph].

[328] M. Valdes et al., *The nature of dark matter from the global high redshift HI 21 cm signal*, Mon. Not. Roy. Astron. Soc. **429**, 1705 (2013), arXiv:1209.2120 [astro-ph.CO].

[329] Y. Ali-Haïmoud, P. D. Meerburg, and S. Yuan, *New light on 21 cm intensity fluctuations from the dark ages*, Phys. Rev. D **89**, 083506 (2014), arXiv:1312.4948 [astro-ph.CO].

[330] C. Evoli, A. Mesinger, and A. Ferrara, *Unveiling the nature of dark matter with high redshift 21 cm line experiments*, JCAP **11**, 024 (2014), arXiv:1408.1109 [astro-ph.HE].

[331] L. Lopez-Honorez et al., *The 21 cm signal and the interplay between dark matter annihilations and astrophysical processes*, JCAP **1608**, 004 (2016), arXiv:1603.06795 [astro-ph.CO].

[332] V. Poulin, P. D. Serpico, and J. Lesgourgues, *A fresh look at linear cosmological constraints on a decaying dark matter component*, JCAP **1608**, 036 (2016), arXiv:1606.02073 [astro-ph.CO].

[333] M. Cirelli, F. Iocco, and P. Panci, *Constraints on Dark Matter annihilations from reionization and heating of the intergalactic gas*, JCAP **0910**, 009 (2009), arXiv:0907.0719 [astro-ph.CO].

[334] H. Liu, T. R. Slatyer, and J. Zavala, *Contributions to cosmic reionization from dark matter annihilation and decay*, Phys. Rev. **D94**, 063507 (2016), arXiv:1604.02457 [astro-ph.CO].

[335] A. Cohen et al., *Charting the Parameter Space of the Global 21-cm Signal*, Mon. Not. Roy. Astron. Soc. **472**, 1915 (2017), arXiv:1609.02312 [astro-ph.CO].

[336] A. Cohen, A. Fialkov, and R. Barkana, *Charting the Parameter Space of the 21-cm Power Spectrum*, Mon. Not. Roy. Astron. Soc. **478**, 2193 (2018), arXiv:1709.02122 [astro-ph.CO].

[337] J. O. Burns et al., *Dark Cosmology: Investigating Dark Matter & Exotic Physics in the Dark Ages using the Redshifted 21-cm Global Spectrum*, (2019), arXiv:1902.06147 [astro-ph.CO].

[338] S. Furlanetto et al., *Astro 2020 Science White Paper: Fundamental Cosmology in the Dark Ages with 21-cm Line Fluctuations*, (2019), arXiv:1903.06212 [astro-ph.CO].

[339] J. B. Muoz et al., *Towards a measurement of the spectral runnings*, JCAP **1705**, 032 (2017), arXiv:1611.05883 [astro-ph.CO].

[340] A. Pourtsidou, *Synergistic tests of inflation*, (2016), arXiv:1612.05138 [astro-ph.CO].

[341] T. Sekiguchi et al., *21 cm Angular Power Spectrum from Minihalos as a Probe of Primordial Spectral Runnings*, JCAP **1802**, 053 (2018), arXiv:1705.00405 [astro-ph.CO].

[342] J. B. Muoz, Y. Ali-Hamoud, and M. Kamionkowski, *Primordial non-gaussianity from the bispectrum of 21-cm fluctuations in the dark ages*, Phys. Rev. **D92**, 083508 (2015), arXiv:1506.04152 [astro-ph.CO].

[343] J. L. Bernal et al., *Signatures of primordial black holes as seeds of supermassive black holes*, J. Cosmology Astropart. Phys. **2018**, 017, 017 (2018), arXiv:1712.01311 [astro-ph.CO].

[344] O. Mena et al., *Constraining the primordial black hole abundance with 21-cm cosmology*, Phys. Rev. D **100**, 043540 (2019), arXiv:1906.07735 [astro-ph.CO].

[345] D. J. Bacon et al., *Cosmology with Phase 1 of the Square Kilometre Array: Red Book 2018: Technical specifications and performance forecasts*, Submitted to: Publ. Astron. Soc. Austral. (2018), arXiv:1811.02743 [astro-ph.CO].

[346] C. L. Carilli, J. N. Hewitt, and A. Loeb, *Low frequency radio astronomy from the moon: Cosmic reionization and more*, in Workshop on Astrophysics Enabled by the Return to the Moon Baltimore, Maryland, November 28-30, 2006 (2007), arXiv:astro-ph/0702070 [ASTRO-PH].

[347] S. Jester and H. Falcke, *Science with a lunar low-frequency array: From the dark ages of the Universe to nearby exoplanets*, New Astronomy Reviews **53**, 1 (2009).

[348] J. O. Burns, T. J. W. Lazio, and W. Bottke, *Astrophysics Conducted by the Lunar University Network for Astrophysics Research (LUNAR) and the Center for Lunar Origins (CLOE)*, (2012), arXiv:1209.2233 [astro-ph.CO].

[349] J. Burns et al., *FARSIDE: A Low Radio Frequency Interferometric Array on the Lunar Farside*, in Bulletin of the American Astronomical Society, Vol. 51 (Sept. 2019), p. 178, arXiv:1907.05407 [astro-ph.IM].

[350] J. Silk et al., *A White Paper on Cosmology with a Lunar Radio Array*, in preparation.

[351] S. A. Wouthuysen, *On the excitation mechanism of the 21-cm (radio-frequency) interstellar hydrogen emission line.* The Astronomical Journal **57**, 31 (1952).

[352] G. B. Field, *The Spin Temperature of Intergalactic Neutral Hydrogen.* The Astrophysical Journal **129**, 536 (1959).

[353] C. M. Hirata, *Wouthuysen-Field coupling strength and application to high-redshift 21 cm radiation*, Mon. Not. Roy. Astron. Soc. **367**, 259 (2006), arXiv:astro-ph/0507102 [astro-ph].

[354] G. Field, *Excitation of the Hydrogen 21-CM Line*, Proceedings of the IRE **46**, 240 (1958).

[355] M. Kuhlen, P. Madau, and R. Montgomery, *The spin temperature and 21cm brightness of the intergalactic medium in the pre-reionization era*, Astrophys. J. **637**, L1 (2006), arXiv:astro-ph/0510814 [astro-ph].

[356] H. Liszt, *The spin temperature of warm interstellar h I*, Astron. Astrophys. **371**, 698 (2001), arXiv:astro-ph/0103246 [astro-ph].

[357] V. Poulin, P. D. Serpico, and J. Lesgourgues, *Dark Matter annihilations in halos and high-redshift sources of reionization of the universe*, JCAP **1512**, 041 (2015), arXiv:1508.01370 [astro-ph.CO].

[358] A. Pillepich, C. Porciani, and S. Matarrese, *The bispectrum of redshifted 21-cm fluctuations from the dark ages*, Astrophys. J. **662**, 1 (2007), arXiv:astro-ph/0611126 [astro-ph].

[359] S. Bharadwaj and S. S. Ali, *The CMBR fluctuations from HI perturbations prior to reionization*, Mon. Not. Roy. Astron. Soc. **352**, 142 (2004), arXiv:astro-ph/0401206 [astro-ph].

[360] D. N. Limber, *The Analysis of Counts of the Extragalactic Nebulae in Terms of a Fluctuating Density Field.* The Astrophysical Journal **117**, 134 (1953).

[361] M. LoVerde and N. Afshordi, *Extended Limber Approximation*, Phys. Rev. **D78**, 123506 (2008), arXiv:0809.5112 [astro-ph].

[362] D. Blas, J. Lesgourgues, and T. Tram, *The Cosmic Linear Anisotropy Solving System (CLASS) II: Approximation schemes*, JCAP **07**, 034 (2011), arXiv:1104.2933 [astro-ph.CO].

[363] J. Chluba and R. M. Thomas, *Towards a complete treatment of the cosmological recombination problem*, Mon. Not. Roy. Astron. Soc. **412**, 748 (2011), arXiv:1010.3631 [astro-ph.CO].

[364] P. J. E. Peebles, *Recombination of the Primeval Plasma*, Astrophys. J. **153**, 1 (1968).

[365] S. Seager, D. D. Sasselov, and D. Scott, *A new calculation of the recombination epoch*, Astrophys. J. Lett. **523**, L1 (1999), arXiv:astro-ph/9909275.

[366] J. Chluba, *Could the Cosmological Recombination Spectrum Help Us Understand Annihilating Dark Matter?*, Mon. Not. Roy. Astron. Soc. **402**, 1195 (2010), arXiv:0910.3663 [astro-ph.CO].

[367] Y. Ali-Haimoud and C. M. Hirata, *HyRec: A fast and highly accurate primordial hydrogen and helium recombination code*, Phys. Rev. **D83**, 043513 (2011), arXiv:1011.3758 [astro-ph.CO].

[368] T. R. Slatyer, *Energy Injection And Absorption In The Cosmic Dark Ages*, Phys. Rev. **D87**, 123513 (2013), arXiv:1211.0283 [astro-ph.CO].

[369] X.-L. Chen and M. Kamionkowski, *Particle decays during the cosmic dark ages*, Phys. Rev. **D70**, 043502 (2004), arXiv:astro-ph/0310473 [astro-ph].

[370] S. Galli et al., *Systematic Uncertainties In Constraining Dark Matter Annihilation From The Cosmic Microwave Background*, Phys. Rev. **D88**, 063502 (2013), arXiv:1306.0563 [astro-ph.CO].

[371] T. R. Slatyer, *Indirect Dark Matter Signatures in the Cosmic Dark Ages II. Ionization, Heating and Photon Production from Arbitrary Energy Injections*, Phys. Rev. **D93**, 023521 (2016), arXiv:1506.03812 [astro-ph.CO].

[372] H. Liu, G. W. Ridgway, and T. R. Slatyer, *DarkHistory: A code package for calculating modified cosmic ionization and thermal histories with dark matter and other exotic energy injections*, (2019), arXiv:1904.09296 [astro-ph.CO].

[373] X.-L. Chen and J. Miralda-Escude, *The spin - kinetic temperature coupling and the heating rate due to Lyman - alpha scattering before reionization: Predictions for 21cm emission and absorption*, Astrophys. J. **602**, 1 (2004), arXiv:astro-ph/0303395.

[374] S. Furlanetto and J. R. Pritchard, *The Scattering of Lyman-series Photons in the Intergalactic Medium*, Mon. Not. Roy. Astron. Soc. **372**, 1093 (2006), arXiv:astro-ph/0605680.

[375] S. R. Furlanetto, *The Fundamentals of the 21-cm Line*, (2019), arXiv:1909.13740 [astro-ph.CO].

[376] A. Natarajan and D. J. Schwarz, *Dark matter annihilation and its effect on CMB and Hydrogen 21 cm observations*, Phys. Rev. **D80**, 043529 (2009), arXiv:0903.4485 [astro-ph.CO].

[377] J. Hisano et al., *Non-perturbative effect on dark matter annihilation and gamma ray signature from galactic center*, Phys. Rev. **D71**, 063528 (2005), arXiv:hep-ph/0412403 [hep-ph].

[378] R. A. Fisher, *The Logic of Inductive Inference*, Journal of the Royal Statistical Society **98**, 39 (1935).

[379] M. Tegmark, A. Taylor, and A. Heavens, *Karhunen-Loeve eigenvalue problems in cosmology: How should we tackle large data sets?*, Astrophys. J. **480**, 22 (1997), arXiv:astro-ph/9603021 [astro-ph].

[380] A. H. Jaffe, M. Kamionkowski, and L.-M. Wang, *Polarization pursuers' guide*, Phys. Rev. **D61**, 083501 (2000), arXiv:astro-ph/9909281 [astro-ph].

[381] L. Knox and Y.-S. Song, *A Limit on the detectability of the energy scale of inflation*, Phys. Rev. Lett. **89**, 011303 (2002), arXiv:astro-ph/0202286 [astro-ph].

[382] M. Kesden, A. Cooray, and M. Kamionkowski, *Separation of gravitational wave and cosmic shear contributions to cosmic microwave background polarization*, Phys. Rev. Lett. **89**, 011304 (2002), arXiv:astro-ph/0202434 [astro-ph].

[383] M. Zaldarriaga, S. R. Furlanetto, and L. Hernquist, *21 Centimeter fluctuations from cosmic gas at high redshifts*, Astrophys. J. **608**, 622 (2004), arXiv:astro-ph/0311514 [astro-ph].

[384] T. J. Mozdzen et al., *Improved measurement of the spectral index of the diffuse radio background between 90 and 190 MHz*, Mon. Not. Roy. Astron. Soc. **464**, 4995 (2017), arXiv:1609.08705 [astro-ph.IM].

[385] F. Calore et al., *A Tale of Tails: Dark Matter Interpretations of the Fermi GeV Excess in Light of Background Model Systematics*, Phys. Rev. **D91**, 063003 (2015), arXiv:1411.4647 [hep-ph].

[386] I. Cholis, T. Linden, and D. Hooper, *A Robust Excess in the Cosmic-Ray Antiproton Spectrum: Implications for Annihilating Dark Matter*, Phys. Rev. **D99**, 103026 (2019), arXiv:1903.02549 [astro-ph.HE].

[387] E. Bulbul et al., *Detection of An Unidentified Emission Line in the Stacked X-ray spectrum of Galaxy Clusters*, Astrophys. J. **789**, 13 (2014), arXiv:1402.2301 [astro-ph.CO].

[388] A. Boyarsky et al., *Unidentified Line in X-Ray Spectra of the Andromeda Galaxy and Perseus Galaxy Cluster*, Phys. Rev. Lett. **113**, 251301 (2014), arXiv:1402.4119 [astro-ph.CO].

[389] J.-C. Park, S. C. Park, and K. Kong, *X-ray line signal from 7 keV axino dark matter decay*, Phys. Lett. **B733**, 217 (2014), arXiv:1403.1536 [hep-ph].

[390] M. Drewes et al., *A White Paper on keV Sterile Neutrino Dark Matter*, JCAP **1701**, 025 (2017), arXiv:1602.04816 [hep-ph].

[391] C. Cosme, J. G. Rosa, and O. Bertolami, *Scalar field dark matter with spontaneous symmetry breaking and the* 3.5 *keV line*, Phys. Lett. **B781**, 639 (2018), arXiv:1709.09674 [hep-ph].

[392] P. Stcker et al., *Exotic energy injection with ExoCLASS: Application to the Higgs portal model and evaporating black holes*, JCAP **1803**, 018 (2018), arXiv:1801.01871 [astro-ph.CO].

[393] J. B. Muoz, E. D. Kovetz, and Y. Ali-Hamoud, *Heating of Baryons due to Scattering with Dark Matter During the Dark Ages*, Phys. Rev. **D92**, 083528 (2015), arXiv:1509.00029 [astro-ph.CO].

[394] H. Tashiro, K. Kadota, and J. Silk, *Effects of dark matter-baryon scattering on redshifted 21 cm signals*, Phys. Rev. **D90**, 083522 (2014), arXiv:1408.2571 [astro-ph.CO].

[395] L. Roszkowski, E. M. Sessolo, and S. Trojanowski, *WIMP dark matter candidates and searches—current status and future prospects*, Rept. Prog. Phys. **81**, 066201 (2018), arXiv:1707.06277 [hep-ph].

[396] E. O. Nadler et al., *Constraints on Dark Matter Microphysics from the Milky Way Satellite Population*, Astrophys. J. Lett. **878**, [Erratum: Astrophys.J.Lett. 897, L46 (2020), Erratum: Astrophys.J. 897, L46 (2020)], 32 (2019), arXiv:1904.10000 [astro-ph.CO].

[397] E. O. Nadler et al., *Milky Way Satellite Census. III. Constraints on Dark Matter Properties from Observations of Milky Way Satellite Galaxies*, Phys. Rev. Lett. **126**, 091101 (2021), arXiv:2008.00022 [astro-ph.CO].

[398] K. Maamari et al., *Bounds on velocity-dependent dark matter-proton scattering from Milky Way satellite abundance*, Astrophys. J. Lett. **907**, L46 (2021), arXiv:2010.02936 [astro-ph.CO].

[399] K. K. Rogers, C. Dvorkin, and H. V. Peiris, *New limits on light dark matter - proton cross section from the cosmic large-scale structure*, (2021), arXiv:2111.10386 [astro-ph.CO].

[400] J. B. Bauer et al., *Intensity Mapping as a Probe of Axion Dark Matter*, Mon. Not. Roy. Astron. Soc. **500**, 3162 (2020), arXiv:2003.09655 [astro-ph.CO].

[401] J. L. Bernal, A. Caputo, and M. Kamionkowski, *Strategies to Detect Dark-Matter Decays with Line-Intensity Mapping*, Phys. Rev. D **103**, 063523 (2021), arXiv:2012.00771 [astro-ph.CO].

[402] A. Fialkov, R. Barkana, and A. Cohen, *Constraining Baryon–Dark Matter Scattering with the Cosmic Dawn 21-cm Signal*, Phys. Rev. Lett. **121**, 011101 (2018), arXiv:1802.10577 [astro-ph.CO].

[403] A. Lidz and L. Hui, *Implications of a prereionization 21-cm absorption signal for fuzzy dark matter*, Phys. Rev. D **98**, 023011 (2018), arXiv:1805.01253 [astro-ph.CO].

[404] J. B. Muñoz and A. Loeb, *A small amount of mini-charged dark matter could cool the baryons in the early Universe*, Nature **557**, 684 (2018), arXiv:1802.10094 [astro-ph.CO].

[405] J. B. Muñoz, C. Dvorkin, and A. Loeb, *21-cm Fluctuations from Charged Dark Matter*, Phys. Rev. Lett. **121**, 121301 (2018), arXiv:1804.01092 [astro-ph.CO].

[406] R. Barkana, *Possible interaction between baryons and dark-matter particles revealed by the first stars*, (2018), eprint: 1803.06698.

[407] J. D. Bowman et al., *An absorption profile centred at 78 megahertz in the sky-averaged spectrum*, Nature **555**, 67 (2018), arXiv:1810.05912 [astro-ph.CO].

[408] S. Singh et al., *On the detection of a cosmic dawn signal in the radio background*, Nature Astronomy, 10.1038/s41550-022-01610-5 (2022), arXiv:2112.06778 [astro-ph.CO].

[409] D. C. Price et al., *Design and characterization of the Large-aperture Experiment to Detect the Dark Age (LEDA) radiometer systems*, MNRAS **478**, 4193 (2018), arXiv:1709.09313 [astro-ph.IM].

[410] D. R. DeBoer et al., *Hydrogen Epoch of Reionization Array (HERA)*, Publ. Astron. Soc. Pac. **129**, 045001 (2017), arXiv:1606.07473 [astro-ph.IM].

[411] D. J. Bacon et al., *Cosmology with Phase 1 of the Square Kilometre Array: Red Book 2018: Technical specifications and performance forecasts*, Publ. Astron. Soc. Austral. **37**, e007 (2020), arXiv:1811.02743 [astro-ph.CO].

[412] A. Lewis, *Linear effects of perturbed recombination*, Phys. Rev. D **76**, 063001 (2007), arXiv:0707.2727 [astro-ph].

[413] S. Naoz and R. Barkana, *Growth of linear perturbations before the era of the first galaxies*, Mon. Not. Roy. Astron. Soc. **362**, 1047 (2005), arXiv:astro-ph/0503196.

[414] D. Tseliakhovich, R. Barkana, and C. Hirata, *Suppression and Spatial Variation of Early Galaxies and Minihalos*, Mon. Not. Roy. Astron. Soc. **418**, 906 (2011), arXiv:1012.2574 [astro-ph.CO].

[415] D. Tseliakhovich and C. Hirata, *Relative velocity of dark matter and baryonic fluids and the formation of the first structures*, Phys. Rev. D **82**, 083520 (2010), arXiv:1005.2416 [astro-ph.CO].

[416] N. Dalal, U.-L. Pen, and U. Seljak, *Large-scale BAO signatures of the smallest galaxies*, JCAP **11**, 007 (2010), arXiv:1009.4704 [astro-ph.CO].

[417] A. Fialkov et al., *Impact of the Relative Motion between the Dark Matter and Baryons on the First Stars*, Mon. Not. Roy. Astron. Soc. **424**, 1335 (2012), arXiv:1110.2111 [astro-ph.CO].

[418] L. Senatore, S. Tassev, and M. Zaldarriaga, *Cosmological Perturbations at Second Order and Recombination Perturbed*, JCAP **08**, 031 (2009), arXiv:0812.3652 [astro-ph].

[419] Y. Ali-Haimoud and C. M. Hirata, *Ultrafast effective multi-level atom method for primordial hydrogen recombination*, Phys. Rev. D **82**, 063521 (2010), arXiv:1006.1355 [astro-ph.CO].

[420] Y. Ali-Haimoud and C. M. Hirata, *HyRec: A fast and highly accurate primordial hydrogen and helium recombination code*, Phys. Rev. D **83**, 043513 (2011), arXiv:1011.3758 [astro-ph.CO].

[421] A. Lewis and A. Challinor, *The 21cm angular-power spectrum from the dark ages*, Phys. Rev. D **76**, 083005 (2007), arXiv:astro-ph/0702600.

[422] T. Driskell et al., *Bounds on dark matter-baryon scattering from the global 21 cm signal and the suppressed matter power spectrum*, In prep. (2022).

[423] C. Kraus et al., *Final results from phase II of the Mainz neutrino mass search in tritium β decay*, The European Physical Journal C **40**, 447–468 (2005).

[424] J. R. Bond, G. Efstathiou, and J. Silk, *Massive Neutrinos and the Large Scale Structure of the Universe*, Phys. Rev. Lett. **45**, 1980 (1980).

[425] W. Hu, D. J. Eisenstein, and M. Tegmark, *Weighing neutrinos with galaxy surveys*, Phys. Rev. Lett. **80**, 5255 (1998), arXiv:astro-ph/9712057 [astro-ph].

[426] J. Lesgourgues and S. Pastor, *Massive neutrinos and cosmology*, Phys.Rept. **429**, 307 (2006), arXiv:astro-ph/0603494 [astro-ph].

[427] R. Jimenez et al., *Can we measure the neutrino mass hierarchy in the sky?*, JCAP **2010**, 035, 035 (2010), arXiv:1003.5918 [astro-ph.CO].

[428] C. Wagner, L. Verde, and R. Jimenez, *Effects of the neutrino mass splitting on the non-linear matter power spectrum*, Astrophys. J. **752**, L31 (2012), arXiv:1203.5342 [astro-ph.CO].

[429] S. Alam et al., *Completed SDSS-IV extended Baryon Oscillation Spectroscopic Survey: Cosmological implications from two decades of spectroscopic surveys at the Apache Point Observatory*, Physical Review D **103**, 10.1103/physrevd.103.083533 (2021).

[430] N. Palanque-Delabrouille et al., *Hints, neutrino bounds, and WDM constraints from SDSS DR14 Lyman-α and Planck full-survey data*, Journal of Cosmology and Astroparticle Physics **2020**, 038–038 (2020).

[431] F. Simpson et al., *Strong Bayesian evidence for the normal neutrino hierarchy*, JCAP **2017**, 029, 029 (2017), arXiv:1703.03425 [astro-ph.CO].

[432] H. Murayama and C. Pena-Garay, *Neutrinoless double beta decay in light of SNO salt data*, Phys. Rev. D **69**, 031301 (2004), arXiv:hep-ph/0309114.

[433] M. J. Dolinski, A. W. P. Poon, and W. Rodejohann, *Neutrinoless Double-Beta Decay: Status and Prospects*, Ann. Rev. Nucl. Part. Sci. **69**, 219 (2019), arXiv:1902.04097 [nucl-ex].

[434] A. Giuliani et al., *Double Beta Decay APPEC Committee Report*, (2019), arXiv:1910.04688 [hep-ex].

[435] R. T. Cox, *Probability, frequency and reasonable expectation*, Am.J.Th.Phys **14**, 1 (1946).

[436] A. Jaffe, *H_0 and Odds on Cosmology*, Astrophys.J. **471**, 24 (1996), eprint: arXiv:astro-ph/9501070.

[437] R. Trotta, *Applications of Bayesian model selection to cosmological parameters*, Mon.Not.R.Astron.Soc **378**, 72 (2007), eprint: arXiv:astro-ph/0504022.

[438] A. R. Liddle, *How many cosmological parameters?*, Mon.Not.R.Astron.Soc **351**, L49 (2004), eprint: arXiv:astro-ph/0401198.

[439] D. J. MacKay, *Information theory, inference and learning algorithms* (Cambridge university press, 2003).

[440] A. F. Heavens and E. Sellentin, *Objective Bayesian analysis of neutrino masses and hierarchy*, JCAP **2018**, 047, 047 (2018), arXiv:1802.09450 [astro-ph.CO].

[441] M. Gerbino et al., *A novel approach to quantifying the sensitivity of current and future cosmological datasets to the neutrino mass ordering through Bayesian hierarchical modeling*, Physics Letters B **775**, 239 (2017), arXiv:1611.07847 [astro-ph.CO].

[442] M. Blennow, *On the Bayesian approach to neutrino mass ordering*, JHEP **01**, 139 (2014), arXiv:1311.3183 [hep-ph].

[443] S. Hannestad and T. Schwetz, *Cosmology and the neutrino mass ordering*, JCAP **2016**, 035, 035 (2016), arXiv:1606.04691 [astro-ph.CO].

[444] S. Vagnozzi et al., *Unveiling ν secrets with cosmological data: Neutrino masses and mass hierarchy*, PRD **96**, 123503, 123503 (2017), arXiv:1701.08172 [astro-ph.CO].

[445] A. J. Long et al., *Neutrino mass priors for cosmology from random matrices*, PRD **97**, 043510, 043510 (2018), arXiv:1711.08434 [astro-ph.CO].

[446] S. R. Choudhury and S. Hannestad, *Updated results on neutrino mass and mass hierarchy from cosmology with Planck 2018 likelihoods*, JCAP **2020**, 037, 037 (2020), arXiv:1907.12598 [astro-ph.CO].

[447] S. Gariazzo and O. Mena, *Cosmology-marginalized approaches in Bayesian model comparison: The neutrino mass as a case study*, PRD **99**, 021301, 021301 (2019), arXiv:1812.05449 [astro-ph.CO].

[448] L. T. Hergt et al., *Bayesian evidence for the tensor-to-scalar ratio r and neutrino masses m_ν : Effects of uniform versus logarithmic priors*, PRD **103**, 123511, 123511 (2021), arXiv:2102.11511 [astro-ph.CO].

[449] C. Mahony et al., *Target neutrino mass precision for determining the neutrino hierarchy*, PRD **101**, 083513, 083513 (2020), arXiv:1907.04331 [astro-ph.CO].

[450] M. Aker et al., *Improved Upper Limit on the Neutrino Mass from a Direct Kinematic Method by KATRIN*, Phys. Rev. Lett. **123**, 221802 (2019), arXiv:1909.06048 [hep-ex].

[451] O. Elgaroy et al., *A New limit on the total neutrino mass from the 2dF galaxy redshift survey*, Phys. Rev. Lett. **89**, 061301 (2002), arXiv:astro-ph/0204152.

[452] G. Hinshaw et al., *Nine-Year Wilkinson Microwave Anisotropy Probe (WMAP) Observations: Cosmological Parameter Results*, Astrophys. J. Suppl. **208**, 19 (2013), arXiv:1212.5226 [astro-ph.CO].

[453] P. A. R. Ade et al., *Planck 2013 results. XVI. Cosmological parameters*, Astron. Astrophys. **571**, A16 (2014), arXiv:1303.5076 [astro-ph.CO].

[454] A. J. Cuesta, V. Niro, and L. Verde, *Neutrino mass limits: Robust information from the power spectrum of galaxy surveys*, Physics of the Dark Universe **13**, 77 (2016), arXiv:1511.05983.

[455] R. E. Kass and A. E. Raftery, *Bayes Factors*, Journal of the American Statistical Association **90**, 773 (1995).

[456] M. S. Turner, *The Road to Precision Cosmology*, arXiv e-prints, arXiv:2201.04741, arXiv:2201.04741 (2022), arXiv:2201.04741 [astro-ph.CO].

[457] L. Goodenough and D. Hooper, *Possible Evidence For Dark Matter Annihilation In The Inner Milky Way From The Fermi Gamma Ray Space Telescope*, (2009), arXiv:0910.2998 [hep-ph].

[458] D. Hooper and L. Goodenough, *Dark Matter Annihilation in The Galactic Center As Seen by the Fermi Gamma Ray Space Telescope*, Phys. Lett. B **697**, 412 (2011), arXiv:1010.2752 [hep-ph].

[459] D. Hooper and T. Linden, *On The Origin Of The Gamma Rays From The Galactic Center*, Phys. Rev. D **84**, 123005 (2011), arXiv:1110.0006 [astro-ph.HE].

[460] F. Calore, I. Cholis, and C. Weniger, *Background Model Systematics for the Fermi GeV Excess*, JCAP **03**, 038 (2015), arXiv:1409.0042 [astro-ph.CO].

[461] M. Ajello et al., *Fermi-LAT Observations of High-Energy γ-Ray Emission Toward the Galactic Center*, Astrophys. J. **819**, 44 (2016), arXiv:1511.02938 [astro-ph.HE].

[462] T. Daylan et al., *The characterization of the gamma-ray signal from the central Milky Way: A case for annihilating dark matter*, Phys. Dark Univ. **12**, 1 (2016), arXiv:1402.6703 [astro-ph.HE].

[463] K. N. Abazajian et al., *Astrophysical and Dark Matter Interpretations of Extended Gamma-Ray Emission from the Galactic Center*, Phys. Rev. D **90**, 023526 (2014), arXiv:1402.4090 [astro-ph.HE].

[464] K. J. Mack and D. H. Wesley, *Primordial black holes in the Dark Ages: Observational prospects for future 21cm surveys*, arXiv e-prints, arXiv:0805.1531, arXiv:0805.1531 (2008), arXiv:0805.1531 [astro-ph].

[465] A. Loeb and M. Zaldarriaga, *Measuring the small - scale power spectrum of cosmic density fluctuations through 21 cm tomography prior to the epoch of structure formation*, Phys. Rev. Lett. **92**, 211301 (2004), arXiv:astro-ph/0312134 [astro-ph].

[466] Y. Mao et al., *How accurately can 21cm tomography constrain cosmology?*, Phys. Rev. D **78**, 023529, 023529 (2008), arXiv:0802.1710 [astro-ph].

[467] X. Chen et al., *Reconstructing the Inflationary Landscape with Cosmological Data*, Phys. Rev. Lett. **121**, 161302 (2018), arXiv:1806.05202 [astro-ph.CO].

[468] X. Chen, P. D. Meerburg, and M. Münchmeyer, *The Future of Primordial Features with 21 cm Tomography*, JCAP **09**, 023 (2016), arXiv:1605.09364 [astro-ph.CO].

[469] M. Shiraishi et al., *Violation of statistical isotropy and homogeneity in the 21-cm power spectrum*, Phys. Rev. D **93**, 103506 (2016), arXiv:1603.01206 [astro-ph.CO].

[470] S. Singh et al., *On the detection of a cosmic dawn signal in the radio background*, Nature Astronomy **6**, 607 (2022), arXiv:2112.06778 [astro-ph.CO].

[471] A. Mesinger and S. Furlanetto, *Efficient Simulations of Early Structure Formation and Reionization*, ApJ **669**, 663 (2007), arXiv:0704.0946 [astro-ph].

[472] A. Mesinger, S. Furlanetto, and R. Cen, *21CMFAST: a fast, seminumerical simulation of the high-redshift 21-cm signal*, MNRAS **411**, 955 (2011), arXiv:1003.3878 [astro-ph.CO].

[473] S. Singh et al., *SARAS 2: A Spectral Radiometer for probing Cosmic Dawn and the Epoch of Reionization through detection of the global 21 cm signal*, Exper. Astron. **45**, 269 (2018), arXiv:1710.01101 [astro-ph.IM].

[474] K. Hoffmann et al., *Signatures of cosmic reionization on the 21-cm two- and three-point correlation function I: quadratic bias modelling*, MNRAS **487**, 3050 (2019), arXiv:1802.02578 [astro-ph.CO].

[475] M. McQuinn and A. D'Aloisio, *The observable 21cm signal from reionization may be perturbative*, J. Cosmology Astropart. Phys. **2018**, 016, 016 (2018), arXiv:1806.08372 [astro-ph.CO].

[476] J. Park et al., *Inferring the astrophysics of reionization and cosmic dawn from galaxy luminosity functions and the 21-cm signal*, MNRAS **484**, 933 (2019), arXiv:1809.08995 [astro-ph.GA].

[477] P. Villanueva-Domingo and F. Villaescusa-Navarro, *Removing Astrophysics in 21 cm Maps with Neural Networks*, ApJ **907**, 44, 44 (2021), arXiv:2006.14305 [astro-ph.CO].

[478] M. McQuinn and R. M. O'Leary, *The Impact of the Supersonic Baryon-Dark Matter Velocity Difference on the z ~20 21 cm Background*, ApJ **760**, 3, 3 (2012), arXiv:1204.1345 [astro-ph.CO].

[479] A. Fialkov et al., *Impact of the relative motion between the dark matter and baryons on the first stars: semi-analytical modelling*, MNRAS **424**, 1335 (2012), arXiv:1110.2111 [astro-ph.CO].

[480] J. B. Muñoz, *Robust Velocity-induced Acoustic Oscillations at Cosmic Dawn*, Phys. Rev. D **100**, 063538 (2019), arXiv:1904.07881 [astro-ph.CO].

[481] A. Font-Ribera et al., *DESI and other dark energy experiments in the era of neutrino mass measurements*, JCAP **05**, 023 (2014), arXiv:1308.4164 [astro-ph.CO].

[482] T. Essinger-Hileman et al., *CLASS: the cosmology large angular scale surveyor*, in Millimeter, Submillimeter, and Far-Infrared Detectors and Instrumentation for Astronomy VII, Vol. 9153, edited by W. S. Holland and J. Zmuidzinas, Society of Photo-Optical Instrumentation Engineers (SPIE) Conference Series (July 2014), p. 91531I, arXiv:1408.4788 [astro-ph.IM].

[483] S. Bryan et al., *Measuring Reionization, Neutrino Mass, and Cosmic Inflation with BFORE*, J. Low Temp. Phys. **193**, 1033 (2018), arXiv:1707.01488 [astro-ph.IM].

[484] T. Matsumura et al., *Mission design of LiteBIRD*, J. Low Temp. Phys. **176**, 733 (2014), arXiv:1311.2847 [astro-ph.IM].

[485] M. Alvarez et al., *PICO: Probe of Inflation and Cosmic Origins*, (2019), arXiv:1908.07495 [astro-ph.IM].

[486] M. Moresco et al., *Constraining the time evolution of dark energy, curvature and neutrino properties with cosmic chronometers*, JCAP **12**, 039 (2016), arXiv:1604.00183 [astro-ph.CO].

[487] S. Mishra-Sharma, D. Alonso, and J. Dunkley, *Neutrino masses and beyond-Λ CDM cosmology with LSST and future CMB experiments*, Phys. Rev. D **97**, 123544, 123544 (2018), arXiv:1803.07561 [astro-ph.CO].

[488] T. Brinckmann et al., *The promising future of a robust cosmological neutrino mass measurement*, J. Cosmology Astropart. Phys. **2019**, 059, 059 (2019), arXiv:1808.05955 [astro-ph.CO].

[489] A. Ashtari Esfahani et al., *Determining the neutrino mass with cyclotron radiation emission spectroscopy—Project 8*, J. Phys. G **44**, 054004 (2017), arXiv:1703.02037 [physics.ins-det].

[490] C. Adams et al., *The Long-Baseline Neutrino Experiment: Exploring Fundamental Symmetries of the Universe*, in Snowmass 2013: Workshop on Energy Frontier (July 2013), arXiv:1307.7335 [hep-ex].

[491] R. Acciarri et al., *Long-Baseline Neutrino Facility (LBNF) and Deep Underground Neutrino Experiment (DUNE): Conceptual Design Report, Volume 2: The Physics Program for DUNE at LBNF*, (2015), arXiv:1512.06148 [physics.ins-det].

[492] R. Acciarri et al., *Long-Baseline Neutrino Facility (LBNF) and Deep Underground Neutrino Experiment (DUNE): Conceptual Design Report, Volume 1: The LBNF and DUNE Projects*, (2016), arXiv:1601.05471 [physics.ins-det].

[493] J. P. Gardner et al., *The James Webb Space Telescope*, Space Sci. Rev. **123**, 485 (2006), arXiv:astro-ph/0606175 [astro-ph].

[494] J. O. Burns et al., *Probing the First Stars and Black Holes in the Early Universe with the Dark Ages Radio Explorer (DARE)*, Adv. Space Res. **49**, 433 (2012), arXiv:1106.5194 [astro-ph.CO].

[495] J. Chluba et al., *Effect of primordial magnetic fields on the ionization history*, Mon. Not. Roy. Astron. Soc. **451**, 2244 (2015), arXiv:1503.04827 [astro-ph.CO].

[496] G. Hutsi et al., *WMAP7 and future CMB constraints on annihilating dark matter: implications on GeV-scale WIMPs*, Astron. Astrophys. **535**, A26 (2011), arXiv:1103.2766 [astro-ph.CO].

[497] J. M. Bernardo, *The concept of exchangeability and its applications*, Far East J. Mathematical Sciences **4**, 111 (2006).

[498] B. de Finetti, *Funcione Caratteristica Di Un Fenomeno Aleatorio*. Atti Dela Reale Accademia Nazionale Dei Lincei, serie 6 **4**, 251 (1931).

[499] J. M. Bernardo and A. F. Smith, *Bayesian Theory*, John Wiley & Sons **405** (2009).

[500] J. O. Berger, J. M. Bernardo, and D. Sun, *The formal definition of reference priors*, The Annals of Statistics **37**, 10.1214/07-aos587 (2009).